UNIVERSITÀ DI PARMA

UNIVERSITA' DEGLI STUDI DI PARMA

DOTTORATO DI RICERCA IN

Scienze del Farmaco

CICLO XXXVI

"Inhibition of *Staphylococcus aureus* iron acquisition: a double approach targeting proteins involved in hemophore and siderophore-mediated pathways"

Coordinatore:
Chiar.mo Prof. Marco Mor

Tutore:
Chiar.mo Prof. Stefano Bettati

Dottoranda:
Monica Cozzi

Anni Accademici 2020/2021 – 2022/2023

Monica Cozzi performed part of the thesis experiments in the following laboratory:

Service de Chimie Bioorganique et de Marquage, Institut de Biologie Frédéric Joliot, CEA Paris-Saclay.

Supervisor: Dr. Jean-Christophe Cintrat

Period: November-December 2023

Potential disruptors of IsdB-Hb complex were synthesized by the group of Prof. Lazzarato (University of Turin). Monica Cozzi validated the molecules' activity. The identified hit compounds were then analyzed by STD-NMR, performed by Prof. Serena Faggiano (University of Parma), to evaluate their binding to hemoglobin.

Potential inhibitors of *Sa*SbnA were identified by structure-based virtual screening and molecular docking by the group of Prof. Francesca Spyrakis (University of Turin), and purchased from Specs (Zoetermeer, Netherlands). Monica Cozzi validated the molecules' activity. The identified hit compounds and molecules that presented solubility issues or were not commercially available were synthesized by the group of Prof. Lazzarato (University of Turin).

Table of contents

Abstract

In the upcoming decades, one of the biggest risks to public health will be antimicrobial resistance (AMR), with *Staphylococcus aureus* being one of the most threatening multidrug resistant pathogens. Indeed, in 2017 the World Health Organization (WHO) drew up a Global Priority Pathogen list for antibiotic-resistant bacteria, indicating *S. aureus* methicillin and vancomycin resistant variants as a “high priority”. Furthermore, during the COVID-19 pandemic, the battle against AMR had faded into the background, contributing even more to its strengthening and diffusion.

Iron acquisition has been demonstrated as a necessity for *S. aureus* pathogenicity in human infections. Indeed, the human host has evolved a defense mechanism, called "nutritional immunity", that regulates iron trafficking in an effort to lessen free iron toxicity and inhibit microbial growth. In turn, *S. aureus* has developed different strategies to overcome the host nutritional immunity, as the hemophore and siderophore-mediated systems for iron retrieval. The former bacterial strategy involves the Iron-regulated Surface Determinant (Isd) system enabling iron acquisition from the host hemoglobin (Hb), while the latter consists of small iron chelators that retrieve the iron bound to host proteins in the extracellular compartment. The Isd system consists of nine proteins, called hemophores, of which IsdB and IsdH are found on the bacterium surface and are involved in Hb binding and in the extraction and transfer of the heme to the downstream Isd effectors. In this context, only IsdB out of the two surface-exposed hemophores has been identified as an *S. aureus* virulence factor, essential for the bacterium pathogenesis. Despite different efforts have been reported in literature to develop antibacterials or vaccines targeting IsdB, no product has become commercially available yet, leaving ground for strategy improvements.
At the same time, *S. aureus* has also evolved strategies for the retrieval of inorganic iron from the extracellular media of the host, mainly involving Staphyloferrin A (SA) and Staphyloferrin B (SB) siderophores. Both siderophores have been identified as *S. aureus* virulence factors, but only SB has been reported to be produced by the most invasive strains, and thus considered to be the greatest support of virulence. Within the SB biosynthetic pathway, the first step is catalysed by SbnA which, in concerted action with SbnB-catalysed reaction, produces two out of three building blocks needed for SB synthesis. The mutation of either *sbnA* or *sbnB* genes resulted in the abrogation of SB production, highlighting the key role of the two enzymes. A complete structural and functional characterization of SbnA has not been reported in literature yet, and no strategies have been described targeting the enzyme. In this context, the characterization of SbnA structural and functional properties and the identification of potential inhibitors would provide a potential combined strategy for the development of new antimicrobials targeting *S. aureus* iron acquisition pathways.

Within the PhD project, an *in-house* developed immunoassay was exploited as a platform for the evaluation of molecules that interfere with IsdB-Hb complex formation. Notably, three commercial compounds, which had been previously identified, were re-synthesized by Prof. Lazzarato group (University of Turin) and evaluated in this thesis by the immunoassay. The group of Prof. Lazzarato synthesized also different analogues for all three compounds, designed to alleviate the solubility and/or stability issues that were previously encountered. No significant improvements in terms of potency were highlighted by the immunoassay when comparing the derivatives to their parent compounds, therefore further modifications will be required.

The thesis project also encompassed the optimization of the conditions for the recombinant expression in *E. coli* and the purification of *Sa*SbnA. The purified protein was characterized in its functional and regulatory properties by spectroscopic techniques, as UV-Vis and fluorescence spectrophotometry, as well as by an *ad hoc* optimized activity assay. Notably, the optimization of a continuous activity assay allowed to confirm that *Sa*SbnA uses a ping-pong kinetic mechanism with substrate inhibition by L-glutamate. After the enzyme characterization, three assays were set up and validated for the evaluation of potential inhibitors of *Sa*SbnA activity. The assays' optimization allowed the assessment of both the effect of potential inhibitors on *Sa*SbnA activity and their direct binding to the enzyme. For the activity evaluation, a discontinuous assay was optimized to provide a high-throughput evaluation of a broad number of molecules to have a first selection for compounds with a significative inhibitory effect. Subsequently, the optimized continuous assay was exploited for the characterization of the mechanism of action of the active molecules, with the determination of inhibition constants. At last, the binding of the active molecules to *Sa*SbnA was evaluated by fluorescence spectroscopy. The defined testing platform was then exploited to study the effect of intermediates of the SB pathway on *Sa*SbnA activity to potentially identify feedback mechanisms. Among the intermediates, citrate was analysed more carefully since previous studies highlighted its inhibitory effect on two other enzymes of the SB pathway, and its presence was identified in a *Sa*SbnA structure (PDB ID 5D85). Indeed, the intermediate was identified as an active inhibitor, highlighting a more complex regulatory mechanism within the SB pathway. At last, the assays were exploited to test in vitro the first set of molecules, with the identification of one hit inhibitor, which was then further characterized, evaluating its mechanism of action, and measuring inhibition constants. A first derivative of the lead compound was synthesized by collaborators at the University of Turin and was tested using the same platform, highlighting a more potent molecule.
The project also involved the production of a second construct for *Sa*SbnA expression, which was designed for high throughput screening (HTS) experiments due to its improved yields. The purified protein was then exploited in an HTS of compound libraries to find potential inhibitors of *Sa*SbnA activity. The discontinuous activity assay was optimized for HTS conditions and then exploited to screen compound libraries made available by the CEA Paris-Saclay centre. The HTS identified seven molecules that inhibited the activity of *Sa*SbnA by 50% or more at 50 µM concentration. These selected hits were confirmed by further analyses and a preliminary characterization allowed to identify the best compounds for further tests and improvements.

Abbreviations

2-PhMA	2-Phenylmaleic acid
α-KG	α-ketoglutarate
AA	α-aminoacrylate
ACEGA	N-(1-amino-1-carboxy-2-ethyl)-glutamic acid
AlaDH	Alanine dehydrogenase
AMMP	2-amino-6-mercapto-7-methylpurine
AMR	AntiMicrobial Resistance
APS	Ammonium
BmcA, BmcB	Baulamycins A and B
CcpA	Catabolite control protein A
CHIPS	CHemotaxis Inhibitory Protein of Staphylococcci
ClfA	Clumping factor A
Cryo-EM	Cryo-Electron Microscopy
Dae	1,2-diaminoethane
DMSO	Dimethyl sulfoxide
DMT1	divalent metal transporter 1
ECMC	ExtraCellular Matrix Component
Fhu	Ferric hydroxamate uptake
Fpn	Ferroportin
FRET	Fluorescence Resonance Energy Transfer
Fur	Ferric Uptake Repressor
GEM	Group Epitope Mapping
Hb	Hemoglobin
Hla-g	hemolysins alpha and gamma
HO	Heme Oxygenase
Hp	Haptoglobin
HPX	Hemopexin
HssRS	Heme sensor system
HrtAB	Heme-regulated transporter

HTS	High throughput screening
IgG	Immunoglobulin G
IL-6	Interleukin-6
IMAC	Immobilized Metal Affinity Chromatography
IPTG	Isopropyl-β-D-1-thiogalactopyranoside
Isd system	Iron-regulated Surface Determinant system
L-Dap	(S)-(+)-2,3-Diaminopropionic Acid Hydrochloride
LB	Luria Bertani
Lf	Lactoferrin
L-Glu	L-glutamate
L-OPS	*O*-phospho-L-serine
Mb	Myoglobin
MD	Molecular Dynamics
MESG	7-Methyl-6-thioguanosine
metHb	methemoglobin
MntC	Manganese transport protein C
MSCRAMMs	Microbial Surface Components Recognizing Adhesive Matrix Molecules
NAD	Nicotinamide adenine dinucleotide
NEAT domain	NEAr iron Transporter domain
NGAL	Neutrophil Gelatinase-Associated Lipocalin
NRAMP1	Natural Resistance-Associated Macrophage Protein 1
Nramp2	Natural resistance-associated macrophage protein 2
OAS	*O*-acetyl-L-serine
OASS	*O*-acetyl-L-serine sulfhydrylase
OCD	Ornithine cyclodeaminase
PAMPs	Pathogen-Associated Molecular Patterns
PBS	Phosphate Buffered Saline
PCR	Polymerase Chain Reaction
PDB	Protein Data Bank

PLP	Pyridoxal 5’-phosphate
PMSF	Phenylmethylsulfonyl fluoride
PNP	Purine Nucleoside Phosphorylase
PPI	Protein-protein interaction
PRRs	Pattern Recognition Receptors
RBC	Red Blood Cell
ROS	Reactive Oxygen Species
SA	Staphyloferrin A
SB	Staphyloferrin B
SdrD-E	Serine-aspartate repeat-containing protein D and E
SEB	Staphylococcal enterotoxin B
SEC	Size-Exclusion Chromatography
Sir	Staphylococcal iron-regulated
SpA	Staphylococcal Protein A
SrtA	Sortase A
SR	Serine Racemase
SrtB	Sortase B
SSMD	strictly standardized mean difference
STD-NMR	Saturation-Transfer Difference - Nuclear Magnetic Resonance
StP	Staphylophine
TCA	Trichloroacetic acid
TCA cycle	Tricarboxylic acid cycle
TCEP	Tris(2-carboxyethyl) phosphine hydrochloride
TEMED	Tetramethyl ethylenediamine
Tf	Transferrin
TfR1	Transferrin Receptor 1
TLR	Toll-Like Receptor
TMB	3,3’,5,5’-tetramethylbenzidine
TR-XSS	Time-Resolved X-ray Solution Scattering

vWbp	von Willebrand factor binding protein
WHO	World Health Organization

Introduction

1 *Staphylococcus aureus*

Staphylococcus aureus is one of the first bacterial pathogens to be recognized [1], and it belongs to the family of Gram-positive cocci Staphylococcaceae. The Scottish surgeon Sir Alexander Ogston was the first to identify and coin the genus Staphylococcus by observing grape-like clusters of bacteria from pus of surgical abscesses [2]. Indeed, the term "Staphylococcus" is composed of two words, *staphyle* and coccus. The first term comes from a Greek word which means bunch of grapes due to the ability of these bacteria to form grape-like clusters. The second term means grain or berry[3]. In 1884, the scientist R. J. Rosenbach was the first to differentiate *S. aureus* from other species of staphylococci based on pigmentation. The epithet "*aureus*", identifying the species, was assigned for the golden pigmentation characteristic of the colonies, which has been associated with more pathogenic Staphylococci strains [4]. Different studies have identified the carotenoid pigments responsible for the colour of *S. aureus* colonies as virulence factors because of their reported antioxidant activity [5–7]. Beyond colour observation, the identification of pathogenic strains is performed also through the coagulase test [8], which assesses the presence of bacterium protein factors that induce the activation of the host coagulation, namely coagulases and the von Willebrand factor binding protein (vWbp). These bacterial proteins interact with prothrombin, activating the host coagulation cascade and thus leading to bacterial encapsulation followed by abscess development [9]. This mechanism is considered a bacterium virulence strategy since it aids in the persistence of the infection and the evasion from the immune system of the host.

1.1 *S. aureus* infections and virulence factors

S. aureus is one of human most common commensal residents that is present on skin, mucous membranes and nares of healthy individuals with a predominant rate for nares colonization of more than 20% of the population [10]. Although commonly asymptomatic, it can give rise to different infections that can be divided into three categories: (i) superficial lesions such as wound infections, (ii) toxinoses as scalded skin syndrome, toxic shock syndrome and food poisoning, and (iii) systemic and life-threatening diseases including infective endocarditis, pneumonia, osteoarticular infections and bacteremia [11,12]. A breach of the sites of commensal colonization enables the bacterium to get access to contiguous tissues and the bloodstream, thus initiating infections [13]. Unlike many other bacterial pathogens which frequently rely on only one or a few toxins to promote disease, *S. aureus* produces an incredible variety of virulence factors. They include a wide range of immune evasion factors and toxins, as well as a large number of protein and non-protein factors that allow host colonization during infection [14]. These effectors' main roles include nutrient uptake, immune evasion, cytolytic activity and host adhesion. Because of their importance, intricate regulatory networks have evolved to control that virulence factors are produced only when it is necessary [15,16]. The virulence factor database (VDB) is an online resource for information about virulence factors of pathogens, and a complete list of the Staphylococci factors is listed at http://www.mgc.ac.cn/cgi-bin/VFs/genus.cgi?Genus=Staphylococcus. With the exception of the diseases brought on by specific toxins, as toxic shock syndrome toxins and enterotoxins, no single virulence factor has been found sufficient to promote a staphylococcal infection [12,17]. The infection is rather driven by the coordinated activity of various virulence effectors, which can be surface-exposed proteins and secreted macromolecules (Figure 1). Moreover, the combination of virulence effectors required to lead to disease is likely to be largely dependent on the site of the infection [18].

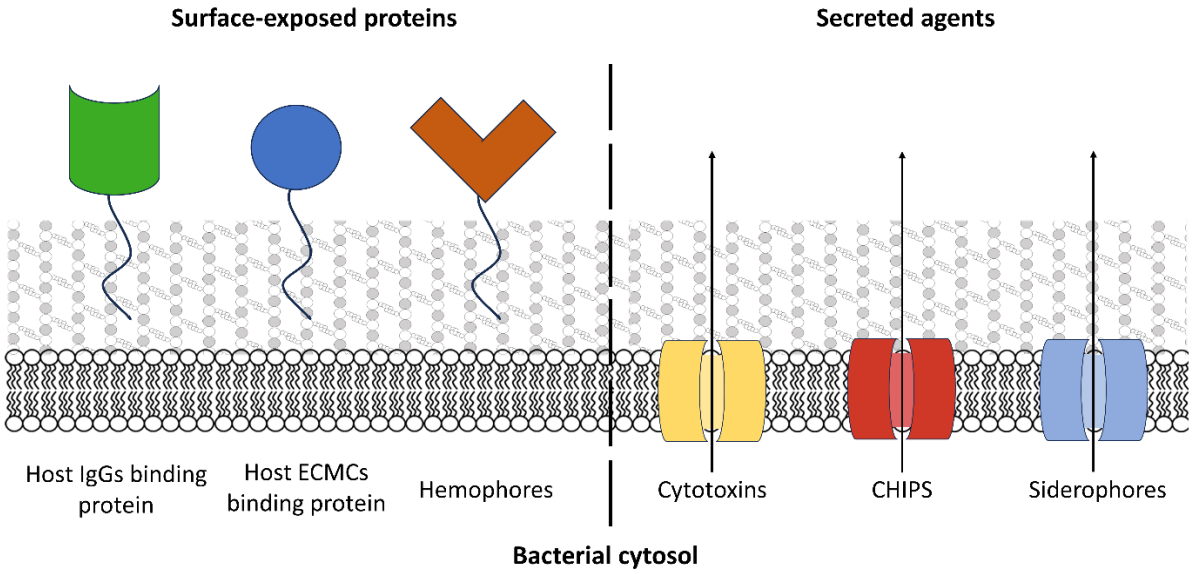

Figure 1: Schematic representation of the *S. aureus* virulence factors that were separated in surface-exposed proteins and secreted macromolecules. Abbreviations used: immunoglobulin G (IgG), extracellular matrix component (ECMC) and chemotaxis inhibitory protein of staphylococci (CHIPS).

1.1.1 Adhesion

S. aureus attachment to the host cell surface allows host colonization and the invasion of tissues and organs from the bloodstream. This course of events requires adhesion and further structural processes mediated by adherence factors [12]. Many of these processes are facilitated by one major class of *S. aureus* adhesins called the Microbial Surface Components Recognizing Adhesive Matrix Molecules (MSCRAMMs) family, which comprises surface-anchored proteins that enable host colonization and immune evasion [14,19]. Originally, the acronym was applied to surface proteins that mediate attachment to the host extracellular matrix components (ECMC, as fibronectin, fibrinogen, and collagen), but more recently the definition has been extended to all the surface proteins that are composed of two adjacent subdomains of IgG-like folds [20]. The majority of the proteins belonging to this family appear to have been naturally selected to perform different functions and this selective pressure is likely due to the limited amount of surface proteins that the bacterium is able to express. Some examples of MSCRAMMs are fibrinogen-binding proteins as clumping factor A and B and the collagen-binding protein Cna [19].

1.1.2 Iron uptake

As many other pathogens, *S. aureus* requires iron for survival [21–23], since it plays a key role in different catalytic processes as the synthesis of DNA, RNA and amino acids, peroxide reduction and electron transport. Humans and many other vertebrates have implemented iron sequestration for its antibacterial effect and this mechanism is part of a type of innate immunity, called nutritional immunity [24,25] (see section 1.3 for details). To counteract this host strategy, *S. aureus* has evolved two advanced types of virulence effectors, hemophores and siderophores, that enable the bacterium to obtain heme-bound and inorganic iron, respectively [26–28]. The primary target of hemophores is hemoglobin (Hb), which however is normally contained inside red blood cells (RBC) and thus, to enhance the amount of free Hb available, *S. aureus* induces the secretion of hemolysins [29]. These latter key virulence factors are pore-forming proteins that induce the lysis of RBC. Furthermore,

heme and free iron may be released by neutrophils and macrophages to induce the production of various bactericidal oxidants in a mechanism called oxidative burst. In such situation, the process of iron retrieval through bacterial acquisition systems lowers the concentration of these microbicidal oxidants thus protecting the pathogen from the attack of the host immune system [30]. *S. aureus* pathogenicity and survival depend on iron uptake and on the bacterium's defence against oxidative damage, which transforms the molecular effectors engaged in both systems into virulence factors [31–33].

1.1.3 Immune evasion

The last class of virulence factor consists of both secreted macromolecules and surface-exposed proteins that interact directly with the host effectors involved in the host immune response. On the bacterial surface, the presence of staphylococcal protein A (SpA) is linked to both opsonophagocytosis failure and B-cell death [34]. To carry out its function, SpA attaches to the Fc portion of the antibody and the Fab portions of the B-cell receptor. Along with SpA, CHIPS and cytotoxins are the two main secreted virulence factors intended to evade the immune system. Notably, CHIPS are able to specifically inhibit neutrophils and monocytes in order to limit the immune system response [35], while examples of cytolytic toxins are leukocidins that act by forming pores onto the leukocytes cell membrane [36].

1.2 *S. aureus* resistance to antibiotics

In 1941, a study conducted before antibiotics development highlighted the huge pathogenicity of *S. aureus* by determining the mortality rate of staphylococcal bacteremia as greater than 80% [37]. Even if *S. aureus* is a valuable target for every antibiotic that is currently in use, its propensity to develop resistance gets the bacterium immune to most of them [38]. This identified propensity is mainly due to its status as an asymptomatic resident in the host [10,39], and the high possibility of strong vertical and horizontal gene transfer [38,40]. In the early 1940s, after the introduction of penicillin, the first *S. aureus* resistant strains were discovered [41], and correlated with the production of the bacterial enzyme penicillinase, which enables the hydrolysis of the penicillin beta-lactam ring, essential for penicillin antibacterial activity [42]. In 1960, methicillin was developed as an antibiotic of the penicillin class that was not subjected to penicillinase activity [43]. Nevertheless, the following year the first *S. aureus* clone resistant to methicillin (MRSA) was discovered [44]. Since then, various MRSA strains have been identified with acquired resistance to a broader array of antibiotics in use [45]. In 1957, an organic chemist isolated a compound from *Streptomyces orientalis* found in a soil sample that was later called vancomycin [46]. In the decade after its discovery, vancomycin was not largely exploited since the drug of choice for the treatment of staphylococcal infections was still methicillin. Nevertheless, vancomycin gained its value after the development and spread of methicillin-resistant strains and is currently the treatment of choice for MRSA-caused infections [47]. The broad and accelerated use of vancomycin induced the insurgence of different resistant strains (VRSA) with different degrees of susceptibility to the antibiotic [46]. All the *S. aureus* resistant variants have a high nosocomial incidence, hence highly increased infection risks for hospitalized debilitated patients and the potential spread within and outside hospitals. *S. aureus*, among five other pathogens, has been listed in the so-called “ESKAPE group” (acronym of the pathogens’ name belonging to the group, hence *Enterococcus faecium*, *Staphylococcus aureus*, *Klebsiella pneumoniae*, *Acinetobacter baumannii*, *Pseudomonas aeruginosa*, and E*nterobacter spp*) since 2008 [48], and in 2017 the World Health

Organization (WHO) drew up a global priority list for antibiotic-resistant bacteria where it indicated MRSA and VRSA as a "high priority" [49].

It is also important to note that several studies have evaluated the impact of the COVID-19 pandemic on *S. aureus* bacteremia and resistance. In particular, a study conducted by Falces-Romero and colleagues reported a higher incidence of *S. aureus* bacteremia in COVID-19 patients over non-COVID patients, as well as over the pre-pandemic period. Moreover, the group also observed a significant increase in mortality by *S. aureus* infections in COVID-19 patients [50]. Even if more studies are required to validate these observations, it is certain that the battle against antimicrobial resistance (AMR) has faded into the background during the COVID-19 pandemic, contributing even more to its strengthening and diffusion. In this context, gaining a better comprehension of the staphylococcal mechanisms of host infection will definitely be the first important step to develop new strategies against this harmful pathogen.

1.3 The human host defence strategy

Living organisms have evolved different mechanisms to counteract invasions by bacterial pathogens that altogether constitute the host immune response. In general, two types of immunity can be distinguished, the innate and the adaptive immunity. The first, also called "natural immunity", consists of the first defence line and reacts to a limited array of antigens that are common to many pathogens, but absent in the host. Whereas the latter, also called "acquired immunity", has evolved to be specific against a single pathogen that has already been encountered by the host [51–53]. In such scenario, cellular immunity, as neutrophils and T-helper cells, participates in both innate and adaptive responses and has been assigned a key role in the host protection against *S. aureus* [54]. Despite the fact that the entire immune system is crucial in the fight against *S. aureus*, this thesis will focus on a particular type of innate immunity known as nutritional immunity.

1.3.1 Innate immunity

S. aureus is an opportunistic pathogen; hence it normally colonizes the human skin and mucosa, but it can become highly pathogenic when it manages to breach the underlying tissues and reach the bloodstream. A distinguishing feature of innate immunity resides in its existence before exposure to pathogens, therefore guaranteeing a very rapid response to invaders. To provide this prompt response, the innate system is set to react to a constrained array of antigens that are normally common and crucial structural components in bacteria [53]. The primary line of defence used to prevent bacterial invasion are indeed physical and physiological barriers, with the first ones being intact skin, the highly acidic stomach environment, a mucociliary clearance system and bacteriolytic enzymes present in the major glandular secretions [55,56]. In support of physical barriers, surface receptors called Toll-like receptors (TLRs) are involved in epithelial recognition of the Gram-positive commensals as *S. aureus* [57], with the ultimate goal being to allow local colonization but preventing systemic invasion. TLRs are surface transmembrane receptors mainly present on dendritic cells and macrophages that stimulate further inflammatory and adaptive immune responses after the recognition of various microbial epitopes [53]. If these early defence strategies are overcome by bacteria, invasion of the surrounding tissues will take place, setting up microbial pathogenesis. The subsequent processes triggered by pathogens exploit pattern recognition receptors (PRRs), which become fundamental for the detection of the pathogen-associated molecular patterns (PAMPs) present on the invaders. The recognition of PAMPs by PRRs activates various defence mechanisms,

that comprise bacterial opsonization, triggering of the complement and coagulation cascades, phagocytosis, induction of pro-inflammatory signalling pathways and apoptosis induction [58]. In support of immune responses to pathogenesis, other advanced systems have evolved in the host to prevent bacteria from accessing free iron, and other trace metals, in a strategy called "nutritional immunity". This process is employed by the host in order to starve pathogens of elements that are necessary for both survival and virulence [24].

1.3.2 Nutritional immunity and iron

1.3.2.1 Iron

A vast array of nutrients makes up the biosphere and has enabled the development of life, with iron being the fourth most abundant metal and the main transition metal in the human body [59]. Almost all living organisms require iron, along with other trace metals, for their survival and its importance is underlined by the fact that both metal excess and deficiency result in the development of several pathologies [60]. Its crucial role in different biological and biochemical processes has evolved due to its chemical properties, in particular the ability to transit between stable ferrous (Fe(II)) and ferric (Fe(III)) oxidation states. Because of these features, iron is utilized in various electron transfer reactions in a wide electrochemical potential (-500 / +500 mV) [61]. In anaerobic and acidic conditions, iron exists in the soluble ferrous form. On the contrary, in aerobic conditions and aqueous solutions, the free ferric oxidation state of iron is highly insoluble, and it forms amorphous hydroxides (the solubility limit is 10^{-18} M) [62]. In this latter form, it requires to be associated with host metalloproteins or hydrophilic chelators in order to be available for biological functions. Indeed, the catalytic activity of components of the oxygenase, oxidoreductase and dehydrogenase families is dependent on non-hemic iron [63–65]. Fe-S clusters play a crucial role in the respiratory electron chain within ferredoxin and are also crucial for iron storage, enzymatic functions, and the modulation of gene expression [66]. On the other side, heme plays a key role in cellular metabolism when attached to cytochromes [67,68], is fundamental for the activity of various catalases and nitric oxide synthases [69,70], and participates in gas sensing, cellular differentiation, and microRNA processing [71–73]. Furthermore, heme is necessary for the binding of oxygen by both Hb and myoglobin (Mb) [74].

Heme consists of an iron atom enclosed within a protoporphyrin IX molecule, altogether forming a macrocyclic molecule (Figure 2). Four pyrrole nitrogens coordinate iron within heme. Since both Fe(II) and Fe(III) favour octahedral coordination geometry [75,76], two additional coordination bonds are formed by hemic-iron, allowing the heme molecule to be embedded within heme-binding proteins and to be able to interact with various ligands. Once the heme molecule is attached to a protein, the two additional axial coordination bonds can either be formed with two amino acid residues, i.e. hexacoordination, or with one amino acid residue and a small molecule, i.e. pentacoordination. Amino acid residues that typically interact with heme are tyrosine, histidine, cysteine and methionine, whereas the main ligands are oxygen, nitric oxide, carbon monoxide and cyanide [75].

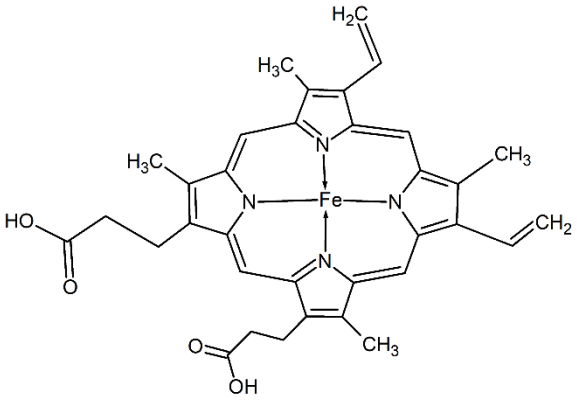

Figure 2: Structure of the heme molecule.

Although essential for many processes, iron is also extremely toxic in the low micromolar range [77]. Indeed, iron can be responsible for the formation of reactive oxygen species (ROS), which are chemical entities that contain oxygen and present unstable bonds or extremely reactive unpaired valence electrons. ROS are either neutral molecules (as hydrogen peroxide), radicals (as hydroxyl radicals), or ions (such as superoxide anion) and they can cause damage to biological macromolecules (lipids, proteins, and nucleic acids), with alteration of the biosynthesis of proteins, lipids and carbohydrates, and an overall impairment of cell proliferation [78,79]. The two chemical redox reactions that define the processes leading to ROS formation were described first by Fenton in 1894, and then by Haber and Weiss in 1974 [80,81].

$$H_2O_2 + Fe(II) \rightarrow Fe(III) + OH^- + OH^{\cdot}$$

$$Fe(III) + O_2^{\cdot -} \rightarrow Fe(II) + O_2$$

In this context, excessive iron concentrations in the biological environment induce ROS accumulation, which in turn is linked to oxidative stress. This latter process has been connected to various diseases as atherosclerosis, carcinogenesis and the insurgence of diabetes and neurodegenerative disorders in mammals [82–84].

1.3.2.2 Iron in the human body: reservoirs and homeostasis

The total quantity of iron in the human body is thought to be between 3 and 5 grams [85,86], and the 70-80% of that iron is contained inside the heme molecule [86,87]. As previously reported, heme is found mostly attached to Hb and Mb for its contribution to aerobic metabolism and delivery of oxygen to peripheral tissue [88]. Indeed, the two main iron reservoirs that exist in biological systems are hemic and non-hemic iron. The first reservoir comprehends the iron contained inside heme, while in the second case, it can be found either by itself as an inorganic cofactor or within Fe-S clusters [66,89]. The importance of iron-binding proteins is due to free iron tendency to become highly insoluble in oxidizing conditions [90]. Moreover, the high iron toxicity and the absence of regulated routes for its secretion make a tight homeostasis indispensable to control iron bioavailability [91]. This meticulous control will also prevent *S. aureus* and many other pathogens from accessing iron, creating what is known as nutritional immunity (Figure 3) [24]. This host antimicrobial strategy enables to limit metal bioavailability, thus counteracting bacterial colonization by metal starvation (iron, but also zinc, manganese and other transition metals) [92]. The following sub-sections of this paragraph

are intended to explain more accurately the processes of host regulation of the free inorganic and heme-bound iron reservoirs.

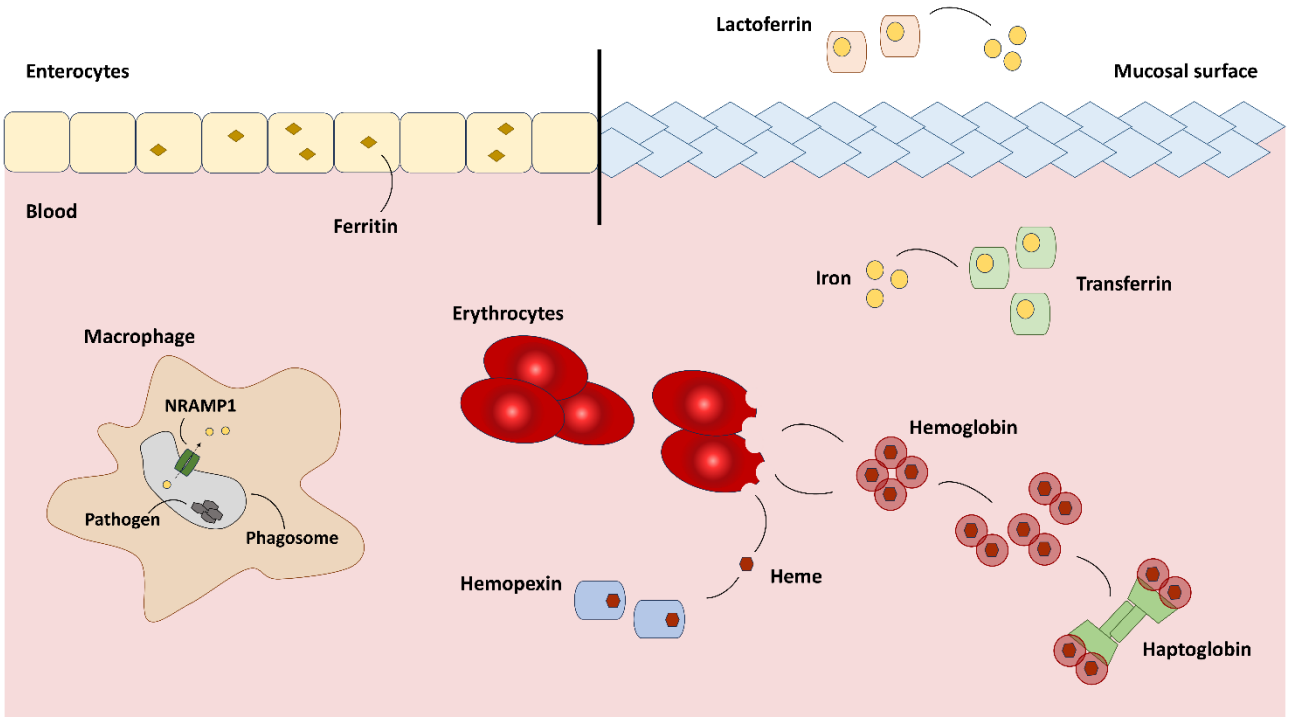

Figure 3: Overview of the host nutritional immunity systems (adapted from Sjodt et al, 2018 [93]).

Hemic iron

As previously reported, the most abundant form of iron in the human body is hemic iron [86,94], which is mostly bound by Hb [88,91,95], that in turn is held inside erythrocytes. Despite the implementation of this strategy to limit bacterial access to this iron source, hemolysis can occur both in physiological and some pathological conditions. Furthermore, *S. aureus* is able to release hemolysins to induce RBCs disruption and gain access to hemic iron [96]. Two host fundamental proteins, haptoglobin (Hp) and hemopexin (HPX), have evolved to counteract both oxidative damage from physiological hemic-iron release and pathogen access to this reservoir [97–99]. When Hb leaks from RBCs and is diluted in the bloodstream, the physiological Hb tetramer has the tendency to dimerize and heme is prone to oxidize and be released from Hb [100]. In this context, the role of Hp is to eliminate free Hb from the vascular compartment, by binding the Hb dimer with an exceedingly high affinity having a K_D lower than 10^{-12} M [101,102]. The mechanism of clearance starts with Hp stabilization of Hb, which is followed by the identification of the Hp-Hb complex by CD163 macrophage scavenger receptor [103]. Once recognized, the complex is internalized into macrophages, Hb is then degraded inside lysosomes and a specific oxygenase called HO-1 disassembles heme in order to release iron and bilirubin [104]. Hp is mostly produced by the liver under physiological conditions and it is found in plasma with a concentration between 0.5 and 3 g/L, an amount that allows for Hb removal when mild hemolysis occurs. In addition to physiological conditions, Hp is also an acute-phase protein, hence its expression is strongly increased (up to 5-fold) when pro-inflammatory cytokines (as interleukin-6 (IL-6), IL-1 and others) are produced due to the development of infection and inflammation [105,106]. Another correlated function of IL-6, along with other ILs, is the induction of expression of HO-1 oxygenase and CD163 receptor [107,108]. Three different phenotypes of Hp can be found among

humans (Hp1-1, Hp1-2 and Hp2-2) which derive from two distinct Hp variants, Hp-1 and Hp-2. The three phenotypes are correlated to different features, hence changes in the quaternary structure, in the binding to the CD163 receptor and differences in Hb affinity [102,109]. The population that presents the Hp2-2 phenotype is more susceptible to vascular risk and worse outcomes of infections. This is due to this phenotype's reduced affinity for Hb, which translates into a decreased plasmatic clearance of Hb and hence a more severe oxidative damage [110]. Apart from free Hb, which may release heme before being bound by Hp, additional hemoproteins trigger the loss of the prosthetic group into the bloodstream. Physiologically, free heme gets secured inside albumin through a non-specific medium-affinity binding (around 10^{-8} M), that is then substituted with a high affinity binding by HPX (K_D below 10^{-12} M) [111]. The acute-phase glycoprotein HPX, whose expression is strongly correlated with IL-6 and other ILs, may be overexpressed during infections, when free heme concentration may rise [112,113]. The heme-HPX complex gets then recognized by the CD91 receptors present on hepatocytes [114], where an oxygenase specific for heme degrades it in order to recycle iron [99].

Non-hemic iron

Non-hemic iron accounts for the 20-30% of the whole human amount, since the larger iron pool is secured inside the heme molecule. Furthermore, free iron is essentially lacking in mammals, due to its extremely low concentration (less than 10^{-20} M) [115], which is even lower than its 10^{-18} M solubility limit. The iron concentration that bacteria actually need is about 10^{-6} M [116], making such a small amount a perfect example of host nutritional immunity. Non-hemic iron is therefore found attached to different host iron-binding proteins, as transferrin (Tf) [117], ferritin [118] and lactoferrin (Lf) [119]. These three effectors not only control the amount of iron available, but they also guarantee metal transit and storage throughout the body, protecting against iron-dependent oxidative damage. Other minor non-hemic iron reservoirs are Fe-S clusters and iron-dependent enzymes [120]. The majority of the host non-hemic iron pool is stored within ferritin (up to 30% of the whole amount) [121], while the other small portion (around the 0.1%) is managed by the Tf family, which comprehends both Lf and Tf [121,122]. The first iron-storing protein, ferritin, is found mainly inside enterocytes, but also in hepatocytes, erythroblasts and macrophages [123]. Ferritin is a heteropolymeric protein, almost ubiquitous in living organisms because of its essential part in iron metabolism, being involved in both iron detoxification and storage [124]. To reach ferritin localization in the cell, iron gets imported by the specific divalent metal transporter 1 (DMT1) [125], also called natural resistance-associated macrophage protein 2 (Nramp2) [126,127]. At this point, ferritin can incorporate up to 4500 iron ions in crystalline form, which is mainly made of phosphate ions and ferrihydrite [124]. Unlike ferritin, which is localized inside cells, Tf and Lf exert their functions in the extracellular compartment. The former protein is a serum transporter of non-hemic iron throughout the body [128], after it has acquired the metal liberated from lysed cells or the one absorbed from the gut. For Tf to bind iron, the membrane protein ferroportin (Fpn) needs to trigger the release of dietary iron on enterocytes' basal side [123] or the release of the stored iron in hepatocytes. The expression of Fpn on both enterocyte and hepatocyte is mutually controlled, indicating that both participate in iron homeostasis [129,130]. Finally, Fpn is found on macrophages, which are the second-largest host reservoir for storing inorganic iron [120], and where Fpn is predicted to function similarly as on hepatocytes. It's interesting to note that nutritional immunity is directly impacted by the modulation of Fpn expression. Conversely, the erythropoietic process uses the majority of the Tf-bound iron, by incorporating it into the heme molecule and ultimately into Hb [121]. The main Tf properties are its high affinity for iron, with an

estimated K_D of about 10^{-20} M or even lass [115,131,132], and the molar excess compared to free non-hemic iron since the physiological saturation of Tf is around the 30%. This condition guarantees that there is almost no free iron present in the organism [133]. To convey the metal, Tf engages in interaction with a specific receptor (TfR1) that is exposed on the cells that require iron delivery. The cellular intake of iron starts once Tf and its receptor form a complex, after the so-called Tf cycle has taken place [134]. Three main steps compose this Tf cycle, starting with recognition of the iron-Tf complex, followed by the internalization of the complex into specific endosomes, and the ultimate pH-dependent iron release within these dedicated intracellular organelles. At the end of the Tf cycle, the iron that has been released from Tf gets pumped out of endosomes into the cytosol by the DMT1 transporter [135], inducing apo-Tf transport back to the extracellular compartment. The other component of the Tf family is Lf, which is responsible for iron chelation in breast milk, tears, saliva and seminal fluid [132], but it can be also released by neutrophils when there is an infection or an inflammatory condition [136]. While Lf's affinity for iron is comparable to Tf's (K_D lower than 10^{-20}), Lf unique capacity to maintain iron affinity in extremely acidic environments (down to pH 3) is essential to guaranteeing iron activity in infection/inflammatory areas [132,136,137]. Moreover, Lf's proteolytic activity demonstrates a direct bactericidal effect [115,131], most likely via a serine protease mode of action. It's interesting to note that previous studies have reported the abrogation of Lf antimicrobial activity in *S. aureus* when there is either a specific serine proteases' inhibitor (phenylmethylsulfonyl fluoride - PMSF) or the staphylococcal hemophore IsdA [138]. Remarkably, Lf is among the most prevalent antistaphylococcal proteins found in human nasal secretions, and its function may be supported by its proteolytic activity [138].

Iron homeostasis becomes significantly more complex when bacterial pathogens attack the host, requiring the strengthening of nutritional immunity. A portion of the proteins involved in nutritional immunity are referred to as "acute-phase proteins" because their expression is regulated, typically increasing, in the early stages of infection. The first issue may result from the conflict between macrophages' iron intake through DMT1, which is intended to store the metal for the oxidative burst, and intracellular bacterial pathogens residing in phagosomes, which may profit from the elevated iron concentration at their colonization site. In this context, the specific natural resistance-associated macrophage protein 1 (NRAMP1) drives iron out of the compartment, inducing bacterial iron starvation. Extracellular bacterial pathogens have evolved multiple strategies in order to retrieve iron when host nutritional immunity works to limit its availability. Small molecules known as siderophores are among them; they have an exceptional affinity for non-hemic iron, and they are secreted by bacteria, that later on internalize them as iron-siderophore complexes. To counteract invasive bacterial strategies, the host nutritional immunity induces Tf expression [139]. Furthermore, neutrophils release a specific pool of proteins known as siderocalins (also known as neutrophil gelatinase-associated lipocalin, or NGAL) that interact with bacterial siderophores (both in the apo and iron-bound form) with a high affinity, blocking bacterial retrieval [140,141].

A more refined strategy for iron starvation of pathogenic bacteria depends on hepcidin, a small peptide hormone expressed mostly by hepatocytes [123]. Active erythropoiesis and hypoxia suppress hepcidin expression in the liver, but lower plasmatic iron concentrations increase it [142,143]. Hepcidin has a critical role in modulating cellular iron efflux by its interaction with Fpn [123], the primary enzyme involved in iron intake and mobilization from metal reservoirs [129,130]. Hepcidin and Fpn interact directly, and once the hepcidin-Fpn complex is created, its internalization and degradation are

triggered [130]. As a result of hepcidin release, there is less iron absorbed in the bowel and also less stored in the reservoirs.

1.4 The bacterium response to nutrient availability

The typical sign of a staphylococcal infection is shown in the development of purulent abscesses, which have been reported to occur in four stages [144]. The bacteria commence their dissemination to peripheral tissues in the first stage, as they attempt to remain alive in the bloodstream. The second stage requires that pathogenic cells arrive at the tissue site where the abscess would be formed. The development of a huge mass of invading bacteria identifies stage three. When the mature abscess finally ruptures its borders in stage four, bacteria spread out and new infection sites are formed. Crucial nutrients are required in the setting of stage two. Because of host nutritional immunity, iron is one of the hardest nutrients to recover. To address the issue, *S. aureus* can modify its expression profile by the ferric uptake repressor (Fur) modulation [137], and induce a metabolic rearrangement to survive in iron-restricted conditions, in a process called the iron-sparing response [145].

1.4.1 Fur transcriptional regulation

The main effector of *S. aureus* response to nutrient availability is the repressor Fur, which is a widely conserved transcription factor that can be found in almost all gram-negative and gram-positive bacteria. Fur regulatory system comprises both direct and indirect control of the genetic targets. It acts primarily as a gene repressor, sensing the intracellular iron concentration by taking advantage of Fe(II)'s corepressor properties. This system allows the bacterium to maximize the control of iron concentrations both inside and outside of cells. Nevertheless, different studies have highlighted that Fur can also be needed as an activator of the expression of different genes [146–148], implying a complicated multifactorial effect on bacterial metabolism. Notably, studies have shown a direct correlation between the presence of Fur and the pathogenicity of harmful bacteria [149]. This is also true for *S. aureus*, as Fur controls the expression of nearly every protein that is recruited by the pathogen for iron acquisition [27,137,150]. To regulate gene transcription, Fur recognizes a specific 19-bp target sequence, referred to as the "Fur box", overlapping the binding site for RNA polymerase. Therefore, when ferrous iron is replete in the cell, it acts as a corepressor by forming a Fe(II)-Fur complex that can bind the specific Fur target sequence, thus effectively preventing RNA polymerase from getting in contact with the promoter [151]. Interestingly, Fur has low-micromolar affinity for iron, whereas the repressor's holo-form has a nanomolar affinity towards its DNA target. On the other hand, Fur mutants unable to bind iron cannot identify and interact with their corresponding DNA target sequence. When the concentration of iron within the bacterial cell decreases, the Fe(II)-Fur complex gets dissociated from the DNA, releasing Fur that in turn allows the transcription of the Fur-modulated genes [152]. In the context of iron acquisition, Fur regulates almost all the *S. aureus* genes that are involved in heme uptake, siderophore-mediated iron absorption, and ferrous iron uptake; i.e the operons comprehend *fhu*, *sir*, *sbn*, *hts*, *sfa* and *feo* [153–156]. Beyond its involvement in iron acquisition, Fur has been shown to modulate the expression of genes encoding for immunomodulatory and virulence factors as well as genes involved in oxidative stress response, reinforcing *S. aureus* ability to survive in the host environment [15]. Indeed, Fur broad regulation suggests its essential role in several aspects of infection establishment [148,157]. An excellent example concerns the transcriptional modulation of KatA, a catalase that controls oxidative stress, which is

directly regulated by Fur [147]. This function is performed in combination with the transcription regulator PerR, which is in turn in charge of modulating the expression of Fur, bacterial ferritins MrgA and FtnA, and alkyl hydroxyperoxide reductase AhpC [147,158,159]. Contrary to the typical mode of action, a previous study revealed that Fur regulates the expression of the Eap/Emp pathway, implicated in biofilm production, in an iron-independent manner [146]. Moreover, Fur acts also concertedly with various other transcription factors (i.e. Sae, Agr and Rot), as in the case of the transcriptional modulation of IsdA and IsdB hemophores, regulated by both Fur and Sae [148]. The ultimate significant effect of Fur transcriptional regulatory network is most likely accomplished by small regulatory RNAs (sRNAs)-dependent regulation [160,161], which in turn affects the modulation of the tricarboxylic acid (TCA) cycle. This process is included in a broad Fur-dependent response towards low-iron stress, called the "iron-sparing response", which will be further discussed in the next paragraph.

1.4.2 The-iron sparing response and the effect on central metabolism

In condition of iron depletion, *S. aureus* undergoes a general metabolic rearrangement modulated through the Fur regulatory network, with the aim to reduce the bacterial iron demand. This reaction to low-iron stress is called "iron-sparing response" and has also been found in other bacteria besides *S. aureus* [162–165]. In physiological conditions, *S. aureus* metabolism consists of a sophisticated network of tightly regulated enzymes that supply the cell with energy, but also provide a wide range of metabolic building blocks that enable cell division and growth. The primary metabolic engine is central metabolism, which comprises the glycolytic and pentose phosphate pathways and the TCA cycle [3]. The first two are responsible for the entrance of carbohydrates within central metabolism and their catabolism to pyruvate. The latter pathway occurs when pyruvate is converted to acetyl-CoA and it is crucial for the cell's ability to generate a reducing potential and for providing the building blocks required for anabolic pathways such as the production of amino acids and nucleic acids [3]. The preferential *S. aureus* carbon source is glucose, and the catabolite control protein A (CcpA) regulates its utilization [166,167]. Furthermore, CcpA modulates the TCA cycle by down-regulating it when there is a high glycolytic activity [168]. The downregulation of the TCA cycle occurs also within the iron-sparing response since different iron-dependent metabolic pathways are repressed. As anticipated in the previous paragraph, the most probable effectors of the Fur metabolic control are sncRNAs, which are small non-coding RNA sequences acting as post-transcriptional regulators [169]. Within the iron-sparing response, a recent work by Coronel-Tellez and colleagues highlighted the need for the IsrR sRNA to provide optimal growth of *S. aureus* in iron-restricted conditions [145]. Other recent works have studied sRNA S596, which is regulated by Fur and is homologous to *E. coli* RhyB [170]. sRNA S596 is expected to suppress the expression of iron-correlated genes and TCA cycle enzymes, such as citrate synthase CitZ, hence regulating the generation of Staphyloferrin A (SA) [160,161]. Due to the repression of iron-dependent genes involved in key metabolic processes, *S. aureus* needs a way to compensate for its energetic requirement in iron-restricted conditions. The bacterium strategy is thus the up-regulation of the fermentative pathway, leading to lactate production, which in turn decreases the pH in the extracellular compartment after being exported out of the bacterial cell. Because Fe(III) is more soluble at lower pH values and Tf's affinity for iron is reduced, iron bioavailability is thus increased [137].

A more detailed discussion of the inter-connection between fur-regulated iron acquisition and central metabolism rewiring under iron restriction will be addressed in the chapters about *S. aureus* pathways of iron acquisition.

1.4.3 *S. aureus* iron homeostasis

As for most organisms, an excess of iron within the cell becomes very toxic for *S. aureus*, which is able to store or excrete the surplus of nutrients. The bacterium mechanisms to deal with iron surplus depend on the nutrient form. Indeed, the detection of heme excess is responsibility of the heme sensor system (HssRS), which subsequently upregulates the expression of the heme-regulated transporter (HrtAB). The HrtAB is an efflux pump involved in the detoxification of the prosthetic group [171–174]. If not excreted from the cell, heme is broken down by dedicated heme oxygenases (i.e. IsdG-I) to release iron for metabolic purposes [150]. Another mechanism of heme degradation is performed by FepB, part of the tricomponent protein system (FepABC) and regulated by Fur. FepB is able to bind heme outside the bacterial cell, reduce iron to get it out of the porphyrin ring that remains intact, and then acquire the metal through FepA/FepC-mediated internalization [175,176]. Although its exact function is yet unknown, it has been suggested that this system lowers the extracellular hemic-iron concentration, thus reducing the oxidative burst [176]. On the other hand, non-hemic iron gets stored by bacteria as a building block, when it is not required. Indeed, the expression of ferritin FtnA, similar to other eukaryotic and bacterial ferritins, allows *S. aureus* to store high quantities of non-hemic iron. Additionally, *S. aureus* produces a DNA-protecting effector (MrgA) and a hydroperoxide scavenger (AhpC) to counteract oxidative damage caused by the transient iron excess. Peroxide-responsive repressor (PerR), which collaborates closely with Fur to protect *S. aureus* from iron-related oxidative stress, is in charge of orchestrating FtnA, AhpC, and MrgA [158,159,177]. At last, the regulation of non-hemic and hemic iron processes is intertwined since heme can act as a transcriptional repressor of genes involved in the biosynthesis of the *S. aureus* iron scavenger Staphyloferrin B (SB) [178,179].

The whole complex machinery that is set in motion by *S. aureus* in iron depletion gives an idea of the essential role that iron has in bacterial growth and infection. The following chapters will therefore discuss in-depth the strategies that the bacterium has evolved to acquire iron from the host.

2 *S. aureus* iron uptake systems

In the previous sections, it has been illustrated the crucial role of iron for both the host and the pathogen, highlighting the power play that is created between the two in obtaining this nutrient. This section will focus on the molecular mechanisms that have been developed by *S. aureus* to acquire iron from the host, thus counteracting human nutritional immunity. Since iron uptake appears to be essential for *S. aureus* infection, most of these systems have been identified as virulence factors, making them attractive targets for antimicrobial therapy. Figure 4 sums up *S. aureus* iron acquisition pathways, representing the genetic loci and the proteins involved in the process.

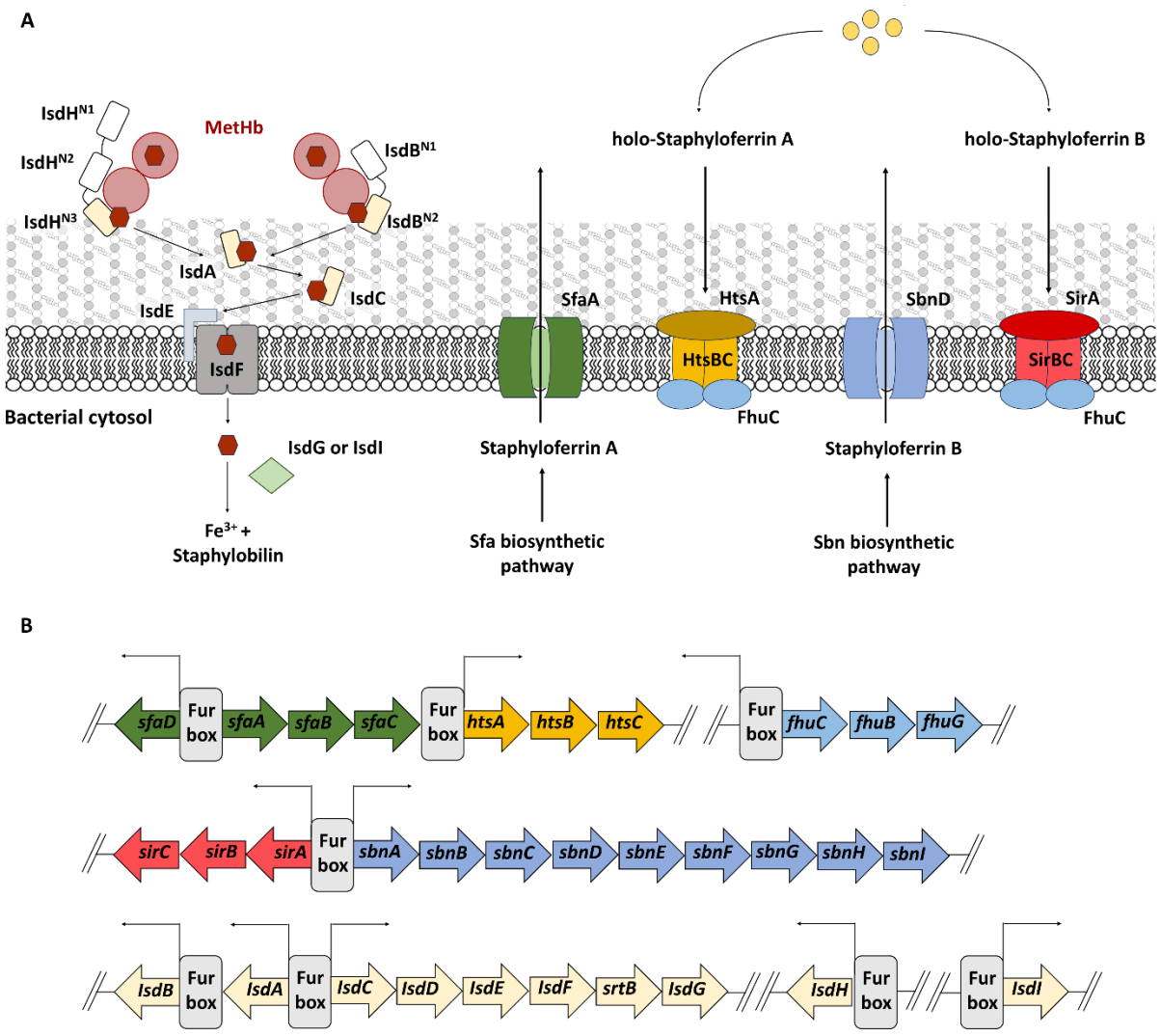

Figure 4: Summary of the iron acquisition pathways adopted by *S. aureus*. (A) Representations of the proteins involved in the iron acquisition process (adapted from Hammer et al, 2011 [23]). (B) Genetic loci employed in *S. aureus* iron acquisition (adapted from Hammer et al, 2011 [23]).

2.1 Heme acquisition system

The *S. aureus* preferred source of iron is heme, and deficiency of the prosthetic group was shown to impair bacterial virulence [180–183]. This preference may have something to do with more effective iron source systems, but it is also correlated with the high amount of hemic iron (up to 70%) in the human body. A fundamental pathway for heme retrieval is the Isd system, which acquires the prosthetic group from human metHb [181]. This latter host protein is the transporter of hemic iron in the oxidized state, and it represents the most prevalent form of Hb as free in the bloodstream, making it likely the only form that is accessible to bacteria. After heme internalization, the Isd system is able to release iron by the action of dedicated heme oxygenases. Nevertheless, a “heme hijacking hypothesis” has been made stating that *S. aureus* would be able to also use the intact heme molecule as prosthetic group [180,184], as in cytochrome biosynthesis. The preference for heme, particularly in cases of iron deficiency, may be partially explained by the bacterium's ability to save metabolic energy through this latter process. Similarly, enlisting cell-wall attached hemophores of the Isd system offers a more economical approach than siderophore production, which can disperse from

the colonization site or be stolen by other bacterial cohabiters [185]. Like many other bacteria, *S. aureus* has developed hemolysins to get access to Hb transported inside erythrocytes. Under iron deprivation, Fur promotes the development of the pore-forming α-toxin (Hla), which is primarily responsible for hemolysis, indicating a connection between Hla and *S. aureus* response to the host nutritional immunity [157]. The capacity of the bacterium to proliferate in the presence of erythrocytes as the only source of iron is a strong indicator of the effectiveness of this mechanism [181]. Other than Hb, also HPX, Mb, and cytochromes can bind the prosthetic group, even if in lesser amounts, and are possible *S. aureus* targets. In reality, HPX doesn't appear to promote *S. aureus* growth, and eventually, the bacteria cannot access cytochromes inside mitochondria [181]. On the other hand, because Mb and the Hb monomers are structurally similar, the first human protein might be a target for the bacteria. The ability of *S. aureus* to successfully colonize Mb-rich myocytes supports Mb's potential role as heme supplier [96,186], even though a clear mechanism is still unknown.

2.1.1 Hb, *S. aureus* preferred iron source

Hb is found within RBCs in physiological conditions as a tetramer of α and β globins (the homodimer is $\alpha_2\beta_2$ of the heterodimer αβ). Each subunit, also referred to as "chain", binds one heme molecule [187]. α-Hb chains are made up of 141 residues forming seven helices joined by short loops, whereas β-Hb chains are composed of 146 residues forming eight helices. RBCs represent the main human source of iron since every erythrocyte contains around 280 million Hb molecules and over one billion iron atoms [188]. Since Hb is highly packed inside RBCs, with a concentration nearly up to 2 mM [75], it gets maintained in its tetrameric form (the K_D of the dimer-tetramer is calculated in the low micromolar range [189,190]). The RBC reductive compartment keeps iron in the ferrous state, which is key for erythrocytes' function since the only form that can bind oxygen is reduced Hb. Within this arrangement, oxygen can be acquired optimally inside the lungs and released to the tissues thanks to the maintenance of the Hb quaternary structure, which in turn preserves the Hb-oxygen positive cooperativity. However, hemolysin-mediated RBC lysis or natural RBC turnover could result in the presence of free Hb in the bloodstream [191]. In this environment, the Hb concentration is significantly lowered, around the μM range [192], and the previously mentioned reductive processes get lost, leading to protein dimerization and heme oxidation [193]. This latter state, namely Hb as metHb, is the only form that can be exploited by pathogens for iron acquisition. Indeed, both IsdB and IsdH are able to extract heme only from ferric heme, even if they can bind both the oxidized and reduced Hb forms [194,195]. This has led to the use of oxyHb and HbCO (reduced Hb in which heme groups are saturated with CO, instead of the physiological ligand O_2) in several *in vitro* studies to avoid heme extraction and assess the pure interaction of the hemophores with Hb chains [196–200]. Moreover, previous studies reported a preference of different *S. aureus* strains towards human Hb as sole iron source over Hb from other mammals. *In vitro* analyses revealed that IsdB has a higher affinity for human Hb than for the murine protein and *in vivo* studies identified a more efficient *S. aureus* colonization of mice that express human Hb[201]. All these findings corroborate the presence of an evolutionary pressure on IsdB by human Hb, which was also identified by phylogenetic studies that highlighted the positive selection of IsdB and Hb at sites involved in their interaction, thus showing a rapid co-evolution and ultimately an intertwined path [202,203].

2.1.2 The Isd system and its moonlighting functions

Heme is the *S. aureus* preferred source of iron, and it is acquired from metHb [181], where it can be found in the oxidized state. In the bloodstream, metHb is the most abundant form of Hb, and it also the only form that can be exploited by bacteria. After hemolysins release Hb from erythrocytes, the Isd system comes into play. Indeed, the Isd system comprises nine proteins (IsdA-I) that allow the bacterium to acquire heme from the host. The process of iron acquisition through this system requires 4 main steps: heme extraction from metHb, transfer through the cell wall, internalization in the cell compartment, and degradation [21,26,27,41,180,184,198,204–211]. The presence of a fur box upstream of the Isd operon allows for an iron-regulated expression of the genes encoding for hemophores, thus enabling *S. aureus* to counteract the iron restriction imposed by the host [21,152,212–214].

From heme extraction to heme degradation

Four proteins anchored to the cell wall and also known as hemophores (heme carriers) are responsible for the first two steps of the acquisition process [215]. These four proteins are divided in two surface-exposed receptors for Hb, called IsdB and IsdH, and IsdA and IsdC hemophores which are partially and completely embedded into the cell wall, respectively (Figure 4). Two sortases are responsible for covalently linking the hemophores to the peptidoglycan: sortase A (SrtA) and sortase B (SrtAB). SrtA is ubiquitous in bacteria, and its gene is under the transcriptional control of Fur but located outside the Isd locus. As SrtA, also SrtB is controlled by Fur but it is located in the Isd cluster, and is the specific sortase of the Isd system [23,26,27,216–221]. SrtA detects a specific molecular pattern, composed of an LPxTG motif and a hydrophobic domain, which is located at the C-terminal portion of IsdB, IsdH and IsdA [213,222]. This sortase catalyses a transpeptidation reaction that enables the attachment of the three hemophores to immature peptidoglycan [223]. Comparably, SrtB is responsible for the attachment of IsdC to the cell-wall, through the recognition of another binding motif, NPQTN [224]. As previously mentioned, the four hemophores are responsible for the first stages of acquisition, heme extraction and transfer through the cell wall. Specifically, the whole process starts with metHb being bound by the two Hb receptors, IsdB and IsdH, exposed on *S. aureus* surface [27,225,226]. After having captured metHb, the two hemophores extract heme and in their holo-form (with heme bound), they are able to transfer the prosthetic group unidirectionally to IsdA [208,209,227]. IsdA then selectively passes heme to IsdC [208,228,229], which then transfers it to IsdE, a heme-specific lipoprotein found on the outer leaflet of the cellular membrane [208,211,230]. The simple transfer of heme by sequential involvement of the four hemophores may not be sufficient for heme to reach the cellular membrane because the cell wall of *S. aureus* is quite thick (approximately 30-100 nm) [221,231]. A potential strategic solution lies in the presence of multiple copies of IsdA and IsdC within the cell wall and the ability of the two hemophores of self-transferring heme, thus possibly allowing the heme transport through the whole peptidoglycan layer [231]. A relay mechanism has been reported in previous *in vitro* studies where a catalytical concentration of IsdB was found to promote the transfer of the cofactor from metHb to IsdA, and through the same process IsdA then was seen promoting the transfer from IsdB to IsdC [195,198,209]. The transfer of the cofactor between the cell-wall anchored hemophores does not require energy supply because the process is carried forward by an increase in hemophores' affinity for heme going from the environment to the cellular membrane [197,229,231,232]. Another driving force in the transfer relies on the formation of ultra-weak complexes between hemophores, thus inducing a transient distortion in the structure of the heme donor binding pocket, leading to the release of the cofactor away from it [210,231]. Indeed, the last highly specific step of heme

transfer from IsdC to the membrane transporter IsdE is allowed by an ultra-weak interaction [231]. The specificity of this last exclusive transfer from IsdC, and not IsdA, to IsdE derives from the difference in the IsdA and IsdC primary sequences, at the level of their interaction region with IsdE [209,231]. Because IsdC and IsdE have a comparable affinity for heme [26], the *in vitro* transfer of the cofactor was found to be "thermodynamically paralyzed" [209,211]. Nevertheless, in *in vivo* conditions, the process is expected to be carried towards the IsdC-IsdE transit since the following step is the internalization of holo-IsdE by means of the Isd ABC transporter (IsdD, IsdE, IsdF). In Gram-positive bacteria, ABC importers are responsible for substrate transfer through the cell membrane, and they are composed of three subunits with distinct functions, a substrate-binding lipoprotein coupled to the extracellular membrane leaflet, a membrane permease and a cytosolic ATPase. In the Isd system, the first heme-binding subunit is represented by IsdE, the permease is IsdF and the last subunit results to be a general ATPase for *S. aureus* iron acquisition systems, called FhuC [230]. The role of the third Isd membrane-anchored protein, IsdD, is not fully known yet, and no other homologs have been discovered in Gram-positive bacteria [93,233]. Nevertheless, it seems to be a component of the Isd pathway since it presents the heme-binding motif, its gene is encoded within the Isd locus [26], and its expression is found up-regulated in MRSA strains under iron-starvation [234]. IsdE is a class III periplasmic protein [235–237] that binds and coordinates heme in hexacoordinated state by interacting with the 229-positioned histidine residue and the 78-positioned methionine residue. These interactions enable the specific selectivity of heme transfer from IsdC over IsdA [205,211,238,239]. Interestingly, only His229 residue was identified as fundamental for heme acquisition both *in vitro* [231] and *in vivo* [238], even if both His229 and Met78 were observed in the electron density map in crystallographic data. The last step of cofactor internalization is performed by IsdF ABC permease, which transfers IsdE-bound heme into the cytoplasm [26,238]. Once heme gets internalized into the cell, it can be either exploited directly as a cofactor for cellular functions or degraded in order to release inorganic iron. In this latter case, *S. aureus* Isd system exploits two heme oxygenases (HOs), IsdG and IsdI, that enable heme degradation with the release of free iron, two distinct staphylobilins and formaldehyde [240]. Both HOs are different from canonical bacterial oxygenases, being able to cleave either at the β- or the δ-meso carbons of the porphyrin ring instead of the common cleavage at the α-meso carbon [240,241]. Since the two *S. aureus* heme degrading enzymes were discovered [242], several IsdG homologs have been found and studied in Gram-positive bacteria [181,243,244] leading to the development of the new "IsdG-family" of HOs. This IsdG-family is characterized by a shared requirement of a NADPH-dependent reductase, IruO in the case of *S. aureus*, which supports heme degradation by catalysing the reaction at the maximum rate [245]. As for the other proteins of the Isd system, IsdG and IsdI expression is regulated by Fur at the transcription level. Both oxygenases are needed for *S. aureus* virulence [150,214], but a recent study from Conger and co-workers identified different biological roles of the two HOs, with IsdG being overexpressed under iron restriction, while IsdI being constitutive and minimizing iron toxicity [246].

Hemophores' NEAT domains

Despite different degrees of sequence identity, hemophores are modular proteins that contain one or more NEAr iron Transporter (NEAT) domains. These domains are made up of about 125 amino acids and are distinguished by an eight-stranded β-sandwich fold that is similar to that of immunoglobulins [23,197,247–251]. These modular domains have been divided into two primary categories, known as "Hb-binding" and "heme-binding" domains, depending on the interactor with which this binding region comes into contact. The "Hb-binding" domain allows a close interaction between the

oxygen transporter and the two surface-exposed receptors IsdB and IsdH, that are composed of one ($IsdB^{N1}$) and two ($IsdH^{N1}$ and $IsdH^{N2}$) domains, respectively [227,252]. Various studies have extensively worked on finding key residues responsible for the affinity towards Hb [196,252–258], and managed to identify a "Hb binding region" containing a coil (loop 2) that undergoes a disordered to α-helix transition upon binding [254,259]. The region's interaction with helices A and E of Hb results to be crucial for complex formation [195,255–257,260], with the presence of hydrophobic residues that seem fundamental for protein reorganization [200,254,256]. In hemophores' Hb-binding domains, key residues composing a specific sequence called "Hb-binding motif" (represented in Figure 5) have been identified as essential for complex formation since an amino acid substitution in this sequence hinders the formation of the complex [196,261,262]. The Hb-binding motif sequences of $IsdB^{N1}$ and $IsdH^{N2}$ are equivalent, while $IsdH^{N1}$ shows some residue changes that cause its selective binding to α-chains of Hb [255].

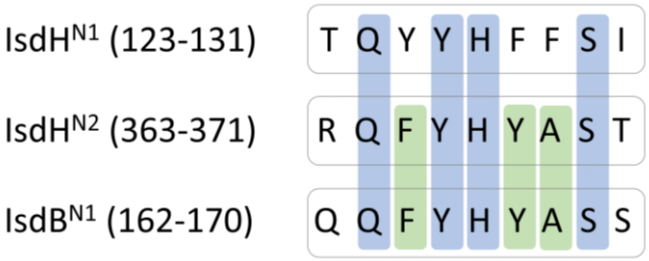

Figure 5: The alignment of the Hb-binding motifs of the hemophores IsdH and IsdB. In light blue are highlighted the residues conserved in all three domains, while in light green the residues conserved just between $IsdB^{N1}$ and $IsdH^{N2}$.

The second type of NEAT domain cited before, the "heme-binding" domain, allows direct contact with the heme cofactor [192,251,252,263], and is present in $IsdH^{N3}$, $IsdB^{N2}$, but also IsdA and IsdC. By exploiting this domain, the first two Hb receptors remove heme from Hb and transport it to IsdA and IsdC. These two latter hemophores do not get directly in contact with the human protein, but they use the NEAT domain just to collect and transfer the cofactor to other downstream hemophores. "Heme-binding" domains are characterized by a hydrophobic heme pocket, composed of a 3_{10}-helix facing the binding site and 6-stranded antiparallel β-sheets. In this latter structural feature, residues of the β7 and β8 strands model a flat surface that takes in the protoporphyrin ring. Moreover, the β8 strand contains the "heme-binding" motif, namely a conserved residue pattern of two tyrosine residues interspaced by three variable amino acids (YxxxY) [197,254,261]. The first tyrosine is responsible for ferric iron coordination through its phenol ring, while the second tyrosine forms a π-stacking interaction with the porphyrin ring and a hydrogen bond with the first tyrosine to support the interaction with the cofactor [93,194,197,228,233,248,251,264–268]. Hemophore-hemic iron penta-coordination architecture is characteristic of IsdH, IsdA and IsdC [248,261,266,269], whereas IsdB presents a hexa-coordination interaction with heme because of the presence of a methionine residue acting as an axial ligand [197]. Despite the difference in this interaction geometry, no distinctions were observed between IsdB and IsdH in terms of removing the heme from Hb or transferring it to other hemophores. The long-standing mystery of why *S. aureus* exposes two redundant Hb receptors has still to be revealed and may undoubtedly be solved with the finding of functional distinctions between the two hemophores.

As in the case of Hb-binding moieties, heme-binding motifs also present key residues that play a critical role in the interaction with Hb-bound heme as well as in heme extraction. The following conveyance of heme across the cell wall depends on the formation of a protein-protein interaction (PPI) between heme-binding NEAT domains, defined as a "handclasp" complex [210], that drives the directional heme transport by an ever-increasing rise of heme transfer kinetics [209,229,232].

Other roles of Isd hemophores

As many other bacterial surface-exposed proteins, hemophores of the Isd system are involved in different activities other than their primary role in hemic iron acquisition, with involvement in bacterial adhesion and immune evasion [20]. Some of these functions have been assigned to a specific hemophore, while others are still not fully characterized, and they are shared between different Isd proteins. For example, IsdA and IsdB collaborate to provide resistance against neutrophil attacks [270]. Moreover, IsdA alone is able to bind various host proteins as transferrin, fibronectin, fetuin, loricrin, involucrin, K10, cytokeratin and asialofetuin. The host protein binding promotes preservation from lactoferrin protease activity and skin fatty acids' antibacterial activity [138], and the bacterial adherence to kidney and epithelial cells [26,225,271–275]. On the other hand, IsdB can bind integrins, fibronectin and vitronectin [20,276–279], enabling contact and internalization in human cells, as well as platelets' aggregation. At last, IsdH is able to convert C3b to C3d rapidly, thus hindering complement activation, with an apparent role in evasion of phagocytosis [280]. In contrast to the other cell-wall anchored hemophores, IsdC is entirely submerged in the cell wall, restricting its access to the external environment, and thus limiting other moonlighting functions. Nevertheless, it retains a potential task in gene regulation of the Isd system components, since its inactivation leads to a down-regulation of the expression of *isdE*, *isdF* and *isdG* genes [26].

According to the definition of MSCRAMMs, the three surface-exposed hemophores IsdB, IsdA and IsdH may be included in this family of bacterial proteins, raising attention to their inhibition. In support of this idea, both IsdH and IsdB possess a YSIRK-GS motif at their N-terminus, which is shared among many MSCRAMMs [218]. Nevertheless, this view needs to be further validated to be confirmed.

2.1.3 IsdB as Hb receptor

As reported in the previous paragraph, IsdB is one of the two *S. aureus* surface-anchored receptors and it is responsible for Hb binding and extraction of the porphyrin cofactor, which is further handled by other Isd effectors. Among the two Hb receptors, IsdH and IsdB, the latter is considered the main *S. aureus* virulence factor, and it will be the focus of this paragraph.

IsdB is composed of two NEAT domains, separated by a 3-helix linker, and the hemophore's role is to bind free Hb ($IsdB^{N1}$) and extract heme ($IsdB^{N2}$). An important IsdB structural component is the 3-helix linker that connects the two NEAT domains and is fundamental for their coordinated function [198,254]. The two Hb receptors share a 70% sequence identity in their linker domains' residues [254]. Moreover, previous studies reported abrogation of IsdH heme extraction after the replacement of the linker domain with a poly-GS peptide [204,206,259].
The heme transfer can occur only from the oxidized form of Hb (metHb), whereas it doesn't take place from oxygen (oxyHb)- or carbon (HbCO)-bound Hb [195,281]. In this context, recent studies conducted by De Bei and colleagues allowed to reveal the mechanism behind the heme extraction process through the determination of the structures of two IsdB:Hb complexes by Cryo-EM [282]. The

first Cryo-EM determined structure, IsdB:HbCO, revealed aspects of the pre-extraction step, while the IsdB:metHb structure provided insights of the process after heme is completely transferred to IsdB. The results of both studies revealed a multistep process that starts with the binding of IsdB to the β-chain of an Hb tetramer (either HbCO [282], or oxyHb [283]), followed by the interaction of another IsdB monomer to the other β-chain of the tetramer. These interactions of IsdB with the free host protein enable the induction of Hb dimerization, allowing IsdB to interact also with the α-chain of the Hb dimer. At this point, the $IsdB^{N2}$ domain is able to extract heme by unfolding the Hb F-helix and by rotating the cofactor, thus completing the heme transfer that results in the dissociation of the IsdB:Hb complex [282].

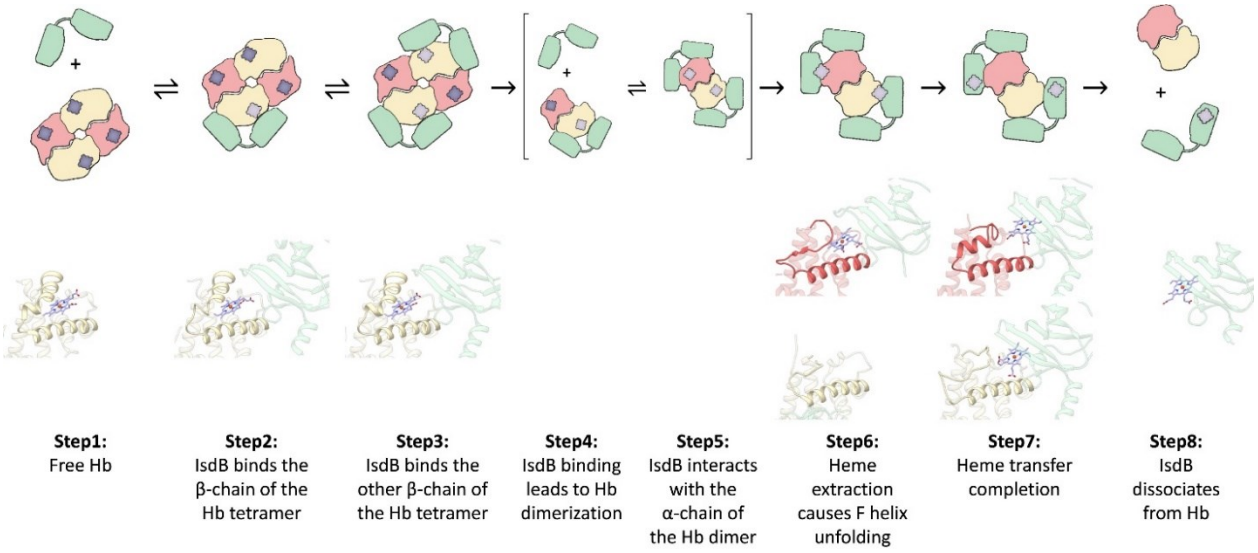

Figure 6: Hb binding and extraction of heme by the hemophore IsdB (modified from De Bei et al 2023 [282]). The sequential process was reported in De Bei et al article [282], and it is a plausible recollection of the series of events that takes place from Hb encounter and binding to heme extraction and dissociation of the complex.

These results were also supported by integrated data obtained by De Bei and colleagues through time-resolved X-ray solution scattering (TR-XSS), TR absorbance, fluorescence and molecular dynamics (MD) simulations, which provided further information about the stoichiometry, local conformational changes, kinetic features and heme transfer regarding the IsdB:Hb complex [283]. Notably, a stoichiometry in solution of 2 IsdB molecules bound to one oxyHb tetramer confirmed the cryo-EM structural data obtained with HbCO. Moreover, also the stoichiometry of the complex with metHb was obtained, showing a $2IsdB:metHb_{dimer}$ ratio [283]. The whole heme extraction process by IsdB gets concluded in about 30 seconds [281], with a rate that is 2,000 times higher than the non-catalyzed process [209]. Microscopic constants reported in Table 1 were extrapolated by fitting data to a 3-step kinetic model, which considered the interaction of two IsdB molecules with a metHb tetramer, metHb dimerization resulting in each dimer bound by one IsdB molecule and the binding of another IsdB molecule leading to the formation of the $2IsdB:metHb_{dimer}$ complex [283].

Table 1: Kinetic constants calculated by De Bei and colleagues through global data fitted to the kinetic model [283].

	STEP 1 (IsdB-Hb tetramer complex)			STEP 2 (Hb dimerization)	STEP 3 (IsdB-Hb dimer complex)		
	$k_{on,1}$ (M^{-1} s^{-1})	$k_{off,1}$ (s^{-1})	$K_{D,1}$ (M)	$k_{on,2}$ (s^{-1})	$k_{on,3}$ (M^{-1} s^{-1})	$k_{off,3}$ (s^{-1})	$K_{D,3}$ (M)
Best fit	1.4×10^{6}	1×10^{-2}	7×10^{-9}	20	2.0×10^{6}	0.5×10^{-2}	3×10^{-9}

The obtained constants are also in agreement with previously published data, that reported a dissociation constant of the IsdB:Hb complex calculated by SPR, thus highlighting the formation of a rather stable complex [281]. The interaction affinity is determined by both NEAT domains and is further enhanced by the linker domain $IsdB^{L}$ [284]. Surprisingly, Hb binding by IsdB is significantly impaired by the Y165A mutation in the Hb-binding motif, but this latter substitution has not been identified as a natural variant among different *S. aureus* strains, suggesting that the binding to Hb is kept under strong selective pressure [196].

2.2 Inorganic iron acquisition systems

As described in the previous chapter, the majority of the non-hemic extracellular iron is bound to Tf or Lf. Since these two host proteins are essential for nutritional immunity, siderophores are the main option to obtain inorganic iron by outcompeting Tf family proteins. Siderophores are small iron scavengers (about 500-1500 Da) that are released by fungi and bacteria and present an even greater affinity for ferric iron than the Tf protein family does. As an alternative, iron can be obtained by taking advantage of the extremely small amount of free ferrous iron present in the bacterial environment, where the majority of Fe(II) is set free from Lf and Tf by catecholamine stress hormones. Indeed, when holo-Tf and holo-Lf, which firmly bind ferric iron, form complexes with dopamine, adrenaline, noradrenaline and L-DOPA, iron is reduced and released in its ferrous state [285]. The growth of various bacterial strains is promoted by iron release triggered by the catecholamines [285–288], and this phenomenon has been linked to the development of staphylococcal biofilms [289], and trauma-induced sepsis derived by *E. coli* [285]. The better-supported hypothesis suggests that catecholamines reduce iron starvation, therefore going against the host nutritional immunity [286,288]. Many bacteria including *E. coli* [290], *Helicobacter pylori* [291], *Campylobacter jejuni* [292], and *Legionella pneumophila* [293], possess the Feo transport system in order to collect ferrous iron. Even if the Feo system hasn't been detected in *S. aureus*, the FepA/FepC complex has been identified as responsible for the import of ferrous iron inside the cell. Along with FepB, which identifies the extracellular heme and releases ferrous iron via a deferrochelation reaction [294], the aforementioned Fep complex is a component of the FepABC system [175,176]. Although its exact function is yet unknown, the FepABC is thought to aid in iron uptake or environmental heme detoxification. The last mechanism for non-hemic iron uptake is less likely to occur since it involves receptors that are specific for the human Tf protein family. This system has been well-defined for some gram-negative bacteria, as the TbpAB receptor complex in *Neisseria spp* [295,296], but it has been identified in few gram-positive bacteria. When it comes to *S. aureus*, the receptors HLf-BP [297] and StbA [225] have been found to bind Lf and Tf, respectively. However, it is unclear if these Tf family receptors are used to retrieve iron or if they are necessary for cell adhesion, making them virulence factors [32]. It's

interesting to note that StbA is now recognized as IsdA, a component of the Isd system essential for the acquisition of hemic iron and staphylococcal pathogenesis.

2.2.1 Siderophore acquisition systems

Bacteria under iron deficiency release siderophores, which are secondary metabolites able to acquire ferric iron free in the environment by forming soluble Fe(III) complexes, even at extremely low iron concentrations [298]. Other than by bacteria, siderophores are produced also by plants and fungi [299], but they will not be described in this thesis. The key properties of siderophores regard their great selectivity and high affinity for ferric iron [299]. Indeed, because of these chelators' extraordinarily low K_D (up to 10^{-52} M) within the human host [300–302], bacteria are able to directly compete for iron with the Tf protein family [23,93], or to solubilize the precipitates of ferric hydroxides. Moreover, strongly negatively charged electron donors found in the binding site are responsible for the higher selectivity for Fe(III) [303], which in turn allows to stem the metal reactivity and import iron exclusively, by lowering the redox potential and hindering the damaging Fe(II)-Fe(III) cycle [62]. One reason for the exclusive selectivity of siderophores for ferric iron, and not ferrous iron, may derive from the presence in the extracellular compartment of different dipositive cations as zinc, copper, manganese and nickel that would hamper Fe(II) selectivity, thus driving the selection towards Fe(III). Moreover, the most common method used by bacteria to retrieve intracellular iron from the Fe-siderophore complex is metal reduction, which prevents the assimilation of harmful or unnecessary tripositive cations (including gallium, cobalt, and aluminum) that could not be reduced effectively [62,299,302].
Different types of siderophores are known among the bacterial genera. The primary siderophore classification divides them into three main classes based on the functional groups participating in iron coordination: hydroxamates, catecholates and (α-hydroxy)carboxylates. Apart from these, there are also other less represented groups, called "mixed type" siderophores that contain α-hydroxyimidazole, α-aminocarboxylates, and hydrophenyloxazolone [299,304–306].
All these siderophore classes are synthesized through either one of two pathways: the non-ribosomal peptide synthetase (NRPS) or the NRPS-independent siderophore (NIS) pathways. The first pathway consists of NRPS enzymes, which are modular, multiple catalytic domain enzymes that perform a stepwise assembly with covalently bound intermediate to produce siderophores with peptidic scaffolds, usually incorporating also non-proteinogenic amino acids [307–309]. On the contrary, siderophore synthesis through the NIS pathway is performed by individual enzymes that condense alternating dicarboxylic acid subunits (often citrate, α-ketoglutarate, and succinate) with alcohols, amino alcohols and diamines. Further modifications to subunits including oxidation, decarboxylation, and isomerization are carried out by other enzymes that are usually encoded by genes that cluster close to the synthetases' genes [309].
The strong competition for ferric iron between various microbial species or between microorganisms and their hosts has been proposed as the primary driver of the evolution of siderophores' structural variety and the associated receptors to identify the correspondent ferric complexes [310].

While siderophores are primarily defined as growth factors that bind iron and help bacteria grow by retrieving the metal from the extracellular environment, it has also been suggested that these same Fe-scavengers are part of a sophisticated system that facilitates bacterial contact within the same colonization site. Bacteria can compete by starving their close cohabitants of iron, or they can work together to form a stable community through a give-and-take process or even lateral gene transfer [185].

2.2.2 *S. aureus* siderophores

SA and SB are the two main *S. aureus* siderophores [311–314], composed of carboxylate iron-chelating groups and implicated in overcoming iron starvation by the retrieval of inorganic iron from the extracellular media of the host. The redundant presence of two siderophores is justified by their apparent different roles in infections since SA can reach sites beyond the colonized one, whereas SB appears to act at the local level [315]. Moreover, SA is constitutively produced, while SB is produced by the most invasive *S. aureus* strains, thus it is considered to be the greatest support for virulence [316]. SA and SB key role in iron acquisition is confirmed by the fact that the expression of the genes involved in the staphyloferrins' biosynthesis and reuptake is regulated by Fur, increasing gene expression in iron-depleting conditions [317]. The importance of these two siderophores is highlighted by *S. aureus* unavoidable need for at least one of them for growth and colonization in iron-depleted media [318] making them key virulence factors [315,319]. In support of this concept, Courcol and colleagues determined that, compared to *S. aureus* strains that physiologically colonize humans, virulent strains produce up to 100 times more siderophores. Moreover, they also suggest that bacterial chromosomal genes are necessary for constitutive siderophore formation, while the presence of certain plasmids amplifies the iron scavengers' release outside the cell [320].

Below is a list of the different siderophores in this *S. aureus* iron acquisition system, with the exception of Staphyloferrin B, whose biosynthetic pathway, regulation and mechanism will be explained more in detail in the next chapter.

Staphyloferrin A –SA is the constitutively-produced siderophore of *S. aureus* and its expression is regulated by Fur with up-regulation during iron starvation. The genes encoding for the proteins involved in SA biosynthesis and secretion are contained within the *sfa* cluster [156,321]. D-ornithine and citrate serve as the siderophore's building blocks. The first component is produced by the enzyme SfaC, which catalyses the enzymatic racemization of the essential urea cycle intermediate, L-ornithine [156]. The latter SA component is produced by citrate synthase CitZ [322], an enzyme of the TCA cycle. Being so intertwined with citrate production, SA biosynthesis gets repressed in conditions that hamper the TCA cycle, as when the intracellular concentration of glucose is high and throughout iron starvation, since iron is required as a cofactor by different TCA cycle enzymes [322]. Once citrate is available and D-ornithine has been produced by SfaC, the type-A-like NIS synthetases SfaB and SfaD facilitate ornithine condensation with two citrate molecules (Figure 7) [321]. After SA is produced, its secretion is dealt by the SfaA efflux pump [323], while the heme transport system HtsABC is responsible for the import of the iron-bound siderophore [324]. It has been established that a tight complex is formed between SA and the lipoprotein receptor HtsA (with a low nanomolar dissociation constant), while the HtsBC dimer composes an integrated membrane permease that guarantees SA import [156]. In support of the connection between SA and the HtsABC system, the genes encoding for the latter are localized in proximity of the *sfa* operon. Beyond the specific SA system just reported, this iron chelator shares with SB the FhuC non-specific ATPase that enables an ATP-dependent transport of siderophores [156,325]. The *fhuC* gene is contained within the ferric hydroxamate uptake operon (*fhuCBG*) that will be described below in more detail. After the iron-bound siderophore is imported, the bacterium requires a mechanism that allows to recover iron. The reduction of the ferric iron seems to be the most probable system used by *S. aureus* to collect the metal, confirmed by the requirement for the nitroreductase NrtA to use correctly the SA-iron complex [326]. Because siderophore selectivity and affinity are based on ferric iron's negative redox potential, siderophore

binding capability is significantly compromised when the metal is reduced because it lowers thermodynamic stability and increases ligand exchange rates [299,303]. Ultimately, iron retrieval from the complex enables the complete recovery of active siderophores that are then able to start another uptake cycle.

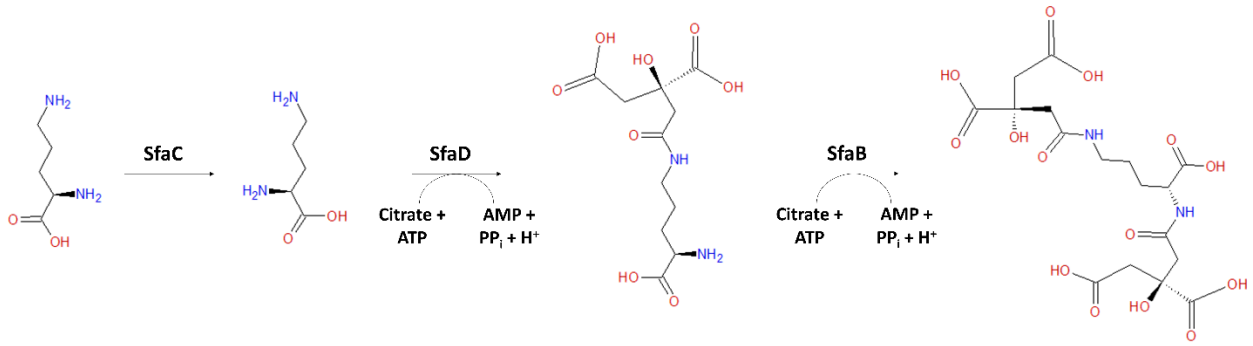

Figure 7: Staphyloferrin A biosynthetic pathway (adapted from Cotton et al, 2009 [321]). The chemical structures were drawn with ACD/ChemSketch.

Other siderophores – Although SA and SB are the two most characterized and main siderophores of *S. aureus*, the bacterium produces and secrets also other iron scavengers. The first to be discovered is the siderophore aureochelin of 577 Da [327], whose structure is actually still unknown [154]. Another siderophore was originally misidentified by Dale and coworkers as SB [154], but a more recent work has recognized it and called it staphylobactin. In this latter study, the author discovered a novel gene cluster, *stb*, which is predicted to encode for NRPSs involved in staphylobactin production in MRSA, suggesting a role in iron acquisition [306]. At last, staphylopine (StP) is a well-described scavenger of dipositive cations, since it can import copper, nickel, cobalt and zinc besides the uptake of ferrous iron. The genes for the biosynthesis and export of StP are encoded in the *cnt* operon, which is regulated by iron and zinc availability through the control of Fur and the zinc uptake regulator Zur, respectively [328–330]. Recent studies have highlighted the importance of StP by observing that *S. aureus* mutants with no StP activity have decreased bacterial fitness both *in vitro* and *in vivo* [329,331], but also by its being fundamental in counteracting zinc starvation in nutritional immunity [332,333].

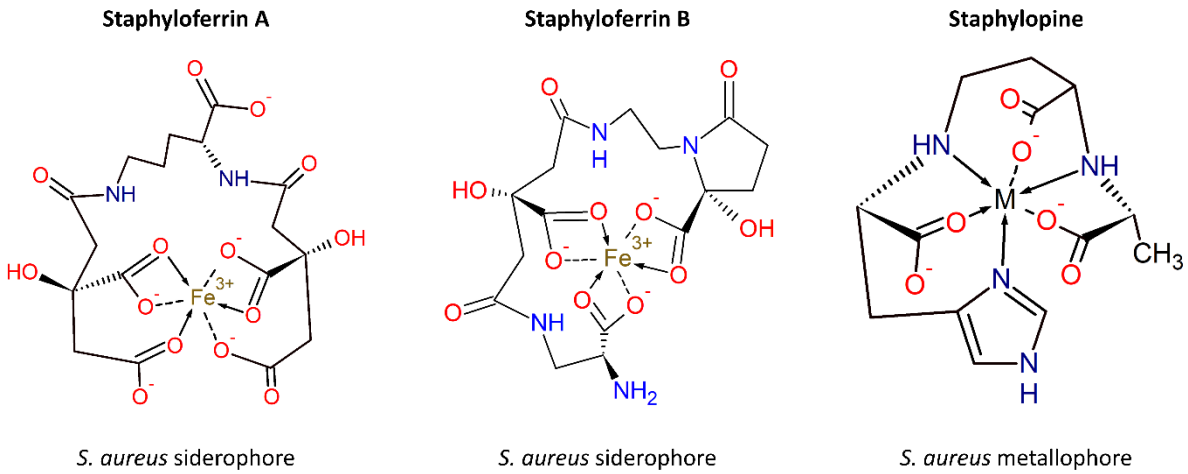

Figure 8: Structure of the main *S. aureus* siderophores drawn by using ACD/ChemSketch (Advanced Chemistry Development Inc., Toronto, Canada).

2.2.3 Xenosiderophores

The term xenosiderophore refers to exogenous siderophores produced by bacteria cohabiting the same niche as the organism of interest. In this context, *S. aureus* ability to exploit also this iron source highlights its high adaptive skill. The pathogen can import both hydroxamate and catechol-type xenosiderophores since it expresses uptake systems on its surface for both siderophore types, the FhuBCDG and SstBCD systems, respectively [319,334]. The two systems present a common structure by being composed of an ATPase (FhuC or SstC), a heterodimeric permease (FhuBG and SstAB), and a ligand-binding lipoprotein (FhuD and SstD). The internalization of xenosiderophores is followed by iron release through the action of the NADPH-dependent oxidoreductase IruO, which reduces iron to Fe(II) and extracts it from hydroxamate siderophores [326,335]. Iron extraction from catecholate siderophores is supposed to take place through an esterase reaction [318,336], but the enzyme that would catalyse such reaction is still not known. By exploiting the same uptake mechanisms, *S. aureus* is able to retrieve stealth siderophores, which are glycated catecholate iron scavengers that have evolved in various pathogens to elude the binding to serum albumin [337] and siderocalin [140], thereby circumventing these particular host defences [202]. Salmochelins and petrobactin, that are secreted by *E. coli*, *Salmonella spp.*, *Klebsiella spp.*, and *Bacillus spp.*, are typical examples of this kind of siderophores [334,336,338]. Also other microorganisms produce stealth-like scavengers (as aerobactin, yersiniabactin, pyoverdins and pyochelin), which are characterized by chemical modifications that enable them to elude serum albumin and siderocalin binding [299]. *S. aureus* appears incapable of producing its own stealth siderophores, therefore it is entirely dependent on other commensal bacteria to make them.

3 Staphyloferrin B

3.1 SB biosynthetic pathway and regulation

SB is the *S. aureus* siderophore that is produced by the most invasive strains of the pathogen, and it shows an important role in severe disease phenotypes [154]. The genes for SB biosynthesis (SbnABCEFGHI) are all encoded in the *sbn* operon (*sbnA-I*), whose expression is under the control of Fur. SB is produced through the NIS biosynthetic pathway from a molecule of citrate, one of α-ketoglutarate (α-KG), and two molecules of the non-proteinogenic amino acid L-2,3-Diaminopropionic acid (L-Dap). As can be observed in the SB chemical structure (Figure 9), the Fe(III)-SB complex is six-coordinate, presenting five oxygen atoms and a nitrogen atom in the SB molecule in a distorted octahedral geometry [339]. L-Dap plays a key role in iron coordination, with its nitrogen atom on the primary amine and a terminal carboxylate oxygen contributing to two out of the six interactions formed [339]. The two other interactions involve the terminal carboxylate and carbonyl groups of the α-KG-derived component. Last, two of the metal ligands are the carboxylate and the hydroxyl substituent derived from the citrate moiety [339].

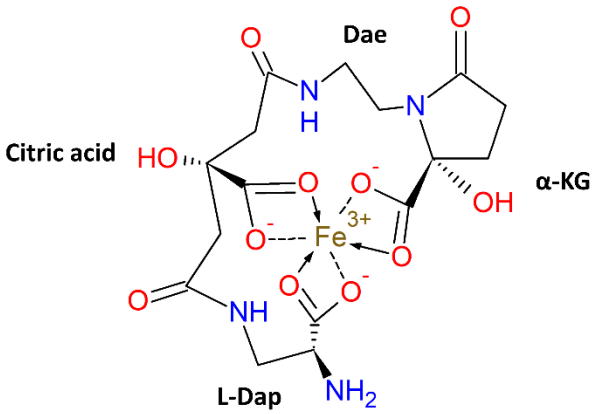

Figure 9: Chemical structure of Staphyloferrin B drawn by ACD/ChemSketch (Advanced Chemistry Development Inc., Toronto, Canada). The image reports the moieties that constitute SB structure. The abbreviation used refers to 1,2-diaminoethane (Dae).

Two SB isoforms exist, showing a linear or a cyclic hemiaminal α-KG form, with this latter being the most likely physiological form found in solution [340]. Even if many aspects of the pathway and the underlying mechanisms have yet to be characterized, all the enzymes composing it have been identified and their functions defined. The first key effector of the pathway is the free serine kinase SbnI which actually has a double role. First, it catalyses the phosphorylation of L-serine to produce *O*-phospho-L-serine (L-OPS), which is a SB precursor. The second SbnI role regards its ability to activate *sbnD-I* gene expression, with a further layer of regulation performed by heme binding to SbnI. Heme binding leads to a drastic decrease in *sbnD-I* gene expression caused by a loss of DNA affinity of the heme-bound form [341]. The product of SbnI reaction, L-OPS, becomes then the substrate for the SbnA-catalysed enzymatic reaction leading to the production of an intermediate that is utilized by SbnB to provide two of the three components needed for SB synthesis, i.e. L-Dap and α-KG. At this point, the NIS synthase SbnE catalyses the condensation between L-Dap and citrate to form citryl-L-2,3-diaminopropionic acid. This step is followed by the decarboxylation of the SbnE product by the PLP-dependent decarboxylase SbnH and the condensation of another L-Dap molecule by the NIS synthase SbnF to form L-2,3-diaminopropionyl-citryl-diamonoethane. The pathway concludes with the incorporation of an α-KG molecule by the NIS synthase SbnC to produce SB [309]. It's interesting to know that SB can be also synthesized *in vitro* by using the three purified synthetases of the pathway, i.e. SbnC, SbnE and SbnF, together with the decarboxylase SbnC and the three precursor substrates, i.e. α-KG, L-Dap and citrate [339,342]. After SB has been produced, its secretion is managed by the SbnD efflux pump [326], but it has to be noted that Hannauer and colleagues have observed a *sbnD* deletion strain that produced levels of intracellular and extracellular SB comparable to WT strains after 36 hours under iron-restricted conditions. These results would implicate the existence of an SbnD-independent export system [343]. Following iron retrieval, the import of the iron-SB complex is actively managed by the staphylococcal iron-regulated (sir) ABC transporter complex (SirABC), that is encoded within the *sirABC* operon under the control of Fur and located near the *sbn* operon, but with opposite direction of transcription [154,344]. The SirABC complex is composed of the substrate-binding lipoprotein SirA and of the heterodimeric integral membrane permease SirBC [344]. The abrogation of either *sirA* or *sirB* leads to growth impairment in an iron-depleted growth medium [154]. As with the Hts system in SA, the non-specific FhuC ATPase provides the energy for the SirABC transporter to properly function [345]. The iron release

mechanism from the Fe(III)-SB complex, once reached the intracellular compartment, is still unexplained, therefore different theories have been considered other than the most compelling one, that is the reductive release mechanism exploited in the SA context [326]. The main substitute of the iron reduction-based mechanism is the siderophore's continuous degradation, leading to iron release. However, this process is quite inconvenient due to the significant metabolic expenses associated with the ongoing requirement to synthesize new siderophores. Since bacteria exploit SB extensively, it is expected that a mechanism allowing for the recovery of the unbroken siderophore has evolved [303].

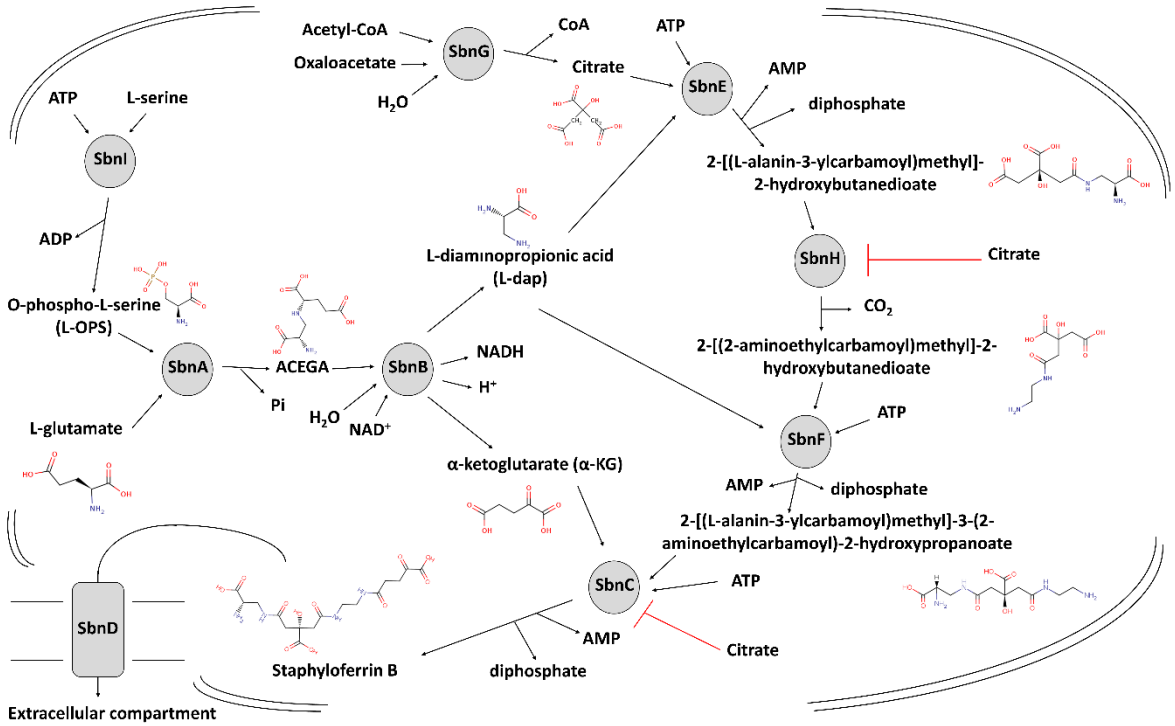

Figure 10: Schematic representation of the SB biosynthetic pathway.

As reported above and in the previous chapter, citrate is a main component in both SA and SB, but the amount of citrate produced by the metabolic machinery in conditions of glucose repletion and iron depletion is considerably low, so as to compromise the biosynthesis of SA [346]. Conversely, SB biosynthesis is not entirely dependent on citrate cellular concentration since the *sbn* operon allocates the gene for a dedicated citrate synthase, called SbnG [347], which guarantees adequate citrate supply for SB production. Nevertheless, previous studies have highlighted the inhibition by citrate of two enzymes of the pathway, SbnH and SbnC, with a calculated IC_{50} of 280 and 83 µM, respectively [348,349]. Furthermore, mutants of *S. aureus* lacking CitZ (the citrate synthase necessary for SA production) showed that SbnG supports exclusively the biosynthesis of SB, freeing it from dependence on metabolic citrate. Nevertheless, a study by Sheldon and coworkers on a *citZ sbnG* double mutant revealed a restoration of SB biosynthesis in the growth-impaired double mutant after complementation with either *citZ* or *sbnG*, thus implying that actually both enzymes can provide citrate for SB production [322]. Nonetheless, it should be noted that another study by Cheng and colleagues reported that SbnG enzyme is approximately 1000-fold less efficient than the TCA cycle citrate synthase CitZ, highlighting a more complex citrate regulation that may lie in the different

conditions of expression of the two proteins, physiological for CitZ and in iron restriction for SbnG [347].

As for citrate, also SbnA substrates, i.e. L-glutamate and L-OPS, need to be available for SB production in iron-restricted conditions. A previous study conducted on *S. aureus* transcriptome revealed two systems for SbnA substrates' production: *gltBD* genes encode for enzymes involved in the L-glutamate biosynthetic pathway, while L-OPS biosynthesis is performed by *serAC* genes. The precursors of both biosynthetic pathways appear to be abundant when *S. aureus* is found in human serum [350]. Both sets of genes are modulated by the CodY regulator, which is a global modulator for virulence and adaptations to nutrient restrictions, mainly present in Gram-positive bacteria [351,352]. The CodY regulon in *S. aureus* appears to enhance siderophore production by boosting the synthesis of metabolic precursors. As for citrate, L-OPS can be produced by two different enzymes, i.e. SbnI and SerC. The first is a component of the SB biosynthetic pathway, while SerC is connected to the glycolytic pathway since its substrate derives from 3-phosphoglycerate [316]. The two enzymes' differential dependence on the glycolytic pathway is the proposed reason for this functional redundancy, thus to separate SB production from glycolysis in iron-restricted conditions. Furthermore, negative feedback regulation controls the serine biosynthetic pathway. Indeed, when L-serine is abundant, it allosterically inhibits SerA, which is metabolically upstream of SerC, potentially limiting the quantity of SerC-derived L-OPS needed for SB production. As a result, it is highly beneficial to have SbnI as an SB-specific enzyme for L-OPS biosynthesis [316]. Unlike L-OPS, L-glutamate doesn't have a synthetase within the SB biosynthetic pathway, but it is produced from L-glutamine by the glutamate synthase, under CodY regulation [351–353].

Because SbnA and SbnB produce two out of the three building blocks needed for SB production, their role is fundamental. Their importance has also been confirmed by observing the lack of SB production in a double *sbnA* and *sbnB* mutant [153]. Because of their importance and relevance to the aim of this thesis, the next chapters will discuss more in detail these two enzymes' structures, mechanisms of action and regulation.

3.2 The first steps of SB biosynthesis

The first two steps of SB biosynthetic pathway are catalysed by SbnA and SbnB, which are encoded by the first two genes of the *sbn* operon, *sbnA* and *sbnB*. The expression of the two genes is regulated by Fur with up-regulation under iron-depleted conditions. It's interesting to note that *sbnA* and *sbnB* are the only two genes of the *sbn* operon to not be subject to SbnI-mediated heme regulation [341].
The key role of these two enzymes in SB synthesis has been demonstrated by Beasley and colleagues, who observed that a mutation in either *sbnA* or *sbnB* genes resulted in the abrogation of SB production, caused by the inability to produce L-Dap [153]. Indeed, the sequential action of the two enzymes enables the production of two out of three building blocks needed for SB synthesis, L-Dap and α-KG [354]. The first studies on SbnA and SbnB revealed a shared sequence homology with *Streptomyces sp* enzymes VioB and VioK, respectively, which are involved in the assembly pathway of viomycin [153,355]. Since the viomycin molecule also presents L-Dap as a structural component, the first studies proposed that VioB and VioK, as SbnA and SbnB, act synergistically as an overall L-Dap synthase [153]. Both enzymes have been then further studied, even if a complete structural and functional characterization has not been reported yet.

3.2.1 SbnA enzyme

SbnA is a fold type II pyridoxal 5'-phosphate (PLP)-dependent enzyme [354], that performs the first step of SB biosynthesis, catalysing the reaction between L-OPS and L-glutamate to produce free inorganic phosphate and the first SB biosynthetic intermediate N-(1-amino-1-carboxy-2-ethyl)-glutamic acid (ACEGA) [354,356]. Homologues of SbnA can be found in other organisms that appear to produce SB [153], or other structurally similar secondary metabolites, such as the antibiotics viomycin [355], zwittermicin A [357], capreomycin [358] and dapdiamide [359]. From results of homology studies, SbnA has been placed within the tryptophan synthase β family, among which the PLP-dependent enzyme *O*-acetyl-L-serine (OAS) sulfhydrylase (OASS) showed the highest similarity. Since a subclass of OASS enzymes exploits OPS as substrate (OPSS enzymes), as SbnA, the difference between the two lies in the use of a nitrogen instead of a sulfur donor for SbnA- and OPSS-catalysed reactions, respectively[354].

SbnA structure

According to their fold-type, PLP-dependent enzymes are categorized into seven classes. The fold-type II class, which SbnA belongs to, includes also tryptophan synthase, serine dehydratase, threonine deaminase and OASS [360–362]. One large and one small domains are characteristic of the fold-type II class sharing a common α/β layout, consisting of a core β-sheet surrounded by different α-helices. The four SbnA X-ray crystallographic structures deposited in the Protein Data Bank (PDB) were all defined by Kobylarz and colleagues in 2016. The structures represent a PLP-bound SbnA (PDB ID 5D84), the α-aminoacrylate intermediate of SbnA catalysis (5D85) and two SbnA variants, the Y152F (5D86) and the Y152F/S185G mutants (5D87) [356].
The PLP-bound SbnA crystal structure was solved as a monomer presenting a single PLP cofactor bound in a cavity between the two domains. The monomer was estimated to be 36 kDa, but the protein in solution forms a dimer of 77 kDa (Figure 11A). About 50 residues contribute to the dimer interface with a buried surface of around 1800 $Å^2$ in each monomer. One monomer's positively charged residues form a wide cleft enclosing the active site, and the same side of the dimer provides access to both active sites. The PLP cofactor is covalently bound to the Lys47 residue located at the base of the cleft through the formation of an internal Schiff base. Furthermore, different hydrogen bonds are formed between the PLP phosphate and serine and threonine residues (Ser185, Thr186, Thr187 and Ser189), as well as with three water molecules. The positive dipole of the α-helix, which spans residues 188–200, stabilizes the phosphate negative charge, while Asn77 and Ser272 residues form hydrogen bonds with the pyridoxal component (Figure 11B). The solvent-exposed *re* face of PLP pyridine ring gives the substrates access to displace the lysine Schiff base and produce an external aldimine.

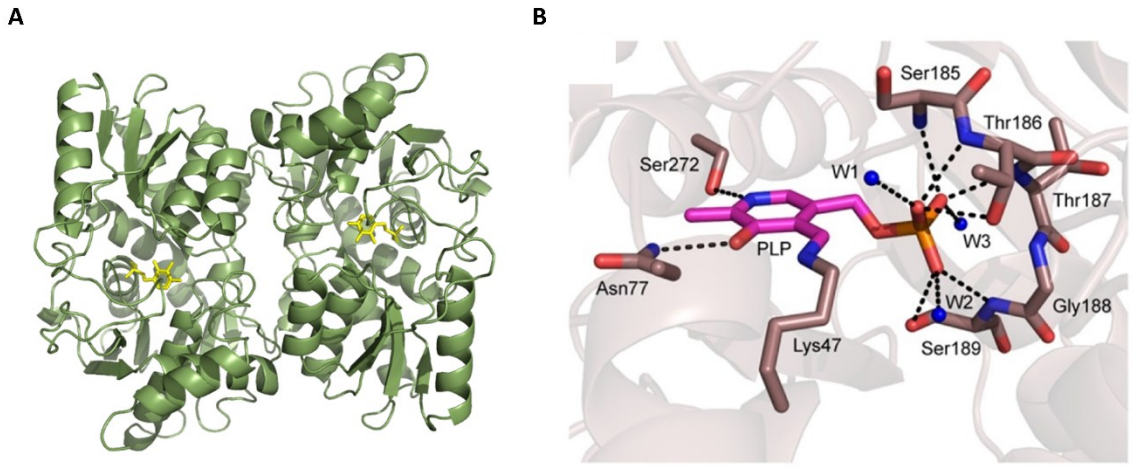

Figure 11: (A) Three-dimensional structure (PDB ID 5D84) of SbnA bound to the PLP cofactor from Kobylarz et al, 2016 [356]. (B) Active site of the PLP-bound SbnA (adapted from Kobylarz et al, 2016 [356]).

The soaking of SbnA crystals with L-OPS leads to the formation of a PLP-α-aminoacrylate (AA) intermediate, where the covalent bond between the PLP cofactor and Lys47 is displaced by PLP-AA formation. This process induces a C-terminal domain rotation towards the N-terminal domain, restricting the active site cleft and also rotating the pyridoxal ring of the PLP cofactor (Figure 12, left panel). This rotation causes new hydrogen bonds to form between the carboxylic acid of the α-aminoacrylate and Thr74, Ser75, Leu78 and Gln151. Moreover, the active site loop, comprising residues 72-76 and containing the highly conserved Ser75, is translated in a position directly above the α-aminoacrylate (Figure 12, middle panel). At last, another binding pocket forms between the two domains right above the PLP-α-aminoacrylate. It is interesting to note that a citrate binding site in the newly originated pocket was identified by serendipity, since citrate had been used in the crystallization medium. A wide hydrogen bond network was observed between citrate and positively charged side chains (residues Lys100, Arg132 and Arg224) and amide groups of the backbone chain (Tyr128, Leu129 and Ser232) (Figure 12, right panel).

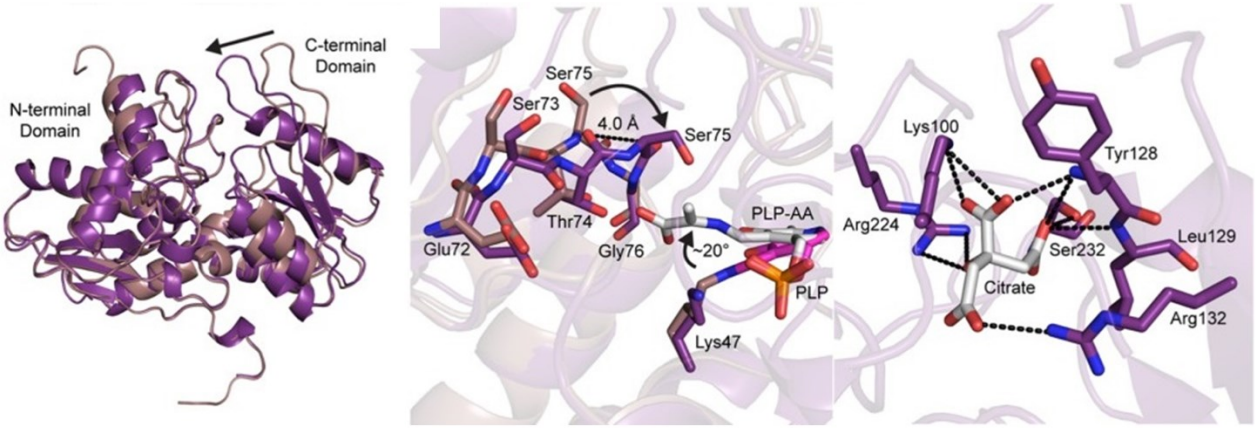

Figure 12: Comparison of SbnA structure when bound to PLP and in the α-aminoacrylate form (adapted from Kobylarz et al, 2016 [356]). (Left panel) The overlay of SbnA-PLP (in brown) and SbnA-AA (in purple) cartoon structures shows significant changes in the C-terminal domain conformation. The directionality of the conformational shift following PLP-α-aminoacrylate formation is indicated by the black arrow. (Middle panel) The overlay of SbnA-PLP (in brown) and SbnA-AA (in purple) active sites shows a significant conformational shift in the loop presenting Ser75. The conformational change for Ser75 and

PLP is represented by the two black arrows. (Right panel) In the SbnA-AA structure, citrate (in white) binds into a pocket above the active site.

The reason behind investigating the crystal structures of SbnA variants Y152F and Y152F/S185G derived from results of a multiple sequence alignment analysis conducted to highlight active site differences that would justify SbnA specificity for OPS. The crystal structure of the Y152F variant showed a minimal conformational change compared to WT SbnA, therefore Y152 seemed not to be directly involved with the AA. Nevertheless, the residue might get in contact with the OPS phosphate group or be involved in the second step of the reaction, regarding the formation of a bond between the AA β-carbon and the L-glutamate amino group. On the contrary, the Y152F/S185G SbnA double mutant structure revealed a significant conformational change compared to WT SbnA. Notably, this variant presents an active site conformation similar to the one of the SbnA AA, showing a translation of the active site loop towards the PLP cofactor and a rotation of the Gln151 residue. The results suggest the variant mimicry of the closed conformation of SbnA active site, potentially inhibiting OPS binding [356].

SbnA characterization and catalysis

Two studies have been published by Kobylarz and colleagues regarding an initial functional and structural characterization of the SbnA enzyme [354,356]. In the first work, Kobylarz and colleagues evaluated spectroscopically the presence of the internal Schiff base between the PLP cofactor and the active site lysine, and they observed also the spectral change induced by the α-aminoacrylate formation after L-OPS addition (Figure 13).

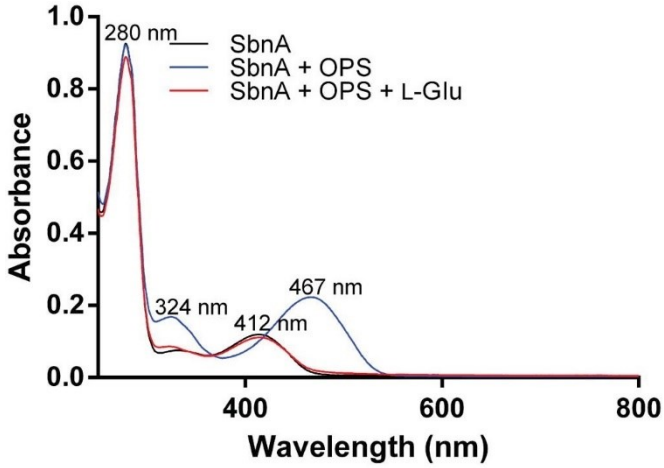

Figure 13: The UV-visible absorption spectra of *S. aureus* SbnA and SbnA after addition of OPS and then of an excess of L-glutamate. The image was adapted from Kobylarz et al, 2014 [354].

Moreover, the study confirmed ACEGA production and highlighted SbnA specificity for L-glutamate as amine donor over various other amino acids [354]. In 2016, the second study was more focused on a structural analysis and an initial functional characterization. Based on SbnA homology to OASS, Kobylarz and colleagues proposed a mechanism of action for SbnA involving different steps: the formation of an external aldimine with the first substrate L-OPS, phosphate release inducing the generation of a PLP-AA intermediate, followed by ACEGA production and release after L-glutamate addition, with the ultimate regeneration of the internal aldimine form of the enzyme [356].

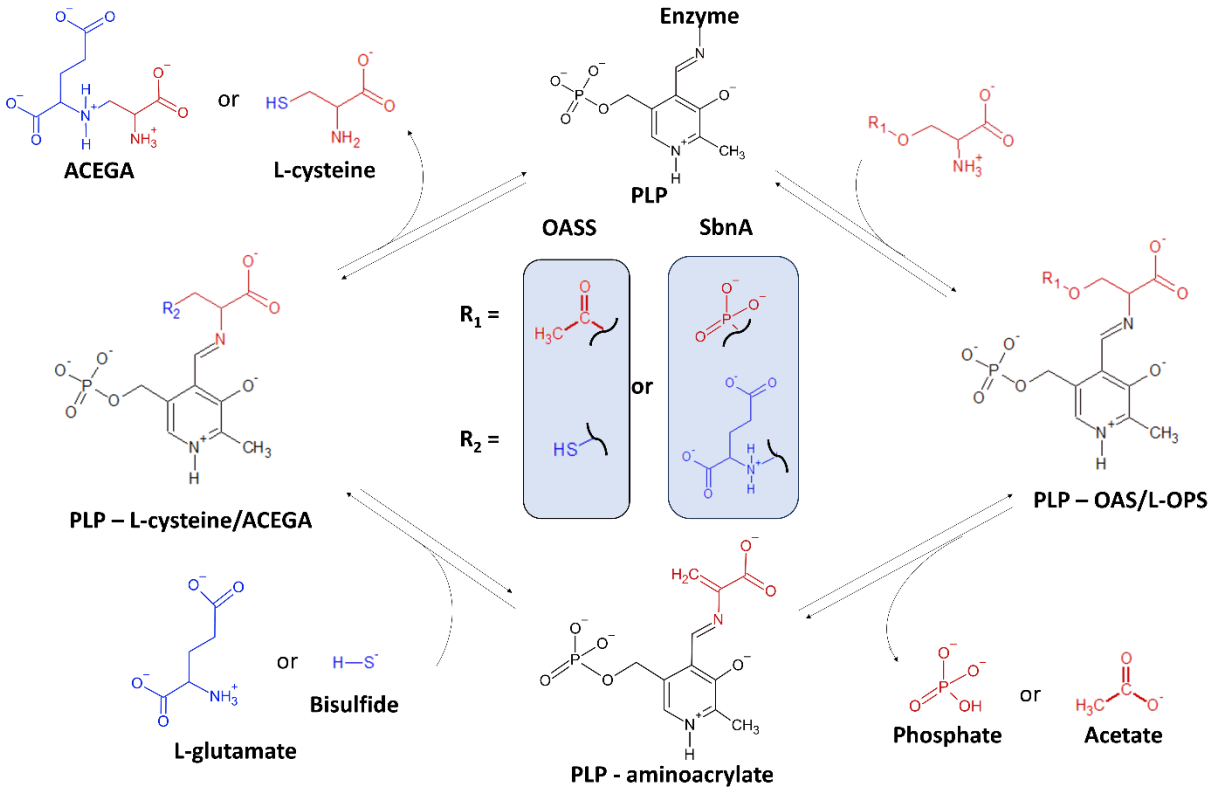

Figure 14: Schematic representation of the SbnA reaction mechanism proposed by comparison with the homologous enzyme OASS (adapted from Kobylarz et al, 2016 [356]).

Even if the study didn't validate this mechanism of action, kinetic parameters of WT SbnA were calculated in steady-state conditions both for L-OPS and L-glutamate (Table 2).

Table 2: Kinetic parameters of wild type SbnA calculated in steady-state conditions (adapted from Kobylarz et al, 2016 [356]).

	K_M (mM)	K_{cat} (s^{-1})	K_{cat} / K_M (M^{-1} s^{-1})
L-OPS	0.072 ± 0.008	2.3 ± 0.06	$3.2 \times 10^4 \pm 3.6 \times 10^3$
L-glutamate	3.2 ± 0.2	3.6 ± 0.06	$1.1 \times 10^3 \pm 7.8 \times 10^1$

The data revealed a nearly 100-fold difference between the K_M values of the two SbnA substrates, which could reflect the relative abundance of L-OPS and L-glutamate in the bacterium under iron restriction [356]. While L-OPS *S. aureus* intracellular concentration has not been determined yet, L-glutamate has been identified as one of the most present amino acids in the *S. aureus* intracellular compartment [353,363].

The group determined also the formation rate of the PLP-AA intermediate in the presence of L-OPS, calculating single turnover kinetic parameters (reported in Table 3).

Table 3: Single turnover kinetic parameters calculated for wild type SbnA (adapted from Kobylarz et al, 2016 [356]).

K_{obs} (s^{-1})	K_d (mM)	K_2 (M^{-1} s^{-1})
$3.1 \times 10^2 \pm 1.2 \times 10^1$	2.8 ± 0.2	$1.1 \times 10^5 \pm 1.0 \times 10^4$

Furthermore, the same kinetic analyses were performed on the S185G variant (the only mutant produced that would provide sufficient and measurable activity). When compared to the WT enzyme, SbnA S185G's catalytic efficiency decreased by almost four times, while the AA formation was impacted by a ~2-fold decrease (second-order rate constant). In this latter analysis of AA formation rate, another mutant was tested, i.e. the Y152F variant, and the data showed an over 1000-fold decrease (second-order rate constant), suggesting Tyr152 involvement in L-OPS binding and PLP-AA formation [356].

At last, Kobylarz and coworkers identified L-cysteine as a competitive inhibitor of SbnA activity by observing the lack of formation of the AA intermediate. Indeed, L-cysteine appears to form a non-productive external aldimine with the PLP cofactor, thus hindering the progression of the reaction [356].

3.2.2 SbnB enzyme

SbnB is the second enzyme of the SB biosynthetic pathway and catalyses the oxidative hydrolysis reaction of ACEGA with NAD^+ as cofactor to produce L-Dap, α-KG and NADH [354]. SbnB has been found to be homologous to the ornithine cyclodeaminase (OCD) protein family (including VioK) and to amino acid dehydrogenases [153]. However, Kobylarz et al. in 2014 demonstrated that SbnB is more closely related to NAD^+-dependent amino acid dehydrogenases, as the alanine dehydrogenase (AlaDH) from *Archaeoglobus fulgidus*, than to OCD since it utilizes NAD^+ as a substrate [354]. The enzyme has not been well described functionally, mainly because a deep characterization of the catalytic mechanism would require the use of the ACEGA molecule, which is commercially unavailable and difficult to synthesize. Nevertheless, different crystallographic structures have been solved and are available on PDB, all deposited by Kobylarz and colleagues [354]. The structures comprise a selenomethionine (SeMet)-labeled SbnB (PDB ID 4MP3), SbnB-NAD^+ in complex with α-KG (PDB ID 5MPD) (Figure 15C), citrate (PDB ID 4MP6) and malonate (PDB ID 5MP8), and a SbnB-NADH structure in complex with ACEGA (PDB ID 4M54) (Figure 15D). The SbnB monomer reveals the presence of two domains, a NAD binding domain and a dimerization domain. The first is composed of helices surrounding a seven-stranded parallel β sheet, while the latter consists almost entirely of a six-stranded antiparallel β sheet (Figure 15A). In solution, SbnB is found mainly as a dimer (Figure 15B), with the interaction interface between the monomers being in the large antiparallel β-sheet region. From data of active site superimposition with AlaDH and OCD, four residues were identified as conserved in all three proteins, i.e. Lys45 and Lys78, Arg122, and Asp313 (considering SbnB numbering). The residues Lys78 and Arg122 are involved in hydrogen bonds with the terminal carboxylate of the substrates bound to SbnB, making the α-carbon atom of the substrate align with the NAD^+ cofactor. A specific SbnB feature is the presence of Arg94 residue, which forms an interaction with the terminal carboxylate of ACEGA via a salt bridge [354].

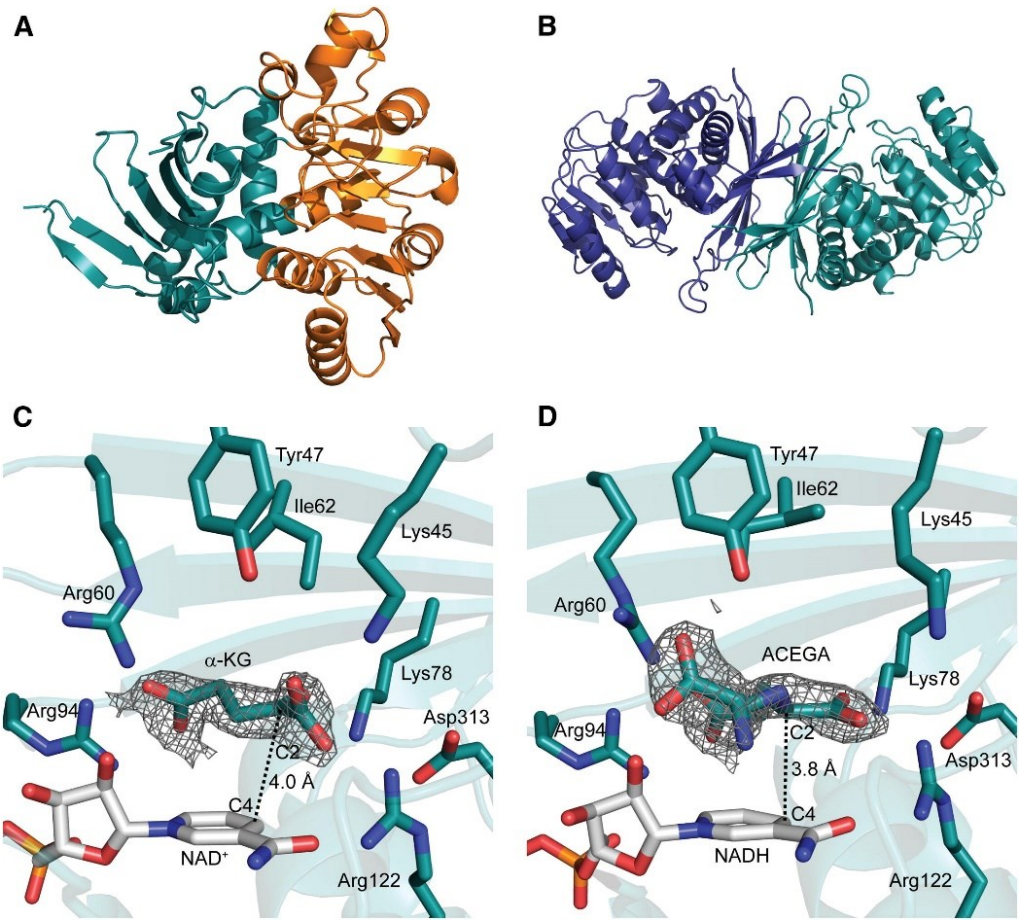

Figure 15: SbnB solved structures from Kobylarz et al (2014) [354]. (A) Apo-SbnB structure, with NAD binding and dimerization domains coloured in orange and green, respectively. (B) SbnB dimer derived from crystallographic symmetry. The monomers are coloured in blue and green. (C) Close-up on the SbnB active site with α-KG bound in presence of NAD^+. (D) Close-up on the SbnB active site with ACEGA bound in presence of NADH.

Even if homology and crystallographic data have helped elucidate some aspects of SbnB function, a whole plethora of new information would be needed to deeply characterize its mechanism of action. The identified key role of this enzyme, together with SbnA, in SB production, and thus in *S. aureus* iron acquisition, makes them important players to better understand the mechanisms of the bacterium response to nutrient deficiency and to potentially develop novel antimicrobial agents.

4 Strategies against *S. aureus* infections

The battle against *S. aureus* infections and the insurgence of resistant strains has become more and more essential over the years. Its importance is highlighted by the addition of *S. aureus* resistant strains in the "high priority" list of antimicrobial-resistant pathogens by the WHO in 2017 [49]. In 2016, AMR caused 70,000 deaths per year, but 10 million deaths were predicted by 2050 in O'Neil report [364], with the likely possibility of an increase after the spread of the COVID-19 pandemic. This scenario has inevitably led to the search for novel strategies against *S. aureus* infections. Different strategies and targets related to the iron uptake process and its effectors can be exploited for the potential development of antimicrobials. Indeed, potential valid targets belong to systems prior to iron uptake (hemolysins' secretion), within iron uptake (iron mimetics and siderophores) and following the iron

uptake (heme degradation). For the scope of this thesis, this chapter will focus on the current strategies, available and under study, against the hemophores' and the siderophores' iron acquisition pathways.

4.1 The Isd system

Iron importance as a trace element makes it essential for *S. aureus* growth and host colonization, even more when the human host implements nutritional immunity to starve the pathogens. In this context, the Isd system is the main bacterial pathway for iron acquisition and its components have been identified as virulence factors [144,181,192,194,196,214,365–369].
Despite being a potentially valuable antimicrobial strategy [246,258,281], interfering with these virulence factors has not received much attention, and no small antimicrobial molecules have been developed or used targeting Isd effectors to date. This context presents a chance for the development of new antimicrobial drugs that could address the antibiotic resistance issue.
This chapter will provide an overview of the effects of Isd proteins' removal on *S. aureus* viability to give an idea of the effect of targeting these virulence factors. Moreover, the chapter will also report the current antimicrobial strategies targeting IsdB in the specific, but also the Isd system in a broader overview.

4.1.1 Inhibition of heme acquisition

The centrality of the cell-wall anchored Isd hemophores (IsdA, IsdB, IsdC and IsdH) in *S. aureus* fitness has been suggested in different studies, by observing a decreased growth and Hb binding ability in SrtA and SrtB mutants when the only source of iron is heme, as well as by the significant attenuation of the sortases' mutants in murine abscess models [26,181,213,367,370–372]. Nevertheless, since SrtA is a ubiquitous sortase, it is challenging to discern the impact on abrogation of Isd protein cell wall attachment from that of other SrtA substrates affecting the bacterium fitness. Contrary to SrtA, SrtB is more specific towards IsdC, therefore it should provide a more precise effect. Nevertheless, previous studies have observed only mild effects of SrtB deletion on the virulence of *S. aureus* [27,371,373]. Some studies have still worked on inhibitor development and identified a natural flavonoid called baicalin as a potential adjuvant for antimicrobials against *S. aureus*, even if implementations are needed [374–376].
IsdA and IsdB hemophores appear to be fundamental in the early infection phases, enabling colonization and abscess development [144,180,201,367,377]. The transcription of both genes, like that of many other virulence factors, depends on the Sae regulatory system, which is induced by Fur under iron restriction [148]. In contrast to IsdH abrogation, inactivating IsdB severely impairs *S. aureus* colonization and virulence [23,181,196,197,201,212,378], disclosing potential IsdB requirement during infection. This is further supported by the 40-fold increase of IsdB expression that was observed in MRSA strains in iron-restricted conditions [234]. Conversely, when the only source of iron is heme, IsdA mutants exhibit growth defects [266]. However, when IsdA is genetically deleted, IsdC is overexpressed, enabling bacteria to partially make up for IsdA absence [26], and thus potentially indicating that IsdA role in virulence is likely connected to its alternative functions [26,367]. At last, if either IsdC or SrtB are inactivated, *S. aureus* is just partially hampered in its ability to generate abscesses [26,367].
Moving to the remaining components of the Isd system, it has been observed that IsdE mutants show restricted acquisition of hemic iron [342], whereas IsdF mutants exhibit significantly impaired growth, though not completely inhibited [26,180]. Lastly, mutants of either oxygenases, IsdG and IsdI,

result in bacterial iron starvation and raise the possibility of heme poisoning [214,246,379]. Targeting bacterial heme oxygenases would be a convenient strategy since they are different compared to the host heme oxygenases, thus providing a very selective target with reduced potential side effects.
In conclusion, the suppression of heme uptake typically results in compromised growth and pathogenesis, but it rarely kills the pathogen. Thus, contrary to the generally desired property of most antibiotics, that is to kill all microbes without selectivity, these anti-infective inhibitors may lessen the selective pressure that leads to the emergence of bacterial resistance [27,202]. This perspective would be particularly significant given the high rate of resistance development reported for *S. aureus*.

4.1.2 Biopharmaceuticals

Pharmaceuticals derived from biotechnological procedures are referred to as biopharmaceuticals, which include, among other things, recombinant proteins, allergenics, gene therapy, blood components, living cells, antibodies, and vaccines. The value of biopharmaceuticals derives from their improved properties over small molecules, as their high specificity and very low resistance rate [380]. Another important factor in the biopharmaceuticals' development is their capacity to induce opsonophagocytic activity by particular antibodies or complement, which guarantees effective clearance and killing of *S. aureus* [381,382]. Even if small molecules targeting the Isd system have yet to be found, some biopharmaceuticals have been proposed within the fight against existing and developing resistant strains [40,383–386].
The next paragraphs will discuss them more in detail, focusing especially on IsdB, which has been identified as the more immunogenic Isd protein and, in certain cases, of the whole *S. aureus* proteome [385]. However, attempts to selectively target this hemophore have not produced yet positive results, prompting subsequent research to concentrate the efforts on multiple targets, either within the same Isd system or searching for additional *S. aureus* virulence factors.

Vaccines against IsdB

One of the most promising IsdB-targeting vaccines, and yet the biggest failure, has been the monovalent V710 produced by Merck and Intercell between 2006 and 2011. The vaccine was developed for active immunization against IsdB and showed positive immune responses in humans within Phase I trials. Nevertheless, low vaccine efficacy and safety issues led to the termination of phase 2b/3 [387,388]. The reason for the V710 safety issues might be correlated to the formation of a multicomplex consisting of staphylococcal protein A, IsdB, anti-IsdB antibody, Hb and Hp that was observed to be involved in *S. aureus* internalization and survival within macrophages [389].
Another noteworthy failure in vaccine development, yet not involving IsdB, regards SA4Ag by Pfizer, which is a 4-antigen vaccine comprising ClfA, MntC and both CP5 and CP antigens. The SA4Ag vaccine failed during Phase IIb clinical trials because it couldn't prevent *S. aureus* infections [390–393].
Currently, the most promising candidate is the rFSAV five-antigen vaccine by Olymvax, which it's being tested in Phase II clinical trials [394]. The inclusion of Spa and Hla in the rFSAV formulation aims at inhibiting *S. aureus* immune evasion strategies, implementing previous vaccines. Nevertheless, the presence of IsdB will require more safety controls due to the results observed for the V710 vaccine [394,395].
Despite different vaccines have been developed (or are under study) against IsdB and other Isd system targets, no vaccine has been commercialized yet [54,382,396,397]. It is important to note that even

if preventing the pathogenesis is vaccines' primary objective, they should also be evaluated based on their varying degrees of protective activity. Future research investigations may find that lowering the severity and mortality of staphylococcal infections is still a significant outcome [397].

Table 4: Summary of the previous and current vaccines targeting the Isd system. The abbreviations used refer to: serine-aspartate repeat-containing protein D and E (SdrD-E), clumping factor A (ClfA), hemolysins alpha and gamma (Hla-g), staphylococcal protein A (SpA), staphylococcal enterotoxin B (SEB), and manganese transport protein C (MntC).

Target	Activity	Reference
IsdB	Merck V710 Mice were protected from lethal *S. aureus* infections. Anti-IsdB antibodies were stimulated in rhesus macaques and the vaccine showed positive immune responses in human (Phase I trials).	398,399
IsdB, IsdA, SdrD and SdrE	Opsonophagocytic antibodies were induced. Mice were protected from lethal challenge after infections with different *S. aureus* strains.	400
IsdB, ClfA and Hlg	Increased *in vitro* phagocytosis, bacterial load was reduced in mice spleen and mice were protected in intraperitoneal challenge.	401,402
IsdB and ClfA	Antibody response induced by opsonophagocytic killing (OPK) activity	403
$IsdB^{N2}$, Hla, SpA, SEB and MntC	Olymvax rFSAV Significant protection in lethal sepsis and in pneumonia mouse model, humoral and complete cellular immune response were induced. Phase II is currently ongoing.	394,404,405

IsdB within the antimicrobial therapy

Targeting IsdB, or other components of the Isd system, is a valuable antimicrobial strategy and different efforts have been made to develop antibodies against the hemophores (Table 5) [406,407].
Interestingly, antibodies developed against Isd proteins led to the formation of macromolecular complexes that, in addition to their functions as a marker for the host's humoral immune response, can actively block heme uptake [377].
In a very recent work, Valenciano-Bellido and colleagues reported positive results for a novel camelid antibody targeting IsdB and IsdH that showed inhibition of heme acquisition and led to reduced growth of three MRSA strains [408]. Further tests will be of course needed for the development of this new potential antibody.

Table 5: Summary of the current antibodies targeting the Isd system.

Target	Activity	Reference
IsdB	Murine monoclonal antibodies (mAbs) showing partial OPK activity and efficacy for mice challenge models	[409]
IsdB	Human mAbs with *in vitro* high OPK activity. Protection of rats was shown in lethal sepsis models.	[381,410]
IsdB and IsdA	Inhibition of heme acquisition leading to protection towards abscess formation and lethal challenge.	[377]
IsdB	Antibodies use within the adaptive immune system, with IsdB recognition and direct inhibition.	[411,412]
IsdB and IsdH	*In vitro* evaluation.	[408]

4.2 Siderophores within the antimicrobial therapy

As already discussed in detail, iron is an essential element for *S. aureus* growth and host colonization, especially when the human host implements nutritional immunity to starve invading pathogens. Siderophore-mediated iron acquisition is an important pathway for the bacterium to retrieve the trace metal, and the system presents different potential target options for the development of novel antibiotics. It is important to note that the use of small molecules to competitively inhibit SA and SB receptors from binding their ligands is not an exploitable strategy since their binding affinity is within the nanomolar range [324]. For this reason, the current most promising approach reported in literature exploits siderophores for the development of siderophore-antibiotic conjugates in a "Trojan horse" strategy. Other valuable strategies include the inhibition of siderophores' biosynthesis and transport systems, but not many positive results have been obtained in this field yet [413]. Since no antimicrobial agent has been developed against the first two enzymes involved in SB biosynthesis, SbnA and SbnB, the following paragraphs will provide a more general overview of the current strategies to target iron uptake in *S. aureus* by exploiting or targeting siderophores.

4.2.1 Siderophores as Trojan Horses

The main antimicrobial strategy involving siderophores exploits these iron chelators as "Trojan horses", namely siderophore-antibiotic conjugates are produced to deceive bacteria into internalizing therapeutic agents. Indeed, the so-formed siderophore-antibiotic conjugate can often be still recognized and internalized into bacteria through the same dedicated transporter used by the siderophore alone [414–416]. Before being used to good advantage for human infection treatments, this strategy is exploited first and foremost by bacteria themselves to deliver antibiotics towards competing organisms able to acquire xenosiderophores.

Conjugated siderophores involved in "Trojan horse" strategies consist of three components: an antimicrobial agent, a linker, and an iron-chelating siderophore that can be natural or mimetic. After the whole conjugate has been internalized, it gets cleaved, allowing the release of the antibiotic that can thus perform its action [415,416]. Since every bacterium synthetizes and employs different siderophores, these conjugates are typically more selective compared to conventional antibiotics.

"Trojan horses" with artificial siderophores and conjugates that differ greatly from their parent structures can still be transferred into the targeted bacterial cells by means of siderophore transporters' structural tolerance. The most effective approach, nevertheless, is to replicate natural siderophores in order to successfully produce a synthetic conjugate [417,418].

Several efforts are reported in literature for the development of siderophore-antibiotic conjugates valuable for antimicrobial therapy. An attempt to exploit *S. aureus*-produced siderophores was made by Milner and colleagues, who combined ciprofloxacin and norfloxacin fluoroquinolones with the SA molecule [419]. Despite SA good properties, the first results reported no activity towards ciprofloxacin or norfloxacin resistant strains and the potency was significantly lower than the original antibiotics. To date actually no effective conjugate against Gram-positive bacteria has been identified [413], probably due to the development of too highly modified conjugates difficult to be imported by staphylococcal transporters, the need for antibiotic release from the conjugate and ultimately the existence of redundant iron acquisition systems [420]. Therefore, the "Trojan horse" strategy is promising, but it definitely needs further improvement.

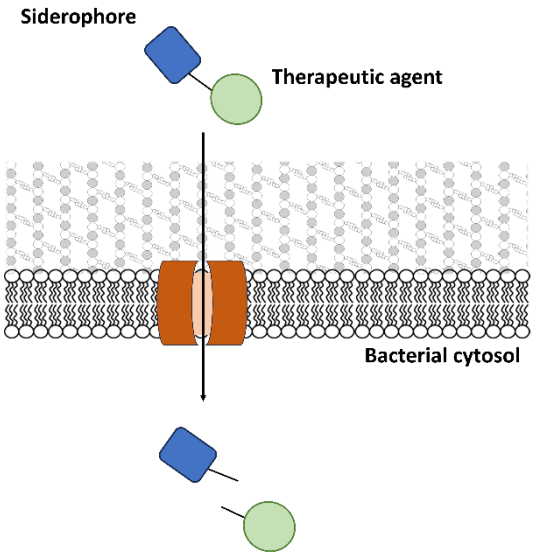

Figure 16: Schematic representation of the "Trojan horse"-like strategy exploiting siderophore-antibiotic conjugates (adapted from Cela et al, 2023 [421]). The internalization of the siderophore-antibiotic conjugate is followed by the cleavage of the conjugate, allowing the antibiotic to reach its target.

4.2.2 Inhibitors of the biosynthesis and transport of siderophores

Along with the hemic iron uptake, siderophore-mediated iron acquisition is one of the most important iron uptake systems for *S. aureus*, therefore hindering siderophore biosynthesis or internalization can be a valid strategy. Among *S. aureus* siderophores, SB is found in the most invasive strains, therefore it has gained more importance in the antimicrobial fight.

Tripathi and colleagues have targeted SB biosynthesis [422] by inhibiting the NIS synthase SbnE, which is involved in the catalysis of citric acid and L-Dap condensation [423]. The group managed to obtain two novel antimicrobials, baulamycins A and B (BmcA and BmcB, respectively) through the screening of a library derived from natural product extracts from marine microbes. It was observed that the two compounds function as reversible competitive inhibitors against SbnE, but also towards *B. anthracis* AsbA, showing the ability to inhibit the growth of both Gram-positive and negative bacteria

in liquid cultures. Furthermore, these molecules have the potential to develop into broad-spectrum antibiotics, since the class of enzymes to which their primary target belongs is common among many pathogenic bacteria [424–426]. Nevertheless, further studies are needed to confirm the molecules' safety and their activity *in vivo*.

Overall, different strategies have been studied and developed in the search for novel antimicrobial therapies, but no efficient solution has actually been identified.

Aim of the thesis

The thesis comprised activities aimed at providing a study on a potential double approach for the interference with *S. aureus* iron acquisition that would target both the hemophore and siderophore-mediated pathways. The project thus contained two work streams connected in a double strategy. Regarding the hemophores' stream of the project, the activities aimed at the evaluation of compounds' ability to disrupt the formation of the IsdB-Hb complex by the exploitation of an *in-house* developed immunoassay. Indeed, different *in vivo* investigations reported IsdB as an *S. aureus* virulence factor, critical for pathogenesis, and its interaction with human Hb was found to facilitate bacterial iron acquisition, required for the pathogen's growth and proliferation, as well as for infection establishment. In this context, IsdB appeared to be a good target for the development of new antimicrobials. For this reason, molecules that had been previously selected by *in silico* and *in vitro* screening conducted on commercial compound libraries were synthesized by collaborators at the University of Turin and tested by the immunoassay. Derivatives of the selected molecules were also synthesized and tested by the immunoassay to obtain more potent inhibitors with improved compounds' solubility and/or stability. In principle, the discovery of potent and selective PPI inhibitors could be exploited for the development of antimicrobials, reducing iron availability for the bacterium. Interestingly, although the functional and regulatory specificities between IsdB and IsdH hemophores still remain unclear, their heme retrieval mechanism from Hb seems similar. Consequently, the platform optimized for targeting IsdB could be easily modified to evaluate the impact of the identified molecules on the formation of the IsdH-Hb complex in order to identify promising molecules that would be active on both *S. aureus* Hb receptors.
On the other hand, the siderophores' part of the project contained activities that aimed at the characterization of the first step in SB biosynthesis, namely the SbnA-catalysed reaction, whose concerted action with SbnB was reported to produce two out of three building blocks of SB. Indeed, the functional characterization of the SbnA enzyme provided a deeper understanding of the mechanism of action of the protein. All the information acquired within the enzyme characterization aimed at providing tools for the evaluation of potential inhibitors of SbnA activity. For this purpose, a testing platform was optimized and validated by evaluating the effect of intermediates of the SB biosynthetic pathway on SbnA activity to identify potential feedback mechanisms within the pathway. The project also aimed at the evaluation of the effect of different compounds on SbnA activity to identify potential inhibitors. The identification was performed by a double approach to widen the possibilities of identifying inhibitors with different physicochemical properties and chemotypes, as well as different mechanisms of action. First, a structured-based strategy for active-site targeting involved the testing of molecules from an *in silico* analysis that were subsequently modified to improve potency. The second approach aimed at identifying compounds from commercial and proprietary libraries by high-throughput screening, performed in the Service de Chimie Bioorganique et de Marquage at CEA Paris-Saclay.

Overall, the following activities were performed during the thesis:

- Expression and purification of IsdB Y165A variant, which was reported to have decreased affinity for Hb. Because of its properties, the variant was exploited within the immunoassay used for the evaluation of potential IsdB-Hb PPI disruptors, since it had increased the assay sensitivity for the first sets of possibly weak inhibitors.
- Optimization of an immunoassay for the IsdB Y165A variant exploited as a platform for the evaluation of potential disruptors of the IsdB-Hb complex.

- Evaluation of a set of small molecules for the disruption of the IsdB-Hb complex by the immunoassay. The selected molecules were synthesized by collaborators at the University of Turin based on results of previous *in silico* and *in vitro* screening conducted on commercial libraries of compounds. Evaluation of synthesized derivatives of the best hit compounds.
- Optimization of the conditions for the expression and purification of SbnA enzyme exploiting two different constructs. Spectroscopic characterization of SbnA by UV-visible absorbance and fluorescence spectrophotometry. Optimization of the conditions of a continuous coupled enzyme assay for the evaluation of SbnA enzymatic activity, with characterization of its mechanism of action.
- Set-up of a testing platform for the evaluation of potential inhibitors of SbnA activity. The platform comprehended the evaluation of compounds' inhibitory activity and mechanism of action, as well as their binding to SbnA.
- Evaluation of the effect of intermediates of the SB biosynthetic pathway on SbnA activity through the testing platform for the identification of potential feedback mechanisms within the pathway.
- Evaluation of *in silico* selected molecules to identify potential inhibitors of SbnA activity, and analysis of the mechanism of action of the best hits.
- Set-up, optimization and exploitation of a high-throughput screening assay to evaluate compound libraries for the identification of SbnA inhibitors. Characterization of the best hits. This part of the work has been conducted at the CEA Paris-Saclay centre in Paris, France.

Chapter I – Evaluation of potential disruptors of IsdB-Hb PPI

1 Objectives

This chapter presents an *in-house* developed immunoassay as a platform for the evaluation of molecules that might interfere with IsdB-Hb complex formation. Indeed, several *in vivo* investigations have reported that IsdB is critical for *S. aureus* pathogenesis, and its PPI with human Hb facilitates iron uptake, which is required for bacterial growth and proliferation, as well as for infection establishment. Given this experimental evidence and the MRSA and VRSA threat, IsdB seems to be a good target for the development of novel antimicrobial drugs.

Theoretically, the discovered PPI inhibitors might be used as best-in-class antimicrobials, reducing iron availability for the bacterium. Furthermore, the binding of the compounds to Hb should reduce the relevance of bacterial target mutations in the development of resistance and may allow interference with the interaction of many hemophore systems, beginning with IsdB and IsdH. Interestingly, although the functional and regulatory distinctions between IsdB and IsdH remain unclear, their system for heme uptake from Hb appears to be similar. Consequently, the testing platform that is being presented could be readily modified to evaluate the impact of the identified molecules on the formation of the IsdH-Hb complex in order to identify promising molecules that would be active on both *S. aureus* Hb receptors.

An *in-silico* screening campaign was originally conducted by the research group of Professor Francesca Spyrakis (University of Turin) to identify compounds to be tested by the implemented immunoassay. The ultimate objective was to identify compounds that bind free Hb in plasma without compromising Hb activity within red blood cells. The purpose of these compounds was to directly compete with hemophores interaction with Hb. Only molecules presenting low lipophilicity were chosen, in an effort to select compounds able to scavenge free Hb in the bloodstream without entering the red blood cells. In a previous analysis, the immunoassay was performed on 54 commercially available compounds, selected by the *in-silico* screening. The results of the screening allowed to select 6 molecules able to reduce by 50% or more the IsdB:Hb complex formation at a concentration of 1 mM. 4 of these were later confirmed to bind Hb through Saturation Transfer Difference (STD)—NMR experiments carried out by Prof. Serena Faggiano (University of Parma). Within this thesis activities, 3 of the 4 compounds were synthesized by the group of Professor Loretta Lazzarato (University of Turin) and re-tested by the immunoassay and STD-NMR to verify their ability to reduce IsdB:Hb complex formation and to confirm their binding to Hb. Ultimately, analogues of the three best compounds were synthesized by Prof. Lazzarato with the aim of improving the molecules' physicochemical properties. Indeed, this initial evaluation aimed at finding potential parent compounds to be inserted into a new screening campaign of synthesized derivatives.

2 Material and methods

If not otherwise specified, all reagents were purchased from Sigma Aldrich (St. Louis, MO, USA) at the best available commercial quality, and used as received.

2.1 Protein expression and purification

2.1.1 Growing media

Luria-Bertani (LB) agar plates were prepared by the addition of 15 g/L agar to LB broth, which contains:

- 5 g/L yeast extract
- 10 g/L tryptone
- 10 g/L NaCl

M9 minimal broth contained:

- 1x M9 salts (33.9 g/L Na_2HPO_4, 15 g/L KH_2PO_4, 3.5 g/L NaCl, 5 g/L NH_4Cl)
- 240 mg/L $MgSO_4$
- 11 mg/L $CaCl_2$
- M9 was supplemented with 0.4% glucose

2.1.2 IsdB Y165A variant over-expression system

For IsdB Y165A variant over-expression, *in-house* available *E. coli* BL21(DE3) cells were exploited that had been previously transformed with the pASK-IBA3plus plasmid coding for the IsdB Y165A mutant. The transformed cells were plated on LB agar supplemented with 100 µg/mL ampicillin and grown at 37°C overnight. A single colony was selected and inoculated in 10 mL of LB broth supplemented with 100 µg/mL ampicillin and grown at 37°C overnight, under 250 RPM agitation. The overnight grown culture was diluted 1:100 in M9 medium supplemented with 100 µg/mL ampicillin. The cells were grown at 37°C, under 250 RPM agitation, until the midlog phase (OD600 around 0.5 – 0.6) was reached, which normally took 5 hours. Cells were then induced for 3 hours at 37°C by the addition of 0.2 µg/mL anhydrotetracycline (ATH). Cells were collected from the broth by centrifugation at 5000 RPM for 10 minutes, then they were washed once with phosphate buffered saline (PBS) solution and ultimately frozen at -80°C in aliquots coming from 500 mL of culture.

2.1.3 Y165A IsdB variant purification

Y165A IsdB variant purification process started with the resuspension of the cell pellet in lysis buffer composed by buffer W (100 mM Tris pH 8, 150 mM NaCl, 1 mM EDTA) in presence of 1 mg/mL lysozyme, 0.2 mM benzamidine, 0.2 mM PMSF and 1.5 µM pepstatin A. The amount of lysis buffer used for resuspension is equal to a 10:1 ratio of $Volume_{lysis\ buffer}$: $weight_{pellet\ (grams)}$. Sonication was performed to complete cell lysis, with approximately three cycles 1 minute long (10s ON/30s OFF). Centrifugation for 1 hour at 4°C and 16,000 x g removed cell debris, after which the pH of the supernatant was set above 8. The adjusted supernatant was loaded onto a pre-equilibrated XK 16/200 column (GE Healthcare), that had been previously packed *in house* with 3 mL of Strep-Tactin® XT resin (IBA Lifesciences, Göttingen, Germany). The column was connected to an AKTA Prime Liquid Chromatography System (GE Healthcare) supplied with a single wavelength UV detector (280 nm)

and one conductivity meter. Protein elution was accomplished with Buffer BXT 10X (IBA Lifesciences, Göttingen, Germany), diluted to 1X in water. To separate the protein monomer from the dimer, a final step of Size Exclusion Chromatography (SEC) was performed exploiting an HiLoad 16/600 Superdex 75 pg prepacked column (GE Healthcare). The column, used for preparative purposes, has a separating range of 3-70 kDa. The cleaning of the column was performed every five purification processes, after which the column was calibrated with blue dextran (void volume), conalbumin (75 kDa), ovalbumin (43 kDa), carbonic anhydrase (29 kDa) and myoglobin (17 kDa) in order to validate the separation performance. All the chromatographic steps were performed at 4°C. In the experimental conditions, the IsdB dimer eluted distinctly separated from the monomeric form. The final protein preparation had a purity above 95%. The concentration of the IsdB Y165A variant was calculated by UV-Visible absorption spectra using its extinction coefficient ε_{280} = 46,300 M^{-1} cm^{-1} and molecular weight MW = 43,100 g/mol. Given that heme from *E. coli* is partially acquired by IsdB during its overexpression, the quantity of holo-IsdB within the preparation was evaluated by calculating heme concentration through the specific extinction coefficient ε_{405} = 90,500 M^{-1} cm^{-1} reported in literature. The equation used to calculate holo-IsdB amount is the following:

$$\textbf{Eq. 1}: \%\ holo - IsdB \quad = \frac{\frac{OD_{405}}{\varepsilon_{405}}}{\frac{OD_{280}}{\varepsilon_{280}}} \cdot 100$$

2.1.4 UV-Visible absorption spectroscopy

UV-Visible absorption spectra of IsdB Y165A variant were collected on an Agilent Cary 4000 spectrophotometer supplied with a temperature-controlled cell-holder. For the spectra, Hellma™ Far UV Quartz Cuvettes (pathlength of 1 cm) were exploited unless otherwise reported.

2.1.5 PolyAcrylamide Gel Electrophoresis (PAGE)

Sodium Dodecyl Sulphate PAGE (SDS-PAGE)

Protein samples were run under denaturing conditions on 0.75 mm freshly casted mini gels. Standard 12% gels, constituted of two distinct gel layers (stacking and separating gels), were prepared as reported in Table 6. Gels were run inside a Bio-Rad Mini-PROTEAN Tetra Vertical Electrophoresis Cell that was powered by a Bio-Rad PowerPac™ Basic Power Supply set at 200V. Precision Plus Protein™ Unstained Protein Standards (Bio-Rad) was utilized as MW marker. After the electrophoretic run, the gel was incubated in Coomassie staining solution for 10-15 minutes. Afterwards, multiple destaining steps were performed until the protein bands reached the desired visualization point.

Table 6 Recipe for SDS-PAGE. The solution volumes reported are sufficient to prepare 0.75 mm Bio-Rad Mini-PROTEAN gels. Abbreviations used in the table are: tetramethyl ethylenediamine (TEMED) and ammonium persulfate (APS).

Stacking gel (acrylamide/bis, 4% final)	Volume (µL)
Acrylamide/bis, 30% 29:1	400
0.5 M Tris/HCl pH 6.8	750
Water	1730
SDS at 10%	30
APS at 10%	20
TEMED	6

Separating gel (acrylamide/bis, 12% final)	Volume (µL)
Acrylamide/bis, 30% 29:1	1992
0.5 M Tris/HCl pH 6.8	1250
Water	1662
SDS at 10%	50
APS at 10%	40
TEMED	8

Sample buffer 4X	Volume (mL)
0.5 M Tris/HCl pH 6.8	2
SDS at 10%	4
β-mercaptoethanol	0.4
Bromophenol blue 0.5%	0.8
Glycerol at 100%	2.8
Running solution (10X)	**g in 500 mL**
Tris base	15.1
SDS	0.5
Glycine	72.1
Water	To final volume

Coomassie staining solution	Volume (mL)
Coomassie blue	2.5 g
Glacial acetic acid	100
Ethanol	200
Water	700
Coomassie destaining solution	**Volume (mL)**
Glacial acetic acid	100
Ethanol	200
Water	700

Native PAGE

The native PAGE optimized protocol utilizes a 1 mm continuous freshly casted mini gel, whose preparation followed Table 7 recipe. The protocol proposed by McLellan [427] was adapted for the purpose of our analysis.

Table 7 Recipe for native PAGE. * the pH of the running buffer solution does not have to be adjusted.

Separating gel solution for a single gel	**Volume (µL)**
Acrylamide/bis-acrylamide, 30% 29:1	2250
Running buffer 5X (see below)	1500
APS 10%	100
TEMED	12
Water	3750
Running buffer 5X*	
HEPES	41.71 g/L
Imidazole	14.64 g/L
Sample buffer 3X	**Volume (µL)**
Running buffer 5X	1000
Glycerol at 50%	2000
Malachite green solution at 1%	200

About 3 µg of each sample was normally analysed after sample dilution in 20 µL of sample buffer 1X. The running buffer 5X solution was diluted to 1X solution at each electrophoretic run, while the external running buffer was used for several analyses. Both the internal and external buffers were cooled to 4°C overnight before the analysis. A Bio-Rad Mini-PROTEAN Tetra Vertical Electrophoresis Cell was exploited to run the casted mini gels. The apparatus was placed into an ice bath in order to keep the temperature below 10°C for the whole electrophoretic run, and a Bio-Rad PowerPac™ Basic Power Supply was used to power the system. Three steps were performed to keep the voltage below 200 V during the whole electrophoretic run: the first 10 minutes were performed at 20 mA, followed by 10 minutes at 15 mA and ended with 330 minutes at 11 mA. The purified monomeric and dimeric forms of IsdB were exploited as internal markers for the analysis. After the electrophoretic run, the mini gel was incubated for 10-15 minutes in the Coomassie staining solution and then various destaining steps were carried out until the protein bands were visualized as desired. A densitometric analysis of the stained mini gel was performed to quantify the protein bands' relative composition.

Mini gels were visualized through a ChemiDoc MP imaging system (Bio-Rad©) and the Image Lab™ software (Bio-Rad©) was used for densitometry.

2.2 Immunoassay

2.2.1 In silico screening

The group of Prof. Spyrakis (University of Turin) performed a structure-based virtual screening using as target the structures of metHb and metHb in complex with Hp, which were retrieved from PDB (PDB ID 3P5Q and 4X0L, respectively). Three commercial libraries (Specs, Vitas-M Laboratory, Ltd., and Enamine Ltd.) were retrieved from the ZINC database and screened against the target. The molecules were filtered with a logD > 0 to select more hydrophilic compounds that would stay in the bloodstream without crossing the cellular membranes. The compounds selected by this first filter were submitted to a virtual screening and molecular docking campaign, which screened for polar molecules able to establish hydrogen bonds with the target and prevent IsdB recognition.

2.2.2 Sample preparation and compounds solubilization

IsdB Y165A was prepared as above reported. The hemophore, as well as Hb, was exchanged from buffer W to binding buffer (2 mM EDTA, 140 mM NaCl, and 25 mM TRIS/HCl pH 7.6), which was selected as working solution for all the immunoassay steps following the suggestions of the microplate manufacturer.

The compounds under evaluation were synthesized by Prof. Loretta Lazzarato at the University of Turin. The compounds were re-synthesized based on preliminary results obtained with commercial molecules (Specs, Vitas-M Laboratory, Ltd., and Enamine Ltd.) that were selected and tested previously on the basis of the virtual screening campaign carried out by the group of Prof. Spyrakis (University of Turin). The compounds synthesized *in-house* were solubilized in deuterated (D_6)-dimethyl sulfoxide (DMSO) at 100 mM concentration. When compounds resulted partially or entirely insoluble, they were subjected to a sonication cycle using an ultrasonic bath (Bormac CE-5700, 41300303). If the sonication step was not sufficient for solubilization, the compounds were heated at 37 °C for ten minutes using a thermoblock. At last, some compounds required a decrease in the concentration of the stock solution to reach complete solubilization. Molecules that presented high insolubility were produced as TRIS salts.

The absorption spectra of the solubilized molecules alone or in the presence of 10 µM oxyHb were acquired in a UV-transparent, 384-well microplate (Greiner UV-STAR® plate – 781801) using a microplate reader (TECAN Spark® 10M). A 2 mM intermediate dilution of the compounds in binding buffer was performed, and the pH of the diluted solutions was adjusted between 6.5-7.5. Subsequently, the compounds were tested at 1 mM concentration to evaluate the presence of any absorbance signal around 450 nm that could interfere with the immunoassay. Moreover, oxyHb spectra in the presence of the solubilized compounds were used to evaluate the potential oxidizing activity of the compounds on Hb. Notably, Hb Q bands present high sensitivity towards the redox state of the heme within Hb. Because of this property, Q bands were selected as a marker for Hb oxidation, and the oxidized Hb characteristic peak at 640 nm was the most used for this analysis. The effect of each compound on the oxyHb spectrum was evaluated in the same experimental conditions as the immunoassay. Indeed, the spectrum of compounds alone or in presence of oxyHb was acquired after 2 hours to have a time delay that would be comparable with the total length of the immunoassay. Also, the incubation steps were performed at 4°C, hence in the same conditions as

the immunoassay. To evaluate the potential oxidizing activity of compounds, the contribution of the blank solution and the compounds were subtracted to the final spectrum.

2.2.3 Immunoassay

The immunoassay had been previously developed *in-house* (Figure 17). In this section are reported the final aspects of the immunoassay that were optimized during this thesis.

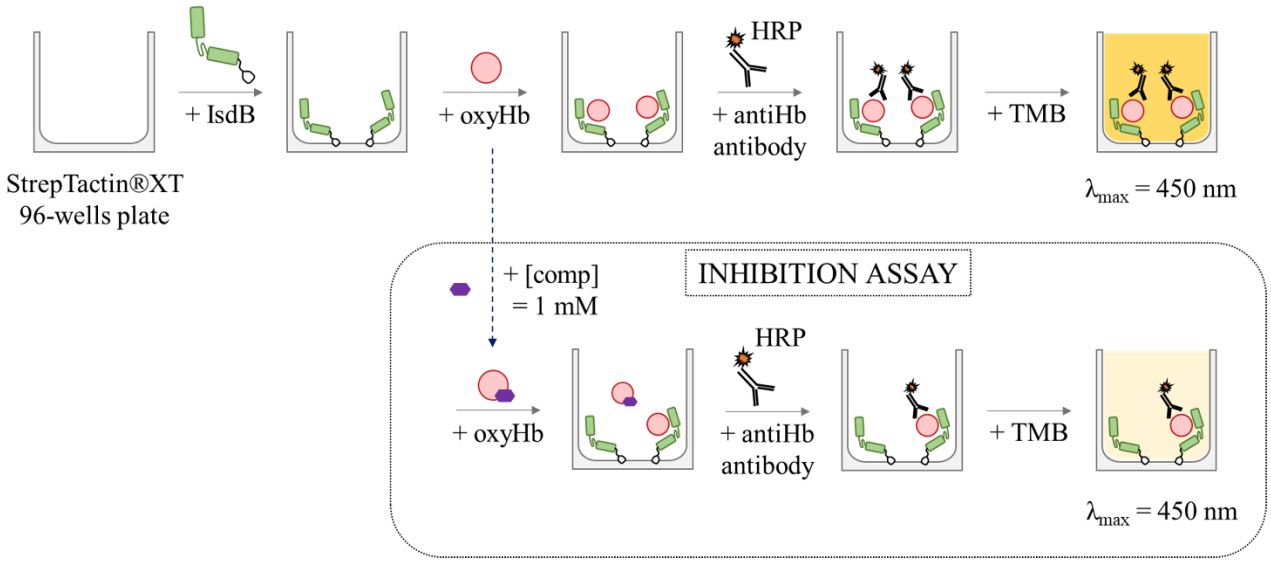

Figure 17: Schematic representation of the immunoassay.

As previously arranged in the *in-house* development, the IsdB Y165A variant was used in the optimization of the immunoassay to reduce the risk of auto-oxidation of oxyHb. Indeed, the Hb concentration in the assay should be maintained close to its dissociation constant for IsdB, with the aim of increasing the assay sensitivity for weak Hb interactors. Nevertheless, the Hb dissociation constant for wt IsdB is lower (around 35 nM) than the dissociation constant for the tetrameric/dimeric forms of oxyHb (around 250 nM [281]), therefore oxyHb tested in the assay with wt IsdB would be mainly found in the dimeric form, which is more likely to undergo auto-oxidation [282]. Furthermore, oxyHb dissociation constant for IsdB Y165A is predicted to be significantly greater (about 80 µM ± 11 mM [428]) according to literature data [196]. Thus, the exploitation of IsdB Y165A in the assay would allow to use an Hb concentration for IsdB half-saturation that is enough for the stabilization of Hb tetrameric form, which in turn is less prone to auto-oxidation.

Within this set-up, commercially available Strep-Tactin®XT coated microplates (IBA Lifesciences) were acquired to take advantage of the recombinant protein C-terminal StrepTag®II for hemophore immobilization at the bottom of the plate. Following the producer's recommendations, the functionalized wells were incubated O/N at 4°C with 2 pmol StrepTag®II- IsdB Y165A. The microplate was then washed with washing buffer (binding buffer containing 0.05% Tween-20), followed by the incubation for 1 hour at 4°C of 30 µM oxyHb. After another washing step, a horseradish peroxidase (HRP)-coupled anti-Hb polyclonal antibody, purchased from Abcam (Ab, Abcam ab19362), was incubated for 1 hour at 4°C. After the final washing step, 100 µL of the HRP colorimetric substrate 3,3',5,5'-tetramethylbenzidine (TMB) was added to the microplate wells. This latter product was purchased from Acros Organics (328051000, Acros Organics, Waltham, Massachusetts, USA) and

Merck (T4319, Darmstadt, Germany). After TMB addition, the reaction was developed for 30 seconds at 4°C, and then it was stopped with 100 µL of 1 N H_2SO_4. Exploiting this set-up, several Ab dilutions (ranging from 1:100 to 1:1,500) were employed to evaluate the impact of Ab concentration on the assay outcome. Furthermore, other Ab dilutions (between 1:1,000 and 1:10,000) were also tested using different Hb concentrations to evaluate the potential effect on the complex stability. To evaluate if the Hb incubation time in the functionalized wells would affect the assay, the conditions used were 2 pmol of StrepTag®II- IsdB Y165A, 30 µM oxyHb and 1:1,000 Ab dilution. At last, it was also evaluated the potential impact on the quantity of bound Hb detected when the number of washing steps was increased from three to six. The immunoassay protocol was optimized as follows:

Functionalization of the plate: Strep-Tactin®XT coated microplate is incubated O/N at 4 °C with 2 pmol StrepTag®II-IsdB. The solution is then removed, and the microplate wells are washed three times with washing buffer.

oxyHb binding: oxyHb solution is added to the microplate and incubated for 1 hour at 4°C. The solution is then removed, and the microplate wells are washed three times with washing buffer.

Detection: an Ab 1:1,000 dilution in binding buffer is added to the microplate well and incubated for 1 hour at 4 °C. The solution is then removed, and the plate is washed three times with washing buffer. Subsequently, 100 µL of TMB solution is added to the well and incubated for 30 s at 4 °C. The reaction is then stopped by adding 100 µL of 1 N H_2SO_4 solution. The absorption intensity related to the HRP reaction product is acquired at 450 nm with a microplate reader (Dynamica Halo LED 96). In the data analysis, the background absorbance values from TMB solutions were subtracted from each reading.

2.2.4 Evaluation of potential disruptors of IsdB-Hb PPI

The interaction between IsdB and Hb was analyzed in either the absence or the presence of the investigated, re-synthesized compounds at 1 mM concentration. The molecules under study were expected to bind Hb, therefore a pre-incubation step was required for the solutions containing Hb (at a sub-saturating concentration of 30 µM) together with each compound (final 110 µL/well). The pre-incubation was performed for one hour at 4 °C in the dark in a not-functionalized plate (Sarstedt AG & Co., 83.3924.500). After the pre-incubation step, the Hb-compound solutions were added to the functionalized plate and the immunoassay procedure (Figure 17) was followed from this point further. The presence of an active inhibitor would decrease the quantity of IsdB bound to Hb. The assay results are thus expressed as a percentage of bound Hb, that was calculated in relation to the negative control's absorbance at 450 nm. All measurements were performed at least in duplicate.

3 Results and discussion

3.1 IsdB Y165A variant overexpression and purification

E. coli BL21 (DE3) cells transformed with pASK-IBA3plus::IsdB Y165A plasmid were exploited for the variant overexpression in M9 minimal medium and purification (Figure 18). The hemophore was purified by affinity chromatography and then the monomeric population was separated from the dimeric form by SEC (Figure 18C). The yield of purification was about 14 mg of monomeric protein from 1 L of bacterial culture, with a final purity of about 95% and the amount of holo protein lower than 5%.

The presence of IsdB Y165A monomeric and dimeric forms was also characterized qualitatively by native PAGE (Figure 18D). The principle of the separation derives from the different motion of the two protein populations within the gel matrix because of their different sizes, even if their charge to mass ratio is the same. The protocol used for the analysis was adapted from a 1982 study by McLellan [427], and the protein isoelectric point was calculated by ProtParam online tool and resulted to be around 8.9.

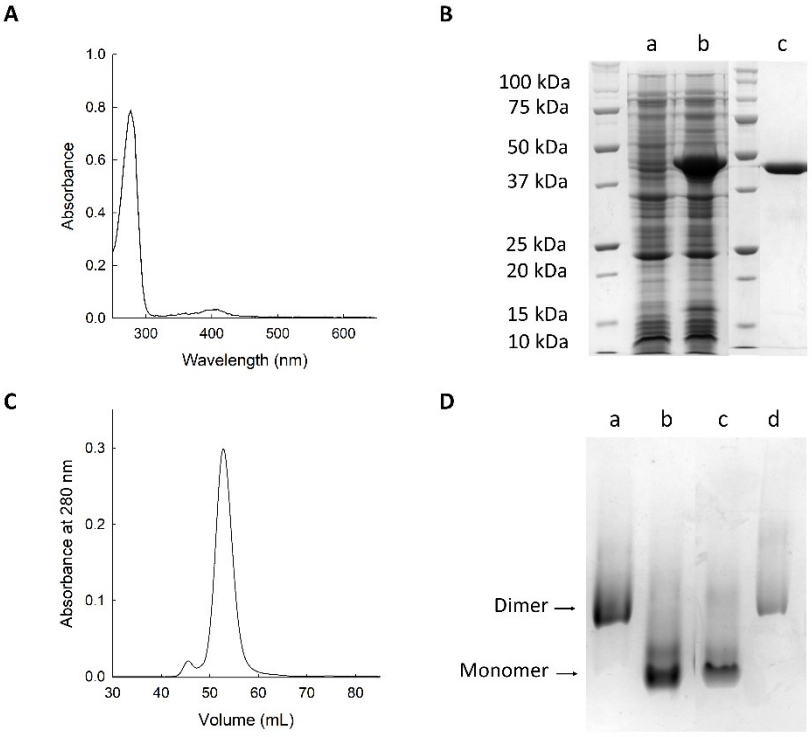

Figure 18: IsdB Y165A variant overexpression in M9 minimal medium. (A) UV-Vis absorption spectrum of the mutant. The amount of holo-IsdB calculated was lower than 5%. (B) The SDS-PAGE gel for (a) non-induced cells, (b) induced cells and (c) the purified protein. (C) SEC analysis for the separation of IsdB Y165A monomer and dimer, with the most represented population (main peak) being the monomeric form. (D) Native PAGE with (a) 3 µg of dimeric IsdB Y165A, (b) 3 µg of monomeric IsdB Y165A, (c) 3 µg of monomeric wt IsdB used as reference, (d) 3 µg of dimeric wt IsdB used as reference.

3.2 Immunoassay optimization

The *in-house* developed immunoassay was implemented as a platform for the evaluation of small compounds that would potentially interfere with IsdB-Hb complex formation. The immunoassay had been previously optimized using wt IsdB. In this thesis, the optimization of the assay conditions with IsdB Y165A completed the implementation of the platform. As previously stated, the reduced ligated form of Hb, namely oxyHb, was exploited for the immunoassay. The reason for this choice derived from the ability of IsdB to bind oxyHb, but its inability to extract heme from it. In this context, the pure binding could be evaluated without any complications derived from the subsequent Hb dimerization and cofactor extraction, which leads to the dissociation of Hb from the hemophores.

The assay was optimized using the procedures reported in Materials and Methods.

Since preliminary analyses have already been performed to confirm that the single reagents didn't cause any aspecific signals and to assess the right amount of IsdB to be attached at the bottom of the microplate [429], the optimization continued with further aspects of the assay. The effect of Ab dilutions (between 1:100 and 1:1,500) on the assay was assessed, using 2 pmol of StrepTag®II-IsdB Y165A and 30 µM oxyHb. As reported in Figure 19A the results highlighted a dose-dependent signal. Further Ab dilutions (from 1:1,000 to 1:10,000) were also tested in dose-response experiments and demonstrated that Ab dilution does not impact the calculated affinity of the complex (Figure 19B). Ultimately, the 1:1,000 Ab dilution was chosen as optimal condition for the immunoassay.

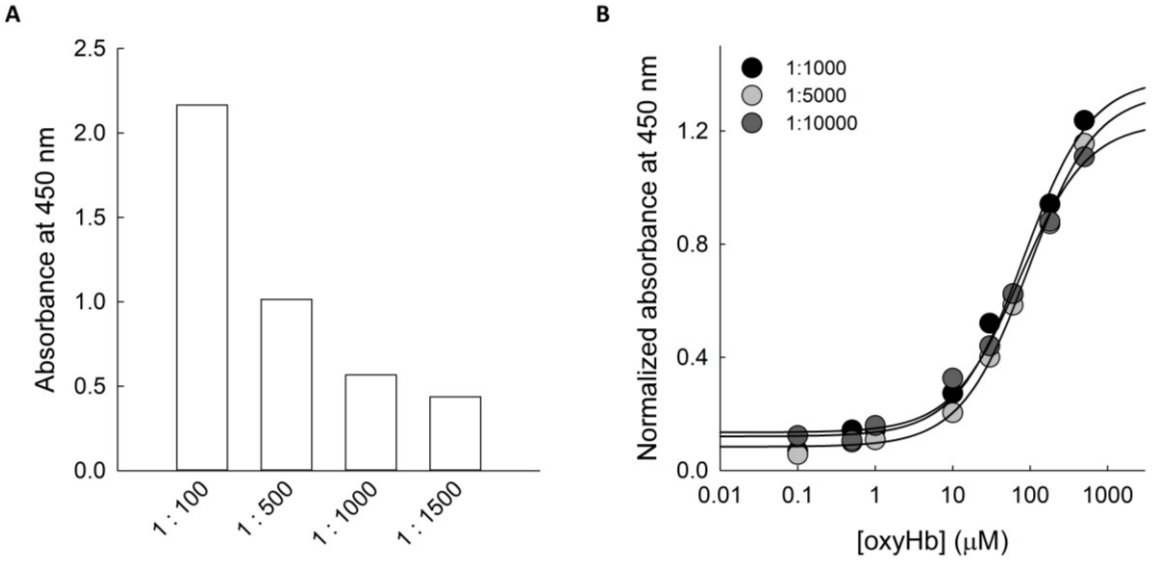

Figure 19: Optimization of Ab dilution for the immunoassay set-up. (A) Evaluation of the optimal Ab concentration at a fixed quantity of IsdB Y165A and Hb (2 pmol and 30 µM, respectively). Four Ab dilutions were tested. (B) Evaluation of the effect of three Ab dilutions on the IsdB:Hb binding.

After Ab evaluations, different oxyHb incubation times were tested, hence 1, 2 and 3 hours (Figure 20A). The experiments were performed using 2 pmol of StrepTag®II-IsdB Y165A, 30 µM oxyHb and a 1:1,000 Ab dilution. Since the results reported comparable signal intensities, 1 hour incubation was chosen for the final assay set-up. Ultimately, the effect of the number of plate washes on the signal and stability of the IsdB-Hb-Ab complex was assessed. The experiments were performed using 2 pmol of StrepTag®II-IsdB Y165A, 30 µM oxyHb and a 1:1,000 Ab dilution (Figure 20B). Three steps require the washing of the plate: after the hemophore functionalization step and after the Hb and

Ab incubation steps. The procedure recommended by the vendor consisted of three washings after each step, and the analysis confirmed that doubling the number of washings would not affect the amount of bound oxyHb detected. For this reason, the number of washings was set at three for each step.

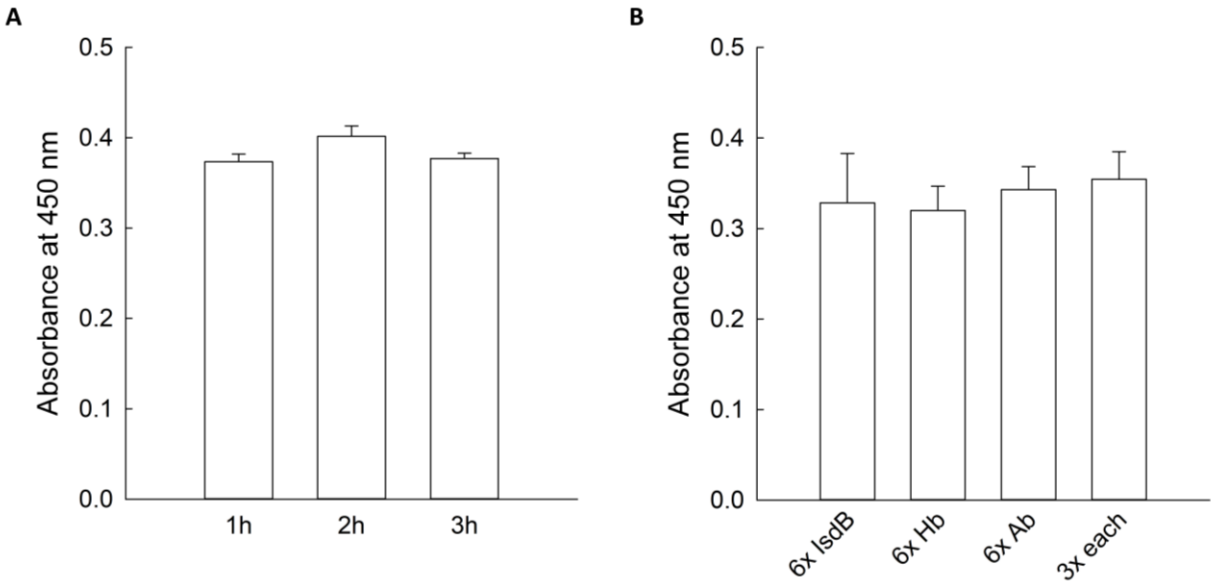

Figure 20: Optimization of the immunoassay set-up. (A) Evaluation of the effect of oxyHb incubation time with the IsdB Y165A-functionalized plate. (B) Evaluation of IsdB:Hb complex stability when changing the number of plate washes. The steps of the assay for which washes are required are the following: after IsdB Y165A functionalization, Hb incubation and Ab incubation. The reference corresponds to three washes after each step.

3.3 PPI inhibitor testing

The in-silico structure-based virtual screening and molecular docking were previously performed by the team of Prof. Spyrakis at the University of Turin to select molecules as potential PPI inhibitors. A first selection was performed by filtering commercial libraries for more hydrophilic compounds that would likely remain in the bloodstream without crossing red cell membranes, therefore targeting free Hb without affecting the intracellular Hb pool. The campaign of structure-based virtual screening and molecular docking led to the identification of 54 small molecules, expected to bind to Hb at a surface pocket contributing to the interaction area with IsdB [429].

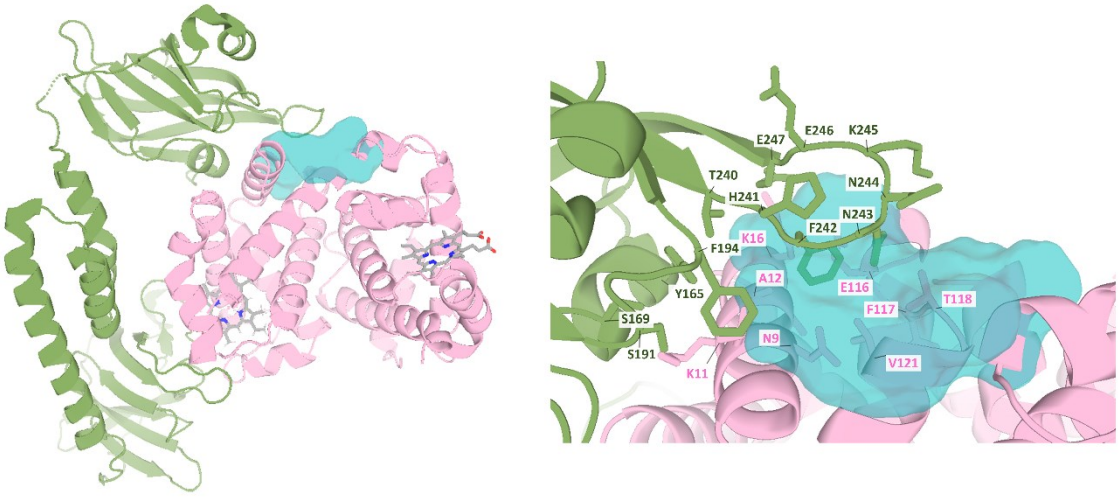

Figure 21: Representation of the IsdB-Hb complex. 3D model of IsdB (green) and Hb (pink), heme is represented as sticks and the targeted pocket on Hb surface, taking part in the interaction area with IsdB, is represented in teal. On the right, a close-up of the interaction interface, with the residues of IsdB shown as sticks and labelled based on their PBD numbering. The structure comes from PDB ID 5VMM**.**

The 54 compounds were purchased from commercial suppliers and tested by the immunoassay, followed by re-synthesis and confirmation of Hb binding for the best hits from the immunoassay. This initial evaluation allowed the identification of four compounds (C35, C41, C44, C53), that reduced the binding of IsdB to Hb by 50% or more. The binding of all these four hits to Hb was then confirmed by STD-NMR experiments conducted in collaboration with Prof. Faggiano at the University of Parma. Even if all compounds confirmed the binding, C41 revealed that only one methyl group of the compound was engaged in interactions with Hb, therefore it was excluded from further analyses.

Table 8: Summary of the hits identified within 54 commercial candidates and re-synthesized in-house by the group of Prof. Lazzarato (University of Turin). The chemical structures were drawn by using ACD/ChemSketch (Advanced Chemistry Development Inc., Toronto, Canada).

ID	Structure	MW
C35	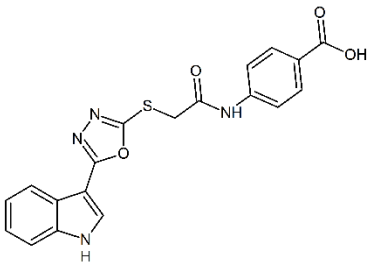	394.4
C44	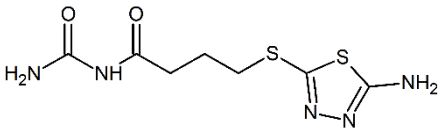	261.3

C53	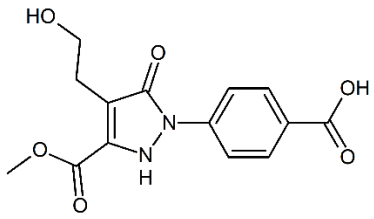	306.3

In this thesis, the three synthesized compounds C35, C44 and C53 (the structures are reported in Table 8) were solubilized in D_6-DMSO at 100 mM. Among them, C44 presented solubility problems in D_6-DMSO, probably due to the formation of stacking interactions among molecules. The commercial version of the compound didn't actually show solubility issues, therefore it was likely that the synthesized compound crystallized differently than the commercial one. Each compound's stock solution was diluted in binding buffer to 1 mM and the maintenance of pH of the solution around 7.6 ± 0.5 was confirmed. Using the diluted solutions, compounds were characterized by the acquisition of absorbance spectra in the range between 350 and 700 nm to rule out any interference at the absorbance wavelength of the immunoassay (450 nm) (Figure22). As expected, the spectrum of compound C44 showed a signal offset representing the not complete solubility of the molecule at 1 mM concentration.

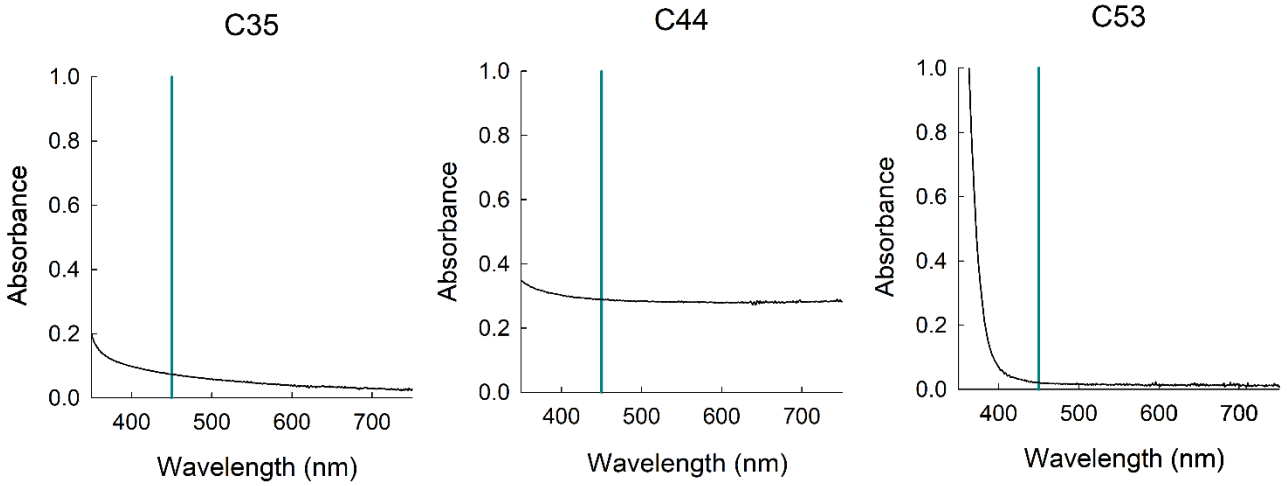

Figure 22: Visible spectra of the synthesized compounds at 1 mM concentration in binding buffer. The teal line is a reference at 450 nm, the wavelength of the immunoassay detection.

Moreover, the absorption spectra of Hb solutions were collected in the presence of each compound at 1 mM to evaluate the reactivity of the molecules towards Hb. Notably, absorption spectra of Hb in solution were acquired within the Q bands region (450-650 nm, Figure 23), that is sensitive to the redox state of Hb. Indeed, compounds that accelerate the conversion of oxyHb to metHb, which would then be susceptible to heme extraction by IsdB, could affect the assay results. None of the compounds significantly oxidized Hb within the 2-hour incubation.

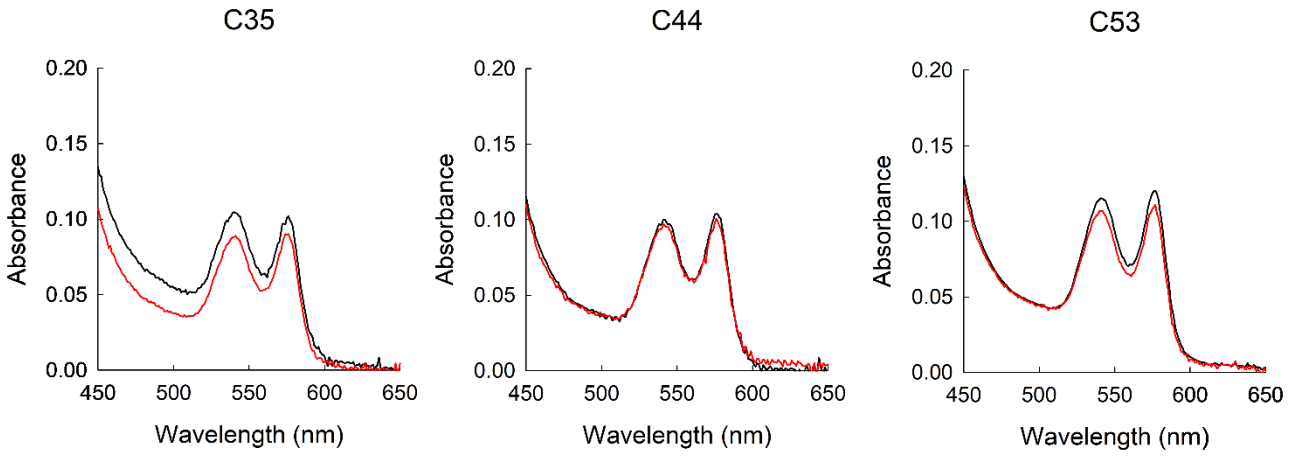

Figure 23: Comparison of Hb spectra in the Q bands region acquired before (black lines) and after (red lines) having incubated Hb with the compounds.

Before performing the actual assay, an immunoassay experiment without Hb was performed in order to exclude the potential interference of the tested compounds with the immunoassay (data not shown). The three hits were then analysed to confirm their ability to reduce the binding between IsdB and oxyHb. The results highlighted C35 as the best compound, since it presented a percentage of IsdB bound to Hb of ~ 40%, while compounds C44 and C53 produced a percentage above 60% (Figure 24).

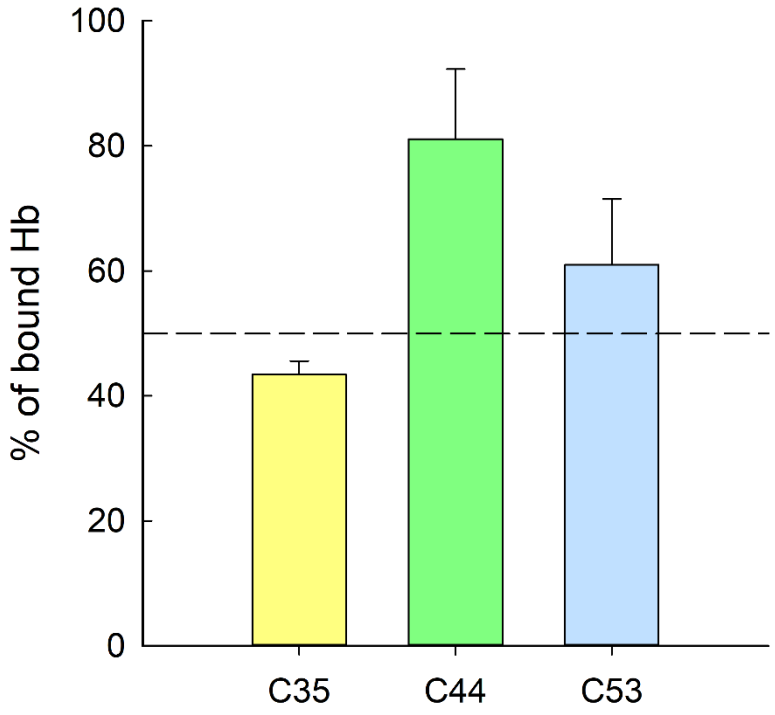

Figure 24: Results of the immunoassay conducted on the synthesized hits, reported as percentage of Hb bound to the IsdB Y165A variant in the presence of *in-house* synthesized hits at 1 mM concentration. The dotted line corresponds to 50% inhibition, which has been set as the threshold for the identification of promising molecules. Each analysis derives from the average of at least 2 replicates.

STD-NMR experiments were repeated by Prof. Faggiano (University of Parma) on the synthesized C35 and C53 compounds to confirm the data previously obtained for the commercial molecules.

Both molecules confirmed their binding to HbCO (which was used as an oxidation-resistant analogue of oxyHb). Furthermore, group epitope mapping (GEM) was conducted on C35 and C53 STD-NMR spectra, allowing to identify the binding epitopes that are more involved in the interaction with the HbCO surface.

After the promising results obtained by the immunoassay, the team of Prof. Lazzarato at the university of Turin synthesized different analogues for all three compounds designed to alleviate the solubility and/or stability issues that were previously encountered. Table 9 reports the list of the synthesized compounds and their derivatives (the serial number attributed to the synthesized derivatives continues the numeration used for the original commercial molecules).

Table 9: Summary of the synthesized hits and their derivatives. The chemical structures were drawn using ACD/ChemSketch (Advanced Chemistry Development Inc., Toronto, Canada).

ID	Parent compound	Purpose of synthesis	Structure	MW
C58	C53	Solubility improvement	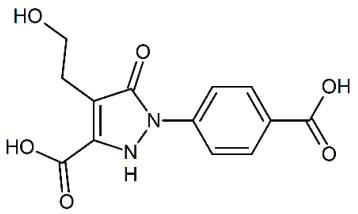	292.2
C59	C35	Stability improvement	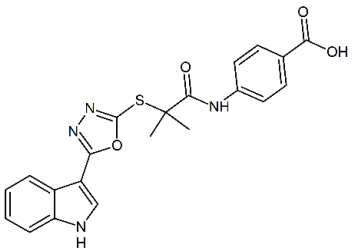	422.5
C60	C44	Solubility improvement	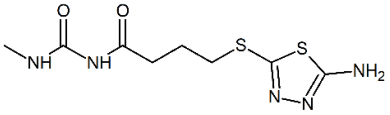	275.3
C61	C35	Stability improvement	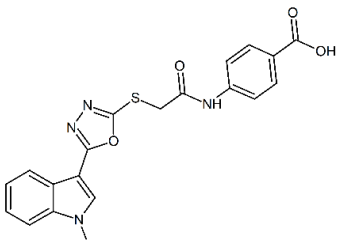	408.4

C63	C35	Solubility improvement	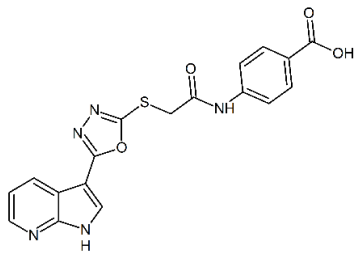	395.4
C65	C35	Solubility improvement	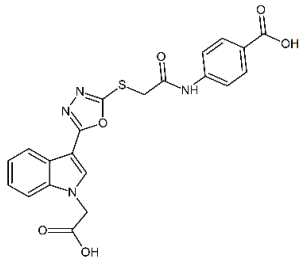	452.4

Indeed, commercial C35 was previously found to be poorly water soluble, and the alkaline treatment that was used to induce solubilization of the commercial stock was proved to lead to a compound rearrangement [429]. For this reason, two series of C35 analogues were synthesized in order to improve the compound stability and/or solubility. Notably, the first series of analogues (named C59 and C61) was synthesized to improve C35 stability, with C59 presenting two methyl groups that replace the two α-carbon's protons of the carbonyl group and C61 presenting a methyl group on the indole ring. The second series of analogues (named C63 and C65) was synthesized to improve C35 solubility, where C63 showed a replacement of the C35 indole ring with an azaindole ring and C65 presented the substituent -CH_2COOH on the indole ring. Both derivatives of C44 and C53 were synthesized to improve the compound solubility. The analogue of C44, i.e. C60, was synthesized with a methyl substituent on the urea moiety, while C58 is the acid analogue of the C53 methyl ester. Unfortunately, the solubility of the hit compounds was not improved by the modifications that were introduced. As a different strategy, TRIS salts were synthesized for the poorly soluble C35 derivates, which present a carboxylic moiety.

As for the parent compound, each derivative's stock solution was diluted in binding buffer to 1 mM and the maintenance of pH of the solution around 7.6 ± 0.5 was confirmed. Using the diluted solutions, also derivatives were characterized by the acquisition of absorbance spectra to rule out any interference at the absorbance wavelength of the immunoassay (450 nm) (Figure 25). C60 showed a similar signal offset than its parent compound C44, indicating the incomplete solubility of the molecule at 1 mM concentration.

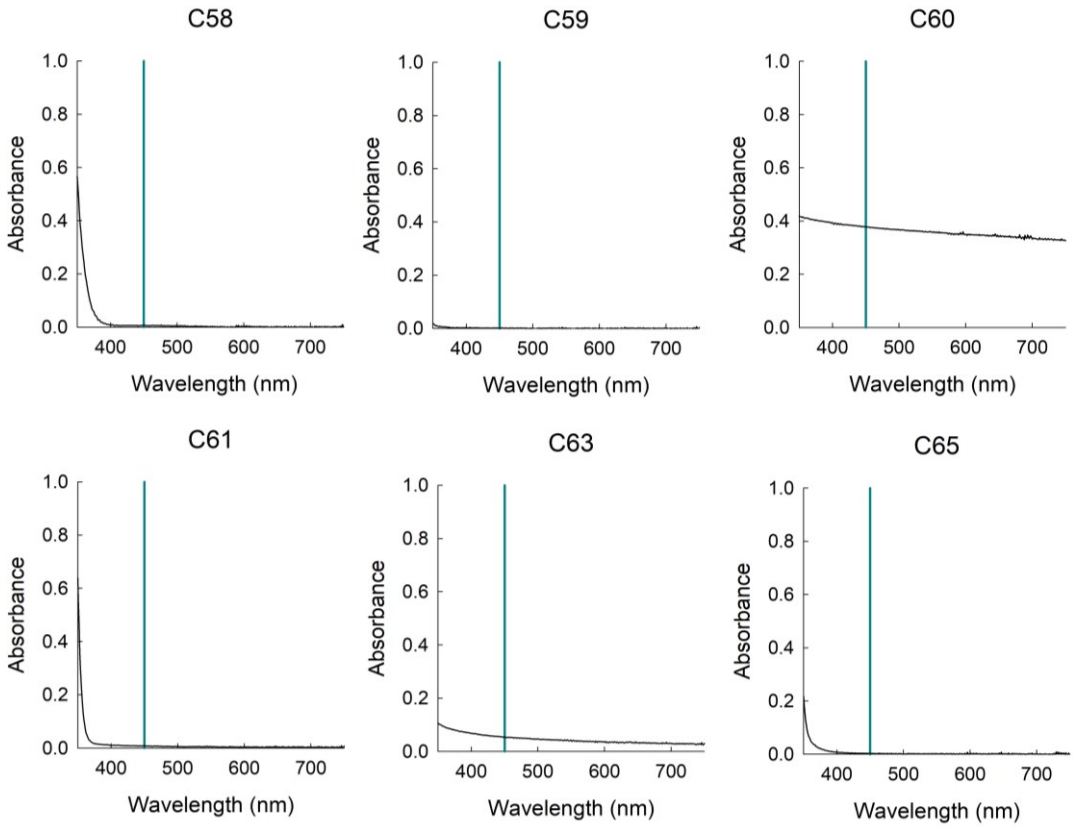

Figure 25: Visible absorbance spectra of the synthesized derivatives at 1 mM concentration in binding buffer. The teal line is a reference at 450 nm, the wavelength of the immunoassay detection.

The characterization was then ultimated by the acquisition of the absorption spectra of Hb solutions in the presence of each derivative to evaluate the potential reactivity of the molecules towards Hb (Figure 26). The analysis was conducted as above reported and the results revealed slightly scattered spectra, a symptom of the poor solubility of the derivatives. Nevertheless, no derivative significantly oxidized Hb within the 2-hour incubation.

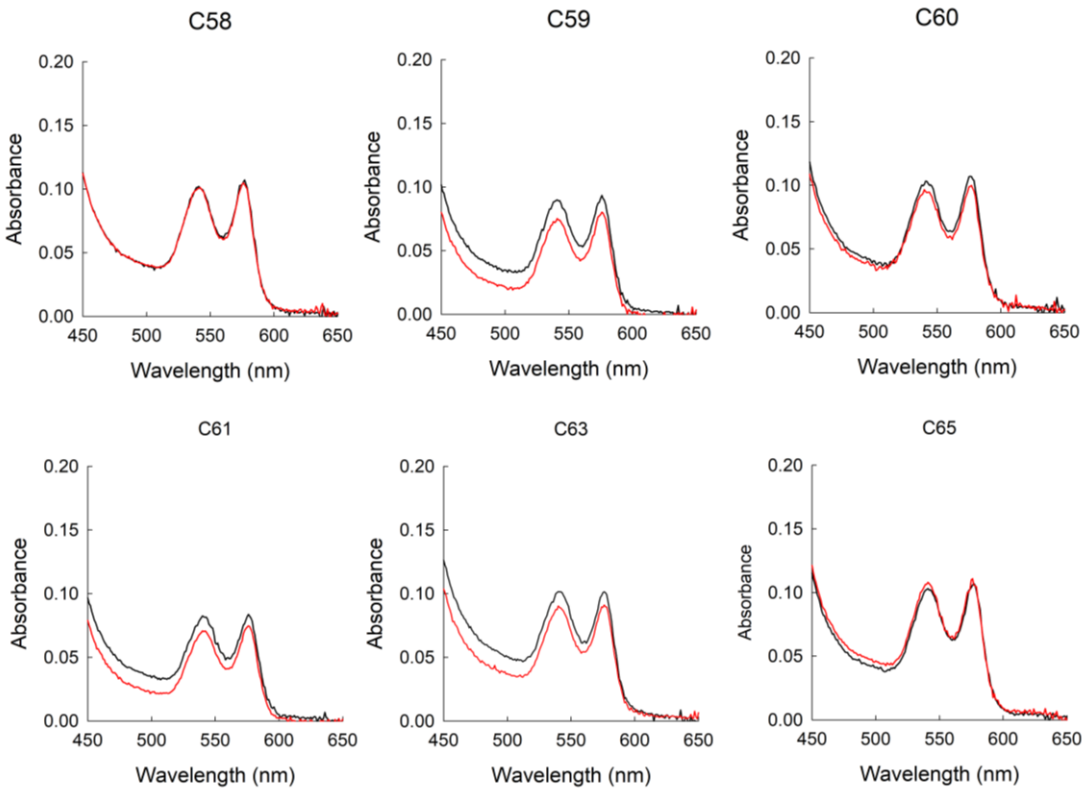

Figure 26: Comparison of Hb spectra in the Q bands region acquired before (black lines) and after (red lines) having incubated Hb with the compounds.

Ultimately, no significant improvement was highlighted by the immunoassay in terms of the ability of the derivatives to reduce IsdB binding to Hb, compared to their parent compounds (Figure 27). Consequently, further modifications will be required to provide improvements to the hit compounds. The identification of the most promising hits will continue with the evaluation of their affinity to Hb by techniques as Isothermal Titration Calorimetry, allowing an estimation of the thermodynamic parameters of the interaction.

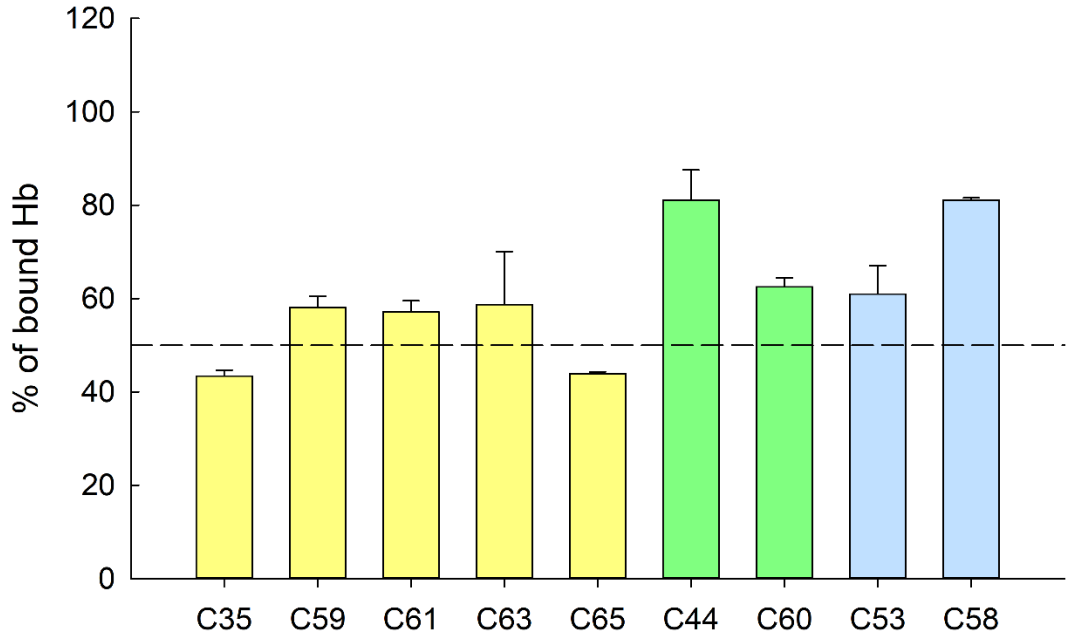

Figure 27: Results of the immunoassay conducted on the synthesized hits and their derivatives, reported as percentage of Hb bound to the IsdB Y165A variant in the presence of *in-house* synthesized molecules at 1 mM concentration. The dotted line corresponds to 50% inhibition, which has been set as the threshold for the identification of promising molecules. Each analysis derives from the average of at least 2 replicates.

Chapter II – Production and characterization of SbnA

1 Objectives

One of the project objectives concerned the characterization of the first step of SB biosynthesis in *S. aureus*, which is catalysed by the enzyme SbnA. The key role of this protein in SB synthesis has been already demonstrated in literature. Indeed, SbnA activity, together with SbnB-catalysed reaction, enables the production of two out of the three building blocks needed for SB synthesis, L-Dap and α-KG.

Despite previous investigations, a complete and detailed structural and functional characterization of SbnA is still missing.

For this reason, the main aim of work reported in this chapter was the full functional characterization of SbnA. To achieve the goal, recombinant *Sa*SbnA was produced at high yields and good homogeneity. The protein was then submitted to a detailed spectroscopic characterization to provide information about *Sa*SbnA exploitable spectroscopic properties. The characterization also involved the optimization of an assay for the evaluation of *Sa*SbnA activity, which could be exploited to validate the enzyme mechanism of action. All the information acquired within the enzyme characterization may potentially guide and provide tools for the evaluation of potential inhibitors of the *Sa*SbnA activity (discussed in the next chapter).

2 Material and methods

HEPES for buffer solutions and sodium chloride were acquired from PanReac Applichem ITW Reagents (Darmstadt, Germany). Tris base for buffer solutions was purchased from VWR International Srl (Milano, MI, Italy), 7-Methyl-6-thioguanosine (MESG) was purchased from Cayman (Ann Arbor, MI, USA) and Tris(2-carboxyethyl) phosphine hydrochloride (TCEP) from Apollo Scientific (Stockport, UK). Purine Nucleoside Phosphorylase (PNP) and all other chemicals were purchased from Merck (Darmstadt, Germany), unless otherwise specified.

2.1 Protein expression and purification

2.1.1 Growing media

Luria-Bertani (LB) agar plates were prepared as reported in Chapter I.

LB broth (for culture growth) contained:

- 5 g/L yeast extract
- 10 g/L tryptone
- 10 g/L NaCl

2.1.2 Expression systems for *Sa*SbnA

*Sa*SbnA expression system consisted of an *in-house* available pSH21p::TrxA-SbnA plasmid. The plasmid presented the synthetic gene of *sbnA* from *S. aureus* (UniProt entry A6QDA0) optimized for *E. coli* expression. The selected vector allowed to obtain the gene sequence *in-frame* to the sequence encoding for HisTag-Thioredoxin at the N-terminus separated by a sequence coding for the cleavage site of TEV protease.

2.1.3 *Sa*SbnA over-expression

For *Sa*SbnA over-expression, *E. coli* BL21 ArcticExpress (DE3) cells (Agilent Technologies, Santa Clara, CA, United States) were transformed with pSH21p::TrxA-SbnA plasmid. The transformed cells were plated on LB agar supplemented with 20 µg/mL gentamycin and 100 µg/mL ampicillin and grown at 37 °C overnight. A single colony was selected and inoculated in 10 mL of LB broth supplemented with 20 µg/mL gentamycin and 100 µg/mL ampicillin and grown at 37 °C overnight, under 250 RPM agitation. The overnight grown culture was diluted 1:100 in LB medium supplemented with 20 µg/mL gentamycin and 100 µg/mL ampicillin and grown at 30 °C for 3 hours in 0.5 L of LB medium. Afterward, the temperature was reduced to 4 °C and the culture was let equilibrate for about 20 minutes, after which the cells were induced with 1 mM isopropyl-β-D-1-thiogalactopyranoside (IPTG) at 4 °C for 24 hours. Cells were then collected by centrifugation (10,000 × g for 10 min at 4 °C), washed once with PBS solution and ultimately frozen at -20 °C in aliquots coming from 1 L of culture.

2.1.4 *Sa*SbnA purification

The thawed pellet was resuspended and incubated in lysis buffer (50 mM Tris, 100 mM NaCl, 1 mM TCEP, 0.2 mM PLP, 1 mg/mL lysozyme, 0.2 mM PMSF, 0.2 mM benzamidine and 1.5 µM pepstatin pH 8) for 1 hour at 4 °C. Subsequently, 5 cycles of sonication 20 seconds long (1s ON/1s OFF) were

performed to completely break down cells. Centrifugation was then performed at 18,000 × g for 1 hour at 4 °C to separate the soluble from the non-soluble components. Immobilized Metal Affinity Chromatography (IMAC) on a Talon Superflow™ resin (Cytiva, Marlborough, MA, USA) was performed to purify the N-terminal His6-tagged *Sa*SbnA. Indeed, the poly-histidine tag attached to the recombinant protein allowed the purification through the preferential interaction with the functionalized cobalt-based IMAC resin. Two wash steps were performed at 10 mM and 20 mM imidazole added to the Tris buffer (50 mM Tris, 100 mM NaCl, pH 8 at 4 °C) supplemented with 1 mM TCEP, in order to remove potential aspecific interactions with the cobalt resin of other histidine-rich proteins present in the crude extract. *Sa*SbnA was then eluted with the elution buffer (50 mM Tris pH 8, 100 mM NaCl, 250 mM imidazole, pH 8 at 4 °C) supplemented with 1 mM TCEP, which contained a higher imidazole concentration that allowed protein purification. The eluted fractions were pooled together for the removal of the histidine tag and thioredoxin portion of the construct by a TEV protease enzymatic cleavage. Together with 5-fold molar excess PLP, TEV protease was added to the protein solution in a $1_{\text{TEV protease}}$:$100_{Sa\text{SbnA}}$ weight ratio, and the overall solution was dialyzed overnight at 4 °C against Tris buffer (50 mM Tris, 100 mM NaCl, pH 8 at 4 °C) in order to remove imidazole. The following day, the solution was loaded again on a Talon Superflow™ resin to purify *Sa*SbnA, which was then concentrated up to 1.8 mg/mL, then aliquoted and finally stored at −80 °C.

2.2 UV-Visible spectroscopy

2.2.1 Absorption spectroscopy

Absorption spectra were acquired in the range 250-600 nm in a quartz microcuvette of 1 cm path length using a Cary4000 spectrophotometer (Agilent Technologies, Santa Clara, CA, USA). Measurements were carried out in 50 mM HEPES buffer, pH 7.8 at 25 °C. The concentration of *Sa*SbnA was estimated exploiting the extinction coefficients calculated by the ProtParam server, ε_{280} = 34,380 M^{-1} cm^{-1}. In the analysis involving *Sa*SbnA and its substrates, the enzyme was used at 14 µM, while L-OPS and L-Glu were added sequentially at 0.035 mM and 30 mM, respectively.

2.2.2 Fluorescence spectroscopy

Fluorescence spectra were collected in a quartz microcuvette of 3 mm pathlength on a Fluoromax-4 spectrofluorometer (Horiba Jobin Yvon, Kyoto, Japan) equipped with a thermostated water bath. Measurements were conducted in 50 mM HEPES buffer, pH 7.8 with the cuvette holder at 20 °C. Emission spectra were recorded in the wavelength range 315-580 nm by excitation at 298 nm, after the solution was pre-incubated for 2 minutes at 20 °C to reach the required temperature. *Sa*SbnA was analyzed at 5 µM, while L-OPS and L-Glu were added separately at 0.3 mM and 30 mM, respectively. Emission spectra of *Sa*SbnA alone or with either substrate were also collected by excitation at the absorbance maximum of the substrate in analysis, hence 467 nm for L-OPS and 412 nm for L-Glu.

2.3 Optimization of an assay to evaluate *Sa*SbnA activity

2.3.1 Optimized continuous coupled assay

The activity of *Sa*SbnA enzyme was evaluated by a continuous assay coupled with PNP. The coupled reaction exploits MESG and the phosphate produced in the *Sa*SbnA-catalyzed reaction as substrates

to produce ribose 1-phosphate and 2-amino-6-mercapto-7-methylpurine (AMMP) (Figure 28). This latter product provides an absorbance signal that can be monitored at 360 nm.

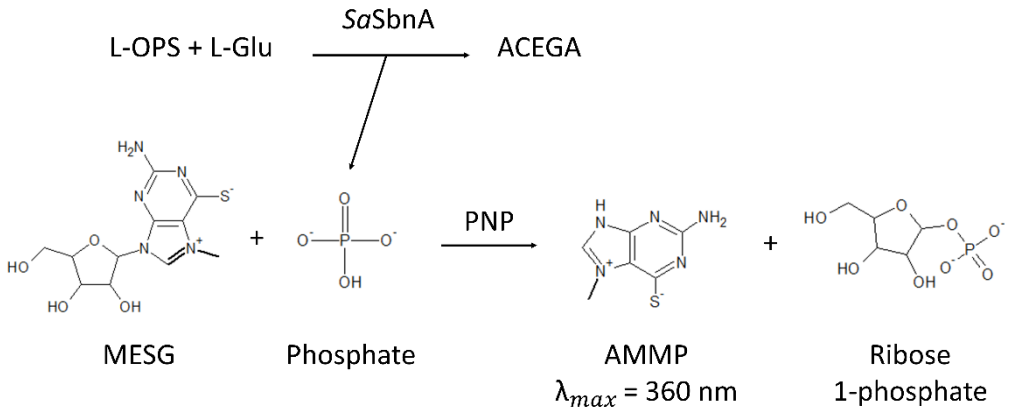

Figure 28: Scheme of the mechanism of the continuous enzymatic assay coupled with PNP, optimized to evaluate *Sa*SbnA activity.

The bacterial PNP was purchased from Merck. The PNP protein cake was dissolved in PNP storage buffer (20 mM Tris pH 8, 100 mM NaCl, 10% glycerol, 1 mM TCEP). The mixture was centrifuged to recollect the supernatant, which was then dialyzed against the storage buffer in order to remove traces of inorganic phosphate that would interfere with the assay. PNP concentration was calculated exploiting the protein's absorbance peak at 278 nm and its extinction coefficient of 8,940 M^{-1} cm^{-1} obtained from ProtParam online tool (https://web.expasy.org/protparam/). As suggested by the manufacturer, all MESG solutions were prepared in 100% DMSO flowed under nitrogen atmosphere. MESG concentration was calculated exploiting its absorbance peak at 331 nm and its extinction coefficient of 32,000 M^{-1} cm^{-1}. PNP specific activity was evaluated for the stock solution in the presence of 0.7 mM potassium phosphate. A unit of PNP was defined as the enzyme amount that converts 1 µmole of MESG in AMMP in 1 minute when 0.7 mM potassium phosphate is present in the reaction. The continuous assays were performed in HEPES buffer 50 mM pH 7.8 (25 °C) as above specified and the mixtures were supplemented with TCEP 1 mM, 100 µM MESG and 216 mU PNP. For *Sa*SbnA functional characterization, different concentrations of *Sa*SbnA substrates were used ranging from 0.035 to 0.72 mM for L-OPS and 0.1 to 150 mM for L-Glu, depending on the experiment. Each reaction was performed in a shielded quartz microcuvette of 1 cm path length and pre-incubated for 2 minutes at 25 °C in the cuvette holder of a Cary4000 spectrophotometer (Agilent, Santa Clara, CA, USA). After the solution had been thermostated, the absorbance signal without the enzyme was recorded at 360 nm for 1-2 min. The reactions were then triggered by the addition and careful mixing of *Sa*SbnA and the initial reaction velocity was evaluated within the stationary phase. At last, the velocity was converted to the rate of AMMP production by exploiting a Δε at 360 nm of 15,675 M^{-1} cm^{-1} (calculated from the difference of MESG and AMMP spectra). The assay was found linear up to 100 µM of phosphate within the assay mixture.

Within the assay optimization, different conditions were tested which are reported below and within the Results and Discussion corresponding sections. Nevertheless, all the reactions were performed in a shielded quartz microcuvette of 1 cm path length using a Cary4000 spectrophotometer (Agilent, Santa Clara, CA, USA).

Effects on *Sa*SbnA activity of different buffers and pH

The effect of different buffers (Tris, BTP, TEA and HEPES at 50 mM) on *Sa*SbnA activity was monitored at pH 8 (25 °C). The effect of pH on *Sa*SbnA activity was monitored in HEPES 50 mM. The pH of HEPES solutions was adjusted with 5 M NaOH to reach pH 7, 7.5, 7.8 and 8 at 25 °C. In both analyses, the mixtures were supplemented with TCEP 1 mM, 100 µM MESG and 216 mU PNP. *Sa*SbnA was used at 50 nM and L-OPS and L-Glu at saturating concentrations (based on the K_M reported in Kobylarz et al, 2016 [356]).

Effect of monovalent and bivalent ions on *Sa*SbnA activity

The effect of pH on *Sa*SbnA activity was monitored in 50 mM HEPES pH 7.8 (25 °C). The reaction mixtures were supplemented with TCEP 1 mM, 100 µM MESG and 216 mU PNP. *Sa*SbnA was used at 50 nM and L-OPS and L-Glu at saturating concentrations (based on data reported in Kobylarz et al, 2016 [356]).

Determination of the extinction coefficient for the MESG-AMMP conversion

MESG conversion to AMMP was monitored through the acquisition of absorption spectra at 50 µM MESG in the wavelength range 250-400 nm in a quartz microcuvette of 1 cm path length using a Cary4000 spectrophotometer (Agilent Technologies, Santa Clara, CA, USA). The absorbance difference at 360 nm between MESG and AMMP limit spectra was exploited to calculate the correct molar extinction coefficient through the Lambert-Beer equation:

$$\textbf{Eq. 2}: A = \varepsilon \times C \times l$$

where A is the absorbance at a specific wavelength, ε is the molar coefficient, C is the concentration of the analyzed solution (in molarity) and l is the path length (in cm). All measurements were collected in 50 mM HEPES buffer, pH 7.8 at 25 °C.

Dependence of *Sa*SbnA activity on PNP, MESG and *Sa*SbnA concentration

The dependence of the reaction rate on the coupled enzyme concentration was evaluated in the range between 216 and 1080 mU PNP at 50 nM *Sa*SbnA and L-OPS and L-Glu at saturation.
The dependence of the reaction rate on the MESG concentration was evaluated at 50 nM of *Sa*SbnA, L-OPS and L-Glu at saturation and 216 mU PNP.
The linear dependence of the reaction rate on the enzyme concentration was evaluated at saturation of both substrates and in the 25-100 nM range of *Sa*SbnA concentration, which approximately corresponds to an initial velocity of 5.7-17.3 µM/min.
All measurements were collected in 50 mM HEPES buffer, pH 7.8 at 25 °C.

2.4 *Sa*SbnA kinetic characterization

To evaluate *Sa*SbnA mechanism of action, *Sa*SbnA enzymatic activity was measured at concentrations of L-Glu (substrate B) ranging from 0.1 to 150 mM, while L-OPS (substrate A) was tested at three fixed concentrations, 0.72 mM, 0.08 mM and 0.035 mM. Michaelis Menten plots were then globally fitted using a double displacement equation with inhibition by one substrate reported by Segel [430].

Eq. 3: $$v = \frac{V_{max} \cdot [L-OPS] \cdot [L-Glu]}{\left((K_{M\,L-Glu} \cdot [L-OPS]) + \left(K_{M\,L-OPS} \cdot [L-Glu] \cdot \left(1 + \frac{[L-Glu]}{K_{i\,L-Glu}}\right)\right) + \cdot ([L-Glu] \cdot [L-OPS])\right)}$$

2.4.1 Evaluation of α-aminoacrylate stability

The continuous assay was exploited to evaluate the stability of the α-aminoacrylate intermediate. The 7 µM *Sa*SbnA added to the reaction mixture, while 0.035 mM L-OPS was used to trigger the reaction, after about 2 minutes of baseline signal recording. After the kinetic reached a plateau, 30 mM L-Glu was added to the solution and the signal at 360 nm was followed for another 3 minutes.

The deamination assay is a continuous activity assay coupled with the enzyme lactate dehydrogenase (LDH). The assay was performed in HEPES buffer 50 mM, pH 7.8 (25 °C) and the mixtures were supplemented with 1 mM TCEP. The reaction mix was prepared with 11 U LDH in the presence of 0.035 mM L-OPS and 0.1 mM NADH and the assay was performed in a shielded quartz microcuvette of 1 cm path length after pre-incubation for 2 minutes at 25 °C in the cuvette holder of a Cary4000 spectrophotometer (Agilent, Santa Clara, CA, USA). After the solution had been thermostated, the absorbance signal without the enzyme was recorded at 340 nm for 1-2 min and then the reaction was triggered by the addition and careful mixing of 1.3 µM *Sa*SbnA. The signal was recorded for 30 minutes to reach the completion of the reaction. The speed of the reaction was calculated by dividing the initial velocity by the molar coefficient of NADH (ε = 6,220 M^{-1} cm^{-1}).

3 Results and discussion

3.1 *Sa*SbnA protein expression and purification

Recombinant *Sa*SbnA was expressed using the *in-house* available pSH21p::TrxA-SbnA plasmid. Thioredoxin was added to the construct to improve the protein solubility in the initial steps of *Sa*SbnA purification. *E. coli* BL21 ArcticExpress (DE3) cells transformed with pSH21p::TrxA-SbnA plasmid were exploited for protein expression in LB medium, followed by two IMAC purification steps interspersed with the removal of the thioredoxin portion. The final yield of purification was about 2.8 mg per liter of bacterial culture, with a purity of more than 90% (Figure 29).

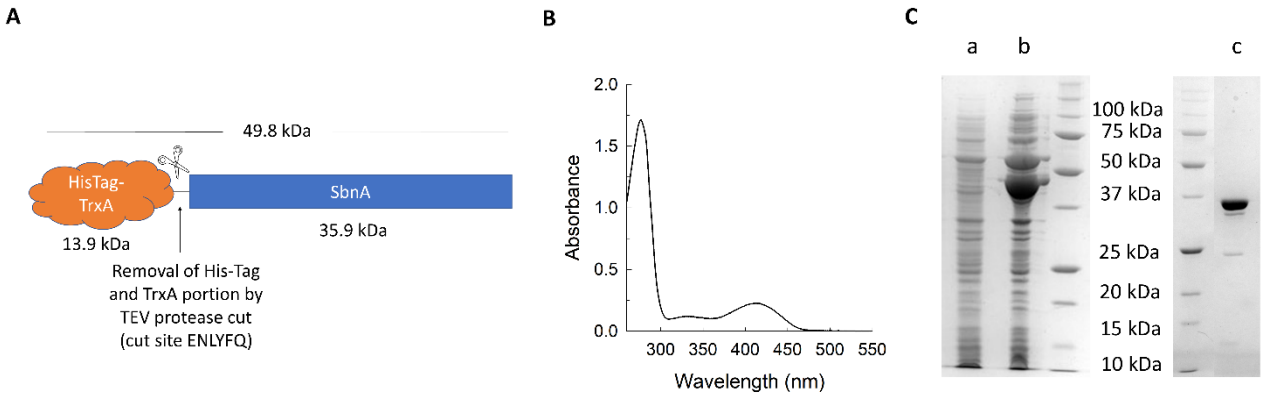

Figure 29: Recombinant production of *Sa*SbnA. (A) Schematic representation of the SbnA construct pSH21p::TrxA. The HisTag-TrxA portion at the N-terminus can be removed by TEV protease cleavage and a second IMAC step. (B) UV-Vis absorption spectrum of the purified *Sa*SbnA stock solution. (C) SDS-PAGE analysis of *Sa*SbnA over-expression and purification, with (a) uninduced sample, (b) induced sample, (c) purified *Sa*SbnA.

The UV-visible spectrum of purified *Sa*SbnA (Figure 29B) showed three peaks, the peak at 278 nm characteristic of aromatic amino acids, and two bands at 330 and 412 nm that are characteristic features of PLP-dependent proteins. Indeed, the PLP cofactor bound to *Sa*SbnA forms a Schiff base, called internal aldimine, which presents tautomerism between the enolimine and ketoenamine forms (Figure 30), that in turn are responsible for the peak at 330 and 412 nm, respectively.

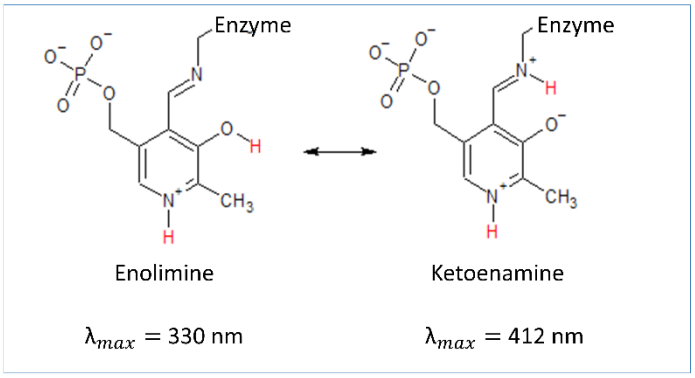

Figure 30: The two tautomeric forms of PLP bound as internal aldimine to *Sa*SbnA.

The ratio between the absorbance of aromatic residues at 278 nm and of PLP cofactor at 412 nm was calculated to be 7.3. Once the SDS-PAGE analysis confirmed that this preparation was sufficiently

homogeneous, the value of the ratio between the absorbance at 278 and 412 could be exploited as a homogeneity index for all protein preparations. The analysis thus confirmed that the purification protocol enabled to obtain a homogeneous preparation with the purified protein correctly interacting with the PLP cofactor.

3.2 *Sa*SbnA spectroscopic characterization

*Sa*SbnA was characterized by spectroscopic techniques as UV-Vis spectroscopy and fluorescence spectrophotometry.

3.2.1 UV-visible absorbance spectroscopy

As just described, the *Sa*SbnA absorption spectrum showed the characteristic features of PLP-dependent proteins, hence the three peaks representing aromatic residues and the two tautomeric forms of the *Sa*SbnA-bound PLP cofactor as internal aldimine. To further characterize the enzyme, absorption spectra were collected after the subsequential addition of its two substrates. In agreement with Kobylarz and colleagues' proposal for SbnA mechanism of action [356], the addition of the enzyme first substrate L-OPS induced the appearance of peaks at 324 and 467 nm, that are characteristic of the formation of the α-aminoacrylate intermediate. Subsequently, by adding the second substrate of the reaction, L-glutamate, the spectral change highlighted the reformation of the internal aldimine after the release of the reaction product ACEGA (Figure 31).

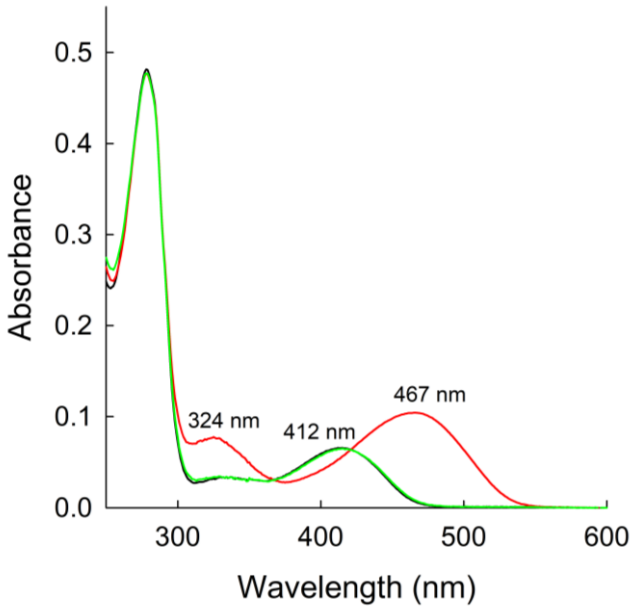

Figure 31: UV-Vis absorption spectra of 14 µM SbnA in the absence of substrates (black line) and after the subsequential addition of 0.035 mM L-OPS (red line) and 30 mM L-Glu (green line).

3.2.2 Fluorescence spectroscopy

Fluorescence spectroscopy was exploited to evaluate and characterize *Sa*SbnA fluorescence properties as a technique sensitive to chemical modifications of the fluorophore, but also to changes in the polarity of the environment around the fluorophore itself. Emission spectra were thus collected by excitation at 298 nm to selectively excite *Sa*SbnA six tryptophans (three for each monomer). The spectra were recorded both in the absence and in the presence of each substrate

(Figure 32). *Sa*SbnA spectrum revealed a tryptophan emission peak centered at 343 nm, suggesting that the residues are exposed to a partially polar environment, and a second peak, much weaker, centered at 500 nm and representative of the internal aldimine emission. This latter can be attributed to a phenomenon of Fluorescence Resonance Energy Transfer (FRET) between one or more of the protein's tryptophans and the PLP cofactor, which emits at 500 nm when excited. The addition of the first substrate in the catalysis, L-OPS, induced the disappearance of the peak at 500 nm and the appearance of a more intense peak at 550 nm. Moreover, the peak at 343 nm decreased its intensity after L-OPS addition (Figure 32A). The addition of the second substrate, L-Glu, induced the appearance of a peak at 500 nm, while the peak at 343 nm remained unchanged (Figure 32B).

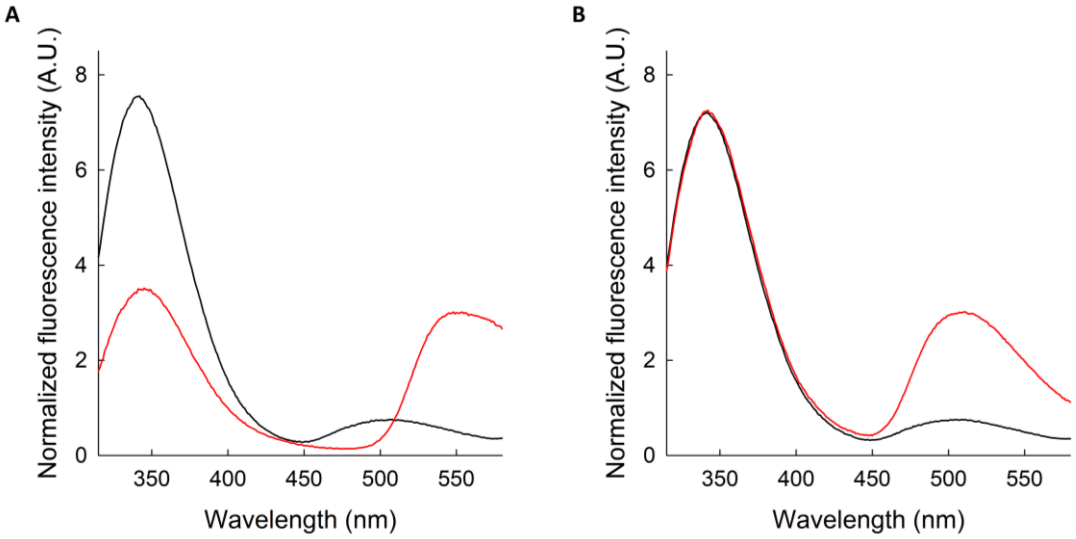

Figure 32: Fluorescence emission spectra of *Sa*SbnA by excitation at 298 nm in the absence and presence of substrates. (A) Emission spectra of *Sa*SbnA in the absence (black line) and in the presence of 0.3 mM L-OPS (red line). (B) Emission spectra of *Sa*SbnA in the absence (black line) and in the presence of 30 mM L-Glu (red line). All measurements were carried out in HEPES buffer 50 mM, pH 7.8.

For a deeper characterization, the two *Sa*SbnA substrates were separately evaluated since the UV-Vis spectra highlighted that their absorbance maximum was centered at different wavelengths. In the case of L-OPS addition, *Sa*SbnA was excited at 467 nm before and after substrate addition and as expected the analysis showed a significant spectral change attributed to the formation of the aminoacrylate intermediate. In this case, the emission signal of the enzyme alone (as reference) was basically absent, which could be traced back to the absence of *Sa*SbnA absorbance at that wavelength. In the case of L-Glu, *Sa*SbnA was excited at 412 nm before and after substrate addition and the spectral change observed was attributed to a change in the polarity of the environment around the PLP cofactor. Other than an increase in intensity after L-Glu addition, the emission peak showed also a red shift (highlighted by the arrow in Figure 33) that can be reconducted to an increased exposition to the solvent.

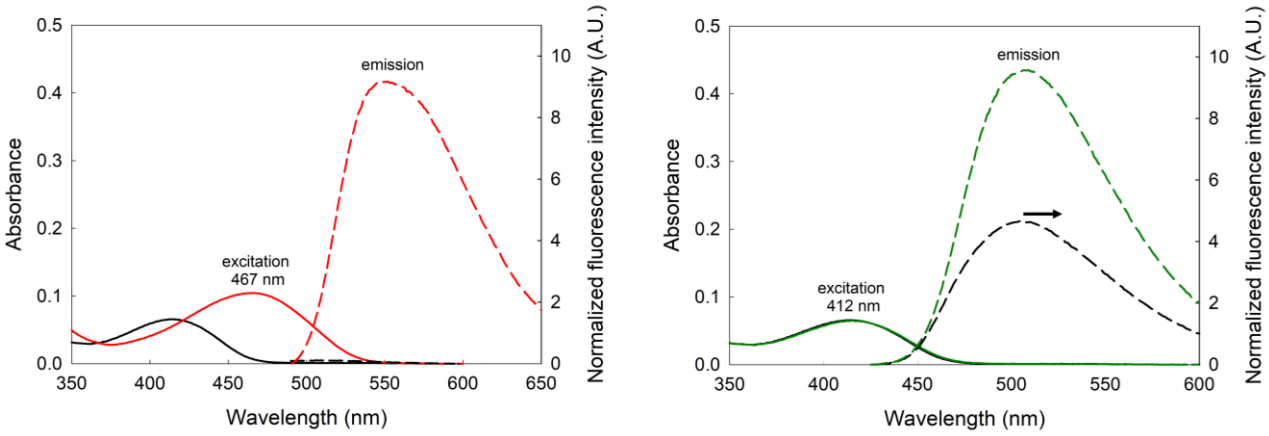

Figure 33: Fluorescence emission spectra of *Sa*SbnA in the absence and presence of either substrate, and comparison with UV-Vis absorbance spectra. (A) Absorbance and fluorescence emission spectra of *Sa*SbnA in the absence (black solid and dotted line, respectively) and in the presence of 0.3 mM L-OPS (red solid and dotted line, respectively). (B) Absorbance and fluorescence emission spectra of *Sa*SbnA in the absence (black solid and dotted line, respectively) and in the presence of 30 mM L-Glu (green solid and dotted line, respectively). All measurements were carried out in HEPES buffer 50 mM, pH 7.8.

The overall fluorescence characterization of *Sa*SbnA confirmed the potential exploitation of this technique to evaluate both chemical modifications of the fluorophore (i.e. formation and degradation of reaction intermediates), and changes in the polarity of the environment around the fluorophore. This feature can be very helpful in the evaluation of the affinity and mechanism of binding of interactors and compounds with potential inhibitory effect.

3.3 Optimization of *Sa*SbnA activity assay

As reported in Material and Methods, the activity of *Sa*SbnA enzyme was evaluated by a continuous assay coupled with the PNP enzyme. The coupled reaction exploits MESG and the phosphate produced in the *Sa*SbnA-catalyzed reaction as substrates to produce a ribose 1-phosphate and AMMP (Figure 28). This latter product provides the absorbance signal that can be monitored at 360 nm, allowing to measure phosphate production and in turn the velocity of *Sa*SbnA-catalyzed reaction. The PNP-coupled continuous assay was already exploited to evaluate phosphate-producing enzymatic activity [431], but also it was used by Kobylarz and colleagues for the evaluation of *Sa*SbnA activity [356]. Despite having been widely reported in literature, no actual complete optimization of the assay was performed to study specifically *Sa*SbnA activity. The assay's conditions were therefore optimized before reaching the final set up reported in Material and Methods, which was then subsequently exploited for the characterization of the enzyme mechanism of action.

Effects on *Sa*SbnA activity of different buffers and pH

The first aspect of the assay to be considered was the type of buffer and salts to be used, even because Kobylarz and colleagues highlighted inhibition of *Sa*SbnA activity in dependence of increasing KCl concentration [356]. Four types of buffer solutions were tested presenting different features: Tris/HCl and BTP (belonging to the Tris family), as well as TEA buffer, were known to form complexes with different metals, while HEPES buffer of the piperazinic family lacked the ability to form complexes with metal ions [432]. The different buffers were tested in the same assay conditions (50 mM of each buffer, at pH 8 and at 25 °C) to evaluate only the effect of the buffer itself. Even if

Tris/HCl was used by Kobylarz and colleagues in the characterization of *Sa*SbnA, the results clearly showed that the enzyme activity was reduced in comparison with TEA and HEPES buffers (Figure 34A). Ultimately, HEPES gave the best result therefore it was selected as the buffer of choice for all the following experiments.

The pH of HEPES buffer solutions can be adjusted in a range between 6.8 and 8.2, even if it is preferable to avoid extremes. For this reason, HEPES buffer solutions at different pH were tested in the range between 7 and 8 (pH 8 used as reference) (Figure 34B). Unlike lower pH, results showed comparable activity at pH 7.8 compared to the reference, which led the choice towards 7.8 to stay more in between the pH range of the HEPES buffer.

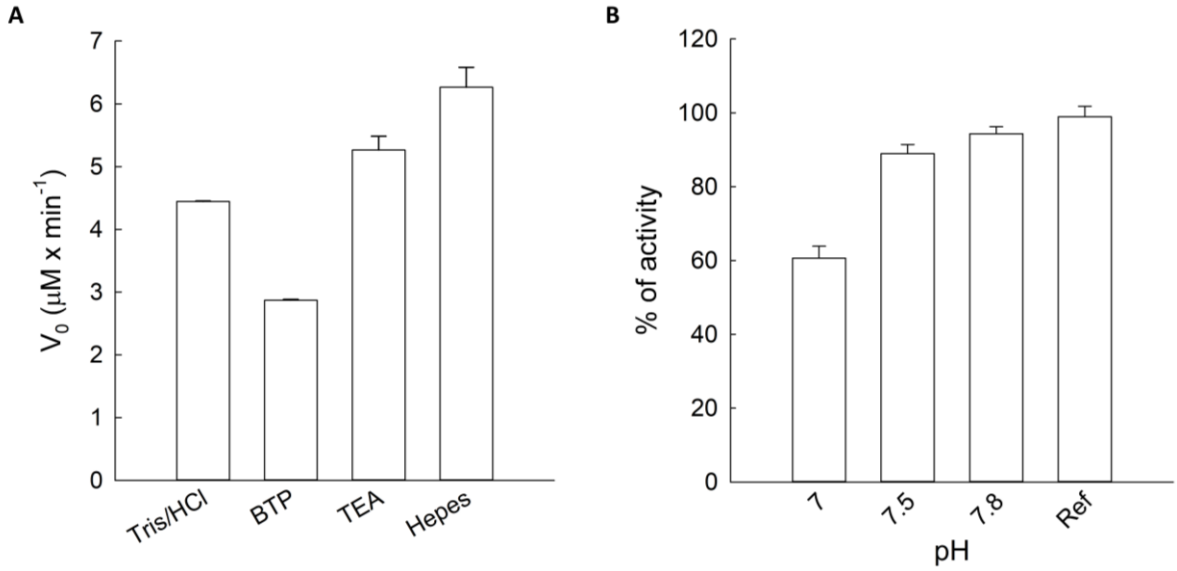

Figure 34: Effects on *Sa*SbnA activity of different buffer solutions and pH. (A) Effect of different types of buffers on *Sa*SbnA activity measured at 50 nM *Sa*SbnA, 0.3 mM L-OPS and 30 mM L-Glu. All measurements were performed at pH 8. (B) Effect of pH on *Sa*SbnA activity measured at 50 nM *Sa*SbnA, 0.3 mM L-OPS and 30 mM L-Glu. The reference is Hepes pH 8 selected from the buffer analysis. Error bars represent the standard error of the mean (s.e.m.) of two replicates.

Effect of monovalent and bivalent ions on *Sa*SbnA activity

Once the buffer was selected, monovalent and bivalent ions were tested to evaluate their effect on *Sa*SbnA activity. Three anionic and three cationic ions were evaluated (Figure 35). Among the three anions tested, Cl^- and Br^- at 200 mM induced a significantly decreased activity, highlighting a potential inhibitory effect by halide anions. Among the cations tested (Figure 35B), Na^+ and K^+ showed a comparable inhibitory effect with a 50% decrease in *Sa*SbnA activity in the presence of 50 mM chloride ions. A higher inhibitory effect was caused by the presence of $MgCl_2$ in solution, which could derive also by the double contribution of chloride relative to NaCl and KCl. As a result of these observations, chlorides and other salts were eliminated from the reaction mixture during the activity assays.

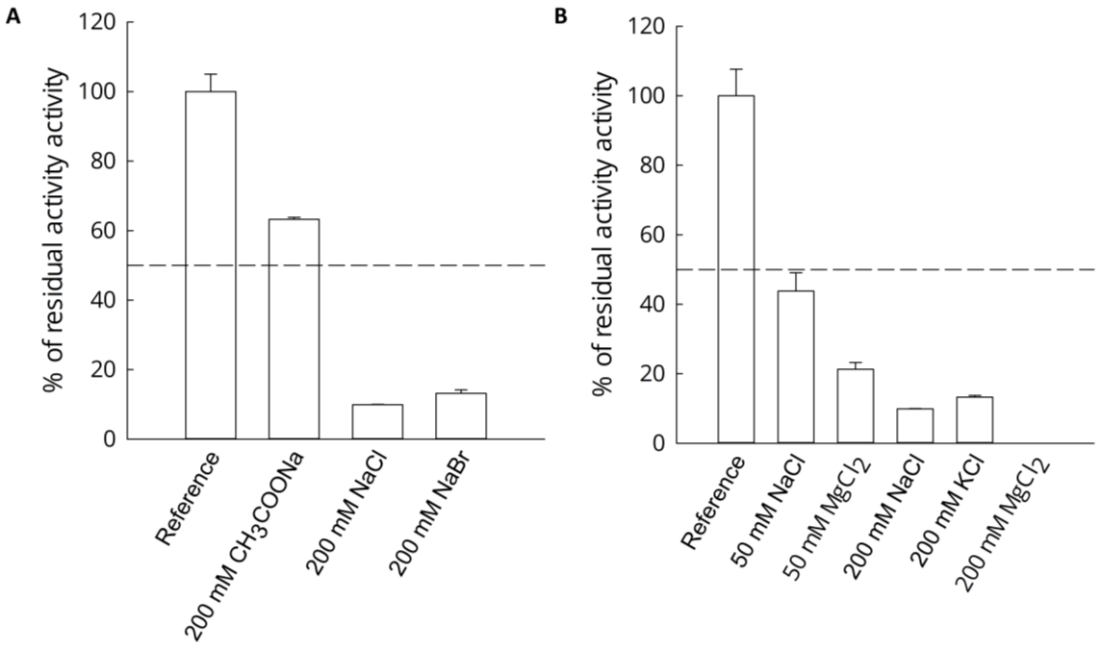

Figure 35: Effects of monovalent and divalent ions on *Sa*SbnA activity. (A) Effect derived from different anions at 200 mM. The reference is HEPES buffer at pH 7.8. (B) Effect derived from different cations at 200 and 50 mM. The reference is HEPES buffer at pH 7.8. Error bars represent the s.e.m. of two replicates.

Determination of the extinction coefficient for the MESG-AMMP conversion

The exploitation of the PNP-coupled continuous assay to evaluate *Sa*SbnA activity required the use of an extinction coefficient for the calculation of the rate of AMMP production. Since the substrate and product of the PNP-coupled reaction (MESG and AMMP, respectively) present absorbance spectra that partially overlap, the final extinction coefficient would have to be extrapolated from the difference between the two limit absorbance spectra at 360 nm. Therefore, the exact Δε of 15,675 M^{-1} cm^{-1} for the final assay conditions was calculated at 360 nm in HEPES buffer pH 7.8 by exploiting the differential absorbance signal and concentration between MESG and AMMP (Figure 36). The extinction coefficient was then utilized in all the following experiments.

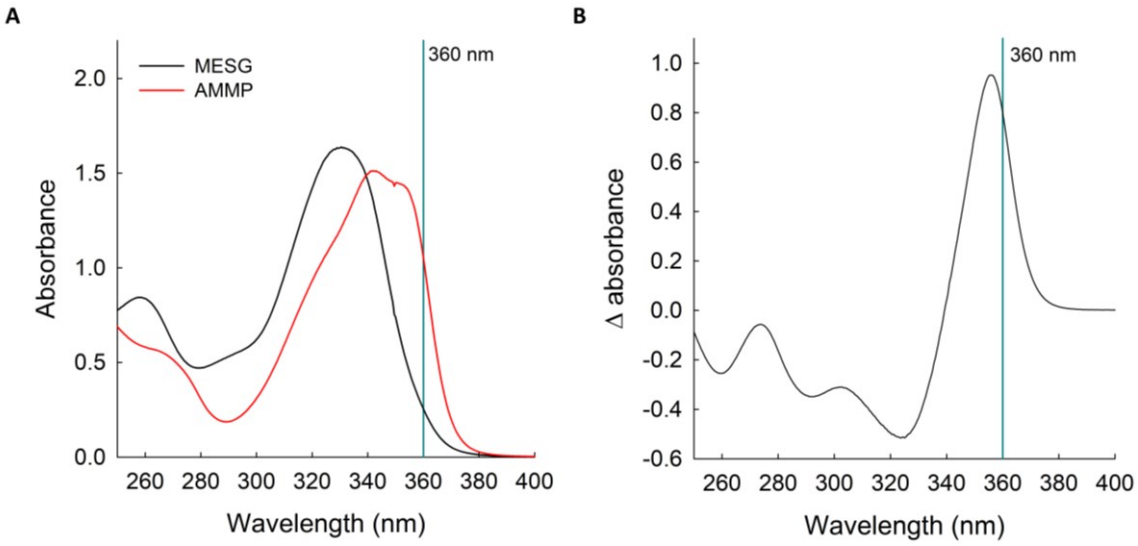

Figure 36: Determination of the extinction coefficient for MESG to AMMP conversion. (A) The limit UV-Vis spectra of MESG at 50 µM and the AMMP final product. (B) The differential spectrum between AMMP and MESG. All spectra were collected in 50 mM HEPES pH 7.8.

Dependence of *Sa*SbnA activity on PNP, MESG and *Sa*SbnA concentration

The exploitation of a continuous coupled assay required the determination of the optimal conditions to evaluate the specific activity of *Sa*SbnA, without the interference of the coupled reaction. For this purpose, the effect of the concentration of the coupled enzyme and its substrate MESG on *Sa*SbnA activity was tested to identify the sufficient amount to avoid limitations from the coupled reaction. Three PNP concentrations were analyzed at fixed concentrations of the other reactants, hence 100 µM MESG, 50 nM *Sa*SbnA and L-OPS and L-Glu at saturating concentrations (based on Kobylarz et al, 2016 [356]). Based on the results, 216 mU PNP was chosen as optimal amount for the following experiments since it did not limit the rate of the primary reaction (Figure 37A).

To identify the optimal concentration of MESG, two concentrations were analyzed using 216 mU PNP and at fixed concentrations of the other reactants, hence 50 nM *Sa*SbnA and L-OPS and L-Glu at saturating concentrations (based on Kobylarz et al, 2016 [356]) (Figure 37B). Since the experiments showed similar kinetics, 100 µM MESG was selected for all the following experiments.

At last, different *Sa*SbnA concentrations were used to determine the dependence of the reaction velocity on the enzyme concentration used in the assay. Five *Sa*SbnA concentrations were analyzed maintaining fixed the other reactants, hence 100 µM MESG, 216 mU PNP and L-OPS and L-Glu at saturating concentrations. This analysis allowed to identify the linearity interval for the continuous assay, that could then be exploited to choose the correct enzyme concentration during the kinetic characterization. The assay resulted linear between 25 and 70 nM *Sa*SbnA, thus a concentration of 50 nM was chosen for the following experiments, if not otherwise specified (Figure 37C).

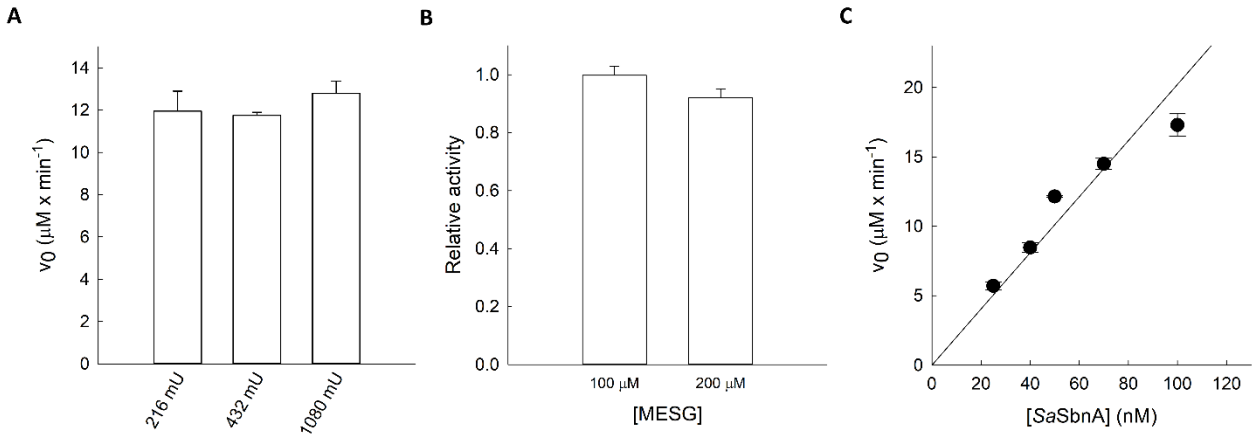

Figure 37: Dependence of *Sa*SbnA activity on the concentration of PNP, MESG and *Sa*SbnA. (A) Dependence of the initial velocity of *Sa*SbnA-catalyzed reaction on the concentration of the PNP coupled enzyme at saturating concentration of L-OPS and L-Glu. (B) Dependence of *Sa*SbnA activity on two different MESG concentrations (100 and 200 µM MESG) performed at non-saturating concentrations of L-OPS and L-Glu. The results are reported as relative activity to the reaction at 100 µM MESG. (C) Dependence of the initial velocity of *Sa*SbnA-catalyzed reaction on *Sa*SbnA concentration at saturating concentration of L-OPS and L-Glu. Error bars represent the s.e.m. of two replicates.

3.4 *Sa*SbnA mechanism of action

In 2016, Kobylarz and colleagues evaluated SbnA reaction mechanism on the basis of crystallographic structures, in particular they resolved the structure of SbnA in complex with its cofactor PLP and the structure of the AA intermediate. Based on their observation, the kinetic mechanism they proposed was a double displacement mechanism, also called ping-pong mechanism, which is characterized by the presence of two substrates (A and B) and the formation of an intermediate during the reaction (E') (Figure 38). Since Kobylarz and co-workers didn't actually validate SbnA mechanism of action, this thesis set as a goal to provide a complete characterization of *Sa*SbnA activity.

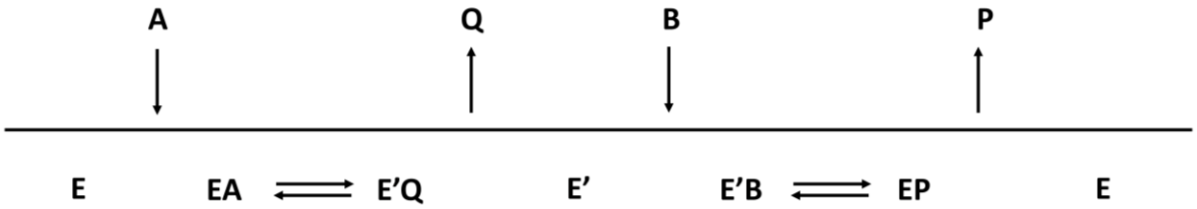

Figure 38: Schematic representation of a double displacement mechanism. In this system, the first substrate (A) binds to the enzyme E, followed by the release of product Q (typically a fragment of A) and the formation of E'. The second substrate (B) then binds and reacts with E' and forms the product P, which is released. Ultimately, the enzyme is restored to its form E.

Exploiting the continuous assay, *Sa*SbnA enzymatic activity was thus evaluated at concentrations of L-Glu (substrate B) ranging from 0.1 to 150 mM, while L-OPS (substrate A) was tested at three fixed concentrations, 0.72 mM, 0.08 mM and 0.035 mM. By plotting each reaction's initial velocity as a function of L-Glu concentrations, substrate inhibition could be observed at high concentrations of L-Glu. Data were thus globally fitted by a double displacement equation with inhibition by one substrate (Eq. 3), in this case L-Glu (Figure 39).

The global fitting allowed to extrapolate kinetic parameters that were comparable to the ones reported in literature for L-Glu, while a value about half of that reported in literature for L-OPS (Table 10).

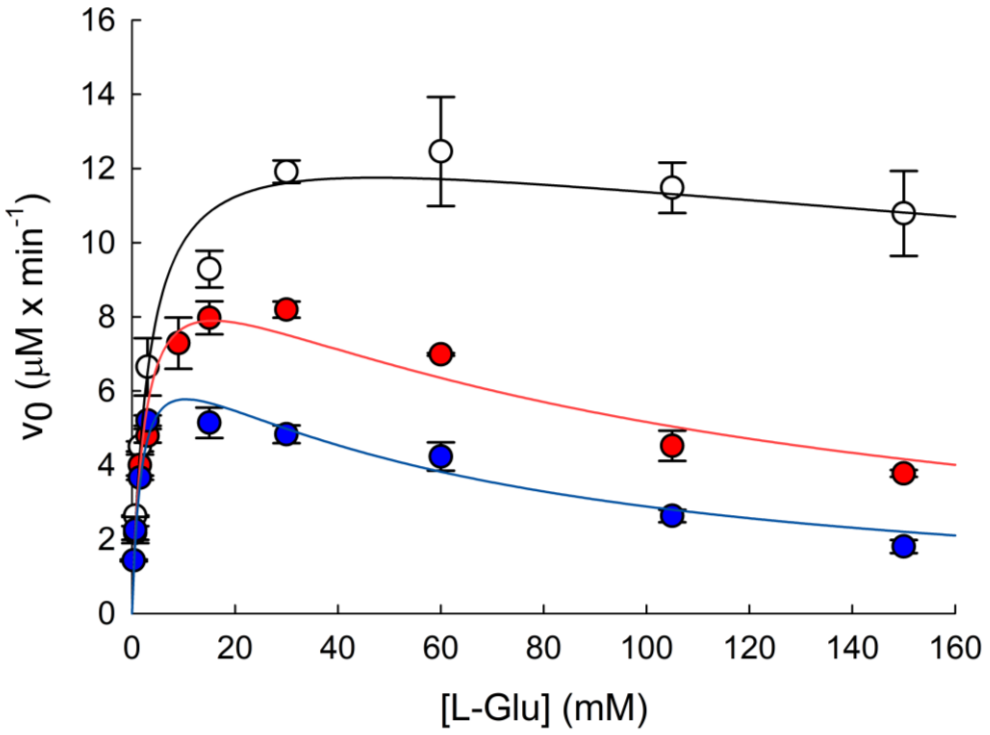

Figure 39: Dependence of *Sa*SbnA initial velocity on L-Glu concentration at 0.72 mM L-OPS (white circles), 0.08 mM L-OPS (red circles) and 0.035 mM L-OPS (blue circles). The solid lines represent the global fitting by a double displacement equation (Eq. 3) with inhibition by one substrate (L-Glu). Error bars represent the s.e.m. of two replicates.

Table 10: Kinetic parameters of *Sa*SbnA estimated by globally fitting data points in figure 39 and by exploiting equation 3, the k_{cat} value is 4.6 ± 0.2 s^{-1}.

	K_M (mM)	**K_i (mM)**	**k_{cat} / K_M (M^{-1} s^{-1})**
L-OPS	0.027 ± 0.006	/	1.7 ± 0.4 x 10^5
L-Glu	3.25 ± 0.36	25.75 ± 7.93	1.4 ± 0.5 x 10^3

Moreover, the fitting of the experimental data points with a double displacement equation confirmed the *Sa*SbnA mechanism of action (Figure 40) previously proposed [356]. The detailed mechanism thus involves the binding and transfer of L-OPS to PLP-bound *Sa*SbnA (internal aldimine) through the formation of an external aldimine with the PLP cofactor. Subsequently, an internal rearrangement would induce phosphate release (Q from Figure 38) and the formation of the aminoacrylate intermediate (E' from Figure 38). The latter would be reactive to L-Glu, which in turn would bind the L-OPS portion of the aminoacrylate intermediate, allowing the release of the final product ACEGA (P from Figure 38). After product release, *Sa*SbnA enzyme would return to its original internal aldimine state, ready for a new cycle.

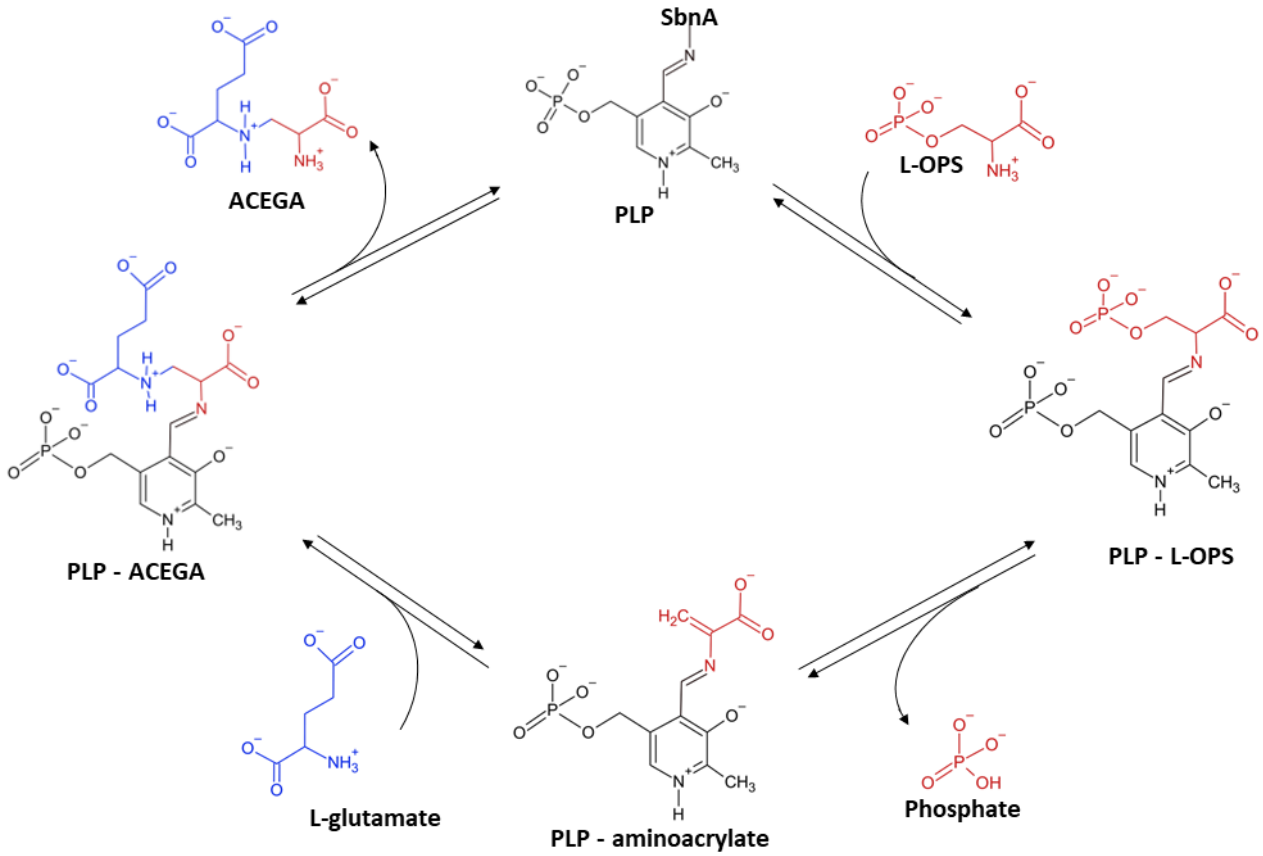

Figure 40: Schematic representation of the *Sa*SbnA mechanism of action.

A typical characteristic of fold-type II PLP-dependent enzymes is the ability to perform a deamination reaction, an ability that was also evaluated for *Sa*SbnA. In this context, the evaluation of single semi-reactions was exploited to isolate the formation of the α-aminoacrylate intermediate, while avoiding the catalytic cycling of the enzyme. The coupled assay was performed using 7 µM *Sa*SbnA, 35 µM L-OPS and a saturating concentration of L-Glu (30 mM). The reaction mix was prepared with *Sa*SbnA without the addition of its two substrates; after about 2 minutes of baseline signal recording, the reaction was triggered by L-OPS addition. The amount of *Sa*SbnA used for the analysis would correspond to a Δabsorbance of 0.1 OD for a single semi-reaction, but the results showed a Δabsorbance of about 0.54 OD that would correspond to a complete consumption of the L-OPS available (Figure 41). This phenomenon was also confirmed by the fact that a subsequent addition of L-Glu didn't alter the trend of the kinetic.

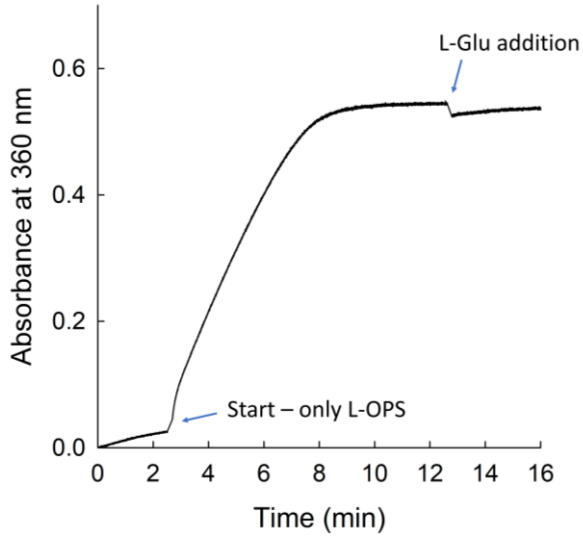

Figure 41: Single semi-reactions were followed by using the continuous assay for phosphate detection. The reaction was triggered by the addition of 0.035 mM L-OPS in the presence of 7 µM *Sa*SbnA. After L-OPS was consumed, 30 mM L-Glu was added to confirm the reaction was completed.

Subsequently, a continuous activity assay coupled with the enzyme lactate dehydrogenase (LDH) was exploited to confirm the hypothesis of the α-aminoacrylate decomposition into pyruvate and ammonia. The LDH-coupled assay allowed the conversion of pyruvate produced from L-OPS into lactate, with the simultaneous oxidation of NADH to NAD^+. The reaction was monitored at 340 nm where NADH presents its characteristic absorption peak. Since NADH oxidized form does not absorb at that wavelength, the reaction signal translated into an absorbance decay (Figure 42), confirming the spontaneous decomposition of the α-aminoacrylate intermediate.

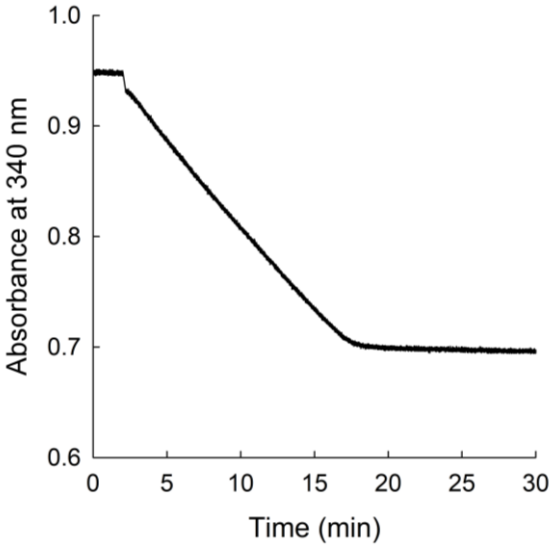

Figure 42: β-elimination reaction followed by coupling *Sa*SbnA (1.3 uM) to LDH (11 U) in the presence of 0.1 mM NADH and 0.035 mM L-OPS.

Chapter III – Evaluation of SbnA inhibitors

1 Objectives

SbnA is an *S. aureus* enzyme that catalyses the first step of the SB biosynthetic pathway and previous studies reported its importance, given that a genetic mutation resulted in the abrogation of SB production [153]. Since SB is involved in *S. aureus* iron acquisition, the inhibition of SbnA activity could affect the bacterium's ability to retrieve this fundamental nutrient and thus provide a new potential antibacterial strategy.

In this context, the aim of the activities reported in this Chapter involved the set-up and validation of three assays for the evaluation of potential inhibitors and the testing *in vitro* of the first set of molecules. The assays were used to evaluate both the effect of the molecules on *Sa*SbnA activity and their direct binding to the enzyme. For the activity assessment, an assay was optimized to provide a high-throughput evaluation of a broad number of molecules to have a first selection for compounds with a significative inhibitory effect. Subsequently, the continuous assay described in Chapter II was exploited for the characterization of the mechanism of action of the active molecules, with the determination of inhibition constants. At last, the binding of the active molecules to *Sa*SbnA was evaluated by fluorescence spectroscopy upon the excitation of the PLP factor.

Once the assays' conditions were defined, it was also exploited to study the effect of intermediates of the SB pathway on *Sa*SbnA activity to potentially identify feedback mechanisms. Among the intermediates, citrate was analysed more carefully since previous studies highlighted an inhibitory effect of citrate on SbnH and SbnC, two enzymes of the SB pathway [348,349]. Moreover, citrate is present in one of the *Sa*SbnA deposited structures (ID 5D85), therefore it was very likely to interact with the enzyme.

2 Materials and methods

HEPES for buffer solutions and sodium chloride were acquired from PanReac Applichem ITW Reagents (Darmstadt, Germany). Tris base for buffer solutions was purchased from VWR International Srl (Milano, MI, Italy), while 7-Methyl-6-thioguanosine (MESG) was purchased from Cayman (Ann Arbor, MI, USA). (S)-(+)-2,3-Diaminopropionic Acid Hydrochloride (L-Dap) was acquired from TCI Europe N.V. (Zwijndrecht, Belgium), citrate from Carlo Erba Reagents (Cornaredo, MI, Italy) and TCEP from Apollo Scientific (Stockport, UK). The malachite green reagent was purchased from ChemCruz® (Santa Cruz Biotechnology Inc., Dallas, TX, USA), while Purine Nucleoside Phosphorylase (PNP), and all remaining chemicals were purchased from Merck (Darmstadt, Germany), unless otherwise specified.

2.1 Protein over-expression and purification

*Sa*SbnA was expressed and purified as reported in Chapter II. A single purified batch was exploited for the functional characterization (Chapter II) and the evaluation of potential inhibitors of *Sa*SbnA activity (discussed in this Chapter).

2.2 Molecules solubilization

Serine, α-KG and citrate aqueous stock solutions were prepared at 100 mM, while L-Dap was solubilized at 356 mM. The pH of each solution, except for serine, was adjusted to neutrality.

The compounds selected from the virtual screening were purchased from Specs (Zoetermeer, Netherlands). Based on their properties, all molecules were first solubilized in 100 µM NaOH solution to reach 100 mM concentration. When the compounds were partially or completely insoluble after solvent addition, a cycle of heating at 37 °C and sonication was performed to increase solubility. If the molecules remained partially or completely insoluble, the concentration of the stock was lowered in a stepwise manner to a maximum of 20 mM and the pH of the solution was adjusted according to their estimated pH-solubility profiles. Four compounds ((R)-1b, (S)-1b, 1d and 10b were synthesized by the group of Prof. Lazzarato at the University of Turin and were salified in Na HEPES before the screening, considering one Na HEPES molecule for carboxylic moiety. The most promising compound of the screening (i.e. 18b) was purchased from Merk, while 2-Phenylmaleic acid (2-PhMA) was purchased from BLD Pharmatech Co. (Cincinnati, Ohio, USA). Both acquired compounds were salified as above reported.

Absorption spectra of the solubilized compounds were acquired in the range 250-700 nm in a quartz microcuvette of 0.3 cm path length using a Cary4000 spectrophotometer (Agilent Technologies, Santa Clara, CA, USA). Each compound was first analysed at 1 mM, but the concentration of some compounds was lowered to obtain a spectrum that would not show signal saturation. All measurements were acquired in HEPES 200 mM, pH 7.8 (25° C).

2.3 Set up of a testing platform for inhibitor assessment

2.3.1 Discontinuous assay

The optimized discontinuous activity assay was performed in 200 mM HEPES buffer pH 7.8 (25 °C) in a 96-well microplate (Sarstedt AG & Co., 83.3924.500). L-OPS and L-Glu were used at 0.03 mM

and 3 mM, respectively. The buffered solution was pre-incubated at 25 ± 0.4 °C, and then the addition and gentle mixing of 70 nM *Sa*SbnA triggered the reactions. For the analysis, sampling of the mixtures was performed at time zero and after 10 minutes from enzyme addition by dispensing 20 µL of the mixture to the corresponding microplate well. The reaction was stopped with 1% (m/v) trichloroacetic acid (TCA), that had been already plated at the bottom of the plate wells. The samples were then incubated with 100 µL of the commercial malachite green reagent for 30 minutes at room temperature in the dark. The absorbance of the complex between the malachite green reagent and inorganic phosphate was measured at 620 nm using a HALO LED 96 microplate reader (Dynamica, Livingstone, UK). A standard curve ranging from 0 to 100 µM phosphate was used to evaluate the assay linearity. The amount of phosphate produced in the presence of the tested compounds was normalized for the production in the reference condition and reported as the percentage of residual activity.

For the validation of the assay, the reaction triggered by the addition of *Sa*SbnA was sampled at different time intervals (stop of the reaction at 1, 2, 3, 4, 5, 10, 20 and 30 minutes).

2.3.2 Continuous assay

The continuous assay (Chapter II) was exploited for the evaluation of the effect on *Sa*SbnA activity of the SB pathway intermediates. The initial velocity of *Sa*SbnA was determined in the absence and in the presence of 1 mM intermediate at concentrations of the enzyme substrates (0.03 mM L-OPS and 3 mM L-Glu) equal to their respective K_M values. All measurements were performed in HEPES 50 mM, pH 7.8 (25 °C).
The assay was also used for the estimation of the IC_{50} value and the evaluation of the mechanism of action of the active molecules. The IC_{50} values were estimated by measuring the activity of *Sa*SbnA at different concentrations of the compounds, ranging from 0.25 to 15 mM for α-KG, 0.1 to 10 mM for citrate, 0.1 to 5 mM for 18b and from 0.005 to 1 mM for the 2-PhMA. Initial velocity as a function of compounds' concentration was measured in the presence of substrate concentrations equal to the K_M for both L-OPS and L-Glu (i.e., 0.03 mM and 3 mm, respectively). The data were then fitted to a binding isotherm (Eq. 4).

Eq. 4: $$\frac{v_i}{v_0} = \frac{IC_{50}}{[I] + IC_{50}}$$

The inhibition mechanisms of citrate, 18b and 2-PhMA were estimated by titration of one of the two substrates at a fixed non-saturating concentration (equal to the K_M value) of the other substrate.
For citrate, Michaelis Menten plots at different concentrations of the tested inhibitor were collected and then globally fitted using the corresponding equation for mixed-type inhibition considering ping-pong enzymatic reactions reported by Segel [430]. To improve the fitting, the K_M values of both substrates extrapolated in Chapter II (K_M = 0.027 mM L-OPS and K_M = 3.25 mM L-Glu) were added as constrained values in the equation.

Eq. 5: Equation for mixed-type inhibition considering a ping-pong enzymatic reaction and varying substrate A

$$v = \frac{V_{max} \cdot [L-OPS]}{\left(K_{M\ L-OPS} \cdot \left(1 + \frac{[citrate]}{K_{i1}}\right) + [L-OPS] \cdot \left(1 + \frac{K_{M\ L-Glu}}{[L-Glu]}\right) \cdot \left(1 + \left(\frac{[citrate]}{K_{i2} \cdot \left(1 + \frac{[L-Glu]}{K_{M\ L-Glu}}\right)}\right)\right)\right)}$$

Eq. 6: Equation for mixed-type inhibition considering a ping-pong enzymatic reaction and varying substrate B

$$v = \frac{V_{max} \cdot [L-Glu]}{\left(K_{M\ L-Glu} \cdot \left(1 + \frac{[citrate]}{K_{i2}}\right) + [L-Glu] \cdot \left(1 + \frac{K_{M\ L-OPS}}{[L-OPS]}\right) \cdot \left(1 + \left(\frac{[citrate]}{K_{i1} \cdot \left(1 + \frac{[L-OPS]}{K_{M\ L-OPS}}\right)}\right)\right)\right)}$$

For 18b and 2-PhMA, Michaelis Menten plots at different concentrations of the tested inhibitor were globally fitted with the corresponding equation for competitive inhibition for the free enzyme in ping-pong enzymatic reactions reported by Segel [430] (Eq. 7,8). To improve the fitting, the K_M values of both substrates extrapolated in Chapter II (K_M = 0.027 mM L-OPS and K_M = 3.25 mM L-Glu) were added as constrained values in the equation.

Eq. 7: Equation for competitive inhibition for the free enzyme considering a ping-pong enzymatic reaction and varying substrate A

$$v = \frac{V_{max} \cdot [L-OPS]}{\left(K_{M\ L-OPS} \cdot \left(1 + \frac{[I]}{K_i}\right) + [L-OPS] \cdot \left(1 + \frac{K_{M\ L-Glu}}{[L-Glu]}\right)\right)}$$

Eq. 8: Equation for competitive inhibition for the free enzyme considering a ping-pong enzymatic reaction and varying substrate B

$$v = \frac{V_{max} \cdot [L-Glu]}{\left(K_{M\ L-Glu} + [L-Glu] \cdot \left(1 + \frac{K_{M\ L-OPS}}{[L-OPS]} + \frac{K_{M\ L-OPS} \cdot [I]}{K_i \cdot [L-OPS]}\right)\right)}$$

Double reciprocal plots were extrapolated from experimental data of the direct plots. The double reciprocal plots at different concentrations of the tested inhibitor were globally fitted using the inverse of the corresponding equation.

Eq. 9: Inverse of the equation (see Eq. 5) for mixed-type inhibition considering ping-pong enzymatic reactions and varying substrate A

$$v = \frac{1}{V_{max}} \left((K_{M\,L-OPS} \cdot \left(1 + \frac{[citrate]}{K_{i1}}\right) \cdot [L-OPS]) + (1 + K_{M\ L-Glu} \cdot [L-Glu]) + \frac{[citrate]}{K_{i2}} \right)$$

Eq. 10: Inverse of the equation (see Eq. 6) for mixed-type inhibition considering ping-pong enzymatic reactions and varying substrate B

$$v = \frac{1}{V_{max}} \left((K_{M\,L-Glu} \cdot \left(1 + \frac{[citrate]}{K_{i2}}\right) \cdot [L-Glu]) + (1 + K_{M\ L-OPS} \cdot [L-OPS]) + \frac{[citrate]}{K_{i1}} \right)$$

Eq. 11: Inverse of the equation (see Eq. 7) for competitive inhibition for the free enzyme considering a ping-pong enzymatic reaction and varying substrate A

$$v = \frac{1}{V_{max}} \left((K_{M\,L-OPS} \cdot \left(1 + \frac{[I]}{K_i}\right) \cdot [L-OPS]) + (K_{M\ L-Glu} \cdot [L-Glu]) + 1 \right)$$

If a global fitting was not possible, each plot at different inhibitor concentrations was fitted singularly by a linear equation.

2.3.3 Fluorescence spectroscopy

Fluorescence spectra were collected in a quartz microcuvette of 3 mm path length on a Fluoromax-4 spectrofluorometer (Horiba Jobin Yvon, Kyoto, Japan) equipped with a thermostated water bath. Measurements were conducted at 20 °C in HEPES buffer pH 7.8, at 50 mM within the evaluation of SB pathway intermediates, while at 200 mM in the analysis of the compounds identified by VS and presenting inhibitory activity. An increased concentration of HEPES was exploited for the compound screening in order to have a buffered solution suitable to test molecules presenting different chemical properties. Emission spectra were recorded in the wavelength range of 425-600 nm by excitation of PLP at 412 nm, after the solution was pre-incubated for 2 minutes at 20 °C to reach the required temperature. *Sa*SbnA was analysed at 5 µM, while the tested molecules were analysed either at 1 mM or 5 mM concentration. The effect of the binding of each compound to *Sa*SbnA was evaluated by subtracting the molecule emission spectrum to its corresponding spectrum with *Sa*SbnA.

3 Results and discussion

3.1 Set-up of a testing platform for the evaluation of inhibitors

Three assays were set up for the evaluation of potential inhibitors enabling to assess the molecules' effect on *Sa*SbnA activity and their binding to the active site (Figure 43). For the activity evaluation, a discontinuous assay was optimized to provide a high-throughput assessment of sets of molecules. The compounds identified with the discontinuous assay would then be further characterized by the continuous assay described in the previous chapter. At last, the binding of the molecules to *Sa*SbnA was evaluated by fluorescence spectroscopy through the acquisition of emission spectra by excitation of the PLP cofactor at 412 nm.

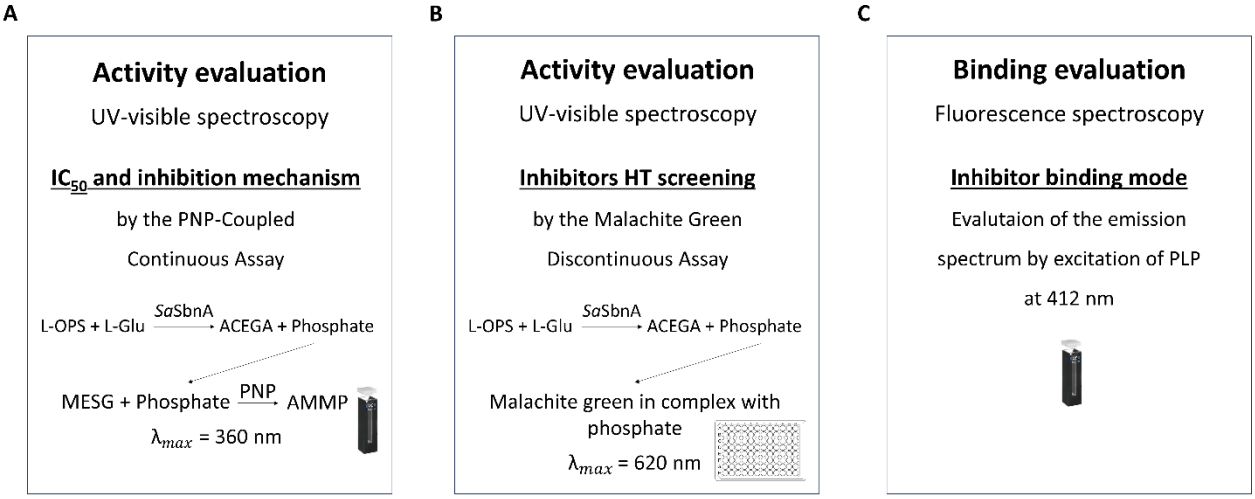

Figure 43: Schematic representation of the three assays set up for the evaluation of potential inhibitors of *Sa*SbnA activity. (A) The PNP-coupled continuous assay for the evaluation of the IC_{50} and inhibition mechanism of the potential inhibitors. (B) The Malachite Green discontinuous assay for the HT screening of the potential inhibitors. (C) Fluorescence spectroscopy to evaluate the inhibitors' binding to *Sa*SbnA.

3.2 Evaluation of the effect on *Sa*SbnA activity of intermediates of the SB pathway

The SB biosynthetic pathway is a multi-step process comprising different intermediates (Figure 44). The final product SB is composed of three building blocks, namely L-Dap, α-KG and citrate, that are produced within the SB pathway itself. Previous studies have reported the existence of a feedback mechanism within the pathway, as the inhibition of SbnH and SbnC activity by citrate [348,349]. Moreover, citrate was present in the *Sa*SbnA crystal structure (ID 5D85) in the closed conformation, therefore it's likely to interact with the enzyme. Because of the potential existence of other mechanisms, an evaluation of the effect of intermediates of the pathway on *Sa*SbnA activity would provide further valuable information about the regulation of the SB biosynthesis. Moreover, the identification of an intermediate with an inhibitory effect could allow its exploitation as a reference for further compound screening.

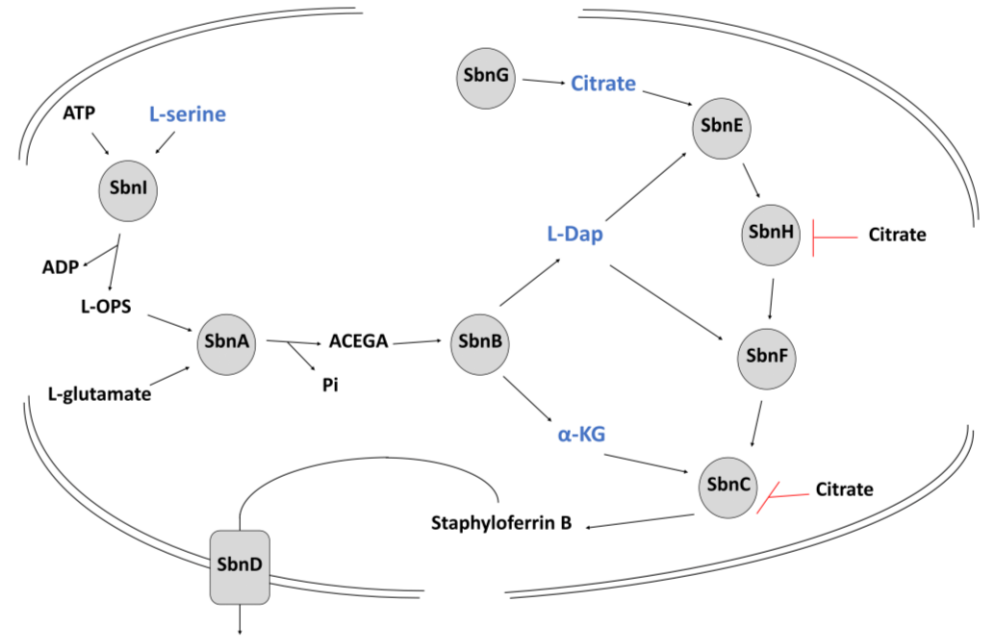

Figure 44: Schematic representation of SB biosynthetic pathway. In bold blue are reported the components of the pathway whose effect on *Sa*SbnA activity was evaluated.

For this purpose, the optimized continuous PNP-coupled assay was exploited to test whether intermediates of the SB pathway would affect *Sa*SbnA activity. The three SB building blocks (L-Dap, α-KG and citrate) were tested at 1 mM concentration each, along with L-serine, the precursor of L-OPS (Figure 45). The effect on *Sa*SbnA activity was determined at unsaturated concentrations of the enzyme substrates (0.03 mM L-OPS and 3 mM L-Glu). The results revealed a significant inhibitory effect by citrate that would reduce the activity of *Sa*SbnA by more or less 50%, highlighting citrate's importance in regulating the different steps of the pathway. Furthermore, also α-KG presents an inhibitory effect, even if *Sa*SbnA activity was reduced only by 35%.

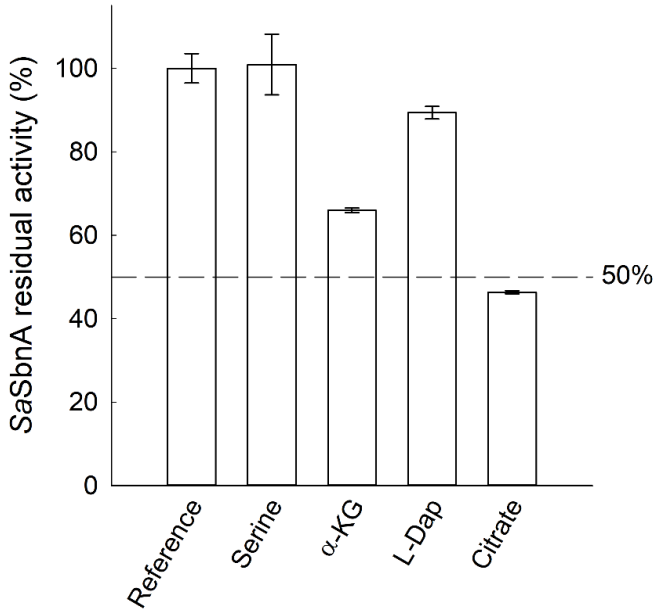

Figure 45: Effect on *Sa*SbnA activity of components of the SB pathway, followed by the continuous assay using 1 mM concentration of each tested effector. Error bars represent the s.e.m. of two replicates.

3.2.1 Evaluation of α-KG inhibitory effect

The dependence of the initial velocity of *Sa*SbnA activity on α-KG concentration was determined at 0.03 mM L-OPS, 3 mM L-Glu and at concentrations of α-KG between 0.25 and 15 mM. The extrapolated IC_{50} value (see Eq. 4) was 2.92 ± 0.22 mM.

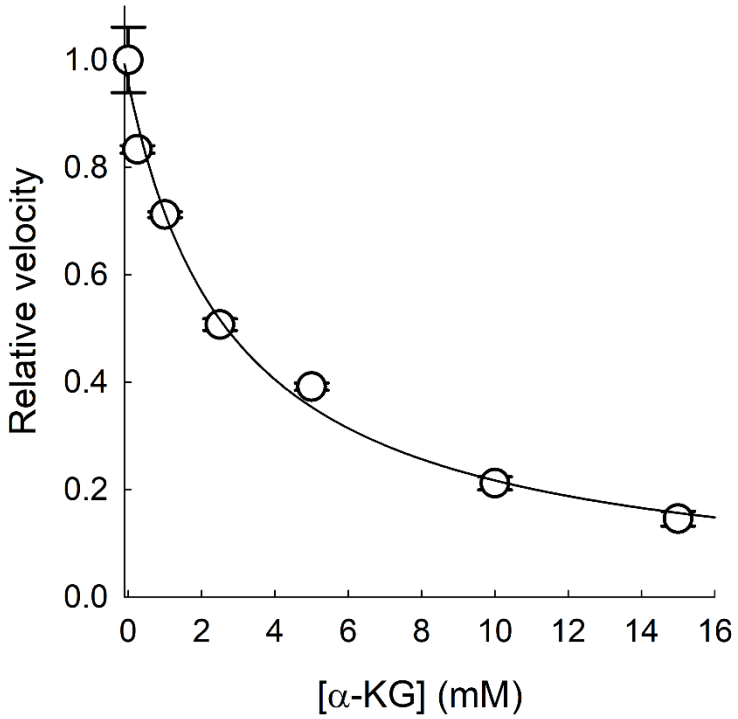

Figure 46: Determination of the IC_{50} for α-KG. Data were fitted to a binding isotherm (solid line, see Eq. 4) and error bars represent the s.e.m. of two replicates.

The binding of α-KG to *Sa*SbnA was evaluated by fluorescence spectroscopy, even if the calculated IC_{50} value revealed a not very potent inhibitor. To evaluate the interaction, fluorescence spectra were acquired by excitation of *Sa*SbnA at 412 nm in the absence and presence of 1 mM α-KG concentration. The results obtained with α-KG (Figure 47) were comparable to the spectral change induced by L-Glu addition (Chapter II, Figure 33B), which was attributed to a change in the polarity of the environment around the PLP cofactor. Moreover, this outcome supported the fact that the spectral change induced by L-Glu was not caused by the formation of the external aldimine, since α-KG could not form it and showed the same signal variation. At last, as in the case of L-Glu, the emission peak after α-KG addition showed a red shift (highlighted by the arrow in Figure 47) which could be reconducted to an increased exposition of PLP to the solvent.

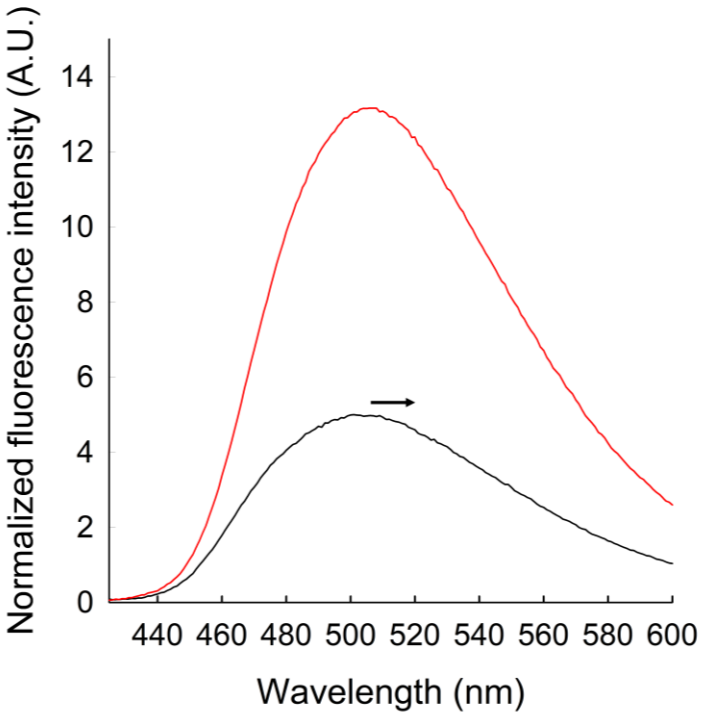

Figure 47: Emission fluorescence spectra of *Sa*SbnA by excitation at 412 nm in the absence (black line) and presence of 1 mM α-KG (red line). The spectra were collected in HEPES buffer 50 mM, pH 7.8.

3.3 Evaluation of citrate mechanism of action

Based on the results of the initial intermediate screening, citrate effects were further characterized to obtain more information about its regulatory properties.

The dependence of the initial velocity of *Sa*SbnA activity on citrate concentration was determined at 0.03 mM L-OPS, 3 mM L-Glu and at concentrations of citrate between 0.1 and 10 mM (Figure 48). The extrapolated IC_{50} value was 0.92 ± 0.09 mM, which corresponds to the physiological intracellular concentration reported for citrate in the wild-type strain *S. aureus* Newman by Ding and colleagues [433].

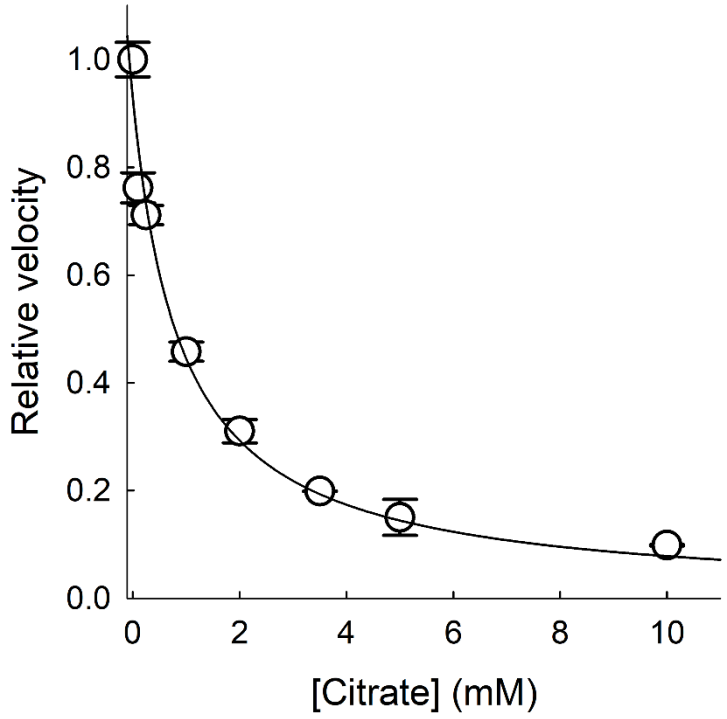

Figure 48: Determination of the IC_{50} for citrate. Data were fitted to a binding isotherm (solid line, see Eq. 4) and error bars represent s.e.m. of two replicates.

Because of the physiological relevance and the effect observed on *Sa*SbnA activity, citrate mechanism of action was investigated by exploiting the optimized continuous assay. Notably, two types of plots were generated by studying the dependence of *Sa*SbnA initial rate by varying either L-OPS or L-Glu at fixed non-saturating concentrations of the other substrate. The dependence was evaluated at three different citrate concentrations. Indeed, the direct and global fit of velocity versus substrate concentration at fixed inhibitor concentrations allowed to have an initial idea of the inhibitor mechanism, but mostly was used to calculate inhibitor constants by fitting the plots globally with the proper equation. On the other hand, double reciprocal or Lineweaver-Burk plots represented the most straightforward means of validating inhibitor modality, since the mechanism could be directly interpreted by the trend of the fitted curves (Figure 49).

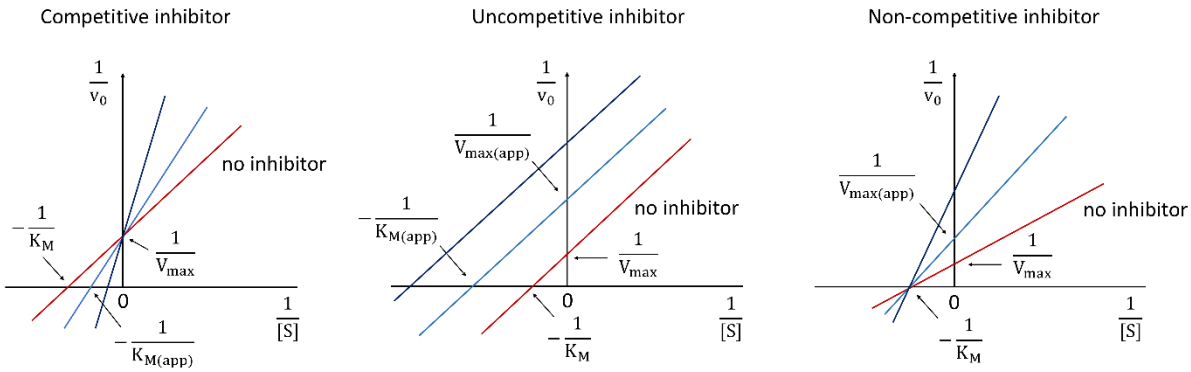

Figure 49: Effect of different types of inhibitors on the trend of the fitted curves. The double reciprocal plot of competitive inhibitors presents the curves' intercept on the y axis (left panel), the plot of uncompetitive inhibitors is characterized by parallel straight lines (centre panel), and the plot of non-competitive inhibitors presents the curves' intercept in the left quadrant (right panel).

In the plots reported in Figure 50, the dependence of *Sa*SbnA initial rate was evaluated by titrating either L-OPS at a fixed unsaturated L-Glu concentration (3 mM) (Figure 50A), or by titrating L-Glu at a fixed unsaturated L-OPS concentration (0.03 mM) (Figure 50B). For each of the two plots, the enzyme activity was tested in the absence or presence of citrate at 1 and 5 mM. Each plot was then globally fitted by its corresponding equation for mixed-type inhibition considering ping-pong enzymatic reactions reported by Segel [430] (Eq. 5,6). To improve the fitting, the K_M values of both substrates extrapolated in Chapter II (K_M = 0.027 mM L-OPS and K_M = 3.25 mM L-Glu) were added as constrained values in the equation.

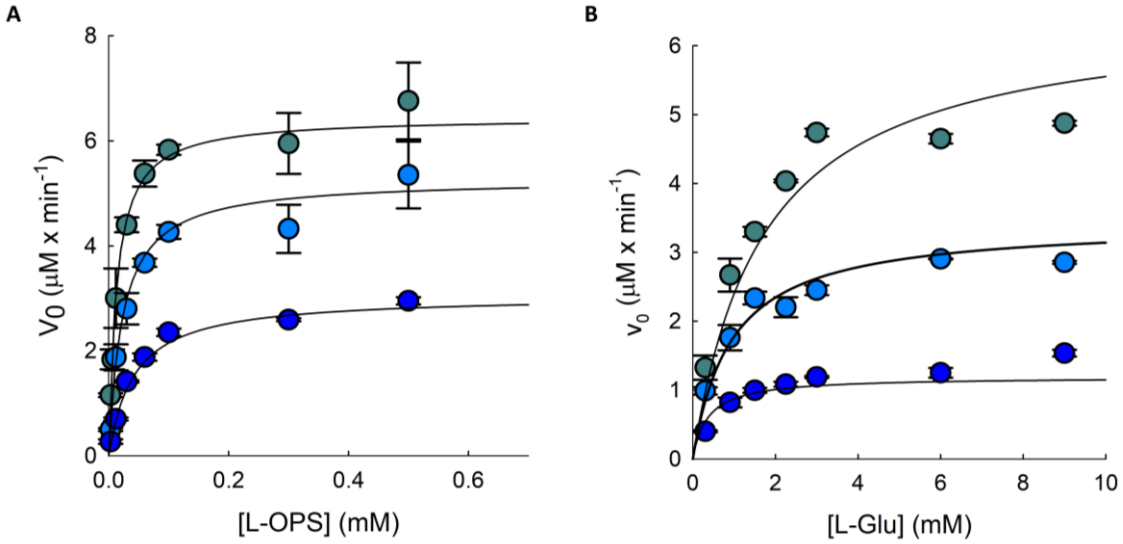

Figure 50: Dependence of *Sa*SbnA initial velocity on varying concentrations of either substrate. (A) Dependences of *Sa*SbnA initial velocity in the presence of fixed 3 mM L-Glu as a function of L-OPS concentrations in the absence of citrate (teal circles), with 1 mM citrate (light blue circles) and 5 mM citrate (dark blue circles). Data were fitted to Eq. 5. (B) Dependences of *Sa*SbnA initial velocity in the presence of fixed 0.03 mM L-OPS as a function of L-Glu concentrations in the absence of citrate (teal circles), with 1 mM citrate (light blue circles) and 5 mM citrate (dark blue circles). Data were fitted to Eq. 6. All measurements were conducted at 50 nM *Sa*SbnA in HEPES 50 mM pH 7.8 at 25 °C. Error bars represent s.e.m. of two replicates.

The global direct fitting of the Michaelis-Menten curves allowed to extrapolate the inhibition constants Ki_1 and Ki_2, which refer to the free enzyme (E) and to the α-aminoacrylate intermediate (E'), respectively (Table 11). The inhibition constant Ki_2, extrapolated from L-Glu titration plots, could not be considered reliable because of the associated extremely high error. The reason of this result could be associated with the effect of L-Glu substrate inhibition on *Sa*SbnA activity.

Table 11: Parameters extrapolated from the global fitting using the equations for mixed-type inhibition considering ping-pong enzymatic reactions (Eq. 5,6). The K_M values of both substrates extrapolated in Chapter II (K_M = 0.027 mM L-OPS and K_M = 3.25 mM L-Glu) were added as constrained values in the equation to improve the fitting.

	V_{max}	K_{i1}	K_{i2}
L-OPS titration	13.4 ± 0.2 µM/min	0.9 ± 0.1 mM	2.3 ± 0.3 mM
L-Glu titration	12.3 ± 0.4 µM/min	0.5 ± 0.1 mM	32.6 ± 178 mM

Experimental data points were then fitted to the inverse of the equation for mixed-type inhibition of ping-pong enzymatic reactions, when varying either substrate A (Eq. 10) or substrate B (Eq. 11). This type of analysis was performed to directly visualize the modality of citrate inhibition (Figure 51).

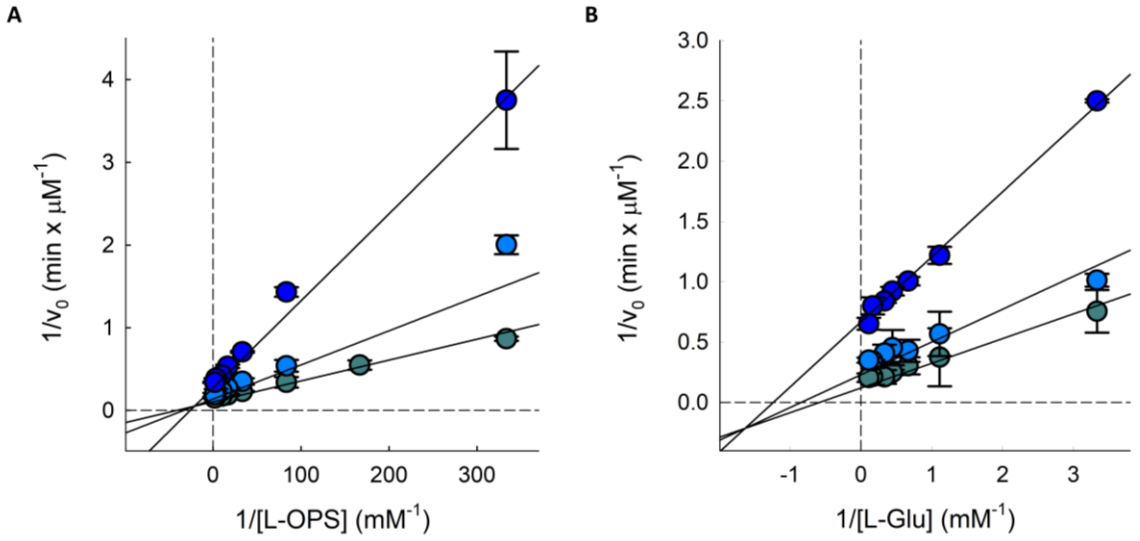

Figure 51: Lineweaver—Burk double-reciprocal plot of *Sa*SbnA initial velocity at varying concentrations of either substrate. (A) Double reciprocal plot of *Sa*SbnA initial velocity in the presence of fixed 3 mM L-Glu as a function of L-OPS concentrations in the absence of citrate (teal circles), with 1 mM citrate (light blue circles) and 5 mM citrate (dark blue circles). Data were fitted to Eq. 9 (straight lines). (B) Double reciprocal plot of *Sa*SbnA initial velocity in the presence of fixed 0.03 mM L-OPS as a function of L-Glu concentrations in the absence of citrate (teal circles), with 1 mM citrate (light blue circles) and 5 mM citrate (dark blue circles). Data were fitted to Eq. 10 (straight lines). All measurements were conducted at 50 nM *Sa*SbnA in HEPES 50 mM pH 7.8 at 25 °C. Error bars represent s.e.m. of two replicates.

Based on the whole characterization results, citrate presented a mixed-type inhibition profile with the ability to interact with both the free enzyme and the aminoacrylate intermediate, presenting a slightly greater affinity for the former.

At last, the binding of citrate to *Sa*SbnA was evaluated through the acquisition of fluorescence emission spectra by excitation of the PLP cofactor at 412 nm and 467 nm, The two wavelengths were exploited to independently excite and assess the effect of citrate on *Sa*SbnA in the presence of either L-Glu or L-OPS, respectively. Indeed, the two *Sa*SbnA substrates were separately evaluated since UV-Vis spectra highlighted that their absorbance maximum was centered at different wavelengths, as reported in Figure 34 Chapter II. Notably, the α-aminoacrylate intermediate, formed after L-OPS addition, absorbs at 467 nm, while L-Glu doesn't react with the internal aldimine, thus the absorbance maximum remains at 412 nm after its addition.

The addition of 1 mM citrate to *Sa*SbnA induced a slight reduction in the peak intensity, that could be attributed to a change in the environment polarity around the PLP (Figure 52A). Likewise, a comparable slight reduction in the peak intensity was observed in the emission spectra of the aminoacrylate intermediate after the addition of 1 mM citrate (Figure 52B). At last, the most significative spectral change was observed by the addition of 1 mM citrate to the *Sa*SbnA

spectrum after the previous addition of L-Glu (Figure 52C). The overall phenomenon induced by citrate was the reduction of fluorescence intensity, more likely attributed to a change in the environment polarity around the PLP cofactor.

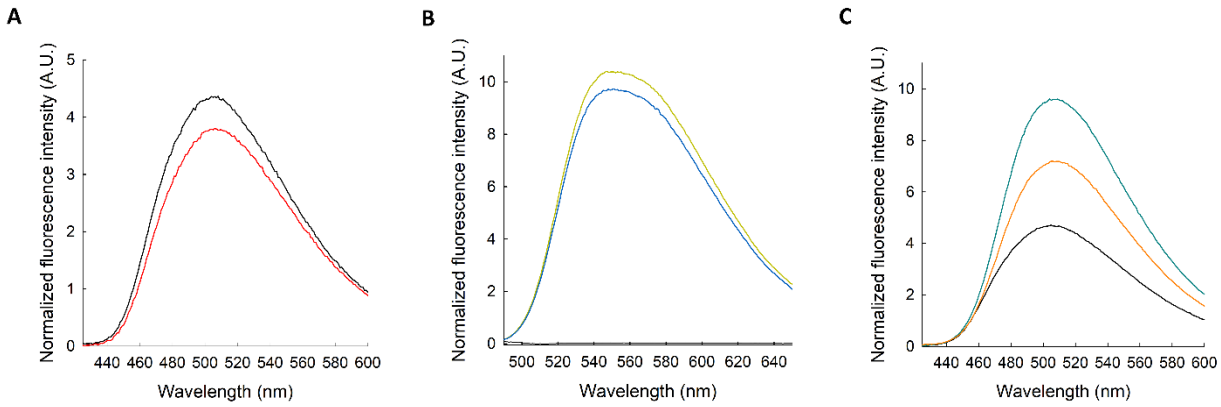

Figure 52: Fluorescence emission spectra of *Sa*SbnA in the absence and presence of substrates and citrate. (A) Emission spectra of *Sa*SbnA by excitation at 412 nm in the absence (black line) in the presence of 1 mM citrate (red line). (B) Emission spectra of *Sa*SbnA by excitation at 467 nm in the absence (black line) and after the addition of 0.3 mM L-OPS (light green line) and then 1 mM citrate (blue line). (C) Emission spectra of *Sa*SbnA by excitation at 412 nm in the absence (black line) and after the addition of 30 mM L-Glu (light blue line) and then 1 mM citrate (orange line). All measurements were carried out in HEPES buffer 50 mM, pH 7.8.

3.4 Validation of the discontinuous assay

The malachite green discontinuous assay had become a widely used enzymatic assay, becoming the standard in the study of phosphatases since its first introduction in the 1960s [434]. The conditions of the assay were adapted to study *Sa*SbnA activity for the screening of potential inhibitors, as reported in Material and Methods.

To validate the assay, phosphate production in the *Sa*SbnA-catalysed reaction was evaluated in the absence and in the presence of citrate at 1 and 5 mM concentration (Figure 53A). The kinetic plots allowed to extrapolate the reactions' initial velocities, then converted into *Sa*SbnA residual activity (Figure 53B). The analysis allowed to estimate citrate IC_{50}, which resulted in accordance with the one obtained with the continuous assay, therefore validating the method.

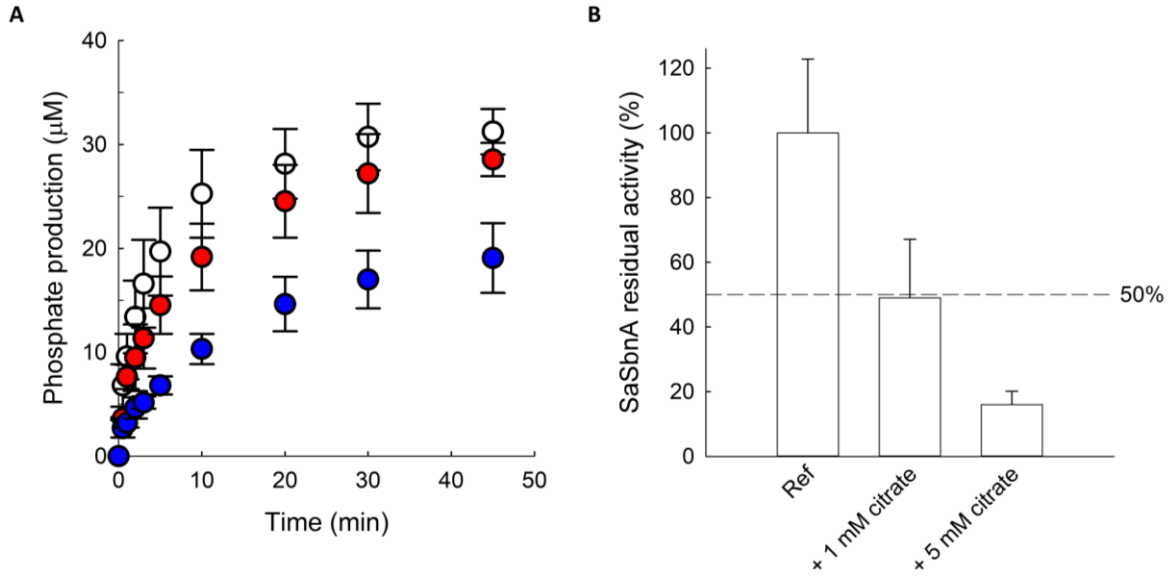

Figure 53: Validation of the discontinuous assay for the evaluation of *Sa*SbnA potential inhibitors. (A) Phosphate production in the *Sa*SbnA-catalysed reaction was evaluated by the discontinuous assay in the absence (white circles) and in the presence of 1 mM (red circles) and 5 mM (blue circles) citrate. (B) Evaluation of the effect of citrate on *Sa*SbnA initial velocity. The values of the reactions' initial velocities were extrapolated from the Michaelis Menten plots (panel A).
All measurements were conducted in 50 mM HEPES pH 7.8 (25 °C). Error bars represent the s.e.m. of two replicates.

Ultimately, the conditions of the discontinuous assay for the HT screening were set with reaction sampling at time 0 and after 10 minutes of incubation to optimize the compromise between the linearity of the assay, phosphate production and absorbance signal intensity.

3.5 Screening of potential *Sa*SbnA inhibitors

The discontinuous assay was exploited to test the potential inhibitory activity of a first set of compounds that had been identified by the group of Prof. Spyrakis at the University of Turin. Fifteen compounds were selected after molecular docking of 25 molecules using the deposited SbnA structure in open conformation (ID 5D84) (Table 12). These molecules had been pre-identified as inhibitors of PLP-dependent enzymes, in particular OASS and serine racemase (SR) enzymes, which are structurally highly homologous to SbnA. At last, an extra precision (XP) docking of the fifteen compounds to the *Sa*SbnA active site was performed exploiting the deposited closed conformation structure (ID 5D85).

Table 12: List of the fifteen commercial compounds selected by virtual screening. The chemical structures were drawn by using ACD/ChemSketch (Advanced Chemistry Development Inc., Toronto, Canada) based on the ones reported by Specs site (https://www.specs.net/).

	ID		Structure	Homologous target
	SPECS	Internal code		
1	AC-907/34133001	1a	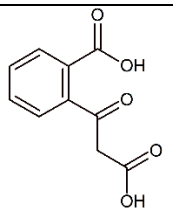	OASS
2	AG-205/07908015	1b	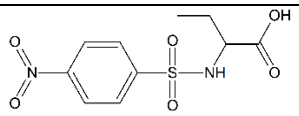	SR
3	AE-641/00361044	2a	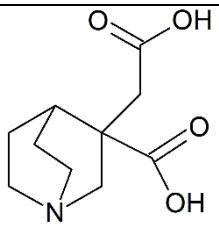	OASS/SR
4	AG-670/36765032	6b	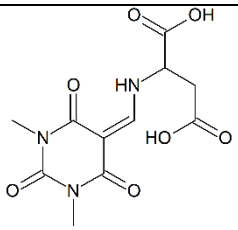	SR
5	AG-690/34035030	8b	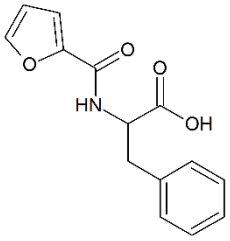	OASS
6	AI-942/42301799	9a	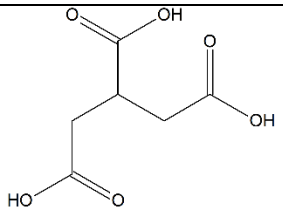	OASS/SR

7	AK-079/09930008	9b	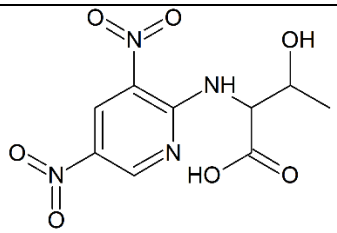	SR
8	AJ-333/09217010	10a	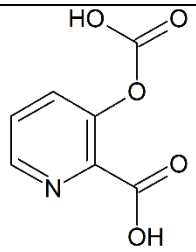	OASS
9	AO-623/14653116	10b	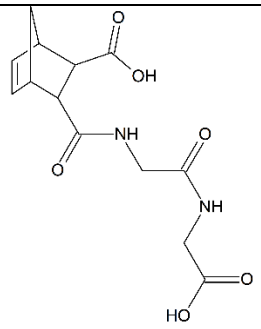	OASS
10	AG-690/11214033	11b	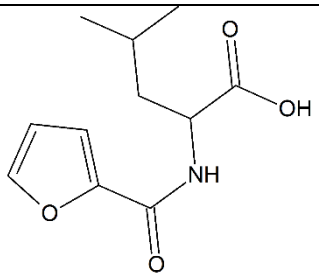	OASS
11	AG-690/36829059	12b	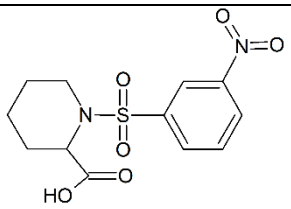	OASS
12	AP-060/40977348	13b	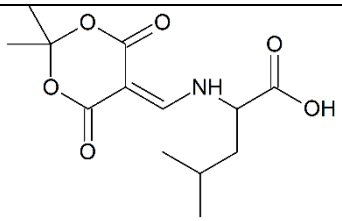	OASS

13	AK-968/12383180	14b	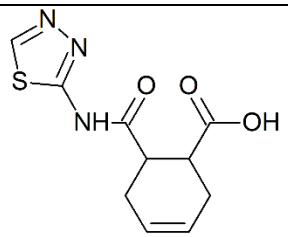	OASS
14	AQ-390/43356434	17b	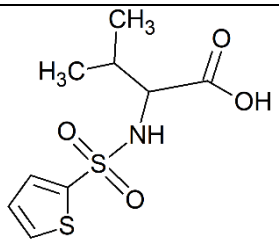	OASS
15	AD-232/25000151	18b	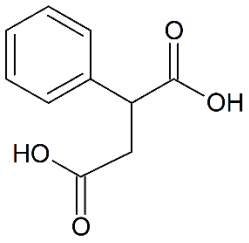	OASS

The molecules selected from the virtual screening, available for purchase, were acquired from Specs (Zoetermeer, Netherlands) as lyophilized powder. Based on their properties, all molecules were first solubilized in 100 µM NaOH solution to reach 100 mM concentration. When the compounds were partially or completely insoluble after solvent addition, a cycle of heating and sonication was performed to increase solubility. If the molecules still remained partially or completely insoluble, the concentration of the stock was lowered to a maximum of 20 mM and the pH of the solution was adjusted according to their estimated pH-solubility profiles. The final concentration and pH of the stock solution are reported in Table 13. A measure of the pH of two solutions at 1 and 5 mM of each compound in 200 mM HEPES pH 7.8 (25 °C) was performed to confirm that the addition of compounds at high concentrations wouldn't change the pH of the working solution.

Table 13: Solubilization of the first set of tested commercial compounds.

ID compound	Stock concentration (mM)	Solubilization in NaOH solution (mM)	pH of the stock solution
1a	20 (not solubilized)	20	6
2a	100	0.1	2.5
6b	30	19	4
9a	100	0.1	2.5
9b	30	16.5	6
10a	100	0.1	4
10b	100	0.1	2.5
12b	20 (not solubilized)	20	8
13b	25	15	6.5
17b	25	16	6
18b	50	1	4

Absorbance spectra of each compound were acquired to characterize them spectroscopically and evaluate their potential interference at the wavelengths corresponding to the three assays used for inhibitor identification (Figure 54). No compound showed absorbance at 620 nm (discontinuous activity assay), while only compound 9b presented significative absorbance at both 360 and 412 nm (continuous activity assay and fluorescence binding evaluation, respectively). The results of the compounds' spectroscopic characterization were exploited to decide the best conditions for the following analyses.

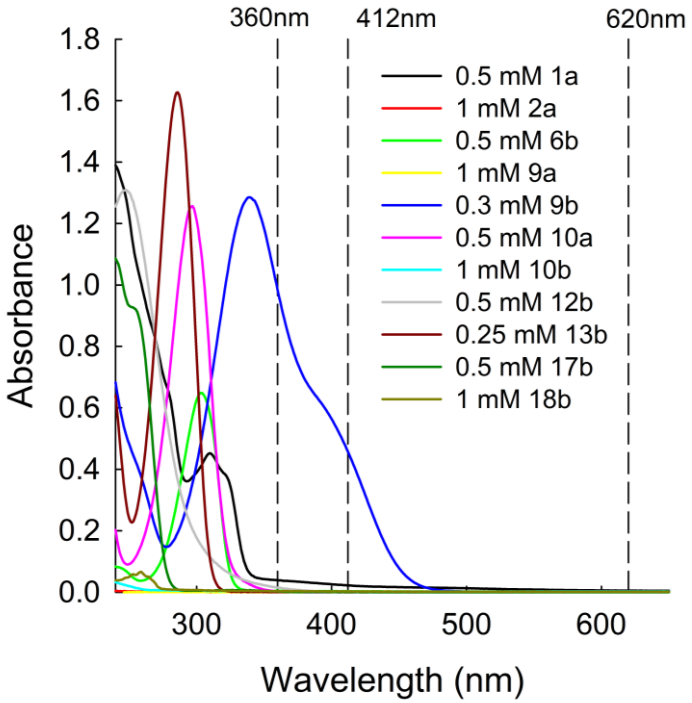

Figure 54: Absorbance spectra of purchased compounds acquired in the range 240-650 nm in a 0.3 cm quartz cuvette. The compounds were tested at different concentrations to keep the absorbance below 2 OD, with 1 mM as maximal concentration. The dotted lines represent the three wavelengths exploited for inhibitor identification (360 nm in the continuous activity assay, 412 nm for fluorescence spectroscopy and 620 nm in the discontinuous activity assay).

The optimized discontinuous assay was exploited for the screening of the first set of compounds identified by virtual screening (Figure 55). The production of phosphate by *Sa*SbnA was evaluated at 10 minutes in the absence and in the presence of the commercial compounds, at 5 mM final concentration, with the exploitation of citrate as positive control. The results highlighted the presence of four compounds (1a, 9a, 10b and 18b) that could inhibit by 50% or more the production of phosphate by *Sa*SbnA. Among the four molecules, compound 1a presented solubility problems therefore its inhibitory activity would need further confirmation, while 9a was a citrate analogue therefore it was not analysed further. At last, the analysis identified 18b as the best hit. Despite the good results obtained, the analyses performed on the commercial molecules needed further validation to exclude false positive results due to the not optimal purity (90%) guaranteed by SPECS.

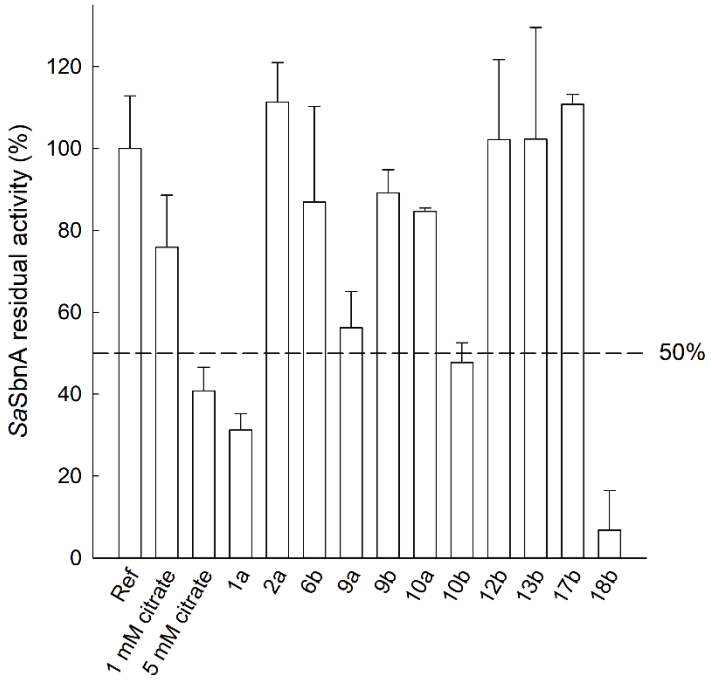

Figure 55: Screening of the compounds selected by VS followed at 50 nM *Sa*SbnA, 0.03 mM L-OPS, 3 mM L-Glu and at 5 mM of each compound. Citrate was exploited as reference for an active inhibitor. Error bars represent s.e.m. of two replicates.

The binding of the molecules to SaSbnA was evaluated by fluorescence spectroscopy for the active compounds. The binding was evaluated by the acquisition of emission fluorescence spectra of 5 µM *Sa*SbnA upon excitation at 412 nm in the absence and in presence of 5 mM of each compound, except for compound 1a that was tested at 1.8 mM (Figure 56). The results highlighted different effects of binding to *Sa*SbnA for the four molecules: compound 10b seemed to cause a modification in the environment polarity as the spectral change resembled the one in the presence of L-Glu. Despite the same spectral changes were observed for compound 1a, the solubility issues of the molecule could have caused some interferences with the analysis. At last, no significant spectral changes were observed for compounds 9a and 18b.

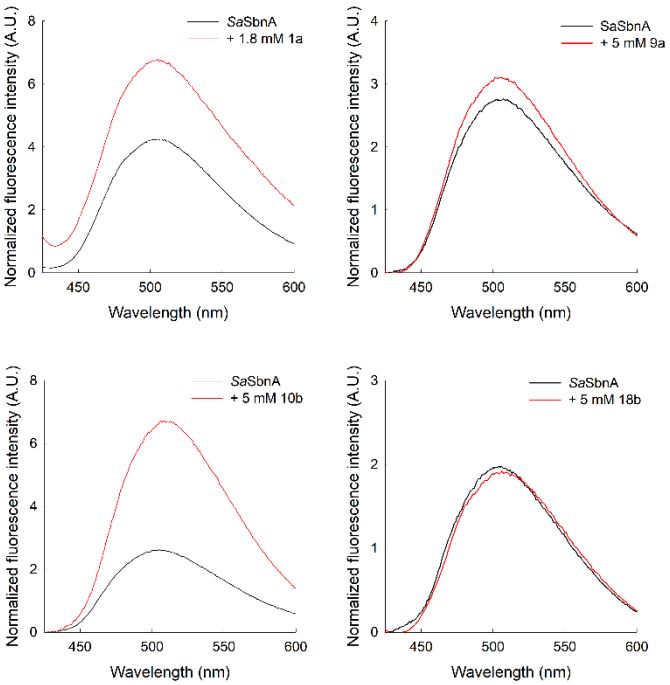

Figure 56: Emission fluorescence spectra of the four compounds presenting inhibitory activity. Spectra of *Sa*SbnA at 5 µM were acquired by excitation at 412 nm in the absence and in presence of 5 mM of each compound, except for compound 1a that was tested at 1.8 mM. All measurements were carried out in HEPES buffer 200 mM, pH 7.8.

To confirm the data obtained with the commercial molecules, the compounds that resulted active in the screening were further tested. An analogue of compound 1a (named 1d) was synthesized by the team of Prof. Lazzarato at the university of Turin to potentially increase the molecule solubility, along with the synthesis of compound 10b. Compound 18b was purchased from Merk at a higher purity. Moreover, the group of Prof. Lazzarato synthesized also one of the molecules that were identified in the virtual screening but not available for purchase by SPECS, compound 1b, that was synthesized in both R and S configurations. All the molecules were salified to increase solubility and avoid potential pH adjustments, heating and sonication steps during solubilization. Indeed, the compounds were then solubilized in aqueous solution at 100 mM, without any solubility issue. The molecules were then screened by following the production of phosphate in the *Sa*SbnA-catalysed reaction by the discontinuous assay. The reaction was followed in the same conditions as the initial screening and the result confirmed only 18b as a compound able to inhibit by 50% or more the production of phosphate by *Sa*SbnA at 5 mM concentration (Figure 57). The compound 1b, tested for the first time, didn't present any inhibitory effect on *Sa*SbnA activity in both configurations.

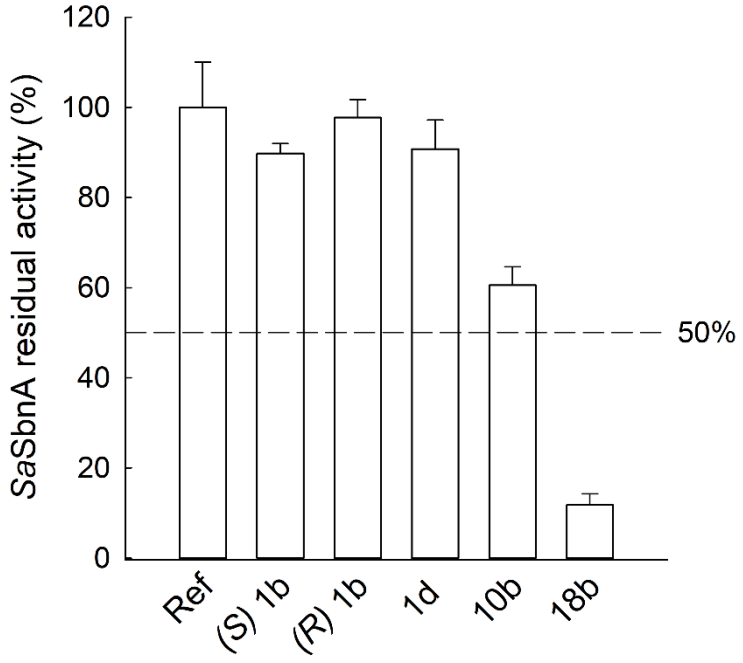

Figure 57: Screening of compounds synthesized by Prof. Lazzarato (University of Turin). The production of phosphate in the *Sa*SbnA-catalysed reaction was followed at 50 nM *Sa*SbnA, 0.03 mM L-OPS, 3 mM L-Glu and at 5 mM of each compound. All measurements were carried out in HEPES buffer 200 mM, pH 7.8. Error bars represent s.e.m. of two replicates.

Based on the results reported in this chapter, 18b was selected as the best hit and was further characterized, potentially becoming the parent compound in a future drug design and screening campaign.

3.6 Evaluation of 18b mechanism of action

The best hit identified by the HT screening of the first set of compounds was further characterized by the exploitation of the three assays for inhibitor identification, to define its inhibition mechanism.

First, the dependence of the initial velocity of *Sa*SbnA activity in the presence of increasing concentrations of 18b was determined at 0.03 mM L-OPS and 3 mM L-Glu (Figure 58). The 18b compound was tested at concentrations between 0.1 and 5 mM. The extrapolated IC_{50} value (see Eq. 4) was 0.366 ± 0.037 mM.

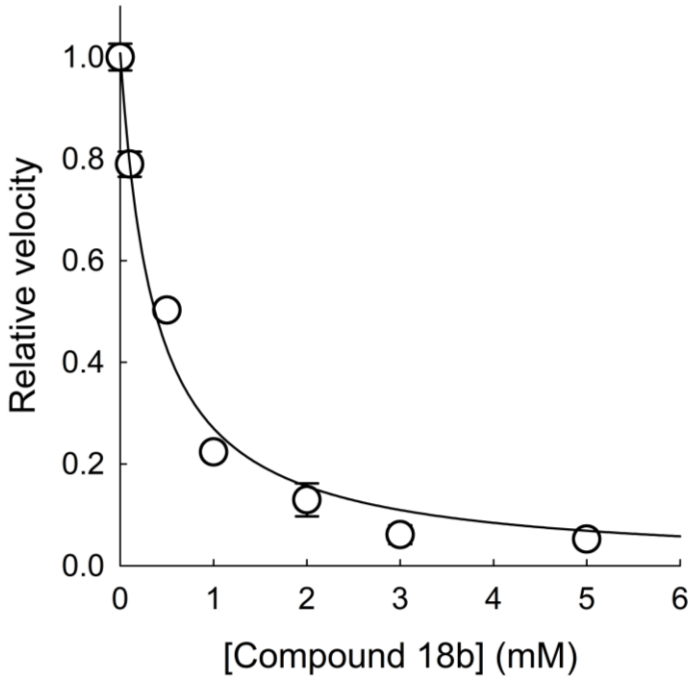

Figure 58: Determination of the IC_{50} for compound 18b. Data were fitted to Eq. 4 (solid line) and error bars represent s.e.m. of two replicates.

In the plots of Figure 59, the dependence of *Sa*SbnA initial rate on substrate concentration was evaluated by titrating either L-OPS at a fixed unsaturated L-Glu concentration (3 mM) (Figure 59A), or by titrating L-Glu at a fixed unsaturated L-OPS concentration (0.03 mM) (Figure 59B). For each of the two plots, the enzyme activity was tested in the absence or presence of 18b at 0.37 and 2 mM. Each plot was then globally fitted with the equation for competitive inhibition for the free enzyme in ping-pong enzymatic reactions reported by Segel [430] (Eq. 7,8). The equations were chosen based on the best fit to the experimental data. To improve the fitting, the K_M values of both substrates extrapolated in Chapter II (K_M = 0.027 mM L-OPS and K_M = 3.25 mM L-Glu) were added as constrained values in the equation.

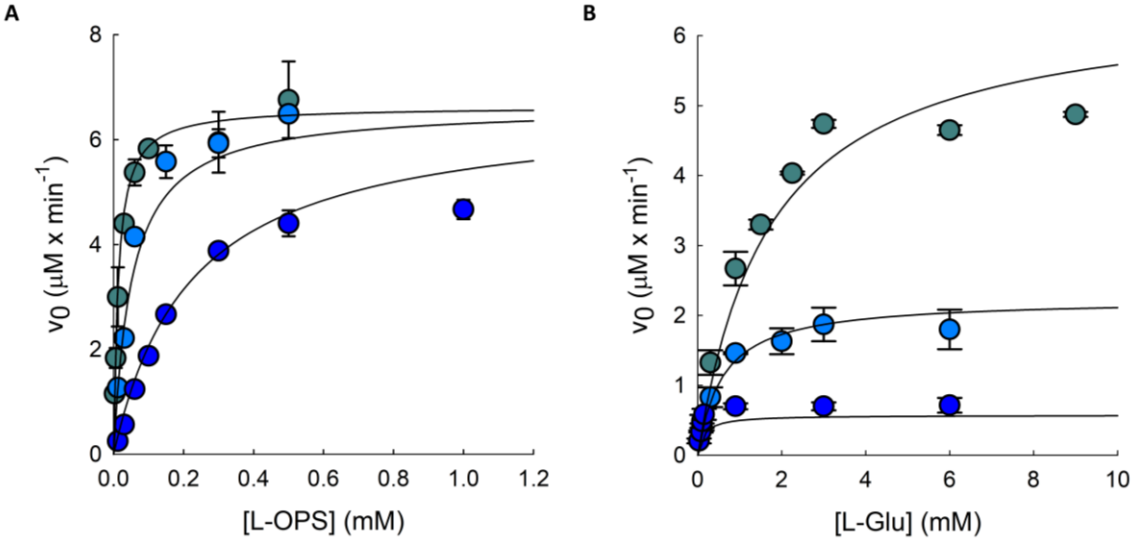

Figure 59: Dependence of *Sa*SbnA initial velocity on varying concentrations of either substrate. (A) Dependences of *Sa*SbnA initial velocity on L-OPS concentrations in the presence of fixed 3 mM L-Glu,

in the absence of 18b (teal circles), with 0.37 mM 18b (light blue circles) and 2 mM 18b (dark blue circles). Data were fitted to Eq. 7. (B) Dependence of *Sa*SbnA initial velocity on L-Glu concentration in the presence of fixed 0.03 mM L-OPS, in the absence of 18b (teal circles), with 0.37 mM 18b (light blue circles) and 2 mM 18b (dark blue circles). Data were fitted to Eq. 8. All measurements were conducted at 50 nM *Sa*SbnA in HEPES 50 mM pH 7.8 at 25 °C. Error bars represent s.e.m. of two replicates.

The global fitting of the plot at various L-OPS concentrations allowed to extrapolate the inhibition constant K_i for the competitive inhibition of 18b for the free enzyme. On the contrary, the global fitting of the plot at various L-Glu concentrations could not provide a correct estimation of V_{max} and K_i parameters, probably due to interferences by L-Glu substrate inhibition.

Table 14: Parameters extrapolated from the global fitting using the equations for competitive inhibition for the free enzyme in ping-pong enzymatic reactions (Eq. 7,8). The K_M values of both substrates extrapolated in Chapter II (K_M = 0.027 mM L-OPS and K_M = 3.25 mM L-Glu) were added as constrained values in the equation to improve the fitting.

	V_{max}	K_i
L-OPS titration	13.8 ± 0.3 µM/min	0.12 ± 0.01 mM
L-Glu titration (incorrect estimation)	12.5 ± 0.4 µM/min	$0.80 \cdot 10^{-4} \pm 0.01 \cdot 10^{-4}$ mM

Experimental data points were then fitted to the inverse of the equation for competitive inhibition for the free enzyme considering a ping-pong enzymatic reaction when varying substrate A (Eq. 11). In the double reciprocal plot the experimental data collected upon varying substrate B were fitted singularly by a polynomial equation to visualize the trend of each data set. Indeed, the fitted data showed two sets of parallel straight lines which cannot be attributed to any mechanism of inhibition, but it's likely due to interferences by L-Glu substrate inhibition. Nevertheless, the analysis could still confirm the modality of 18b inhibition, hence competitive inhibition for the free enzyme.

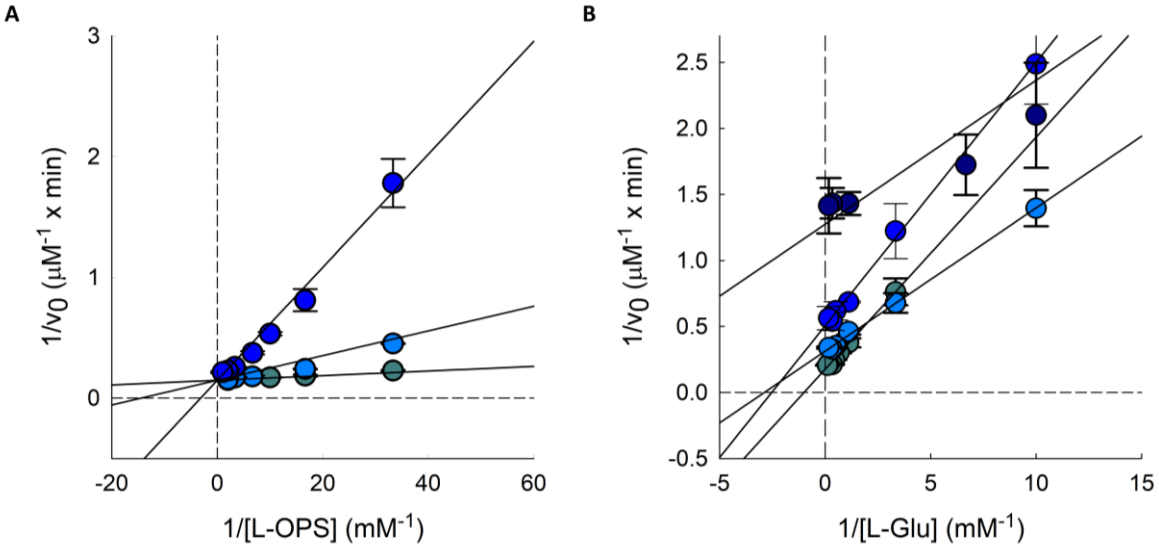

Figure 60: Lineweaver—Burk double-reciprocal plot of *Sa*SbnA initial velocity at varying concentrations of either substrate. (A) Double reciprocal plot of *Sa*SbnA initial velocity in the presence of fixed 3 mM L-Glu as a function of L-OPS concentrations in the absence of 18b (teal circles), with 0.37 mM 18b (light blue circles) and 2 mM 18b (dark blue circles). Data were fitted to Eq. 11 (straight lines). (B) Double

reciprocal plot of *Sa*SbnA initial velocity in the presence of fixed 0.03 mM L-OPS as a function of L-Glu concentration in the absence of 18b (teal circles), with 0.18 mM 18b (light blue circles), 0.37 mM 18b (blue circles) and 2 mM 18b (dark blue circles). Data were fitted singularly by a linear equation (straight lines).

At last, the binding of 18b to *Sa*SbnA was evaluated through the acquisition of fluorescence emission spectra by excitation of the PLP cofactor at 412 nm. The addition of 5 mM 18b to *Sa*SbnA induced a significative reduction in the peak intensity, that could be attributed to a change in the environment polarity around the PLP cofactor (Figure 61).

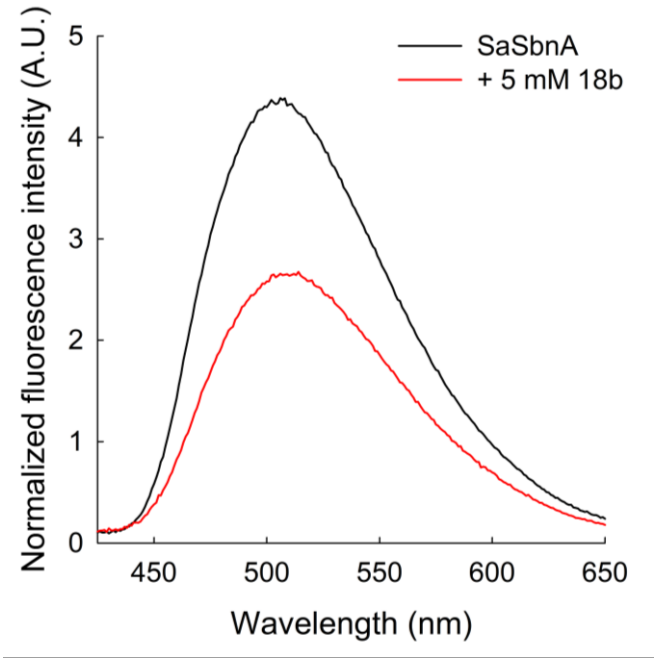

Figure 61: Fluorescence emission spectra of 5 µM *Sa*SbnA, upon excitation at 412 nm of the PLP cofactor, in the absence and in presence of 5 mM 18b. All measurements were carried out in HEPES buffer 200 mM, pH 7.8.

3.7 Evaluation of 2-PhMA mechanism of action

Being 18b the best hit of the screening, the activity of 2-PhMA (Figure 62) was evaluated, since the introduction of a double bond in *Z* configuration restrains the conformational freedom of the molecule and might positively impact on its potency. The isomer in *E* configuration could not be tested because it was not commercially available. The compound was purchased from BLD Pharmatech Co. (Cincinnati, Ohio, USA) and salified in Na Hepes before the screening.

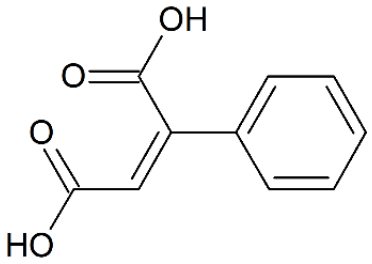

Figure 62: Chemical structure of the 2-PhMA. The structure was drawn by using ACD/ChemSketch (Advanced Chemistry Development Inc., Toronto, Canada).

The dependence of the initial velocity of *Sa*SbnA activity on the concentration of 2-PhMA was determined at 0.03 mM L-OPS and 3 mM L-Glu (Figure 63). 2-PhMA was tested at concentrations between 0.005 and 1 mM. The extrapolated IC_{50} value (see Eq. 4) was 0.037 ± 0.003 mM.

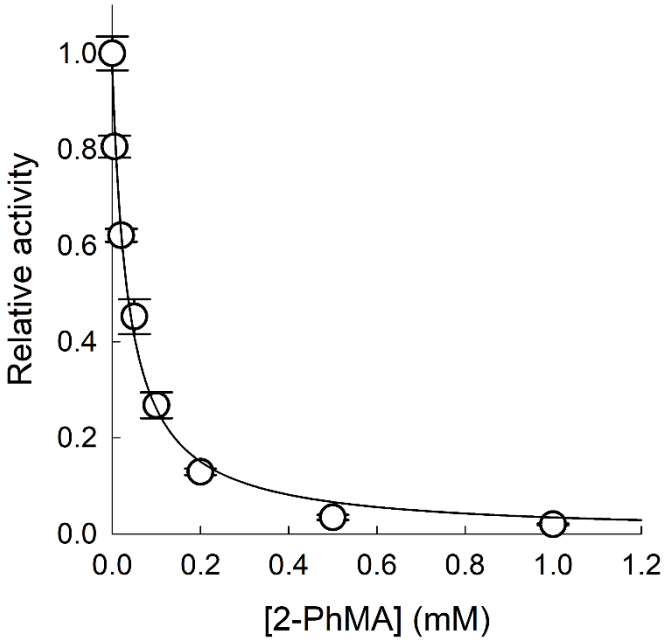

Figure 63: Determination of the IC_{50} for 2-PhMA. Data were fitted to Eq. 4 (solid line) and error bars represent s.e.m. of two replicates.

In the plots reported in Figure 64, the dependence of *Sa*SbnA initial rate was evaluated by titrating either L-OPS at a fixed unsaturated L-Glu concentration (3 mM) (Figure 64A), or by titrating L-Glu at a fixed unsaturated L-OPS concentration (0.03 mM) (Figure 64B). For each of the two plots, the enzyme activity was tested in the absence or presence of 2-PhMA at 0.04 and 0.08 mM. Each plot was then globally fitted by its corresponding equation for competitive inhibition for the free enzyme in ping-pong enzymatic reactions used for the fitting of 18b data set (Eq. 7,8). The equations were chosen based on the best fit to the experimental data. To improve the fitting, the K_M values of both substrates extrapolated in Chapter II (K_M = 0.027 mM L-OPS and K_M = 3.25 mM L-Glu) were added as constrained values in the equation.

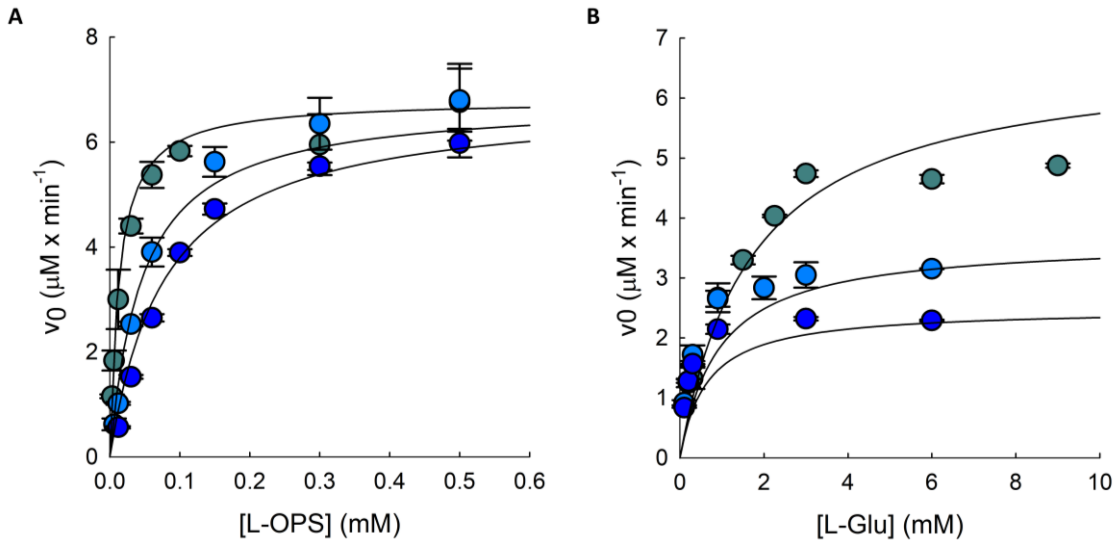

Figure 64: Dependence of *Sa*SbnA initial velocity on varying concentrations of either substrate. (A) *Sa*SbnA initial velocity in the presence of fixed 3 mM L-Glu as a function of L-OPS concentrations in the absence of 2-PhMA (teal circles), with 0.04 mM of 2-PhMA (light blue circles) and 0.08 mM of the 2-PhMA (dark blue circles). Data were fitted to Eq. 7. (B) *Sa*SbnA initial velocity in the presence of fixed 0.03 mM L-OPS as a function of L-Glu concentrations in the absence of 2-PhMA (teal circles), with 0.04 mM of 2-PhMA (light blue circles) and 0.08 mM of 2-PhMA (dark blue circles). Data were fitted to Eq. 8. All measurements were conducted with 50 nM *Sa*SbnA in HEPES 50 mM pH 7.8 at 25 °C. Error bars represent s.e.m. of two replicates.

As for its precursor, the global fitting of the plot at various L-OPS concentrations allowed to extrapolate the inhibition constant K_i for the competitive inhibition of 2-PhMA for the free enzyme (Table 15). On the contrary, also for 2-PhMA, the global fitting of the plot at various L-Glu concentrations could not provide a correct estimation of V_{max} and K_i parameters, probably due to interferences by L-Glu substrate inhibition.

Table 15: Parameters extrapolated from the global fitting using the equations for competitive inhibition for the free enzyme in ping-pong enzymatic reactions (Eq. 7,8). The K_M values of both substrates extrapolated in Chapter II (K_M = 0.027 mM L-OPS and K_M = 3.25 mM L-Glu) were added as constrained values in the equation to improve the fitting.

	V_{max}	**K_i**
L-OPS	14.2 ± 0.3 µM/min	0.016 ± 0.002 mM
L-Glu	12.8 ± 0.6 µM/min	$0.10 \cdot 10^{-4} \pm 0.03 \cdot 10^{-4}$ mM

As for 18b, experimental data points were then fitted to the inverse of the equation for competitive inhibition for the free enzyme considering a ping-pong enzymatic reaction when varying substrate A (Eq. 11). In the double reciprocal plot the experimental data collected upon varying substrate B were fitted singularly by a polynomial equation to visualize the trend of each data set. Indeed, as in the case of 18b, the fitted data showed three straight lines with two different slopes, which cannot be attributed to any mechanism of inhibition, likely due to interferences by L-Glu substrate inhibition. Nevertheless, the analysis could still confirm that the modality of 2-PhMA inhibition was the same as its precursor, hence competitive inhibition for the free enzyme.

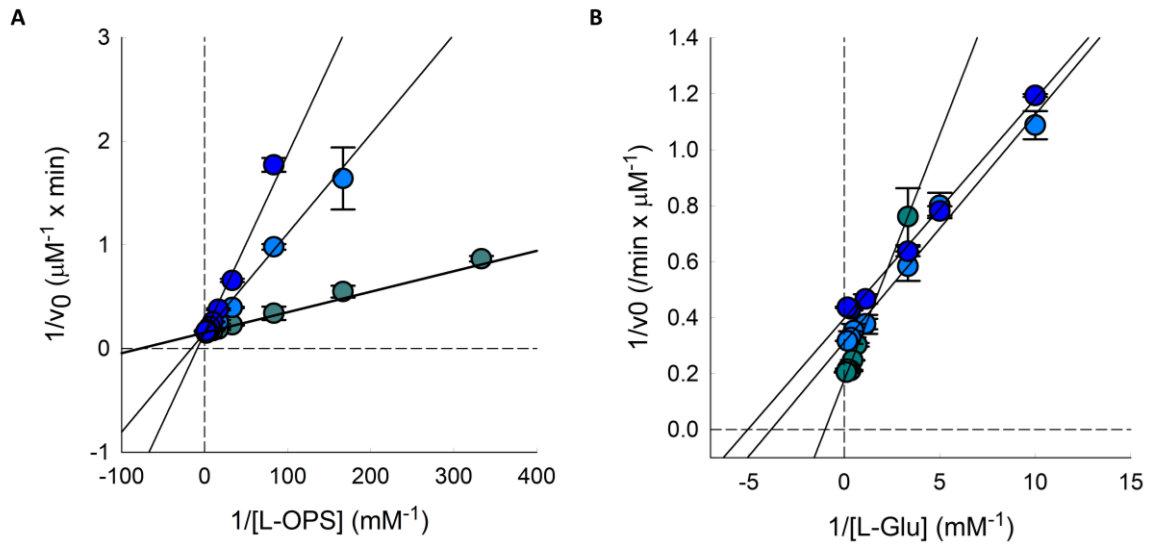

Figure 65: Lineweaver—Burk double-reciprocal plot of *Sa*SbnA initial velocity at varying concentrations of either substrate. (A) Double reciprocal plot of *Sa*SbnA initial velocity in the presence of fixed 3 mM L-Glu as a function of L-OPS concentrations in the absence of 2-PhMA (teal circles), with 0.04 mM of 2-PhMA (light blue circles) and 0.08 mM of 2-PhMA (dark blue circles). Data were fitted to Eq. 11 (straight lines). (B) Double reciprocal plot of *Sa*SbnA initial velocity in the presence of fixed 0.03 mM L-OPS as a function of L-Glu concentrations in the absence of 2-PhMA (teal circles), with 0.04 mM of 2-PhMA (light blue circles) and 0.08 mM of 2-PhMA (dark blue circles). Data were fitted singularly by a polynomial equation (straight lines).

At last, the binding of 2-PhMA to *Sa*SbnA was evaluated in the same conditions as for its precursor. The analysis of the fluorescence emission spectra showed the same spectral change observed for 18b with a significative reduction in the peak intensity. Also in this case, the phenomenon could be attributed to a change in the environment polarity around the PLP cofactor (Figure 66).

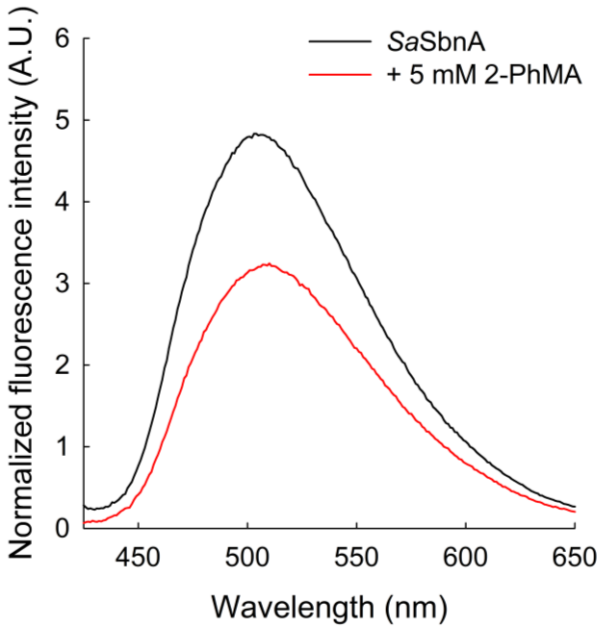

Figure 66: Fluorescence emission spectra of 2-PhMA. *Sa*SbnA spectrum at 5 µM was acquired by excitation at 412 nm of the PLP cofactor in the absence and in presence of 5 mM 2-PhMA. All measurements were carried out in HEPES buffer 200 mM, pH 7.8.

Taken together, the results of the screening of the first set of molecules highlighted the compound 18b as the best hit, with a calculated K_i of 0.12 ± 0.01 mM for the free enzyme. A derivative of the hit compound, 2-PhMA, was identified and characterized, resulting in a more potent inhibitor with a calculated K_i of 0.016 ± 0.002 mM for the free enzyme. The reported results set the ground for further improvements of the molecule, opening the path for a potential modification screening campaign.

Chapter IV – High throughput screening for the identification of SbnA inhibitors

1 Objectives

The screening of potential inhibitors of SbnA activity had never been reported in literature, therefore it represented a novel horizon for the development of new antimicrobials targeting *S. aureus* iron acquisition.

In the previous chapter, an *in silico* structure-based approach was performed by our collaborators at the University of Turin to discriminate and identify molecules that would target SbnA active site, among compounds that had been previously selected to target enzymes homologous to SbnA. Despite the good results obtained with this approach, a structure-based screening limited the identification of inhibitors to the enzyme area that had been chosen for the screening, in this case the active site. Consequently, a whole plethora of other potential inhibitors couldn't be considered in the screening.
For this reason, this chapter reported the results of a pilot screen on two compounds libraries that contain molecules with various properties. The amount and variety of molecules would enable to identify new chemotypes that could be easily modified, as well as inhibitors with good potency, targeting different regions of the enzyme, and possibly having different mechanisms of action.

The chapter reported the results of experiments aimed at producing a construct that would increase the yield of *Sa*SbnA production in order to obtain enough protein within a single batch for the whole HTS. Secondly, the experiments aimed at optimizing the discontinuous assay used in the previous screening to obtain an assay suited for an HTS. At last, the actual pilot HTS was carried out during the PhD secondment at the CEA Paris-Saclay centre (Paris, France) under the supervision of Dr. Jean-Christophe Cintrat. The group of Dr. Cintrat offered its long-lasting expertise in HTS and made available the compounds libraries present in the Laboratory of Bioorganic Chemistry of the CEA Paris-Saclay centre. The screening of these two different libraries allowed to test a total number of 1725 compounds, among which seven hits were identified. A preliminary characterization then allowed to prioritize the hits based on their potency, which could set the ground for further analyses.

2 Materials and methods

HEPES for buffer solutions, sodium chloride, Tris base for buffer solutions, TCEP and the malachite green reagent were purchased as reported in Chapter II and III. All other chemicals were purchased from Merck (Darmstadt, Germany), unless otherwise specified.

For the reagents used during the secondment at CEA Paris-Saclay, the Malachite green oxalate powder, ammonium molybdate tetrahydrate and potassium hydrogen phosphate were purchased from Thermo Scientific (Waltham, Massachusetts, USA). All other chemicals were purchased from Merck (Darmstadt, Germany).

2.1 Protein expression and purification

2.1.1 Growing media

Luria-Bertani (LB) agar plates and LB broth (for culture growth) were prepared as reported in Chapter I and Chapter II, respectively.

2.1.2 *Sa*SbnA expression system for HTS

For HTS, a second expressing system was prepared by subcloning the *sbnA* genetic sequence contained in the pSH21p::TrxA-SbnA plasmid into a pET28a(+) plasmid.

The plasmids pSH21p::TrxA-SbnA and pET28a(+)::IsdBFL were independently transformed through electroporation into *E. coli* XL1blue competent cells, where plasmids were amplified *in vivo* and then extracted and purified by miniprep (Plasmid DNA Extraction mini kit, Fisher Molecular Biology). The pET28a(+)::IsdBFL plasmid was digested first with BamHI in Buffer G (Thermo Fisher Scientific), followed by the separation of the digested linearized product on a 0.8% agarose gel and the extraction of the fragment by the GEL Extraction and PCR Clean Up Kit™ (Fisher Molecular Biology). The eluted product was digested with XhoI in Buffer R (Thermo Fisher Scientific), followed again by the separation of the digested product on a 0.8% agarose gel and the extraction of the vector fragment by the above-reported Kit. The *sbnA* genetic sequence (insert) was amplified through a Polymerase Chain Reaction (PCR) with the PrimeSTAR Max DNA Polymerase contained in the PrimeSTAR Max Premix by In-Fusion® Snap Assembly (Takara Bio Inc, San Jose, CA, USA), following the manufacturer's protocol. The amplification was performed by using primers purchased from Aurogene S.r.l. that had been previously designed with the TakaraBio online tool (https://www.takarabio.com/learning-centers/cloning/primer-design-and-other-tools).

Table 16: PrimeStar kit (Takara Bio) PCR protocol.

PCR mix		
	Final concentration	**Volumes**
PrimerSTAR Premix 2X	1X	12.5 µL
Primer forward GCGGCAGCCATATGGGATCCACCAGTGAAAATCTGT	10 µM	0.75 µL
Primer reverse GGTGGTGGTGCTCGAGTTATTACTCGCTTTTAACACCCTG	10 µM	0.75 µL
pSH21p::TrxA-SbnA	1 ng	1 µL
DNAse free water		up to 25 µL
PCR Program (35 cycles)		
	Temperature	**Time**
Denaturation	98 °C	10 seconds
Annealing	55 °C	5 seconds
Extention	72 °C	6 seconds

The amplified product was then purified using NucleoSpin™ (Macherey Nagel Bioanalysis, Düren, Germany) and the cloning reaction was set up following the manufacturer's protocol by using In-Fusion® Snap Assembly (Takara Bio Inc, San Jose, CA, USA).

Table 17: Ligation reaction using the In-Fusion® Snap Assembly protocol (Takara Bio Inc, San Jose, CA, USA).

Cloning reaction mix	
	Final concentration
Master Mix 5X	1X
Amplified product (insert)	28 ng
BamHI-XhoI digested pET28a(+) (vector)	70 ng
DNAse free water	up to 5 µL

The In-Fusion® Snap Assembly cloning reaction was incubated at 50 °C for 15 minutes and then placed on ice. Subsequently, 2.5 µL of the reaction were transformed by heat shock InFusion® protocol into Stellar Competent Cells (Takara Bio Inc, San Jose, CA, USA), as reported by the manufacturer's protocol. The overnight grown transformed colonies were checked by colony PCR using Phusion Hot Start II High-Fidelity DNA Polymerase (Thermo Fisher Scientific), with the

concomitant preparation of the master plate. To confirm a correct sequence insertion *in-house* available primers were used that attach on the pET28a(+) vector at the N- and C-terminal of the insertion region.

Table 18: Colony PCR reaction. Abbreviations: dNTP: deoxyribonucleotide triphosphate

PCR mix		
	Final concentration	**Volumes**
Buffer GC 5X	1X	2 µL
dNTPs	0.2 mM	0.2 µL
Phusion DNA Polymerase		0.1 µL
Primer pET plus AAATTAATACGACTCACTATAGG	0.5 µM	0.5 µL
Primer pET minus GATATAGTTCCTCCTTTCAGC	0.5 µM	0.5 µL
DMSO	1 ng	0.3 µL
DNAse free water		up to 10 µL
PCR Program		
	Temperature	**Time**
Initial denaturation	94 °C	5 min
Denaturation	94 °C	30 sec
Annealing	49 °C	1 min
Extention	72 °C	1 min 10 sec
Final extention	72 °C	7 min
	4 °C	∞

Three of the colonies that resulted positive by Colony PCR were selected from the master plate and inoculated in 10 mL of LB broth supplemented with 50 µg/mL kanamycin and grown at 37 °C overnight, under 250 RPM agitation. The final pET28a(+)::SbnA plasmid was thus purified by miniprep (Plasmid DNA Extraction mini kit, Fisher Molecular Biology) and the sequence of the final construct was confirmed by sequencing reaction (Microsynth Seqlab GmbH). The sequenced expression plasmid was electroporated into *E. coli* BL21(DE3) cells for subsequent protein over-expression and purification.

2.1.3 Protein over-expression

*Sa*SbnA over-expression was performed in *E. coli* BL21 (DE3) cells, that had been transformed with the pET28a:SbnA plasmid. The transformed cells were plated on LB agar supplemented with 50 µg/mL kanamycin and grown at 37 °C overnight. A single colony was selected and inoculated in 10 mL of LB broth supplemented with 50 µg/mL kanamycin and grown at 37 °C overnight, under 250 RPM agitation. The overnight grown culture was diluted 1:100 in LB medium supplemented with 50 µg/mL kanamycin. The cells were grown at 37 °C, under 250 RPM agitation, until the midlog phase (OD600 around 0.5 – 0.6) was reached, which normally took 2 hours. Cells were then induced for 20 hours at 20 °C by the addition of 1 mM IPTG. Cells were collected from the broth by centrifugation at 5,000 RPM for 10 minutes, then they were washed once with phosphate buffered saline (PBS) solution and ultimately frozen at -80 °C in aliquots coming from 1 L of culture.

2.1.4 Protein purification

The thawed pellet was resuspended and incubated in lysis buffer (50 mM Tris, 100 mM NaCl, 1 mM TCEP, 0.2 mM PLP, 1 mg/mL lysozyme, 0.2 mM PMSF, 0.2 mM benzamidine and 1.5 µM pepstatin pH 8) for 1 hour at 4 °C. Subsequently, 5 cycles of sonication 20 seconds long (1s ON/1s OFF) were performed to completely break down cells. Centrifugation at 18,000 × g for 1 hour at 4 °C was used to separate the soluble from the non-soluble components. Immobilized Metal Affinity Chromatography (IMAC) on a Talon SuperflowTM resin (Cytiva, Marlborough, MA, USA) was performed to purify the N-terminal His6-tagged *Sa*SbnA. The poly-histidine tag attached to the recombinant protein allowed the purification through the preferential interaction with the functionalized cobalt-based IMAC resin. Two washing steps were performed at 5 mM and 10 mM imidazole added to the Tris buffer (50 mM Tris, 100 mM NaCl, pH 8 at 4°C), also supplemented with 1 mM TCEP, in order to remove potential aspecific interactions with the cobalt resin of other histidine-rich proteins present in the crude extract. *Sa*SbnA was then eluted with the elution buffer (50 mM Tris pH 8, 100 mM NaCl, 250 mM imidazole, pH 8 at 4 °C), supplemented with 1 mM TCEP, which contained a higher imidazole concentration that allowed protein purification. The eluted fractions were pooled together and supplemented with 5-molar PLP and 1 mM EDTA before dialyzing the overall solution overnight at 4 °C against Tris buffer (50 mM Tris, 100 mM NaCl, pH 8 at 4 °C) to remove imidazole. The following day, the solution was concentrated up to 4.36 mg/mL, aliquoted and finally stored at −80 °C.

2.2 UV-Visible absorption spectroscopy

Absorption spectra were acquired in the range 250-600 nm in a quartz microcuvette of 1 cm path length using a Cary4000 spectrophotometer (Agilent Technologies, Santa Clara, CA, USA). Measurements were collected in 50 mM HEPES buffer pH 7.8 (25 °C) for protein characterization. *Sa*SbnA concentration was estimated by exploiting the extinction coefficient calculated by the ProtParam server ε_{280} = 34,380 M^{-1} cm^{-1}.

Absorption spectra of compounds were acquired in the range 250-600 nm in a quartz microcuvette of 1 cm path length using a Jasco V-750 spectrophotometer. Compounds were tested at the highest concentration possible up to 200 µM, in order not to show a saturating absorbance signal.

2.3 Optimization of the discontinuous assay for wide HTS

The discontinuous assay optimized in Chapter III was implemented for HTS of compound libraries. In-house preparation of the malachite green reagent was introduced to implement the assay sensitivity and reduce the costs of the analysis.

In-house preparation of malachite green reagent

The malachite green dye mixture was prepared as described by Pegan et al, 2010 [435]. 41 mL of 3 M sulfuric acid were freshly prepared by diluting concentrated sulfuric acid and let cool down to room temperature. The solution was then used to solubilize 50 mg of malachite green dye powder, and the final preparation was stored at room temperature in the dark. Prior to the assay, one volume of malachite green dye was mixed with 1/4 volume of 7.5% ammonium molybdate and 1/50 volume of 11% (v/v) Tween 20. One volume of this mixture was added to four volumes of phosphate-containing solution for signal development.

2.3.1 Discontinuous assay optimization

In all experiments, the absorbance of the complex between the malachite green reagent and orthophosphate was measured at 620 nm using a UV-transparent, 384-well microplate (Greiner UV-STAR® plate – 781801) and a TECAN Spark® 10M microplate reader.

The comparison between the commercial malachite green reagent (Santa Cruz Biotechnology Inc, Dallas, TX, USA, cat n. 569-64-2) and the in-house-prepared solution was performed at different phosphate concentrations ranging from 0 to 50 µM. Even if the total reaction volume was the same, the dyes and the phosphate-containing solutions were mixed in different proportions. Indeed, a phosphate-containing solution to dye ratio of 1:5 was used for the commercial reagent while a 4:1 ratio was used for the in-house prepared one [435,436]. Measurements were collected at different time intervals (15, 30, 60, 90 and 120 minutes) to check the stability of the absorbance at 620 nm of the dye-phosphate complex.

The optimization of the assay was carried out at 0.03 mM L-OPS and 3 mM L-Glu and using the in-house prepared malachite green reagent.

The dependence of phosphate production on *Sa*SbnA concentration was followed at 17.5, 35 and 50 nM *Sa*SbnA at different time intervals up to 15 minutes. The effect of 1% DMSO ad 1 mM TCEP on phosphate production were independently evaluated at 35 nM *Sa*SbnA at different time intervals up to 15 minutes.

2.3.2 Optimized discontinuous assay for the HTS

The discontinuous assay for HTS was performed in 80 mM HEPES buffer pH 7.8 in a 96-well half-area microplate (Greiner Bio-One 675101 PS). L-OPS and L-Glu were used at 0.03 mM and 3 mM, respectively. All the measurements were performed at room temperature and the addition of 35 nM *Sa*SbnA triggered the reactions. The compounds were tested at 50 µM concentration, the commercial compound library also at 10 µM. 2-PhMA at 0.7 mM was exploited as a positive control, while the reaction without any compound was exploited as negative control (reference for 100% of phosphate production). Each library compound was tested in a single reaction for the control without *Sa*SbnA (time 0), while in duplicate for the reactions triggered by the enzyme. Each reaction

was stopped after 5 minutes by addition of 28.8 µL of malachite green reagent and the samples were then incubated for 40 minutes at room temperature in the dark. The absorbance of the complex between the malachite green reagent and inorganic phosphate was measured at 620 nm using a SpectraMax M5^e microplate reader (Molecular Devices, San Jose, CA). A standard curve was obtained from 0 to 40 µM phosphate and used to calculate the amount of phosphate produced for each reaction. The phosphate produced in the presence of compounds was expressed as percentage of the activity relative to the negative control. All experiments were performed in duplicate. In order to assess the robustness of the assay, different statistical parameters can be used to evaluate the statistical effect size. The main analyses were based on SSMD or Z-factor. The Z' factor for each experiment was calculated using Eq. 12.

Eq. 12: $$Z' = 1 - \frac{(3 \cdot Std_{\ Pos\ Ctrl}) + (3 \cdot Std_{Neg\ Ctrl})}{|Mean_{\ Pos\ Ctrl} - Mean_{\ Neg\ Ctrl}|}$$

where the negative and positive control referred to the phosphate production in the absence and in the presence of 2-PhMA at 0.7 mM, respectively.
Indeed, the Z' factor is a value that considers the use of appropriate positive and negative controls and the variability of the assay, representing altogether the reliability of the HTS results. This parameter can assume a value between 0 and 1, with a Z' factor equal to one representing an ideal assay. The Z' factor range with the corresponding HTS evaluation is reported in Table 19.

Table 19: Z' factor values and relative evaluation of the reliability of the HTS assay.

Z' = 1	Ideal assay
1 > Z' ≥ 0.5	Good assay
0.5 > Z' > 0	Not good assay for HTS. Replicates will be required

2.4 HTS of compound libraries

The two types of compound libraries tested were made available by the laboratory of Dr. Cintrat at the CEA Paris-Saclay in Paris (France). The first library, called Drug and Related library, consisted of 160 commercial molecules, many of which are already known drugs (approved, withdrawn or investigational) or bioactive compounds/probes. The second library consisted of 1565 compounds that had all been synthesized in the Service de Chimie Bioorganique et de Marquage at CEA Paris-Saclay from different research programs. This patrimonial library covers a large chemical space and offers very unique chemical scaffolds. The compounds were stocked in DMSO 100% at either 10 or 20 mM concentration and intermediate dilutions were prepared in 80 mM HEPES buffer pH 7.8. The libraries were tested by exploiting the discontinuous assay performed in 80 mM HEPES buffer pH 7.8 in a 96-well half-area microplate Greiner Bio-One 675101 PS plates, lot E230537H. Multichannel pipettes were exploited during the whole HTS for dispensing the reaction mixture, the enzyme and the malachite green reagent. L-OPS and L-Glu were used at 0.03 mM and 3 mM, respectively. All the measurements were performed at room temperature and the addition of 35 nM *Sa*SbnA triggered the reactions. Each reaction was stopped after 5 minutes by the addition of 28.8 µL of malachite

green reagent and the samples were then incubated for 40 minutes at room temperature in the dark. The absorbance of the complex between the malachite green reagent and inorganic phosphate was measured at 620 nm using a SpectraMax M5^e microplate reader (Molecular Devices, San Jose, CA). The results were reported as percentage of inhibition of the *Sa*SbnA-catalysed reaction in the presence of the tested compounds compared to the non-inhibited reference reaction.

The compounds that were identified and confirmed as active inhibitors during the HTS were solubilized at 20 mM in DMSO 100% from their respective stocked powder and the pH of the 0.2 mM solutions in 80 mM HEPES pH 7.8 was checked.

The dependence of the initial velocity of *Sa*SbnA activity on the inhibitor concentration was determined at 0.03 mM L-OPS and 3 mM L-Glu by the optimized discontinuous assay. The IC_{50} value for each compound was calculated by plotting the relative activities as a function of the inhibitor concentration and by fitting the data to a hyperbolic equation either with (eq. 4) or a vertical off-set (eq. 13).

Eq. 13: $$\frac{v_i}{v_0} = y_0 + \frac{a \cdot IC_{50}^*}{IC_{50}^* + [I]}$$

where the IC_{50} indicates the inhibitor concentration that exerts 50% inhibition, while the IC_{50}* indicates the inhibitor concentration at which half the inhibitory effect occurred.

3 Results and discussion

3.1 *Sa*SbnA protein over-expression and purification

Recombinant *Sa*SbnA was over-expressed in LB medium using *E. coli* BL21 (DE3) cells transformed with the pET28a(+)::*Sa*SbnA plasmid. The protein was then purified by IMAC and the final yield of purification was about 27 mg per liter of bacterial culture, with a purity of more than 90% (Figure 67).

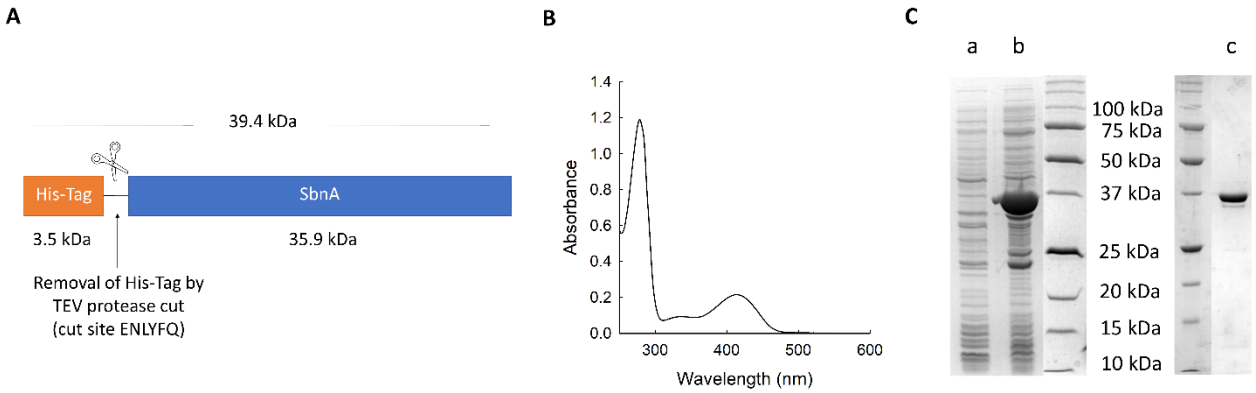

Figure 67: Production of *Sa*SbnA. (A) Schematic representation of the SbnA construct in pET28a(+)::SbnA plasmid. (B) UV-Vis absorption spectrum of the purified *Sa*SbnA stock solution. (C) SDS-PAGE analysis of *Sa*SbnA over-expression and purification, with (a) uninduced cells, (b) induced cells, (c) purified *Sa*SbnA.

The UV-visible spectrum of purified *Sa*SbnA (Figure 67B) showed the three peaks at 278 nm, 330 and 412 nm, already observed for the *Sa*SbnA preparation obtained using the pSH21p::TrxA-SbnA construct reported in Chapter II . The ratio between the absorbance of aromatic residues at 278 nm and of the PLP cofactor at 412 nm was calculated to be 5.5, highlighting a slightly lower value compared to the previous preparation (ratio of 7.3) that could indicate a higher purity of this batch. The spectrum thus confirmed that the protein correctly interacts with the PLP cofactor. Moreover, the final yield allowed to perform all the HTS experiments (optimization and screening) with one single protein batch.

3.2 Optimization of the discontinuous assay for HTS of compound libraries

The exploitation of the discontinuous assay for HTS of compound libraries needed the implementation of some aspects of the assay to increase at maximum the sensitivity while reducing at minimum the variability.

An in-house-prepared malachite green reagent was used for the discontinuous assay. Initially, phosphate standard curves developed with either the commercial or in-house reagents were compared for sensitivity and stability of the signal at 620 nm for up to 120 minutes (Figure 68). The results highlighted that both reagents provide a stable signal between 30 and 120 minutes, but the in-house solution showed a significantly better sensitivity. Indeed, the slope of the standard curve was 0.0120 ± 0.0002 A620/µM for the commercial reagent and 0.0374 ± 0.0005 A620/µM for the in-

house prepared one. Based on the results, the home-made dye was exploited for all further experiments.

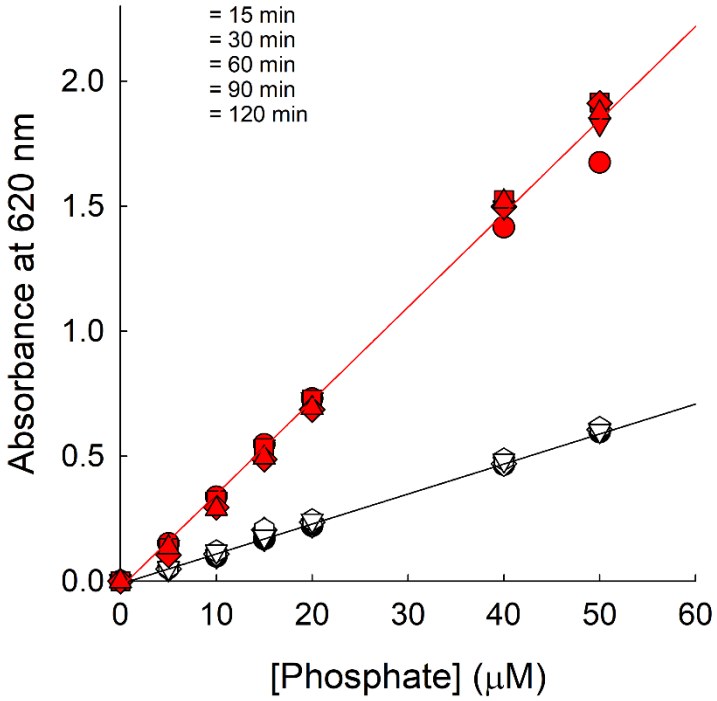

Figure 68: Comparison of phosphate standard curves using commercial (black) and in-house-prepared (red) malachite green reagents. The dependence of the absorbance at 620 nm on phosphate concentration was followed at fixed time intervals (15, 30, 60, 90 and 120 minutes). The lines through data points represent the fitting to a linear equation with slope 0.0120 ± 0.0002 for the commercial reagent and 0.0374 ± 0.0005 for the in-house reagent.

The effect of different *Sa*SbnA concentrations on the phosphate production kinetics and on the duration of the linear (pre-steady state) phase was assessed using three different concentrations. The reactions were followed for 15 minutes at sub-saturating concentrations of both substrates by the discontinuous assay and kinetics at all concentrations were found to be linear up to 5 minutes (Fig. 69A). The dependence of the initial velocity on *Sa*SbnA concentration allowed to assess that concentrations lower than 35 nM are not recommended (Fig. 69B).

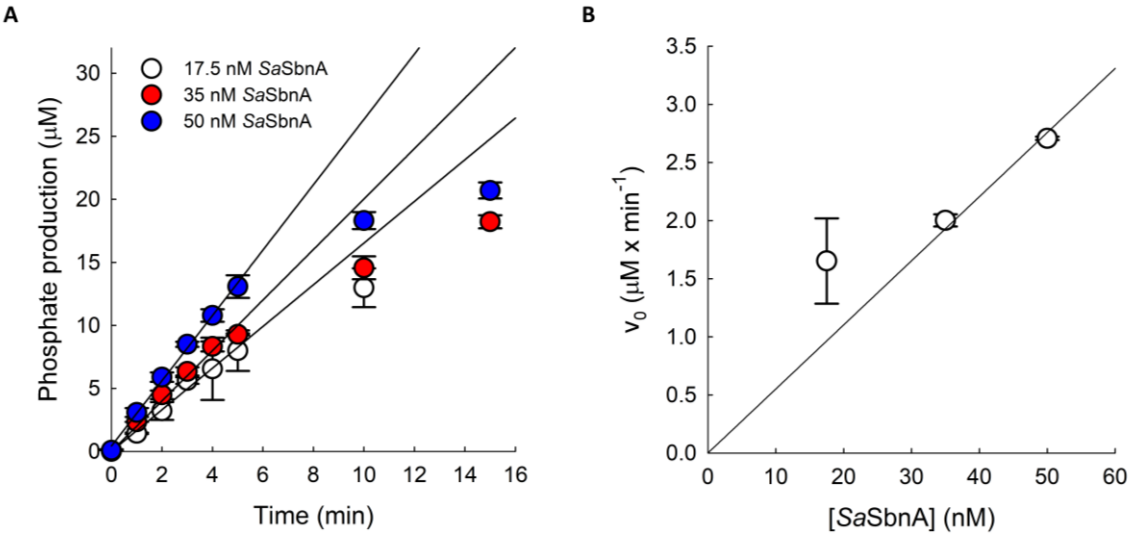

Figure 69: Evaluation of the effect of SbnA concentration on the discontinuous assay performance using the *in-house* malachite green reagent. (A) Dependence of phosphate production kinetics on *Sa*SbnA concentration performed at 0.03 mM L-OPS and 3 mM L-Glu. Experimental data were fitted to a linear equation considering phosphate production up to 5 minutes. (B) Dependence of the reaction initial velocity on *Sa*SbnA concentration. v_0 values were extrapolated from the fitting of experimental data in panel A. Error bars represented the s.e.m. of two replicates.

The effect of either 1% DMSO or 1 mM TCEP on *Sa*SbnA activity was evaluated to complete the assay optimization (Figure 70). Notably, the first condition was tested because all the screened compounds were solubilized in DMSO and the maximal compound concentration analysed in the assay would result in a final 1% DMSO in the reaction mixture. No significant effect of DMSO was observed (Fig. 70A), therefore DMSO addition was avoided in the reference mixture. Likewise, the presence of 1 mM TCEP, that was used in the continuous assay, did not affect phosphate production, therefore it was decided to avoid its use in the assay to exclude any potential artifacts arising, e.g., from redox cycling compounds.

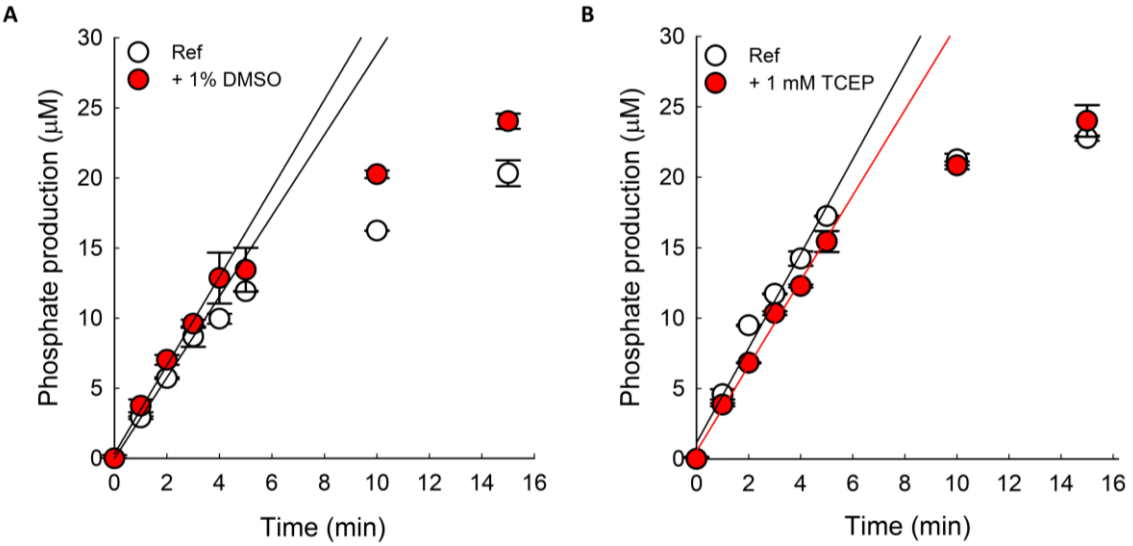

Figure 70: Evaluation of the effect of 1% DMSO and 1 mM TCEP on phosphate production followed at 0.03 mM L-OPS and 3 mM L-Glu, using the in-house-prepared malachite green solution. Experimental data were fitted to a linear equation considering phosphate production up to 5 minutes. Error bars

represented the s.e.m. of two replicates. (A) Phosphate production was followed at 35 nM *Sa*SbnA in the absence and in the presence of 1% DMSO. (B) Phosphate production was followed at 35 nM *Sa*SbnA in the absence and in the presence of 1 mM TCEP.

3.3 HTS of compound libraries

Two types of compound libraries were available and tested in the laboratory of Dr. Cintrat at the CEA Paris-Saclay centre. The first library, called Drug and Related library, consisted of 160 commercial molecules, many of which are already known drugs (approved, withdrawn or investigational) or bioactive compounds/probes that were purchased by the CEA Paris-Saclay centre and stocked in 20 mM DMSO. The library was tested by the optimized HTS discontinuous assay at 50 and 10 µM to provide an immediate evaluation of the dependence on compound concentration of *Sa*SbnA activity thus allowing a better identification of potential false positives. The molecules that inhibited the activity by more than 50 ± 5 % at 50 µM and 10 µM were selected. Five molecules presented an inhibitory effect at 50 µM, while only one molecule confirmed the inhibitory effect at 10 µM (Figure 71). At both concentrations of this latter hit compound, the measured absorbance value of the control reaction (without enzyme addition) was comparable to the one measured for the *Sa*SbnA-catalyzed reaction, therefore the result was considered not reliable, and the compound was excluded from further analysis. Among the four compounds active only at 50 µM, one molecule resulted a false positive since the duplicate didn't provide the same results, while the other three compounds were tested at different concentrations to confirm the results.

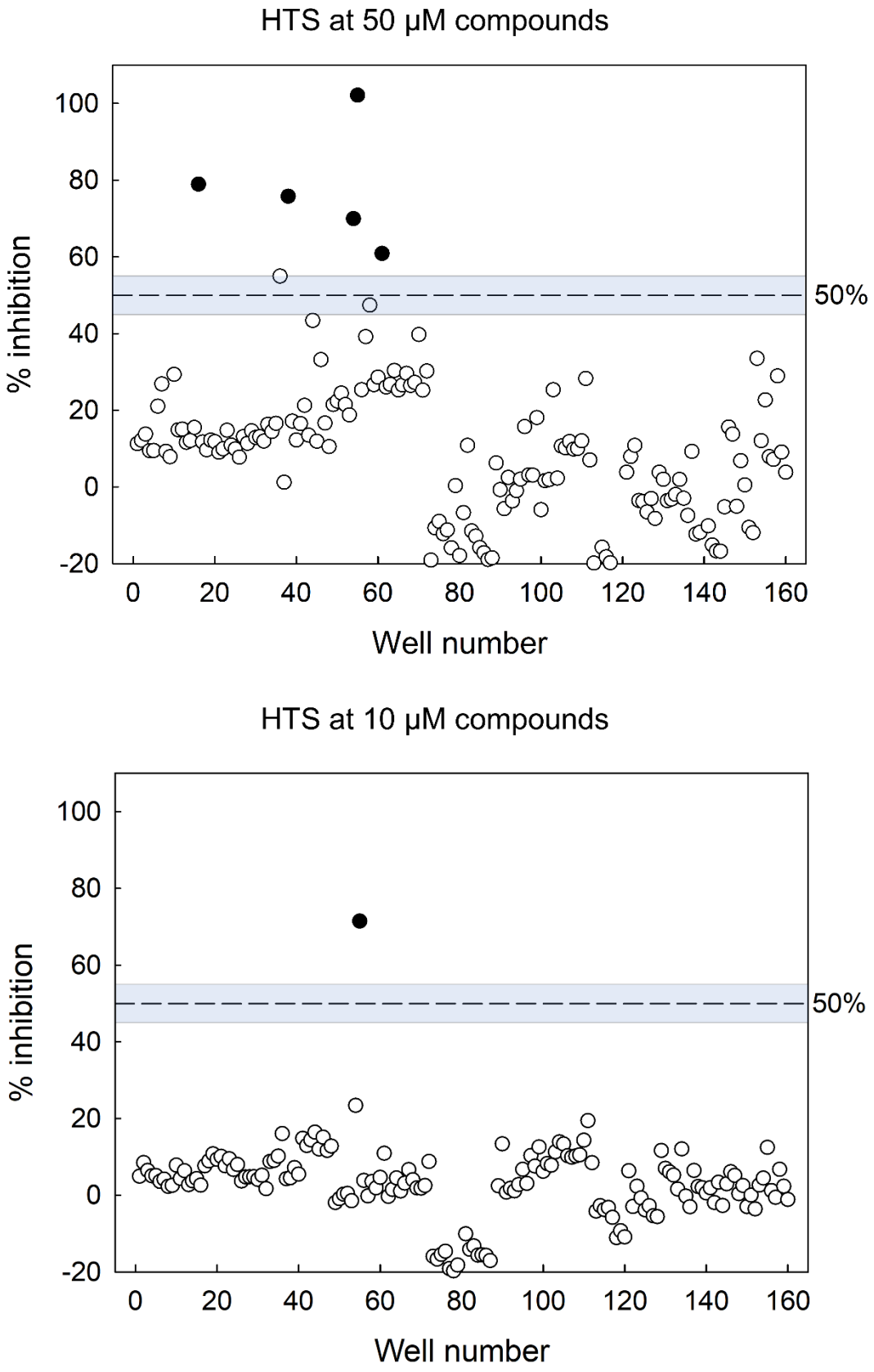

Figure 71: HTS of compounds within the Drug and related library. All measurements were performed in 80 mM HEPES pH 7.8. The compounds were tested at 50 and 10 µM. All the data reported represented the mean of a duplicate experiment.

The dependence of the initial velocity of *Sa*SbnA activity on three concentrations of each active compound was determined at 0.03 mM L-OPS and 3 mM L-Glu (Figure 72). The experimental data were fitted with Eq. 4, except for the hit compound 1 for which data followed a different trend and couldn't be fitted. An IC_{50} value of 21.81 ± 1.63 µM and 38.41 ± 1.52 µM was extrapolated for compound 2 and 3, respectively. Since the hit 3 presented an IC_{50} value comparable to the reference compound (2-PhMA), just compound 2 was selected for further characterization.

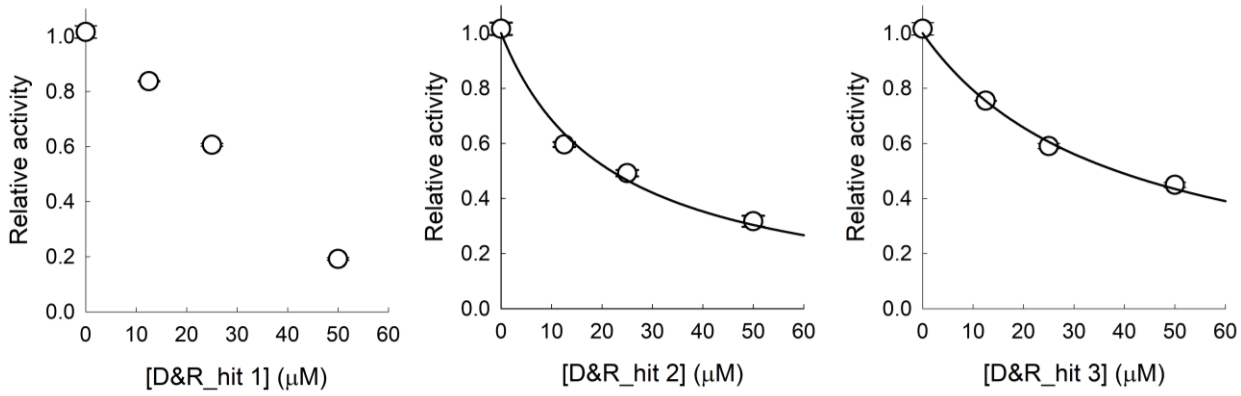

Figure 72: Determination of the IC_{50} value for the inhibitors of *Sa*SbnA-catalysed reaction selected by screening at 50 µM, belonging to the Drug and Related commercial library. Data were fitted to equation 4 with IC_{50} of 21.81 ± 1.63 µM (hit 2) and 38.41 ± 1.52 µM (hit 3). Error bars represented s.e.m. of two replicates.

Similarly, the same HTS was performed on the second library, available at the CEA Paris-Saclay centre, called SCBM library. This library consisted of 1565 compounds that had all been synthesized in the Service de Chimie Bioorganique et de Marquage at CEA Paris-Saclay from different research programs. This patrimonial library covers a large chemical space and offers very unique chemical scaffolds. In this case, due to the larger number of compounds of this library, the screen was performed only at one concentration (50 µM) of each compound. 16 molecules presented an inhibitory effect greater than 50 ± 5% at 50 µM (Figure 73).

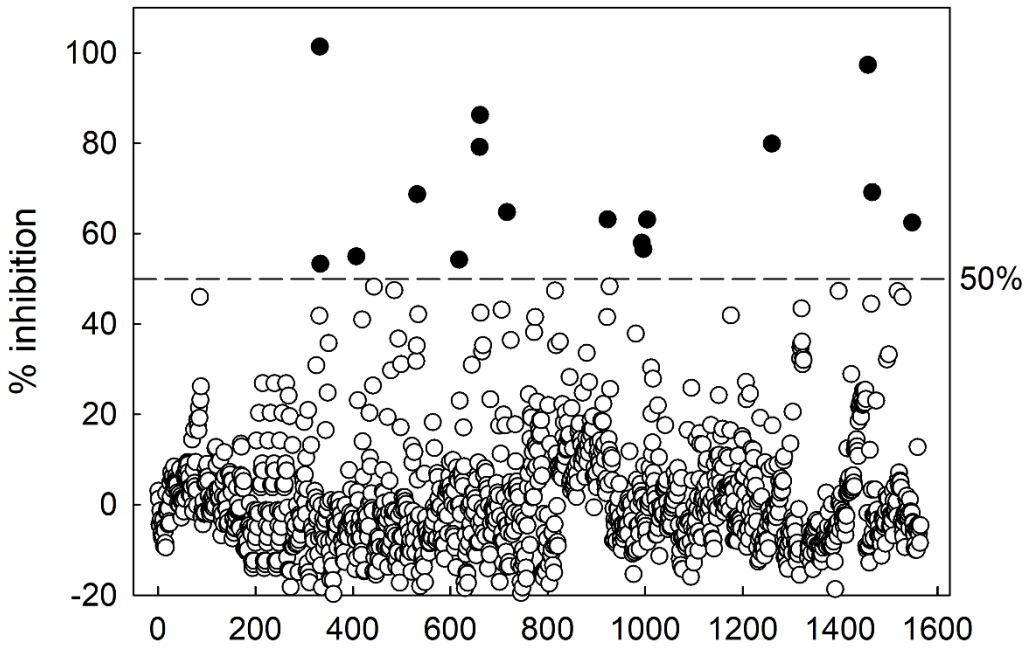

Figure 73: HTS of the synthetic compound library (SCBM library). All measurements were performed in 80 mM HEPES pH 7.8. The compounds were tested at 50 µM. All the data reported represented the mean of a duplicate experiment.

The whole HTS on both the commercial and the synthetic libraries was validated by calculating the Z' factor for each plate analysed. To assess the robustness of an assay, different statistical parameters can actually be used to evaluate the statistical effect size. The main analyses are based on Strictly Standardized Mean Difference (SSMD) or Z-factor values, with the threshold of the latter being stricter than the SSMD threshold. For this reason, the assessment of the screening quality relied on the calculation of the Z-factor for each independent experiment.

The Z' factor values associated to the screen were reported in Figure 74, highlighting the good quality of the assay and thus validating the whole screening and making it amenable to a future automated HTS.

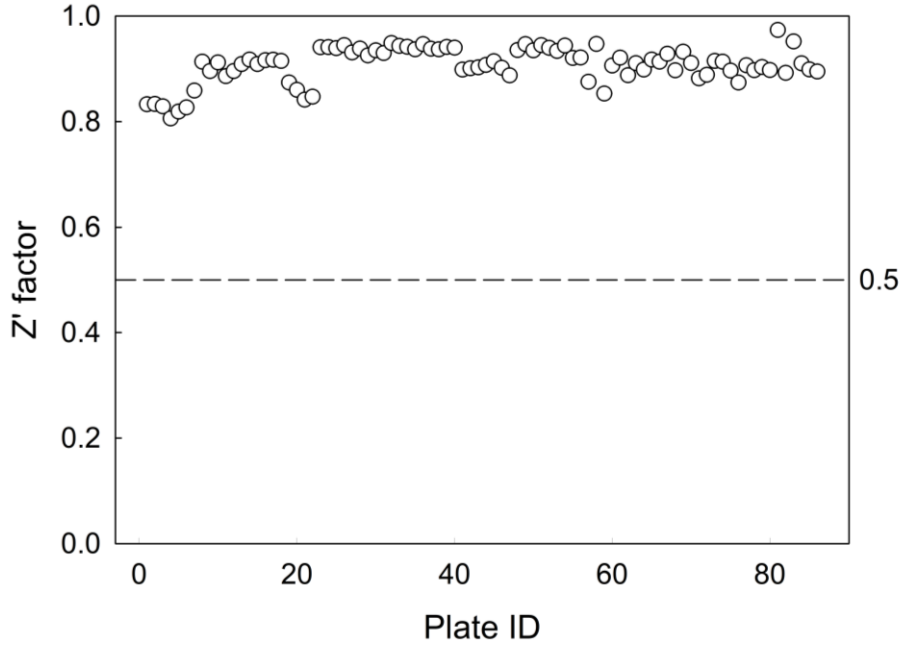

Figure 74: HTS data quality control by Z' factor evaluation of the 86 plates analysed in the screening.

The sixteen active compounds identified in the screen of the SCBM were tested again under the same conditions to confirm their inhibitory effect at 50 µM (Figure 75). Among the sixteen active molecules, only six compounds confirmed an inhibitory effect greater than 50 ± 5%, with the others resulting as false positive hits in the first screening. The compound LCB-7-G2, whose activity fell in the threshold for selection, was re-tested at 25 and 12.5 µM (data not shown). The results revealed that LCB-7-G2 has a similar potency with respect to the reference compound (2-PhMA), therefore it was not further investigated.

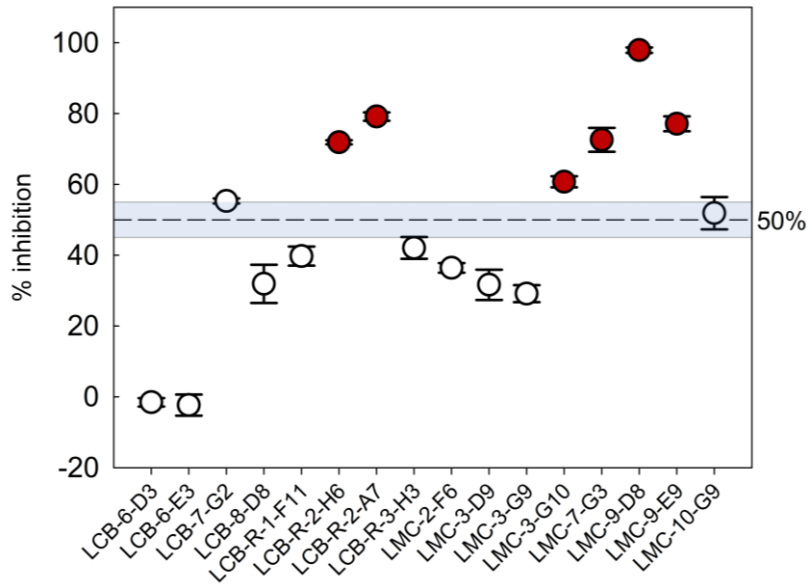

Figure 75: Re-screening of the positive hits identified in the primary screening of the SCBM library. The molecules were tested at 50 µM in the HTS assay conditions.

To summarize the HTS results (Table 20), a total of seven compounds was identified by the HTS at the CEA Paris-Saclay centre, with one compound coming from the commercial Drug and Related library and 6 compounds coming from the SCBM library of synthetic molecules.

Table 20: Summary of the HTS results.

	Drug and related library	**SCBM library**
Number of compounds tested	160	1565
Number of library plates	2	21
Primary active threshold	50 ± 5% inhibitory activity	50 ± 5% inhibitory activity
Number of primary actives	5	16
Number of confirmed actives	1	6

3.4 Characterization of the hit compounds

3.4.1 Preliminary characterization of the hits at CEA Paris-Saclay

All the compounds that were identified as active inhibitors during the HTS were freshly solubilized in DMSO 100% from their respective stocked powder at CEA Paris-Saclay for a preliminary characterization. First, a measure of the pH of solutions at 200 µM of each active compound in 80 mM HEPES pH 7.8 was performed to confirm that the addition of compounds at the tested concentration wouldn't change the pH of the working solution. This analysis was performed to confirm that the inhibitory effect wouldn't derive from the inactivation of the enzyme due to a change in the pH of the solution.

Afterwards, absorbance spectra of the confirmed hit compounds were acquired to characterize them spectroscopically and evaluate any potential interference at the wavelengths used for the discontinuous (620 nm) and continuous (360 nm) enzymatic assays and for the binding assay in fluorescence (412 nm) (Figure 76). No signal interferences were observed at 620 nm, while most of the compounds absorbed at 360 and/or 412 nm. For this reason, further analyses were performed initially using the discontinuous assay.

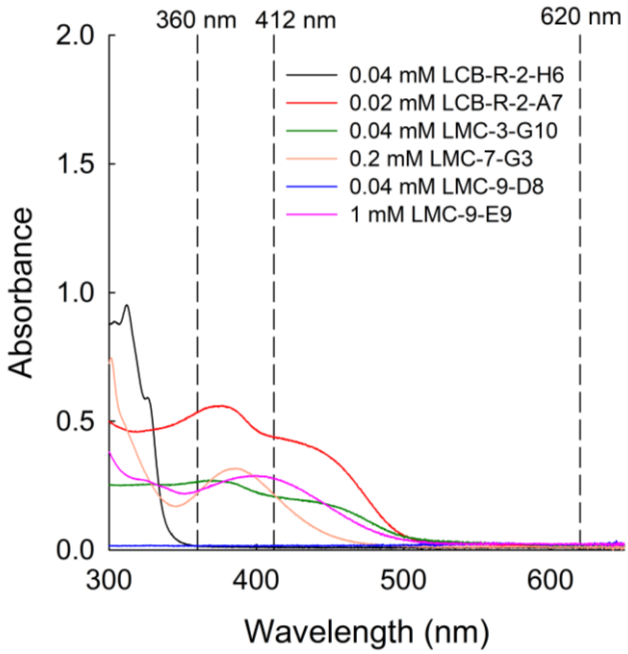

Figure 76: Absorbance spectra of confirmed hit compounds recorded in the 300-650 nm range with a 1 cm quartz cuvette. The compounds were tested at different concentrations to keep the absorbance below 2 OD. The dotted lines represent the three wavelengths of the continuous (360 nm) and the discontinuous (620 nm) activity assays, and for the binding assay in fluorescence (412 nm).

The dependence of the initial velocity of *Sa*SbnA on the concentration of each active compound was determined at 0.03 mM L-OPS and 3 mM L-Glu (data not shown). All compounds gave results in line with the screening results, except for the D&R compound 2 and LMC-3-G10 which reported extrapolated IC_{50} values higher than the expected by comparison with the HTS results. The stocked powders of each hit compound were then shipped to the University of Parma for further characterization.

3.4.2 Characterization of the hits

All the compounds that were identified as active inhibitors during the HTS and preliminary characterized at CEA Paris-Saclay were freshly solubilized in D_6-DMSO from their respective stocked powder.

The dependence of the initial velocity of *Sa*SbnA activity on the concentration of each active compound was determined at 0.03 mM L-OPS and 3 mM L-Glu. Since some compounds are unable to completely abolish enzyme activity even at high concentrations, the dependences were fitted to both Eq. 4 and Eq. 13, this last one incorporating a vertical off-set. The vertical off-set might be due to either low solubility of the compounds at high concentrations or partial inhibition. The fitting parameters obtained with the equation that gave the best R^2 and the lower error regarding the IC_{50} calculated value are reported in Table 21.

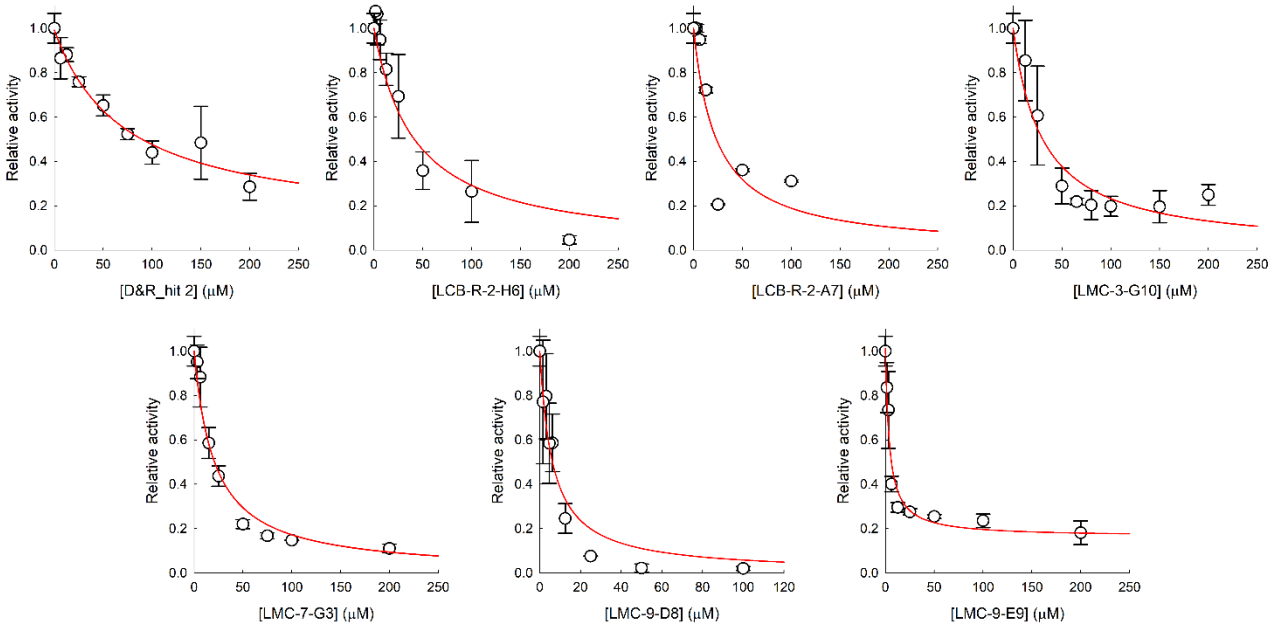

Figure 77: Determination of the IC_{50} value for the confirmed inhibitors of *Sa*SbnA-catalysed reaction. Lines through data points are the fit to either Eq. 4 or 13 (Table 21). Error bars represented s.e.m. of two replicates.

Table 21: Summary of the calculated IC_{50} values for the identified inhibitors of *Sa*SbnA activity by the discontinuous assay.

Compound ID	Fitting equation	IC_{50} value
D&R hit 2	Eq. 4	90.10 ± 8.04 µM
LCB-R-2-H6	Eq. 4	41.28 ± 6.66 µM
LCB-R-2-A7	Eq. 4	23.35 ± 4.20 µM
LMC-3-G10	Eq. 4	30.27 ± 4.15 µM
LMC-7-G3	Eq. 4	20.83 ± 2.07 µM
LMC-9-D8	Eq. 4	6.22 ± 0.10 µM
LMC-9-E9	Eq. 13	4.06 ± 0.89 µM

Ultimately, the screen carried out at the CEA Paris-Saclay centre allowed to identify seven compounds that presented an inhibitory effect of the *Sa*SbnA-catalysed reaction greater than 50%. A preliminary characterization of the best hits allowed to identify the most potent compounds that will be subjected to pharmacomodulation to increase potency based on structure-activity relationship (SAR) studies as well as physicochemical properties (solubility, cell penetration,…).

Conclusions

The project of this thesis comprised activities aimed at studying and targeting the first steps involved in *S. aureus* main pathways of iron acquisition, namely the hemophore and siderophore-mediated systems. Each of these systems is characterized by the presence of virulence factors, as the surface-exposed hemophore IsdB and the siderophore SB, that are key effectors of *S. aureus* pathogenesis and could thus represent promising targets in novel antimicrobial strategies. Previous studies highlighted the requirement of IsdB for bacterial virulence, with the hemophore enabling iron retrieval from human Hb. In this thesis, small molecules identified by virtual screening and molecular docking studies, and newly synthetized analogues, were experimentally tested *in vitro* to evaluate the best hit compounds effective in the disruption of the IsdB:Hb complex formation, laying the foundation for development of more potent compounds. On the other hand, the SB siderophore was reported to be produced by the most invasive *S. aureus* strains and was found to support virulence by the acquisition of inorganic iron from the host. Within the SB iron acquisition system, the first two steps of the siderophore biosynthesis, catalyzed by SbnA and SbnB enzymes, were found to be essential for SB production. Despite previous investigations, a complete and detailed structural and functional characterization of SbnA was still missing. In this context, a full functional characterization of the enzyme was intended to obtain more insights into its mechanism of action and provide tools for the evaluation of potential inhibitors. The following screenings allowed to identify hit compounds to be further characterized, setting the basis for the development of more potent molecules.

Evaluation of disruptors of IsdB-Hb complex formation

With the aim of evaluating the inhibitory effect of potential IsdB-Hb complex disruptors, an *in-house* developed immunoassay was optimized as a platform using a low-affinity IsdB variant, i.e. Y165A IsdB. Indeed, the exploitation of the Y165A IsdB over wt IsdB allowed to use higher Hb concentrations, stabilizing Hb tetrameric form, less prone to autoxidation, thus avoiding potential interferences and increasing the sensitivity of the assay. An *in-silico* screening campaign was originally conducted by the research group of Professor Francesca Spyrakis (University of Turin) to identify compounds that would bind free Hb in plasma without compromising Hb activity within red blood cells. In a previous study, the *in silico*-selected molecules were purchased from commercial suppliers and screened, allowing the identification of 4 hit compounds that were able to disrupt IsdB:Hb complex formation and confirmed their binding to Hb by STD-NMR. According to the STD-NMR analysis, one of the hits presented only one methyl group engaged in interactions with Hb, therefore it was discarded from further analysis, while the other 3 hit compounds were re-synthesized by collaborators and tested in this project by the immunoassay and STD-NMR to verify their ability to reduce IsdB:Hb complex formation and confirm their binding to Hb. Ultimately, analogues of the 3 compounds were also synthesized and screened by the immunoassay. This initial investigation aimed at laying the foundations for a structure-activity relationship (SAR) study for the development of PPI inhibitors as new potential antimicrobials, with the aim of reducing iron availability for the bacterium. The selected molecules should have a lower rate of resistance insurgence and the capacity to maintain the inhibitory effect against various pathogens. Indeed, since the molecules bind Hb, it is reasonable to assume that they will exert a reduced selective pressure on the bacteria, thus decreasing the probability of resistance insurgence. Furthermore, as other bacterial hemophores extract heme from Hb, a molecule bound to Hb may disrupt the activity of other hemophores in addition to staphylococcal IsdB and IsdH.

***Sa*SbnA characterization and identification of potential inhibitors**

With the aim of getting insight of the first step of SB biosynthesis, a detailed spectroscopic characterization of recombinant *Sa*SbnA was performed providing information about its spectroscopic properties that could be exploited for functional and inhibition studies. The optimization of a continuous assay allowed to confirm the ping-pong kinetic mechanism proposed by Kobylarz and colleagues with extrapolation of kinetic parameters. Furthermore, two phenomena have been demonstrated in this work, i.e. substrate inhibition by L-glutamate and the spontaneous decomposition of the α-aminoacrylate intermediate in pyruvate and ammonia.

With the aim of identifying potential inhibitors of *Sa*SbnA activity, three assays were developed to evaluate inhibition of the enzymatic activity and direct binding to the active site. The platform was first exploited to evaluate potential feedback mechanisms on *Sa*SbnA activity by intermediates of the SB pathway. Among the intermediates tested, two out of the three SB building blocks, i.e. α-KG and citrate, showed an inhibitory effect on the *Sa*SbnA activity, with citrate being the more potent inhibitor. Interestingly, previous studies had reported the existence of a feedback mechanism in the SB biosynthesis, in which citrate was identified as inhibitor of SbnH and SbnC enzymes, which catalyse the third to last and last reactions of the pathway, respectively. Moreover, citrate was also identified in the deposited *Sa*SbnA crystal structure (ID 5D85), supporting the results obtained. A more detailed functional characterization revealed a mixed-type inhibition mechanism, i.e. the inhibitor binds with the same affinity to both the free enzyme and the α-aminoacrylate intermediate.

The optimization of a discontinuous assay allowed to evaluate the potential inhibitory effect of a first set of fifteen molecules, which had been previously selected by a structure-based approach through an *in silico* study performed by collaborators. The *in vitro* screening identified one hit compound that significantly reduced *Sa*SbnA activity, with an IC_{50} in the low micromolar range. The full characterization of the compound mode of action revealed a mechanism of competitive inhibition for the free enzyme, in agreement with the change in the polarity of the PLP microenvironment upon binding, as revealed by fluorescence spectroscopy. Moreover, a first derivative was designed, i.e. the 2-PhMA with the aim to decrease the possible conformations of the molecule and thus increase the potency. The characterization of the derivative revealed the same inhibition mechanism of the parent hit compound with an increased potency, therefore setting the ground for further improvements and potentially SAR studies.

With the aim of broadening the plethora of potential inhibitors to be identified, an HTS was performed on compound libraries. This screening detached itself from the limits derived from the constraints of the structure-based approach, i.e. the restricted identification of inhibitors that target *Sa*SbnA active site. Furthermore, the amount and variety of compounds tested by HTS would enable to identify potential inhibitors with high potency and novel chemotypes to be eventually modified. The implementation of the discontinuous assay for the HTS analysis on a total of 1725 compounds allowed to identify 7 hit compounds with an inhibitory effect on *Sa*SbnA activity similar or even higher than 2-PhMA. The selected hits will be subjected to further characterization to identify the most promising compounds in terms of potency, mechanism of action and modifiable chemotypes.

References

1. Ogston, A. Report upon Micro-Organisms in Surgical Diseases. *The British Medical Journal* **1**, 369–375 (1881) DOI:10.1136/bmj.1.1054.369.

2. Ogston, A. Micrococcus Poisoning. *J Anat Physiol* **17**, 24–58 (1882).

3. Somerville, G. A. & Proctor, R. A. The Biology of Staphylococci. In Staphylococci in Human Disease. in 1–18 (Wiley-Blackwell: Oxford, UK, 2009). doi:10.1002/9781444308464.ch1 DOI:10.1002/9781444308464.ch1.

4. Cowan, S. T., Shaw, C. & Williams, R. E. O. Type Strain for Staphylococcus aureus Rosenbach. *J. gen. Microbiol* **10**, 174–176 (1954) DOI:10.1099/00221287-10-1-174.

5. Elmesseri, R. A., Saleh, S. E., Elsherif, H. M., Yahia, I. S. & Aboshanab, K. M. Staphyloxanthin as a Potential Novel Target for Deciphering Promising Anti-Staphylococcus aureus Agents. *Antibiotics* **11**, (2022) DOI:10.3390/antibiotics11030298.

6. Fiedor, J. & Burda, K. Potential role of carotenoids as antioxidants in human health and disease. *Nutrients* **6**, 466–488 (2014) DOI:10.3390/nu6020466.

7. Liu, G. Y. *et al.* Staphylococcus aureus golden pigment impairs neutrophil killing and promotes virulence through its antioxidant activity. *Journal of Experimental Medicine* **202**, 209–215 (2005) DOI:10.1084/jem.20050846.

8. Loeb, L. The Influence of certain Bacteria on the Coagulation of the Blood. *J. Med. Res* **10**, 407–419 (1903).

9. Bonar, E., Międzobrodzki, J. & Władyka, B. The Staphylococcal Coagulases. in *Pet-to-Man Travelling Staphylococci: A World in Progress* 95–102 (Elsevier, 2018). doi:10.1016/B978-0-12-813547-1.00007-8 DOI:10.1016/B978-0-12-813547-1.00007-8.

10. Wertheim, H. F. L. *et al.* The role of nasal carriage in Staphylococcus aureus infections. *Lancet Infect. Dis.* **5**, 751–762 (2005).

11. Tong, S. Y. C., Davis, J. S., Eichenberger, E., Holland, T. L. & Fowler, V. G. Staphylococcus aureus Infections: Epidemiology, Pathophysiology, Clinical Manifestations, and Management. *Clin. Microbiol. Rev.* **28**, 603–661 (2015).

12. Bien, J., Sokolova, O. & Bozko, P. Characterization of Virulence Factors of Staphylococcus aureus : Novel Function of Known Virulence Factors That Are Implicated in Activation of Airway Epithelial Proinflammatory Response . *J Pathog* **2011**, 1–13 (2011) DOI:10.4061/2011/601905.

13. Lowy, F. D. Staphylococcus aureus Infections. *N. Engl. J. Med* **339**, 520–532 (1998).

14. Cheung, G. Y. C., Bae, J. S. & Otto, M. Pathogenicity and virulence of Staphylococcus aureus. *Virulence* **12**, 547–569 (2021) DOI:10.1080/21505594.2021.1878688.

15. Cheung, A. L., Bayer, A. S., Zhang, G., Gresham, H. & Xiong, Y. Q. Regulation of virulence determinants in vitro and in vivo in Staphylococcus aureus. *FEMS Immunol Med Microbiol* **40**, 1–9 (2004) DOI:10.1016/S0928-8244(03)00309-2.

16. Jenul, C. & Horswill, A. R. Regulation of Staphylococcus aureus Virulence . *Microbiol Spectr* **7**, (2019) DOI:10.1128/microbiolspec.gpp3-0031-2018.

17. Fournier, B. & Philpott, D. J. Recognition of Staphylococcus aureus by the innate immune system. *Clin Microbiol Rev* **18**, 521–540 (2005) DOI:10.1128/CMR.18.3.521-540.2005.

18. Vandenesch, F., Lina, G. & Henry, T. Staphylococcus aureus hemolysins, bi-component leukocidins, and cytolytic peptides: a redundant arsenal of membrane-damaging virulence factors? *Front Cell Infect Microbiol* **2**, 12 (2012) DOI:10.3389/fcimb.2012.00012.

19. Foster, T. J. The MSCRAMM Family of Cell-Wall-Anchored Surface Proteins of Gram-Positive Cocci. *Trends Microbiol* **27**, 927–941 (2019) DOI:10.1016/j.tim.2019.06.007.

20. Foster, T. J., Geoghegan, J. A., Ganesh, V. K. & Höök, M. Adhesion, invasion and evasion: The many functions of the surface proteins of Staphylococcus aureus. *Nat Rev Microbiol* **12**, 49–62 (2014) DOI:10.1038/nrmicro3161.

21. Maresso, A. W. & Schneewind, O. Iron acquisition and transport in Staphylococcus aureus. in *BioMetals* vol. 19 193–203 (2006). DOI:10.1007/s10534-005-4863-7.

22. Marchetti, M. *et al.* Iron metabolism at the interface between host and pathogen: From nutritional immunity to antibacterial development. *Int J Mol Sci* **21**, (2020) DOI:10.3390/ijms21062145.

23. Hammer, N. D. & Skaar, E. P. Molecular mechanisms of staphylococcus aureus iron acquisition. *Annu Rev Microbiol* **65**, 129–147 (2011) DOI:10.1146/annurev-micro-090110-102851.

24. Weinberg, E. D. Nutritional Immunity Host's Attempt to Withhold Iron From Microbial Invaders. *JAMA* **231**, 39 (1975).

25. Ganz, T. Iron in innate immunity: starve the invaders. *Curr Opin Immunol* **21**, 63–67 (2009) DOI:10.1016/j.coi.2009.01.011.

26. Mazmanian, S. K. *et al.* Passage of heme-iron across the envelope of Staphylococcus aureus. *Science (1979)* **299**, 906–909 (2003) DOI:10.1126/science.1081147.

27. Mazmanian, S. K., Ton-That, H., Su, K. & Schneewind, O. An iron-regulated sortase anchors a class of surface protein during Staphylococcus aureus pathogenesis. *Proc. Natl. Acad. Sci.* **99**, 2293–2298 (2002).

28. Lindsay,', J. A. & Riley', T. V. Staphylococcal Iron Requirements, Siderophore Production, and Iron-Regulated Protein Expression. *Infect Immun* **62**, 2309–2314 (1994).

29. Bhakdil, S. & Tranum-Jensen, J. Alpha-Toxin of Staphylococcus aureus. *Micorbial. Rev.* **55**, 733–751 (1991).

30. Babior, B. M. Phagocytes and Oxidative Stress. *Am J Med* **109**, 33–44 (2000).

31. Zecconi, A. & Scali, F. Staphylococcus aureus virulence factors in evasion from innate immune defenses in human and animal diseases. *Immunol Lett* **150**, 12–22 (2013) DOI:10.1016/j.imlet.2013.01.004.

32. Trivier, D. & Courcol, R. J. Iron depletion and virulence in Staphylococcus aureus . *FEMS Microbiol Lett* **141**, 117–127 (1996) DOI:10.1111/j.1574-6968.1996.tb08373.x.

33. Cassat, J. E. & Skaar, E. P. Metal ion acquisition in Staphylococcus aureus: Overcoming nutritional immunity. *Semin Immunopathol* **34**, 215–235 (2012) DOI:10.1007/s00281-011-0294-4.

34. Kobayashi, S. D. & DeLeo, F. R. Staphylococcus aureus protein A promotes immune suppression. *mBio* **4**, (2013) DOI:10.1128/mBio.00764-13.

35. De Haas, C. J. C. *et al.* Chemotaxis Inhibitory Protein of Staphylococcus aureus, a Bacterial Antiinflammatory Agent. *Journal of Experimental Medicine* **199**, 687–695 (2004) DOI:10.1084/jem.20031636.

36. Prévost, G. *et al. Panton-Valentine Leucocidin and Gamma-Hemolysin from Staphylococcus Aureus ATCC 49775 Are Encoded by Distinct Genetic Loci and Have Different Biological Activities*. *INFECTION AND IMMUNITY* vol. 63 (1995).

37. Skinner, D. & Keefer, C. S. Significance of Bacteremia Caused by Staphylococcus aureus. *Arch. Intern. Med.* **68**, 851 (1941).

38. Chambers, H. F. & DeLeo, F. R. Waves of resistance: Staphylococcus aureus in the antibiotic era. *Nat Rev Microbiol* **7**, 629–641 (2009) DOI:10.1038/nrmicro2200.

39. Kluytmans, J., Van Belkum, A. & Verbrugh, H. Nasal Carriage of Staphylococcus aureus: Epidemiology, Underlying Mechanisms, and Associated Risks. *Clin Microbiol Rev* **10**, 505–520 (1997).

40. McCarthy, A. J. & Lindsay, J. A. Genetic variation in staphylococcus aureus surface and immune evasion genes is lineage associated: Implications for vaccine design and host-pathogen interactions. *BMC Microbiol* **10**, (2010) DOI:10.1186/1471-2180-10-173.

41. Rammelkamp, C. H. & Maxon, T. Resistance of Staphylococcus aureus> to the Action of Penicillin. *Proceedings of the Society for Experimental Biology and Medicine* **51**, 386–389 (1942) DOI:10.3181/00379727-51-13986.

42. Bondi, A. & Dietz, C. C. Penicillin Resistant Staphylococci. *Exp. Biol. Med.* **60**, 55–58 (1945).

43. Rutenberg, A. M., Greenberg, H. L. & Schweinburg, F. B. Clinical Experiences with 2, 6-Dimethoxyphenyl Penicillin Monohydrate in Staphylococcal Infections. *New England Journal of Medicine* **263**, 1174–1178 (1960).

44. Jevons, M. P. "Celbenin" -resistant Staphylococci. *Br Med J* **1**, 124–125 (1961) DOI:10.1136/bmj.1.5219.124-a.

45. Lakhundi, S. & Zhang, K. Methicillin-Resistant Staphylococcus aureus: Molecular Characterization, Evolution, and Epidemiology. *Clin Microbiol Rev* **31**, (2018) DOI:10.1128/CMR.00020-18.

46. Cong, Y., Yang, S. & Rao, X. Vancomycin resistant Staphylococcus aureus infections: A review of case updating and clinical features. *J Adv Res* **21**, 169–176 (2020) DOI:10.1016/j.jare.2019.10.005.

47. Moellering, R. C. Vancomycin: A 50-Year Reassessment. *Clinical Infectious Diseases* **42**, 3–4 (2006).

48. Rice, L. B. Federal funding for the study of antimicrobial resistance in nosocomial pathogens: No ESKAPE. *Journal of Infectious Diseases* **197**, 1079–1081 (2008) DOI:10.1086/533452.

49. Tacconelli, E. & Magrini, N. *Global Priority List of Antibiotic-Resistant Bacteria to Guide Research, Discovery, and Development of New Antibiotics*. http://www.cdc.gov/drugresistance/threat-report-2013/ (2017).

50. Falces-Romero, I. *et al.* Staphylococcus aureus bacteremia in patients with SARS-CoV-2 infection. *Med Clin (Barc)* **160**, 495–498 (2023) DOI:10.1016/j.medcli.2023.01.012.

51. Hoebe, K., Janssen, E. & Beutler, B. The interface between innate and adaptive immunity. *Nat. Immunol.* **5**, 971974 (2004).

52. Alberts B, Johnson A, Lewis J & et al. Innate Immunity. in *Molecular Biology of the Cell* (ed. New York: Garland Science) (2002).

53. McDonald, D. R. & Levy, O. Innate Immunity. in *Clinical Immunology: Principles and Practice* 39-53.e1 (Elsevier, 2019). doi:10.1016/B978-0-7020-6896-6.00003-X DOI:10.1016/B978-0-7020-6896-6.00003-X.

54. Proctor, R. A. Recent developments for Staphylococcus aureus vaccines: Clinical and basic science challenges. *Eur Cell Mater* **30**, 315–326 (2015) DOI:10.22203/eCM.v030a22.

55. Brandt, S. L., Putnam, N. E., Cassat, J. E. & Serezani, C. H. Innate Immunity to Staphylococcus aureus : Evolving Paradigms in Soft Tissue and Invasive Infections . *The Journal of Immunology* **200**, 3871–3880 (2018) DOI:10.4049/jimmunol.1701574.

56. Turvey, S. E. & Broide, D. H. Innate immunity. *Journal of Allergy and Clinical Immunology* **125**, (2010) DOI:10.1016/j.jaci.2009.07.016.

57. Bekeredjian-Ding, I., Stein, C. & Uebele, J. The innate immune response against Staphylococcus aureus. in *Current Topics in Microbiology and Immunology* vol. 409 385–418 (Springer Verlag, 2017). DOI:10.1007/82_2015_5004.

58. Janeway, C. A. & Medzhitov, R. Innate immune recognition. *Annu Rev Immunol* **20**, 197–216 (2002) DOI:10.1146/annurev.immunol.20.083001.084359.

59. Frey, P. A. & Reed, G. H. The ubiquity of iron. *ACS Chem Biol* **7**, 1477–1481 (2012) DOI:10.1021/cb300323q.

60. Van Gossum, A. & Neve, J. Trace element deficiency and toxicity. *Curr. Opin. Clin. Nutr. Metab. Care* **1**, 499–507 (1998).

61. Williams, R. J. P. Iron in evolution. *FEBS Letters* vol. 586 479–484 Preprint at https://doi.org/10.1016/j.febslet.2011.05.068 (2012) DOI:10.1016/j.febslet.2011.05.068.

62. Dhungana, S. & Crumbliss, A. L. Coordination chemistry and redox processes in siderophore-mediated iron transport. *Geomicrobiol J* **22**, 87–98 (2005) DOI:10.1080/01490450590945870.

63. Wu, L. F., Meng, S. & Tang, G. L. Ferrous iron and α-ketoglutarate-dependent dioxygenases in the biosynthesis of microbial natural products. *Biochim Biophys Acta Proteins Proteom* **1864**, 453–470 (2016) DOI:10.1016/j.bbapap.2016.01.012.

64. Yamamoto, I., Saiki, T., Shiu Mei Liu & Ljungdahl, L. G. Purification and properties of NADP-dependent formate dehydrogenase from Clostridium thermoaceticum, a tungsten-selenium-iron protein. *Journal of Biological Chemistry* **258**, 1826–1832 (1983) DOI:10.1016/s0021-9258(18)33062-x.

65. McDonough, M. A., Loenarz, C., Chowdhury, R., Clifton, I. J. & Schofield, C. J. Structural studies on human 2-oxoglutarate dependent oxygenases. *Curr Opin Struct Biol* **20**, 659–672 (2010) DOI:10.1016/j.sbi.2010.08.006.

66. Johnson, D. C., Dean, D. R., Smith, A. D. & Johnson, M. K. Structure, function, and formation of biological iron-sulfur clusters. *Annu Rev Biochem* **74**, 247–281 (2005) DOI:10.1146/annurev.biochem.74.082803.133518.

67. Chong, G. W., Karbelkar, A. A. & El-Naggar, M. Y. Nature's conductors: what can microbial multi-heme cytochromes teach us about electron transport and biological energy conversion? *Curr Opin Chem Biol* **47**, 7–17 (2018) DOI:10.1016/j.cbpa.2018.06.007.

68. Comer, J. M. & Zhang, L. Experimental methods for studying cellular heme signaling. *Cells* **7**, (2018) DOI:10.3390/cells7060047.

69. Wolf, G., Strahl, A., Meisel, J. & Hammes, W. P. Heme-dependent catalase activity of lactobacilli. *Internauonal Journal of Food Microbiology* **12**, 133 (1991).

70. Förstermann, U. & Sessa, W. C. Nitric oxide synthases: Regulation and function. *Eur Heart J* **33**, (2012) DOI:10.1093/eurheartj/ehr304.

71. Shelver, D., Kerby, R. L., He, Y. & Roberts, G. P. CooA, a CO-sensing transcription factor from Rhodospirillum rubrum, is a CO-binding heme protein. **94**, 11216–11220 (1997).

72. Faller, M., Matsunaga, M., Yin, S., Loo, J. A. & Guo, F. Heme is involved in microRNA processing. *Nat Struct Mol Biol* **14**, 23–29 (2007) DOI:10.1038/nsmb1182.

73. Chen, J.-J. & London, I. M. Hemin Enhances the Differentiation of Mouse 3T3 Cells to Adipocytes. *Cell* **26**, 117 DOI:10.1016/0092-8674(81)90039-8.

74. Itano, H. A. The Human Hemoglobins: Their Properties and Genetic Control. in *Biology of Perceptual Systems* 215–268 (Elsevier, 1957).

75. Berg, J., Tymoczko, J., Gatto, G. J. J. & Stryer, L. *Biochemistry*. (New York, 2015).

76. Venkataraman, D. *et al.* A Coordination Geometry Table of the d-Block Elements and Their Ions. *J Chem Educ* **74**, (1997).

77. Sassa, S. Why Heme Needs to Be Degraded to Iron, Biliverdin IXa, and Carbon Monoxide? *Antixidants & Redox Signaling* **6**, 819–824 (2004).

78. Brieger, K., Schiavone, S., Miller, F. J. & Krause, K. H. Reactive oxygen species: From health to disease. *Swiss Med Wkly* **142**, (2012) DOI:10.4414/smw.2012.13659.

79. Lieu, P. T., Heiskala, M., Peterson, P. A. & Yang, Y. The roles of iron in health and disease. *Mol Aspects Med* **22**, 1–87 (2001).

80. Fenton, H. J. H. LXXIII. - Oxidation of tartaric acid in presence of iron. *Journal of the Chemical Society, Transactions* vol. 65 899–910 Preprint at https://doi.org/10.1039/CT8946500899 (1894) DOI:10.1039/CT8946500899.

81. Rigo, A., Stevanato, R., Finazzi-Agro', A. & Rotilio, G. An attempt to evaluate the rate of the haber-weiss reaction by using ·OH radical scavengers. *FEBS Lett* **80**, 130–132 (1977) DOI:10.1016/0014-5793(77)80422-5.

82. Niedzielska, E. *et al.* Oxidative Stress in Neurodegenerative Diseases. *Mol Neurobiol* **53**, 4094–4125 (2016) DOI:10.1007/s12035-015-9337-5.

83. Halliwell, B., Gutteridge, J. M. C., Andorn, A. C., Britton, R. S. & Bacon, B. R. Lipid peroxidation in brain homogenates: The role of iron and hydroxyl radicals (multiple letters). *J Neurochem* **69**, 1330 (1997) DOI:10.1046/j.1471-4159.1997.69031330.x.

84. Simcox, J. A. & McClain, D. A. Iron and diabetes risk. *Cell Metab* **17**, 329–341 (2013) DOI:10.1016/j.cmet.2013.02.007.

85. Lindley, P. F. Iron in biology: a structural viewpoint. *Rep. Prog. Phys* **59**, 867–933 (1996).

86. Pantopoulos, K., Porwal, S. K., Tartakoff, A. & Devireddy, L. Mechanisms of mammalian iron homeostasis. *Biochemistry* **51**, 5705–5724 (2012) DOI:10.1021/bi300752r.

87. Hentze, M. W., Muckenthaler, M. U., Galy, B. & Camaschella, C. Two to Tango: Regulation of Mammalian Iron Metabolism. *Cell* vol. 142 24–38 Preprint at https://doi.org/10.1016/j.cell.2010.06.028 (2010) DOI:10.1016/j.cell.2010.06.028.

88. Ganz, T. & Nemeth, E. Regulation of iron acquisition and iron distribution in mammals. *Biochim Biophys Acta Mol Cell Res* **1763**, 690–699 (2006) DOI:10.1016/j.bbamcr.2006.03.014.

89. Py, B. & Barras, F. Building Feg-S proteins: Bacterial strategies. *Nat Rev Microbiol* **8**, 436–446 (2010) DOI:10.1038/nrmicro2356.

90. Abbaspour, N., Hurrell, R. & Kelishadi, R. Review on iron and its importance for human health. *Journal of Research in Medical Sciences* (2014).

91. Andrews, N. C. Iron homeostasis: insights from genetics and animal models. *Nat. Rev. Genet.* **1**, 208–217 (2000).

92. Hood, M. I. & Skaar, E. P. Nutritional immunity: transition metals at the pathogen–host interface. *Nat. Rev. Microbiol.* **10**, 525–537 (2012).

93. Sjodt, M. Investigating Hemoglobin Capture and Heme Acquisition by the Pathogen Staphylococcus aureus. *University of California* (2019).

94. Kohgo, Y., Ikuta, K., Ohtake, T., Torimoto, Y. & Kato, J. Body iron metabolism and pathophysiology of iron overload. *Int J Hematol* **88**, 7–15 (2008) DOI:10.1007/s12185-008-0120-5.

95. Oliveira, F., Rocha, S. & Fernandes, R. Iron metabolism: From health to disease. *J Clin Lab Anal* **28**, 210–218 (2014) DOI:10.1002/jcla.21668.

96. Haley, K. P. & Skaar, E. P. A battle for iron: Host sequestration and Staphylococcus aureus acquisition. *Microbes Infect* **14**, 217–227 (2012) DOI:10.1016/j.micinf.2011.11.001.

97. Laurell, C. B. Determination of the haptoglobin group. *Scand J Clin Lab Invest* **11**, 18–19 (1959) DOI:10.3109/00365515909060402.

98. Muller-Eberhard, U. Hemopexin. *Med Sci Sports Exerc* **283**, 1090–1094 (1970) DOI:10.1056/nejm197011122832007.

99. Smith, A. & McCulloh, R. J. Hemopexin and haptoglobin: Allies against heme toxicity from hemoglobin not contenders. *Front Physiol* **6**, (2015) DOI:10.3389/fphys.2015.00187.

100. Schaer, D. J., Buehler, P. W., Alayash, A. I., Belcher, J. D. & Vercellotti, G. M. Hemolysis and free hemoglobin revisited: exploring hemoglobin and hemin scavengers as a novel class of therapeutic proteins. *Blood* **121**, 1276–1284 (2013) DOI:10.1182/blood.

101. Núñez, G., Sakamoto, K. & Soares, M. P. Innate Nutritional Immunity. *The Journal of Immunology* **201**, 11–18 (2018) DOI:10.4049/jimmunol.1800325.

102. Mollan, T. L. *et al.* Redox properties of human hemoglobin in complex with fractionated dimeric and polymeric human haptoglobin. (2014) doi:10.1016/j.freeradbiomed.2014.01.030 DOI:10.1016/j.freeradbiomed.2014.01.030.

103. Kristiansen, M. *et al.* Identification of the haemoglobin scavenger receptor. *Nature* **409**, 198–201 (2001) DOI:10.1038/35051594.

104. Etzerodt, A. & Moestrup, S. K. CD163 and Inflammation: Biological, Diagnostic, and Therapeutic Aspects. doi:10.1089/ars.2012.4834 DOI:10.1089/ars.2012.4834.

105. Raynes, J. G., Eagling, S. & McAdam, K. P. W. J. Acute-phase protein synthesis in human hepatoma cells: differential regulation of serum amyloid A (SAA) and haptoglobin by interleukin-1 and interleukin-6. *Clin Exp Immunol* **83**, (1991) DOI:10.1007/978-94-011-3284-8_31.

106. Andersen, C. B. F. *et al.* Haptoglobin. *Antioxid Redox Signal* **26**, 814–831 (2017) DOI:10.1089/ars.2016.6793.

107. Buechler, C. *et al.* Regulation of scavenger receptor CD163 expression in human monocytes and macrophages by pro- and antiinflammatory stimuli. *J Leukoc Biol* **67**, 97–103 (2000) DOI:10.1002/jlb.67.1.97.

108. Mitani, K., Fujita, H., Kappas, A. & Sassa, S. Heme Oxygenase Is a Positive Acute-Phase Reactant in Human Hep3B Hepatoma Cells. *Blood* **79**, 1255–1259 (1992).

109. Delanghe, J., Allcock, K., Langlois, M., Claeys, L. & De Buyzere, M. Fast determination of haptoglobin phenotype and calculation of hemoglobin binding capacity using high pressure gel permeation chromatography. *Clinica Chimica Acta* **291**, 43–51 (2000) DOI:10.1016/S0009-8981(99)00194-1.

110. Van Vlierberghe, H., Langlois, M. & Delanghe, J. Haptoglobin polymorphisms and iron homeostasis in health and in disease. *Clinica Chimica Acta* **345**, 35–42 (2004) DOI:10.1016/j.cccn.2004.03.016.

111. Tolosano, E. & Altruda, F. Hemopexin: Structure, Function, and Regulation. *DNA Cell Biol* **21**, 297–306 (2002) DOI:0.1089/104454902753759717.

112. Tolosano, E., Fagoonee, S., Morello, N., Vinchi, F. & Fiorito, V. Heme Scavenging and the Other Facets of Hemopexin. *Antioxid Redox Signal* **12**, (2010) DOI:10.1089=ars.2009.2787.

113. Rolla, S. *et al.* Acute-Phase Protein Hemopexin Is a Negative Regulator of Th17 Response and Experimental Autoimmune Encephalomyelitis Development. *The Journal of Immunology* **191**, 5451–5459 (2013) DOI:10.4049/jimmunol.1203076.

114. Hvidberg, V. *et al.* Identification of the receptor scavenging hemopexin-heme complexes. *Blood* **106**, 2572–2579 (2005) DOI:10.1182/blood-2005-03-1185.

115. Aisen, P., Leibman, A. & Zweier, J. Stoichiometric and site characteristics of the binding of iron to human transferrin. *Journal of Biological Chemistry* **253**, 1930–1937 (1978) DOI:10.1016/s0021-9258(19)62337-9.

116. Raymond, K. N., Dertz, E. A. & Kim, S. S. Enterobactin: An archetype for microbial iron transport.

117. Koechlin', B. A. Preparation and Properties of Serum and Plasma Proteins. XXVIII. The β 1 -Metal-combining Protein of Human Plasma 1a, b. *Journal American Chemistry Society* **74**, 2649–2653 (1952).

118. Granick, S. Ferritin IV. Occurrence and Immunological Propertiers Of Ferritin. *Journal of Biological Chemistry* **149**, 157–167 (1943).

119. Montreuil, J., Tonnelat, J. & Mulli~t, S. Préparation et propriétés de la lactosidérophiline (lactotransferrine) du lait de femme. *Biochim Biophys Acta* **45**, 413–421 (1960).

120. Oliveira, F., Rocha, S. & Fernandes, R. Iron metabolism: From health to disease. *J Clin Lab Anal* **28**, 210–218 (2014) DOI:10.1002/jcla.21668.

121. Andrews, N. C. Iron homeostastis: insights from genetics and animal models. *Nat Rev Genet* **1**, 208–217 (2000).

122. Andrews, N. A. Disorders of iron metabolism. *N Engl J Med* **341**, 1986–1995 (1999).

123. Linder, M. C. Mobilization of stored iron in mammals: A review. *Nutrients* **5**, 4022–4050 (2013) DOI:10.3390/nu5104022.

124. Harrison, P. M. & Arosio, P. The ferritins" molecular properties, iron storage function and cellular regulation. *Biochim Biophys Acta* **1275**, 161–203 (1996).

125. Gunshin, H. *et al.* Cloning and characterization of a mammalian proton-coupled metal-ion transporter. *Nature* **388**, 482-488. (1997).

126. Fleet, J. C. Identification of Nramp2 as an Iron Transport Protein: Another Piece of the Intestinal Iron Absorption Puzzle. *Nutr Rev* **56**, 88–89 (1998).

127. Canonne-Hergaux, F., Zhang, A.-S., Ponka, P. & Gros, P. Characterization of the iron transporter DMT1 (NRAMP2/DCT1) in red blood cells of normal and anemic mk/mk mice. *Blood* **98**, (2001) DOI:10.1182/blood.v98.13.3823.

128. Sun, H., Li, H. & Sadler, P. J. Transferrin as a metal ion mediator. *Chem Rev* **99**, 2817–2842 (1999) DOI:10.1021/cr980430w.

129. Abboud, S. & Haile, D. J. A Novel Mammalian Iron-regulated Protein Involved in Intracellular Iron Metabolism*. *Journal of Biological Chemistry* **275**, 19906–19912 (2000) DOI:10.1074.jbc.M000713200.

130. Ramey, G. *et al.* Hepcidin targets ferroportin for degradation in hepatocytes. *Haematologica* **95**, 501–504 (2010) DOI:10.3324/haematol.2009.014399.

131. Pakdaman, R., Petitjean, M. & El Hage Chahine, J. M. Transferrins: A mechanism for iron uptake by lactoferrin. *Eur J Biochem* **254**, 144–153 (1998) DOI:10.1046/j.1432-1327.1998.2540144.x.

132. Baker, E. N., Baker, H. M. & Kidd, R. D. Lactoferrin and transferrin: Functional variations on a common structural framework. *Biochemistry and Cell Biology* **80**, 27–34 (2002) DOI:10.1139/o01-153.

133. Bullen, J. J., Rogers, H. J. & Griffiths, E. Role of Iron in Bacterial Infection. *Curr Top Microbiol Immunol* **80**, 1–35 (1988) DOI:10.1007/978-3-642-66956-9_1.

134. Andrews, N. C. Forging a field: The golden age of iron biology. *Blood* **112**, 219–230 (2008) DOI:10.1182/blood-2007-12-077388.

135. Cheng, Y., Zak, O., Aisen, P., Harrison, S. C. & Walz, T. Structure of the Human Transferrin Receptor-Transferrin Complex and distributing iron. *Cell* **116**, 565–576 (2004).

136. Rosa, L., Cutone, A., Lepanto, M. S., Paesano, R. & Valenti, P. Lactoferrin: A natural glycoprotein involved in iron and inflammatory homeostasis. *Int J Mol Sci* **18**, (2017) DOI:10.3390/ijms18091985.

137. Friedman, D. B. *et al.* Staphylococcus aureus redirects central metabolism to increase iron availability. *PLoS Pathog* **2**, 0777–0789 (2006) DOI:10.1371/journal.ppat.0020087.

138. Clarke, S. R. & Foster, S. J. IsdA protects Staphylococcus aureus against the bactericidal protease activity of apolactoferrin. *Infect Immun* **76**, 1518–1526 (2008) DOI:10.1128/IAI.01530-07.

139. Gruys, E., Toussaint, M. J. M., Niewold, T. A. & Koopmans, S. J. Acute phase reaction and acute phase proteins. *J Zhejiang Univ Sci* **6 B**, 1045–1056 (2005) DOI:10.1631/jzus.2005.B1045.

140. Holmes, M. A., Paulsene, W., Jide, X., Ratledge, C. & Strong, R. K. Siderocalin (Lcn 2) also binds carboxymycobactins, potentially defending against mycobacterial infections through iron sequestration. *Structure* **13**, 29–41 (2005) DOI:10.1016/j.str.2004.10.009.

141. Borregaard, N. & Cowland, J. B. Neutrophil gelatinase-associated lipocalin, a siderophore-binding eukaryotic protein. *BioMetals* **19**, 211–215 (2006) DOI:10.1007/s10534-005-3251-7.

142. Rishi, G., Wallace, D. F. & Subramaniam, V. N. Hepcidin: Regulation of the master iron regulator. *Biosci Rep* **35**, (2015) DOI:10.1042/BSR20150014.

143. De Domenico, I., Ward, D. M. & Kaplan, J. Hepcidin regulation: ironing out the details. *J Clin Invest* **117**, 1755–1758 (2007) DOI:10.1172/JCI31721.

144. Cheng, A. G., DeDent, A. C., Schneewind, O. & Missiakas, D. A play in four acts: Staphylococcus aureus abscess formation. *Trends Microbiol* **19**, 225–232 (2011) DOI:10.1016/j.tim.2011.01.007.

145. Coronel-Tellez, R. H. *et al.* sRNA-controlled iron sparing response in Staphylococci. *Nucleic Acids Res* **50**, 8529–8546 (2022) DOI:10.1093/nar/gkac648.

146. Johnson, M., Cockayne, A. & Morrissey, J. A. Iron-regulated biofilm formation in Staphylococcus aureus newman requires ica and the secreted protein Emp. *Infect Immun* **76**, 1756–1765 (2008) DOI:10.1128/IAI.01635-07.

147. Horsburgh, M. J., Ingham, E. & Foster, S. J. In Staphylococcus aureus, Fur is an interactive regulator with PerR, contributes to virulence, and is necessary for oxidative stress resistance through positive regulation of catalase and iron homeostasis. *J Bacteriol* **183**, 468–475 (2001) DOI:10.1128/JB.183.2.468-475.2001.

148. Johnson, M. *et al.* Fur is required for the activation of virulence gene expression through the induction of the sae regulatory system in Staphylococcus aureus. *International Journal of Medical Microbiology* **301**, 44–52 (2011) DOI:10.1016/j.ijmm.2010.05.003.

149. Troxell, B. & Hassan, H. M. Transcriptional regulation by Ferric Uptake Regulator (Fur) in pathogenic bacteria. *Front Cell Infect Microbiol* **4**, (2013) DOI:10.3389/fcimb.2013.00059.

150. Lojek, L. J., Farrand, A. J., Weiss, A. & Skaar, E. P. Fur regulation of Staphylococcus aureus heme oxygenases is required for heme homeostasis. *International Journal of Medical Microbiology* **308**, 582–589 (2018) DOI:10.1016/j.ijmm.2018.01.009.

151. Escolar, L., Pérez-Martín, J. & De Lorenzo, V. *Opening the Iron Box: Transcriptional Metalloregulation by the Fur Protein*. *JOURNAL OF BACTERIOLOGY* vol. 181 (1999).

152. Allard, M. *et al.* Transcriptional modulation of some Staphylococcus aureus iron-regulated genes during growth in vitro and in a tissue cage model in vivo. *Microbes Infect* **8**, 1679–1690 (2006) DOI:10.1016/j.micinf.2006.01.022.

153. Beasley, F. C., Cheung, J. & Heinrichs, D. E. Mutation of L-2,3-diaminopropionic acid synthase genes blocks staphyloferrin B synthesis in Staphylococcus aureus. *BMC Microbiol* **11**, (2011) DOI:10.1186/1471-2180-11-199.

154. Dale, S. E., Doherty-Kirby, A., Lajoie, G. & Heinrichs, D. E. Role of Siderophore Biosynthesis in Virulence of Staphylococcus aureus: Identification and Characterization of Genes Involved in Production of a Siderophore. *Infect Immun* **72**, 29–37 (2004) DOI:10.1128/IAI.72.1.29-37.2004.

155. Dale, S. E., Sebulsky, M. T. & Heinrichs, D. E. Involvement of SirABC in iron-siderophore import in Staphylococcus aureus. *J Bacteriol* **186**, 8356–8362 (2004) DOI:10.1128/JB.186.24.8356-8362.2004.

156. Beasley, F. C. *et al.* Characterization of staphyloferrin A biosynthetic and transport mutants in Staphylococcus aureus. *Mol Microbiol* **72**, 947–963 (2009) DOI:10.1111/j.1365-2958.2009.06698.x.

157. Torres, V. J. *et al.* Staphylococcus aureus fur regulates the expression of virulence factors that contribute to the pathogenesis of pneumonia. *Infect Immun* **78**, 1618–1628 (2010) DOI:10.1128/IAI.01423-09.

158. Horsburgh, M. J., Clements, M. O., Crossley, H., Ingham, E. & Foster, S. J. PerR controls oxidative stress resistance and iron storage proteins and is required for virulence in Staphylococcus aureus. *Infect Immun* **69**, 3744–3754 (2001) DOI:10.1128/IAI.69.6.3744-3754.2001.

159. Morrissey, J. A., Cockayne, A., Brummell, K. & Williams, P. The Staphylococcal Ferritins Are Differentially Regulated in Response to Iron and Manganese and via PerR and Fur. *Infect Immun* **72**, 972–979 (2004) DOI:10.1128/IAI.72.2.972-979.2004.

160. Mäder, U. *et al.* Staphylococcus aureus Transcriptome Architecture: From Laboratory to Infection-Mimicking Conditions. *PLoS Genet* **12**, (2016) DOI:10.1371/journal.pgen.1005962.

161. Liu, W. *et al.* Assessment of bona fide sRNAs in Staphylococcus aureus. *Front Microbiol* **9**, (2018) DOI:10.3389/fmicb.2018.00228.

162. Oglesby-Sherrouse, A. G. & Murphy, E. R. Iron-responsive bacterial small RNAs: Variations on a theme. *Metallomics* **5**, 276–286 (2013) DOI:10.1039/c3mt20224k.

163. Gaballa, A. *et al.* The Bacillus subtilis iron-sparing response is mediated by a Fur-regulated small RNA and three small, basic proteins. *PNAS* **105**, (2008) DOI:10.1073/pnas.0711752105.

164. Smaldone, G. T. *et al.* A global investigation of the Bacillus subtilis iron-sparing response identifies major changes in metabolism. *J Bacteriol* **194**, 2594–2605 (2012) DOI:10.1128/JB.05990-11.

165. Janagama, H. K. *et al.* Iron-sparing response of mycobacterium avium subsp. paratuberculosis is strain dependent. *BMC Microbiol* **10**, (2010) DOI:10.1186/1471-2180-10-268.

166. Jankovic, I. & Brückner, R. Carbon catabolite repression by the catabolite control protein CcpA in Staphylococcus xylosus. *J Mol Microbiol Biotechnol* **4**, 309–314 (2002).

167. Seidl, K. *et al.* Staphylococcus aureus CcpA affects virulence determinant production and antibiotic resistance. *Antimicrob Agents Chemother* **50**, 1183–1194 (2006) DOI:10.1128/AAC.50.4.1183-1194.2006.

168. Seidl, K. *et al.* Effect of a glucose impulse on the CcpA regulon in Staphylococcus aureus. *BMC Microbiol* **9**, (2009) DOI:10.1186/1471-2180-9-95.

169. Jørgensen, M. G., Pettersen, J. S. & Kallipolitis, B. H. sRNA-mediated control in bacteria: An increasing diversity of regulatory mechanisms. *Biochim Biophys Acta Gene Regul Mech* **1863**, (2020) DOI:10.1016/j.bbagrm.2020.194504.

170. Porcheron, G. *et al.* The small RNA RyhB contributes to siderophore production and virulence of uropathogenic Escherichia coli. *Infect Immun* **82**, 5056–5068 (2014) DOI:10.1128/IAI.02287-14.

171. Torres, V. J. *et al.* A Staphylococcus aureus regulatory system that responds to host heme and modulates virulence. *Cell Host Microbe* **1**, 109–119 (2007).

172. Stauff, D. L., Torres, V. J. & Skaar, E. P. Signaling and DNA-binding activities of the Staphylococcus aureus HssR-HssS two-component system required for heme sensing. *Journal of Biological Chemistry* **282**, 26111–26121 (2007) DOI:10.1074/jbc.M703797200.

173. Wakeman, C. A., Stauff, D. L., Zhang, Y. & Skaar, E. P. Differential activation of Staphylococcus aureus heme detoxification machinery by heme analogues. *J Bacteriol* **196**, 1335–1342 (2014) DOI:10.1128/JB.01067-13.

174. Surdel, M. C., Dutter, B. F., Sulikowski, G. A. & Skaar, E. P. Bacterial Nitric Oxide Synthase Is Required for the Staphylococcus aureus Response to Heme Stress. *ACS Infect Dis* **2**, 572–578 (2016) DOI:10.1021/acsinfecdis.6b00081.

175. Turlin, E., Débarbouillé, M., Augustyniak, K., Gilles, A. M. & Wandersman, C. Staphylococcus aureus FepA and FepB Proteins Drive Heme Iron Utilization in Escherichia coli. *PLoS One* **8**, (2013) DOI:10.1371/journal.pone.0056529.

176. Biswas, L. *et al.* Role of the twin-arginine translocation pathway in Staphylococcus. *J Bacteriol* **191**, 5921–5929 (2009) DOI:10.1128/JB.00642-09.

177. Morikawa, K., Ushijima, Y., Ohniwa, R. L., Miyakoshi, M. & Takeyasu, K. What happens in the staphylococcal nucleoid under oxidative stress? *Microorganisms* **7**, (2019) DOI:10.3390/microorganisms7120631.

178. Laakso, H. A., Marolda, C. L., Pinter, T. B., Stillman, M. J. & Heinrichs, D. E. A heme-responsive regulator controls synthesis of staphyloferrin B in staphylococcus aureus. *Journal of Biological Chemistry* **291**, 29–40 (2016) DOI:10.1074/jbc.M115.696625.

179. Verstraete, M. M. *et al.* The heme-sensitive regulator SbnI has a bifunctional role in staphyloferrin B production by Staphylococcus aureus. *Journal of Biological Chemistry* **294**, 11622–11636 (2019) DOI:10.1074/jbc.RA119.007757.

180. Skaar, E. P., Humayun, M., Bae, T., Debord, K. L. & Schneewind, O. Iron-Source Preference of Staphylococcus aureus Infections. *Science (1979)* **305**, (2004) DOI:10.1126/science.1099930.

181. Torres, V. J., Pishchany, G., Humayun, M., Schneewind, O. & Skaar, E. P. Staphylococcus aureus IsdB is a hemoglobin receptor required for heme iron utilization. *J Bacteriol* **188**, 8421–8429 (2006) DOI:10.1128/JB.01335-06.

182. Pishchany, G., Dickey, S. E. & Skaar, E. P. Subcellular localization of the Staphylococcus aureus heme iron transport components IsdA and IsdB. *Infect Immun* **77**, 2624–2634 (2009) DOI:10.1128/IAI.01531-08.

183. Farrand, A. J., Reniere, M. L., Ingmer, H., Frees, D. & Skaar, E. P. Regulation of host hemoglobin binding by the Staphylococcus aureus Clp Proteolytic system. *J Bacteriol* **195**, 5041–5050 (2013) DOI:10.1128/JB.00505-13.

184. Reniere, M. L., Torres, V. J. & Skaar, E. P. Intracellular metalloporphyrin metabolism in Staphylococcus aureus. in *BioMetals* vol. 20 333–345 (2007). DOI:10.1007/s10534-006-9032-0.

185. Kramer, J., Özkaya, Ö. & Kümmerli, R. Bacterial siderophores in community and host interactions. *Nat Rev Microbiol* **18**, 152–163 (2020) DOI:10.1038/s41579-019-0284-4.

186. Patel, T. A., Belcher, E., Warner, T. D., Harding, S. E. & Mitchell, J. A. Identification and characterization of a dysfunctional cardiac myocyte phenotype: Role of bacteria, toll-like receptors, and endothelin. *Shock* **28**, 434–440 (2007) DOI:10.1097/shk.0b013e31804a55a7.

187. Perutz, M. F. The Croonian Lecture, 1968. The haemoglobin molecule. *Proc R Soc Lond B Biol Sci* **173**, 113–140 (1969) DOI:10.1098/rspb.1969.0043.

188. Cassat, J. E. & Skaar, E. P. Iron in infection and immunity. *Cell Host Microbe* **13**, 509–519 (2013) DOI:10.1016/j.chom.2013.04.010.

189. Ip, S. H. C. & Ackers, G. K. Thermodynamic Studies on Subunit Assembly in Human HemoglobinHEMOGLOBINS*. *J Biol Chem* **252**, 82–87 (1977).

190. Manning, L. R. *et al.* Subunit dissociations in natural and recombinant hemoglobins. *Protein Science* **5**, 775–781 (1996).

191. Wiseman, G. M. The Hemolysins of Staphylococcus aureus. *Bacteriol Rev* **39**, 317–344 (1975).

192. Dryla, A., Gelbmann, D., Von Gabain, A. & Nagy, E. Identification of a novel iron regulated staphylococcal surface protein with haptoglobin-haemoglobin binding activity. *Mol Microbiol* **49**, 37–53 (2003) DOI:10.1046/j.1365-2958.2003.03542.x.

193. Umbreit, J. Methemoglobin - It's not just blue: A concise review. *Am J Hematol* **82**, 134–144 (2007) DOI:10.1002/ajh.20738.

194. Moriwaki, Y. *et al.* Molecular basis of recognition of antibacterial porphyrins by heme-transporter IsdH-NEAT3 of Staphylococcus aureus. *Biochemistry* **50**, 7311–7320 (2011) DOI:10.1021/bi200493h.

195. Bowden, C. F. M. *et al.* Structure-function analyses reveal key features in Staphylococcus aureus IsdB-associated unfolding of the heme-binding pocket of human hemoglobin. *Journal of Biological Chemistry* **293**, 177–190 (2018) DOI:10.1074/jbc.M117.806562.

196. Pishchany, G. *et al.* IsdB-dependent hemoglobin binding is required for acquisition of heme by Staphylococcus aureus. *Journal of Infectious Diseases* **209**, 1764–1772 (2014) DOI:10.1093/infdis/jit817.

197. Gaudin, C. F. M., Grigg, J. C., Arrieta, A. L. & Murphy, M. E. P. Unique heme-iron coordination by the hemoglobin receptor IsdB of staphylococcus aureus. *Biochemistry* **50**, 5443–5452 (2011) DOI:10.1021/bi200369p.

198. Bowden, C. F. M., Verstraete, M. M., Eltis, L. D. & Murphy, M. E. P. Hemoglobin binding and catalytic heme extraction by IsdB near iron transporter domains. *Biochemistry* **53**, 2286–2294 (2014) DOI:10.1021/bi500230f.

199. Sæderup, K. L. *et al.* The Staphylococcus aureus Protein IsdH inhibits host hemoglobin scavenging to promote heme acquisition by the pathogen. *Journal of Biological Chemistry* **291**, 23989–23998 (2016) DOI:10.1074/jbc.M116.755934.

200. Pilpa, R. M. *et al.* Solution Structure of the NEAT (NEAr Transporter) Domain from IsdH/HarA: the Human Hemoglobin Receptor in Staphylococcus aureus. *J Mol Biol* **360**, 435–447 (2006) DOI:10.1016/j.jmb.2006.05.019.

201. Pishchany, G. *et al.* Specificity for human hemoglobin enhances staphylococcus aureus infection. *Cell Host Microbe* **8**, 544–550 (2010) DOI:10.1016/j.chom.2010.11.002.

202. Mozzi, A., Forni, D., Clerici, M., Cagliani, R. & Sironi, M. The diversity of mammalian hemoproteins and microbial heme scavengers is shaped by an arms race for iron piracy. *Front Immunol* **9**, (2018) DOI:10.3389/fimmu.2018.02086.

203. Choby, J. E. *et al.* Molecular Basis for the Evolution of Species-Specific Hemoglobin Capture by Staphylococcus aureus. (2018) doi:10.1128/mBio DOI:10.1128/mBio.

204. Spirig, T. *et al.* Staphylococcus aureus Uses a Novel Multidomain Receptor to Break Apart Human Hemoglobin and Steal Its Heme *. *Journal of Biological Chemistry* **288**, 1065–1078 (2013) DOI:10.1074/jbc.M112.419119.

205. Moriwaki, Y., Terada, T., Tsumoto, K. & Shimizu, K. Rapid heme transfer reactions between NEAr transporter domains of staphylococcus aureus: A theoretical study using QM/MM and MD simulations. *PLoS One* **10**, (2015) DOI:10.1371/journal.pone.0145125.

206. Sjodt, M. *et al.* The PRE-Derived NMR Model of the 38.8-kDa Tri-Domain IsdH Protein from Staphylococcus aureus Suggests That It Adaptively Recognizes Human Hemoglobin. *J Mol Biol* **428**, 1107–1129 (2016) DOI:10.1016/j.jmb.2015.02.008.

207. Choby, J. E. & Skaar, E. P. Heme Synthesis and Acquisition in Bacterial Pathogens. *J Mol Biol* **428**, 3408–3428 (2016) DOI:10.1016/j.jmb.2016.03.018.

208. Muryoi, N. *et al.* Demonstration of the iron-regulated surface determinant (Isd) heme transfer pathway in Staphylococcus aureus. *Journal of Biological Chemistry* **283**, 28125–28136 (2008) DOI:10.1074/jbc.M802171200.

209. Zhu, H. *et al.* Pathway for heme uptake from human methemoglobin by the iron-regulated surface determinants system of Staphylococcus aureus. *Journal of Biological Chemistry* **283**, 18450–18460 (2008) DOI:10.1074/jbc.M801466200.

210. Villareal, V. A. *et al.* Transient weak protein-protein complexes transfer heme across the cell wall of Staphylococcus aureus. *J Am Chem Soc* **133**, 14176–14179 (2011) DOI:10.1021/ja203805b.

211. Tiedemann, M. T. & Stillman, M. J. Heme binding to the IsdE(M78A; H229A) double mutant: Challenging unidirectional heme transfer in the iron-regulated surface determinant protein heme transfer pathway of Staphylococcus aureus. *Journal of Biological Inorganic Chemistry* **17**, 995–1007 (2012) DOI:10.1007/s00775-012-0914-z.

212. Pishchany, G., Dickey, S. E. & Skaar, E. P. Subcellular localization of the Staphylococcus aureus heme iron transport components IsdA and IsdB. *Infect Immun* **77**, 2624–2634 (2009) DOI:10.1128/IAI.01531-08.

213. Mazmanian, S. K., Liu, G., Jensen, E. R., Lenoy, E. & Schneewind, O. Staphylococcus aureus sortase mutants defective in the display of surface proteins and in the pathogenesis of animal infections. *Proc. Natl. Acad. Sci.* **97**, 5510–5515 (2000).

214. Reniere, M. L. & Skaar, E. P. Staphylococcus aureus haem oxygenases are differentially regulated by iron and haem. *Mol Microbiol* **69**, 1304–1315 (2008) DOI:10.1111/j.1365-2958.2008.06363.x.

215. Wandersman, C. & Delepelaire, P. Bacterial iron sources: From siderophores to hemophores. *Annu Rev Microbiol* **58**, 611–647 (2004) DOI:10.1146/annurev.micro.58.030603.123811.

216. Torres, V. J., Pishchany, G., Humayun, † Munir, Schneewind, O. & Skaar, E. P. Staphylococcus aureus IsdB Is a Hemoglobin Receptor Required for Heme Iron Utilization. *J Bacteriol* **188**, 8421–8429 (2006) DOI:10.1128/JB.01335-06.

217. Jacobitz, A. W., Kattke, M. D., Wereszczynski, J. & Clubb, R. T. Sortase Transpeptidases: Structural Biology and Catalytic Mechanism. in *Advances in Protein Chemistry and Structural Biology* vol. 109 223–264 (Academic Press Inc., 2017). DOI:10.1016/bs.apcsb.2017.04.008.

218. DeDent, A., Bae, T., Missiakas, D. M. & Schneewind, O. Signal peptides direct surface proteins to two distinct envelope locations of Staphylococcus aureus. *EMBO Journal* **27**, 2656–2668 (2008) DOI:10.1038/emboj.2008.185.

219. Spirig, T., Weiner, E. M. & Clubb, R. T. Sortase enzymes in Gram-positive bacteria. *Molecular Microbiology* vol. 82 1044–1059 Preprint at https://doi.org/10.1111/j.1365-2958.2011.07887.x (2011) DOI:10.1111/j.1365-2958.2011.07887.x.

220. Ton-That, H., Liu, G., Mazmanian, S. K., Faull, K. F. & Schneewind, O. Purification and characterization of sortase, the transpeptidase that cleaves surface proteins of Staphylococcus aureus at the LPXTG motif. *Proc. Natl. Acad. Sci.* **96**, 12424–12429 (1999).

221. Silhavy, T. J., Kahne, D. & Walker, S. The bacterial cell envelope. *Cold Spring Harb Perspect Biol* **2**, (2010) DOI:10.1101/cshperspect.a000414.

222. Ton-That, H., Marraffini, L. A. & Schneewind, O. Protein sorting to the cell wall envelope of Gram-positive bacteria. *Biochim Biophys Acta Mol Cell Res* **1694**, 269–278 (2004) DOI:10.1016/j.bbamcr.2004.04.014.

223. Navarre, W. W. & Schneewind, O. Surface Proteins of Gram-Positive Bacteria and Mechanisms of Their Targeting to the Cell Wall Envelope. *Microbiology And Molecular Biology Reviews* **63**, 174–229 (1999).

224. Marraffini, L. A. & Schneewind, O. Anchor structure of staphylococcal surface proteins: V. Anchor structure of the sortase B substrate IsdC. *Journal of Biological Chemistry* **280**, 16263–16271 (2005) DOI:10.1074/jbc.M500071200.

225. Taylor, J. M. & Heinrichs, D. E. Transferrin binding in Staphylococcus aureus: Involvement of a cell wall-anchored protein. *Mol Microbiol* **43**, 1603–1614 (2002) DOI:10.1046/j.1365-2958.2002.02850.x.

226. Morrissey, J. A. *et al.* Conservation, surface exposure, and in vivo expression of the Frp family of iron-regulated cell wall proteins in Staphylococcus aureus. *Infect Immun* **70**, 2399–2407 (2002) DOI:10.1128/IAI.70.5.2399-2407.2002.

227. Moriwaki, Y. *et al.* Molecular basis of recognition of antibacterial porphyrins by heme-transporter IsdH-NEAT3 of Staphylococcus aureus. *Biochemistry* **50**, 7311–7320 (2011) DOI:10.1021/bi200493h.

228. Grigg, J. C., Mao, C. X. & Murphy, M. E. P. Iron-coordinating tyrosine is a key determinant of neat domain heme transfer. *J Mol Biol* **413**, 684–698 (2011) DOI:10.1016/j.jmb.2011.08.047.

229. Liu, M. *et al.* Direct hemin transfer from IsdA to IsdC in the iron-regulated surface determinant (Isd) heme acquisition system of Staphylococcus aureus. *Journal of Biological Chemistry* **283**, 6668–6676 (2008) DOI:10.1074/jbc.M708372200.

230. Adolf, L. A. *et al.* Functional membrane microdomains and the hydroxamate siderophore transporter ATPase FhuC govern Isd-dependent heme acquisition in Staphylococcus aureus. *Elife* **12**, (2023) DOI:10.7554/eLife.85304.

231. Abe, R., Caaveiro, J. M. M., Kozuka-Hata, H., Oyama, M. & Tsumoto, K. Mapping ultra-weak protein-protein interactions between heme transporters of Staphylococcus aureus. *Journal of Biological Chemistry* **287**, 16477–16487 (2012) DOI:10.1074/jbc.M112.346700.

232. Moriwaki, Y. *et al.* Heme binding mechanism of structurally similar iron-regulated surface determinant near transporter domains of staphylococcus aureus exhibiting different affinities for heme. *Biochemistry* **52**, 8866–8877 (2013) DOI:10.1021/bi4008325.

233. Grigg, J. C., Ukpabi, G., Gaudin, C. F. M. & Murphy, M. E. P. Structural biology of heme binding in the Staphylococcus aureus Isd system. *J Inorg Biochem* **104**, 341–348 (2010) DOI:10.1016/j.jinorgbio.2009.09.012.

234. Hempel, K., Herbst, F. A., Moche, M., Hecker, M. & Becher, D. Quantitative proteomic view on secreted, cell surface-associated, and cytoplasmic proteins of the methicillin-resistant human pathogen staphylococcus aureus under iron-limited conditions. *J Proteome Res* **10**, 1657–1666 (2011) DOI:10.1021/pr1009838.

235. Ho, W. W. *et al.* Holo- and apo-bound structures of bacterial periplasmic heme-binding proteins. *Journal of Biological Chemistry* **282**, 35796–35802 (2007) DOI:10.1074/jbc.M706761200.

236. Berntsson, R. P. A., Smits, S. H. J., Schmitt, L., Slotboom, D. J. & Poolman, B. A structural classification of substrate-binding proteins. *FEBS Lett* **584**, 2606–2617 (2010) DOI:10.1016/j.febslet.2010.04.043.

237. Rice, A. J., Park, A. & Pinkett, H. W. Diversity in ABC transporters: Type I, II and III importers. *Crit Rev Biochem Mol Biol* **49**, 426–437 (2014) DOI:10.3109/10409238.2014.953626.

238. Grigg, J. C., Vermeiren, C. L., Heinrichs, D. E. & Murphy, M. E. P. Heme coordination by Staphylococcus aureus IsdE. *Journal of Biological Chemistry* **282**, 28815–28822 (2007) DOI:10.1074/jbc.M704602200.

239. Mack, J., Vermeiren, C., Heinrichs, D. E. & Stillman, M. J. In vivo heme scavenging by Staphylococcus aureus IsdC and IsdE proteins. *Biochem Biophys Res Commun* **320**, 781–788 (2004) DOI:10.1016/j.bbrc.2004.06.025.

240. Matsui, T. *et al.* Heme degradation by Staphylococcus aureus IsdG and IsdI liberates formaldehyde rather than carbon monoxide. *Biochemistry* **52**, 3025–3027 (2013) DOI:10.1021/bi400382p.

241. Reniere, M. L. *et al.* The IsdG-family of haem oxygenases degrades haem to a novel chromophore. *Mol Microbiol* **75**, 1529–1538 (2010) DOI:10.1111/j.1365-2958.2010.07076.x.

242. Skaar, E. P., Gaspar, A. H. & Schneewind, O. IsdG and IsdI, Heme-degrading Enzymes in the Cytoplasm of Staphylococcus aureus. *Journal of Biological Chemistry* **279**, 436–443 (2004) DOI:10.1074/jbc.M307952200.

243. Haley, K. P., Janson, E. M., Heilbronner, S., Foster, T. J. & Skaar, E. P. Staphylococcus lugdunensis IsdG liberates iron from host heme. *J Bacteriol* **193**, 4749–4757 (2011) DOI:10.1128/JB.00436-11.

244. Wilks, A. & Heinzl, G. Heme oxygenation and the widening paradigm of heme degradation. *Arch Biochem Biophys* **544**, 87–95 (2014) DOI:10.1016/j.abb.2013.10.013.

245. Loutet, S. A., Kobylarz, M. J., Chau, C. H. T. & Murphy, M. E. P. IruO is a reductase for heme degradation by IsdI and IsdG proteins in staphylococcus aureus. *Journal of Biological Chemistry* **288**, 25749–25759 (2013) DOI:10.1074/jbc.M113.470518.

246. Conger, M. A., Pokhrel, D. & Liptak, M. D. Tight Binding of Heme to Staphylococcus aureus IsdG and IsdI Precludes Design of a Competitive Inhibitor. *Metallomics* **9**, 556–563 (2017) DOI:10.1039/c7mt00035a.

247. Pluym, M., Muryoi, N., Heinrichs, D. E. & Stillman, M. J. Heme binding in the NEAT domains of IsdA and IsdC of Staphylococcus aureus. *J Inorg Biochem* **102**, 480–488 (2008) DOI:10.1016/j.jinorgbio.2007.11.011.

248. Sharp, K. H., Schneider, S., Cockayne, A. & Paoli, M. Crystal structure of the heme-IsdC complex, the central conduit of the Isd iron/heme uptake system in Staphylococcus aureus. *Journal of Biological Chemistry* **282**, 10625–10631 (2007) DOI:10.1074/jbc.M700234200.

249. Andrade, M. A., Ciccarelli, F. D., Perez-Iratxeta, C. & Bork, P. NEAT: a domain duplicated in genes near the components of a putative Fe 3+ siderophore transporter from Gram-positive pathogenic bacteria. *Genome Biol* **3**, (2002).

250. Macdonald, R., Mahoney, B. J., Ellis-Guardiola, K., Maresso, A. & Clubb, R. T. NMR experiments redefine the hemoglobin binding properties of bacterial NEAr-iron Transporter domains. *Protein Science* **28**, 1513–1523 (2019) DOI:10.1002/pro.3662.

251. Watanabe, M. *et al.* Structural basis for multimeric heme complexation through a specific protein-heme interaction: The case of the third NEAT domain of IsdH from Staphylococcus aureus. *Journal of Biological Chemistry* **283**, 28649–28659 (2008) DOI:10.1074/jbc.M803383200.

252. Pilpa, R. M. *et al.* Functionally distinct NEAT (NEAr Transporter) domains within the staphylococcus aureus IsdH/HarA protein extract heme from methemoglobin. *Journal of Biological Chemistry* **284**, 1166–1176 (2009) DOI:10.1074/jbc.M806007200.

253. Sjodt, M. *et al.* Energetics underlying hemin extraction from human hemoglobin by Staphylococcus aureus. *Journal of Biological Chemistry* **293**, 6942–6957 (2018) DOI:10.1074/jbc.RA117.000803.

254. Fonner, B. A. *et al.* Solution structure and molecular determinants of hemoglobin binding of the first NEAT domain of IsdB in staphylococcus aureus. *Biochemistry* **53**, 3922–3933 (2014) DOI:10.1021/bi5005188.

255. Kumar, K. K. *et al.* Structural basis for hemoglobin capture by Staphylococcus aureus cell-surface protein, IsdH. *Journal of Biological Chemistry* **286**, 38439–38447 (2011) DOI:10.1074/jbc.M111.287300.

256. Dickson, C. F. *et al.* Structure of the hemoglobin-isdh complex reveals the molecular basis of iron capture by staphylococcus aureus. *Journal of Biological Chemistry* **289**, 6728–6738 (2014) DOI:10.1074/jbc.M113.545566.

257. Dickson, C. F., Jacques, D. A., Clubb, R. T., Guss, J. M. & Gell, D. A. The structure of haemoglobin bound to the haemoglobin receptor IsdH from Staphylococcus aureus shows disruption of the native α-globin haem pocket. *Acta Crystallogr D Biol Crystallogr* **71**, 1295–1306 (2015) DOI:10.1107/S1399004715005817.

258. Ellis-Guardiola, K. *et al.* The Staphylococcus aureus IsdH Receptor Forms a Dynamic Complex with Human Hemoglobin that Triggers Heme Release via Two Distinct Hot Spots. *J Mol Biol* **432**, 1064–1082 (2020) DOI:10.1016/j.jmb.2019.12.023.

259. Spirig, T. & Clubb, R. T. Backbone 1H, 13C and 15N resonance assignments of the 39 kDa staphylococcal hemoglobin receptor IsdH. *Biomol NMR Assign* **6**, 169–172 (2012) DOI:10.1007/s12104-011-9348-8.

260. Mikkelsen, J. H., Runager, K. & Andersen, C. B. F. The human protein haptoglobin inhibits IsdH-mediated heme-sequestering by Staphylococcus aureus. *Journal of Biological Chemistry* **295**, 1781–1791 (2020) DOI:10.1074/jbc.RA119.011612.

261. Dickson, C. F., Jacques, D. A., Clubb, R. T., Guss, J. M. & Gell, D. A. The structure of haemoglobin bound to the haemoglobin receptor IsdH from Staphylococcus aureus shows disruption of the native α-globin haem pocket. *Acta Crystallogr D Biol Crystallogr* **71**, 1295–1306 (2015) DOI:10.1107/S1399004715005817.

262. Pilpa, R. M. *et al.* Functionally distinct NEAT (NEAr Transporter) domains within the staphylococcus aureus IsdH/HarA protein extract heme from methemoglobin. *Journal of Biological Chemistry* **284**, 1166–1176 (2009) DOI:10.1074/jbc.M806007200.

263. Dryla, A. *et al.* High-affinity binding of the staphylococcal HarA protein to haptoglobin and hemoglobin involves a domain with an antiparallel eight-stranded β-barrel fold. *J Bacteriol* **189**, 254–264 (2007) DOI:10.1128/JB.01366-06.

264. Honsa, E. S., Maresso, A. W. & Highlander, S. K. Molecular and evolutionary analysis of NEAr-Iron Transporter (NEAT) domains. *PLoS One* **9**, (2014) DOI:10.1371/journal.pone.0104794.

265. Brewitz, H. H., Hagelueken, G. & Imhof, D. Structural and functional diversity of transient heme binding to bacterial proteins. *Biochim Biophys Acta Gen Subj* **1861**, 683–697 (2017) DOI:10.1016/j.bbagen.2016.12.021.

266. Grigg, J. C., Vermeiren, C. L., Heinrichs, D. E. & Murphy, M. E. P. Haem recognition by a Staphylococcus aureus NEAT domain. *Mol Microbiol* **63**, 139–149 (2007) DOI:10.1111/j.1365-2958.2006.05502.x.

267. Villareal, V. A., Pilpa, R. M., Robson, S. A., Fadeev, E. A. & Clubb, R. T. The IsdC protein from Staphylococcus aureus uses a flexible binding pocket to capture heme. *Journal of Biological Chemistry* **283**, 31591–31600 (2008) DOI:10.1074/jbc.M801126200.

268. Sakipov, S., Rafikova, O., Kurnikova, M. G. & Rafikov, R. Molecular mechanisms of bio-catalysis of heme extraction from hemoglobin. *Redox Biol* **11**, 516–523 (2017) DOI:10.1016/j.redox.2017.01.004.

269. Vermeiren, C. L., Pluym, M., Mack, J., Heinrichs, D. E. & Stillman, M. J. Characterization of Heme Binding Properties of Staphylococcus aureus IsdA. *Biochemistry* **45**, 12867–12875 (2006).

270. Palazzolo-Ballance, A. M. *et al.* Neutrophil Microbicides Induce a Pathogen Survival Response in Community-Associated Methicillin-Resistant Staphylococcus aureus . *The Journal of Immunology* **180**, 500–509 (2008) DOI:10.4049/jimmunol.180.1.500.

271. Clarke, S. R., Wiltshire, M. D. & Foster, S. J. IsdA of Staphylococcus aureus is a broad spectrum, iron-regulated adhesin. *Mol Microbiol* **51**, 1509–1519 (2004) DOI:10.1111/j.1365-2958.2003.03938.x.

272. Clarke, S. R. & Foster, S. J. Surface Adhesins of Staphylococcus aureus. *Adv Microb Physiol* **51**, 187–224 (2006) DOI:10.1016/S0065-2911(06)51004-5.

273. Clarke, S. R. *et al.* Iron-regulated surface determinant protein A mediates adhesion of Staphylococcus aureus to human corneocyte envelope proteins. *Infect Immun* **77**, 2408–2416 (2009) DOI:10.1128/IAI.01304-08.

274. Corrigan, R. M., Miajlovic, H. & Foster, T. J. Surface proteins that promote adherence of Staphylococcus aureus to human desquamated nasal epithelial cells. *BMC Microbiol* **9**, (2009) DOI:10.1186/1471-2180-9-22.

275. Krismer, B., Weidenmaier, C., Zipperer, A. & Peschel, A. The commensal lifestyle of Staphylococcus aureus and its interactions with the nasal microbiota. *Nat Rev Microbiol* **15**, 675–687 (2017) DOI:10.1038/nrmicro.2017.104.

276. Miajlovic, H. *et al.* Direct interaction of iron-regulated surface determinant IsdB of Staphylococcus aureus with the GPIIb/IIIa receptor on platelets. *Microbiology (N Y)* **156**, 920–928 (2010) DOI:10.1099/mic.0.036673-0.

277. Zapotoczna, M., Jevnikar, Z., Miajlovic, H., Kos, J. & Foster, T. J. Iron-regulated surface determinant B (IsdB) promotes Staphylococcus aureus adherence to and internalization by non-phagocytic human cells. *Cell Microbiol* **15**, 1026–1041 (2013) DOI:10.1111/cmi.12097.

278. Hamzeh-Cognasse, H. *et al.* Platelets and infections - Complex interactions with bacteria. *Front Immunol* **6**, (2015) DOI:10.3389/fimmu.2015.00082.

279. Pietrocola, G. *et al.* The iron-regulated surface determinant B (IsdB) protein from Staphylococcus aureus acts as a receptor for the host protein vitronectin. *J Biol Chem* **295**, 10008–10022 (2020) DOI:10.1074/jbc.RA120.013510.

280. Visai, L. *et al.* Immune evasion by Staphylococcus aureus conferred by iron-regulated surface determinant protein IsdH. *Microbiology (N Y)* **155**, 667–679 (2009) DOI:10.1099/mic.0.025684-0.

281. Gianquinto, E. *et al.* Interaction of human hemoglobin and semi-hemoglobins with the Staphylococcus aureus hemophore IsdB: a kinetic and mechanistic insight. *Sci Rep* **9**, 1–19 (2019) DOI:10.1038/s41598-019-54970-w.

282. De Bei, O. *et al.* Cryo-EM structures of staphylococcal IsdB bound to human hemoglobin reveal the process of heme extraction. *PNAS* **119**, (2022).

283. De Bei, O. *et al.* Time-resolved X-ray solution scattering unveils the sequence of events leading to human Hb heme capture by Staphylococcus aureus IsdB. *BioRxiv* (2023) doi:10.1101/2023.08.04.551941 DOI:10.1101/2023.08.04.551941.

284. Zhu, H., Li, D., Liu, M., Copié, V. & Lei, B. Non-heme-binding domains and segments of the Staphylococcus aureus IsdB protein critically contribute to the kinetics and equilibrium of heme acquisition from methemoglobin. *PLoS One* **9**, (2014) DOI:10.1371/journal.pone.0100744.

285. Freestone, P. P. *et al.* Growth Stimulation Of Intestinal Commensal Escherichia coli By Catecholamines: A Possible Contributory Factor in Trauma-Induced Sepsis.

286. Sandrini, S. M. *et al.* Elucidation of the mechanism by which catecholamine stress hormones liberate iron from the innate immune defense proteins transferrin and lactoferrin. *J Bacteriol* **192**, 587–594 (2010) DOI:10.1128/JB.01028-09.

287. Neal, C. P. *et al.* Catecholamine inotropes as growth factors for Staphylococcus epidermidis and other coagulase-negative staphylococci . *FEMS Microbiol Lett* **194**, 163–169 (2001) DOI:10.1111/j.1574-6968.2001.tb09463.x.

288. Anderson, M. T. & Armstrong, S. K. Norepinephrine mediates acquisition of transferrin-iron in Bordetella bronchiseptica. *J Bacteriol* **190**, 3940–3947 (2008) DOI:10.1128/JB.00086-08.

289. Lyte, M. *et al.* Stimulation of Staphylococcus epidermidis growth and biofilm formation by catecholamine inotropes. *Lancet* **361**, 130–135 (2003) DOI:10.1016/S0140-6736(03)12231-3.

290. Kammler, M., Schon, C. & Hantke, K. Characterization of the Ferrous Iron Uptake System of Escherichia coli. *J Bacteriol* **175**, 6212–6219 (1993).

291. Velayudhan, J. *et al.* Iron acquisition and virulence in Helicobacter pylori: A major role for FeoB, a high-affinity ferrous iron transporter. *Mol Microbiol* **37**, 274–286 (2000) DOI:10.1046/j.1365-2958.2000.01987.x.

292. Naikare, H., Palyada, K., Panciera, R., Marlow, D. & Stintzi, A. Major role for FeoB in Campylobacter jejuni ferrous iron acquisition, gut colonization, and intracellular survival. *Infect Immun* **74**, 5433–5444 (2006) DOI:10.1128/IAI.00052-06.

293. Robey, M. & Cianciotto, N. P. Legionella pneumophila feoAB promotes ferrous iron uptake and intracellular infection. *Infect Immun* **70**, 5659–5669 (2002) DOI:10.1128/IAI.70.10.5659-5669.2002.

294. Létoffé, S., Heuck, G., Delepelaire, P., Lange, N. & Cile Wandersman, C. Bacteria capture iron from heme by keeping tetrapyrrol skeleton intact. *PNAS* **106**, 11719–11724 (2009) DOI:10.1073/pnas.0903842106.

295. Ling, J. M. L., Shima, C. H., Schriemer, D. C. & Schryvers, A. B. Delineating the regions of human transferrin involved in interactions with transferrin binding protein B from Neisseria meningitidis. *Mol Microbiol* **77**, 1301–1314 (2010) DOI:10.1111/j.1365-2958.2010.07289.x.

296. Nau Cornelissen, C. & Sparling, P. F. Binding and Surface Exposure Characteristics of the Gonococcal Transferrin Receptor Are Dependent on Both Transferrin-Binding Proteins. *J Bacteriol* **178**, 1437–1444 (1996).

297. Naidu, A. S., Andersson, M. & Forsgren, A. Identification of a human lactoferrin-binding protein in Staphylococcus aureus. *J. Med. Microbiol* **36**, 177–183 (1992).

298. Zheng, T. & Nolan, E. M. Siderophore-based detection of Fe(iii) and microbial pathogens. *Metallomics* vol. 4 866–880 Preprint at https://doi.org/10.1039/c2mt20082a (2012) DOI:10.1039/c2mt20082a.

299. Hider, R. C. & Kong, X. Chemistry and biology of siderophores. *Nat Prod Rep* **27**, 637–657 (2010) DOI:10.1039/b906679a.

300. Carrano, C. J. & Raymond, K. N. Feric Iron Sequestering Agents. 2. Kinetics and Mechanism of Iron Removal from Transferrin by Enterobactin and Synthetic Tricatechols. *American Chemical Society* **101**, 5401–5404 (1979).

301. Crumbliss, A. L. & Harrington, J. M. Iron sequestration by small molecules: Thermodynamic and kinetic studies of natural siderophores and synthetic model compounds. *Adv Inorg Chem* **61**, 179–250 (2009) DOI:10.1016/S0898-8838(09)00204-9.

302. Matzanke, B. F., Anemüller, S., Schünemann, V., Trautwein, A. X. & Hantke, K. FhuF, Part of a Siderophore-Reductase System. *Biochemistry* **43**, 1386–1392 (2004) DOI:10.1021/bi0357661.

303. Harrington, J. M. & Crumbliss, A. L. The redox hypothesis in siderophore-mediated iron uptake. *BioMetals* **22**, 679–689 (2009) DOI:10.1007/s10534-009-9233-4.

304. Crumbliss, A. L. & Harrington, J. M. Iron sequestration by small molecules: Thermodynamic and kinetic studies of natural siderophores and synthetic model compounds. *Adv Inorg Chem* **61**, 179–250 (2009) DOI:10.1016/S0898-8838(09)00204-9.

305. Holden, V. I. & Bachman, M. A. Diverging roles of bacterial siderophores during infection. *Metallomics* **7**, 986–995 (2015) DOI:10.1039/c4mt00333k.

306. Raisen, C. Investigation of a novel iron-uptake system and other genomic features in mecC Staphylococcus aureus. (University of Cambridge, 2019).

307. Crosa, J. H. & Walsh, C. T. Genetics and Assembly Line Enzymology of Siderophore Biosynthesis in Bacteria. *Microbiology and Molecular Biology Reviews* **66**, 223–249 (2002) DOI:10.1128/mmbr.66.2.223-249.2002.

308. Carroll, C. S. & Moore, M. M. Ironing out siderophore biosynthesis: a review of non-ribosomal peptide synthetase (NRPS)-independent siderophore synthetases. *Crit Rev Biochem Mol Biol* **53**, 356–381 (2018) DOI:10.1080/10409238.2018.1476449.

309. Conroy, B. S., Grigg, J. C., Kolesnikov, M., Morales, L. D. & Murphy, M. E. P. Staphylococcus aureus heme and siderophore-iron acquisition pathways. *BioMetals* **32**, 409–424 (2019) DOI:10.1007/s10534-019-00188-2.

310. Challis, G. L. & Hopwood, D. A. Synergy and contingency as driving forces for the evolution of multiple secondary metabolite production by Streptomyces species. *PNAS* **100**, (2003) DOI:10.1073/pnas.1934677100.

311. Konetschny-Rapp, S., Jung, G., Meiwes, J. & Zähner, H. Staphyloferrin A: a structurally new siderophore from staphylococci. *Eur J Biochem* **191**, 65–74 (1990) DOI:10.1111/j.1432-1033.1990.tb19094.x.

312. Meiwes, J. *et al.* Isolation and characterization of staphyloferrin A, a compound with siderophore activity from Staphylococcus hyicus DSM 20459. *FEMS Microbiol Lett* **67**, 201–206 (1990) DOI:10.1111/j.1574-6968.1990.tb13863.x.

313. Drechsel, H. *et al.* Purification and chemical characterization of staphyloferrin B, a hydrophilic siderophore from staphylococci. *BioMetals* **6**, 185–192 (1993).

314. Haag, H. *et al.* Isolation and biological characterization of staphyloferrin B, a compound with siderophore activity from staphylococci. *FEMS Microbiol Lett* **115**, 125–130 (1994) DOI:10.1111/j.1574-6968.1994.tb06626.x.

315. Perry, W. J. *et al.* Staphylococcus aureus exhibits heterogeneous siderophore production within the vertebrate host. doi:10.6084/m9.figshare.9617633.v4 DOI:10.6084/m9.figshare.9617633.v4.

316. Verstraete, M. M., Perez-Borrajero, C., Brown, K. L., Heinrichs, D. E. & Murphy, M. E. P. SbnI is a free serine kinase that generates O-phospho-L-serine for staphyloferrin B biosynthesis in Staphylococcus aureus. *Journal of Biological Chemistry* **293**, 6147–6160 (2018) DOI:10.1074/jbc.RA118.001875.

317. Lindsay,', J. A. & Riley', T. V. Staphylococcal Iron Requirements, Siderophore Production, and Iron-Regulated Protein Expression. *Infect Immun* **62**, 2309–2314 (1994).

318. Miethke, M. *et al.* Ferri-bacillibactin uptake and hydrolysis in Bacillus subtilis. *Mol Microbiol* **61**, 1413–1427 (2006) DOI:10.1111/j.1365-2958.2006.05321.x.

319. Beasley, F. C., Marolda, C. L., Cheung, J., Buac, S. & Heinrichs, D. E. Staphylococcus aureus transporters Hts, Sir, and Sst capture iron liberated from human transferrin by staphyloferrin A, staphyloferrin B, and catecholamine stress hormones, respectively, and contribute to virulence. *Infect Immun* **79**, 2345–2355 (2011) DOI:10.1128/IAI.00117-11.

320. Courcol, R. J., Lambert, P. A., Fournier, P., Martin, G. R. & Brown, M. R. W. Effects of iron depletion and sab-inhibitory concentrations of antibiotics on siderophore production by Staphylococcus aureus. *Journal of Antimicrobial Chemotherapy* **28**, 663–668 (1991).

321. Cotton, J. L., Tao, J. & Balibar, C. J. Identification and characterization of the Staphylococcus aureus gene cluster coding for staphyloferrin A. *Biochemistry* **48**, 1025–1035 (2009) DOI:10.1021/bi801844c.

322. Sheldon, J. R., Marolda, C. L. & Heinrichs, D. E. TCA cycle activity in Staphylococcus aureus is essential for iron-regulated synthesis of staphyloferrin A, but not staphyloferrin B: The benefit of a second citrate synthase. *Mol Microbiol* **92**, 824–839 (2014) DOI:10.1111/mmi.12593.

323. Hannauer, M., Sheldon, J. R. & Heinrichs, D. E. Involvement of major facilitator superfamily proteins SfaA and SbnD in staphyloferrin secretion in Staphylococcus aureus. *FEBS Lett* **589**, 730–737 (2015) DOI:10.1016/j.febslet.2015.02.002.

324. Grigg, J. C., Cooper, J. D., Cheung, J., Heinrichs, D. E. & Murphy, M. E. P. The Staphylococcus aureus siderophore receptor HtsA undergoes localized conformational changes to enclose staphyloferrin a in an arginine-rich binding pocket. *Journal of Biological Chemistry* **285**, 11162–11171 (2010) DOI:10.1074/jbc.M109.097865.

325. Speziali, C. D., Dale, S. E., Henderson, J. A., Vinés, E. D. & Heinrichs, D. E. Requirement of Staphylococcus aureus ATP-binding cassette-ATPase FhuC for iron-restricted growth and evidence that it functions with more than one iron transporter. *J Bacteriol* **188**, 2048–2055 (2006) DOI:10.1128/JB.188.6.2048-2055.2006.

326. Hannauer, M., Arifin, A. J. & Heinrichs, D. E. Involvement of reductases IruO and NtrA in iron acquisition by Staphylococcus aureus. *Mol Microbiol* **96**, 1192–1210 (2015) DOI:10.1111/mmi.13000.

327. Courcol, R. J., Trivier, D., Bissinger, M.-C., Martin, G. R. & Brown, M. R. W. Siderophore Production by Staphylococcus aureus and Identification of Iron-Regulated Proteins. *Infect Immun* **65**, 1944 (1997).

328. Song, L. *et al.* Mechanistic insights into staphylopine-mediated metal acquisition. *Proc Natl Acad Sci U S A* **115**, 3942–3947 (2018) DOI:10.1073/pnas.1718382115.

329. Fojcik, C. *et al.* Independent and cooperative regulation of staphylopine biosynthesis and trafficking by Fur and Zur. *Mol Microbiol* **108**, 159–177 (2018) DOI:10.1111/mmi.13927.

330. Ghssein, G. *et al.* Biosynthesis of a broad-spectrum nicotianamine-like metallophore in Staphylococcus aureus. *Science (1979)* **352**, 1105–1109 (2016) DOI:10.1126/science.aae0109.

331. Chen, C. & Hooper, D. C. Intracellular accumulation of staphylopine impairs the fitness of Staphylococcus aureus cntE mutant. *FEBS Lett* **593**, 1213–1222 (2019) DOI:10.1002/1873-3468.13396.

332. Remy, L. *et al.* The Staphylococcus aureus Opp1 ABC transporter imports nickel and cobalt in zinc-depleted conditions and contributes to virulence. *Mol Microbiol* **87**, 730–743 (2013) DOI:10.1111/mmi.12126.

333. Grim, K. P. *et al.* The metallophore staphylopine enables staphylococcus aureus to compete with the host for zinc and overcome nutritional immunity. *mBio* **8**, (2017) DOI:10.1128/mBio.01281-17.

334. Sebulsky, M. T., Hohnstein, D., Hunter, M. D. & Heinrichs, D. E. Identification and Characterization of a Membrane Permease Involved in Iron-Hydroxamate Transport in Staphylococcus aureus. *J Bacteriol* **182**, 4394–4400 (2000).

335. Kobylarz, M. J., Heieis, G. A., Loutet, S. A. & Murphy, M. E. P. IruO Uses an FAD Semiquinone Intermediate for Iron-Siderophore Reduction. *ACS Chem Biol* **12**, 1778–1786 (2017) DOI:10.1021/acschembio.7b00203.

336. Abergel, R. J., Zawadzka, A. M., Hoette, T. M. & Raymond, K. N. Enzymatic hydrolysis of trilactone siderophores: Where chiral recognition occurs in enterobactin and bacillibactin iron transport. *J Am Chem Soc* **131**, 12682–12692 (2009) DOI:10.1021/ja903051q.

337. Konopkat, K. & Neilands, J. B. Effect of Serum Albumin on Siderophore-Mediated Utilization of Transferrin Iron+. *Comput. Enhanced Spectrosc. Ljones* **61**, 525–535 (1977).

338. Bister, B. *et al.* The structure of salmochelins: C-glucosylated enterobactins of Salmonella enterica §. *BioMetals* **17**, 471–481 (2004).

339. Grigg, J. C., Cheung, J., Heinrichs, D. E. & Murphy, M. E. P. Specificity of staphyloferrin B recognition by the SirA receptor from Staphylococcus aureus. *Journal of Biological Chemistry* **285**, 34579–34588 (2010) DOI:10.1074/jbc.M110.172924.

340. Madsen, J. L. H., Johnstone, T. C. & Nolan, E. M. Chemical Synthesis of Staphyloferrin B Affords Insight into the Molecular Structure, Iron Chelation, and Biological Activity of a Polycarboxylate Siderophore Deployed by the Human Pathogen Staphylococcus aureus. *J Am Chem Soc* **137**, 9117–9127 (2015) DOI:10.1021/jacs.5b04557.

341. Laakso, H. A., Marolda, C. L., Pinter, T. B., Stillman, M. J. & Heinrichs, D. E. A heme-responsive regulator controls synthesis of staphyloferrin B in staphylococcus aureus. *Journal of Biological Chemistry* **291**, 29–40 (2016) DOI:10.1074/jbc.M115.696625.

342. Cheung, J., Beasley, F. C., Liu, S., Lajoie, G. A. & Heinrichs, D. E. Molecular characterization of staphyloferrin B biosynthesis in Staphylococcus aureus. *Mol Microbiol* **74**, 594–608 (2009) DOI:10.1111/j.1365-2958.2009.06880.x.

343. Hannauer, M., Sheldon, J. R. & Heinrichs, D. E. Involvement of major facilitator superfamily proteins SfaA and SbnD in staphyloferrin secretion in Staphylococcus aureus. *FEBS Lett* **589**, 730–737 (2015) DOI:10.1016/j.febslet.2015.02.002.

344. Heinrichs, J. H., Gatlin, L. E., Kunsch, C., Choi, G. H. & Hanson, M. S. *Identification and Characterization of SirA, an Iron-Regulated Protein from Staphylococcus Aureus*. *JOURNAL OF BACTERIOLOGY* vol. 181 (1999).

345. Speziali, C. D., Dale, S. E., Henderson, J. A., Vinés, E. D. & Heinrichs, D. E. Requirement of Staphylococcus aureus ATP-binding cassette-ATPase FhuC for iron-restricted growth and evidence that it functions with more than one iron transporter. *J Bacteriol* **188**, 2048–2055 (2006) DOI:10.1128/JB.188.6.2048-2055.2006.

346. Sheldon, J. R., Marolda, C. L. & Heinrichs, D. E. TCA cycle activity in Staphylococcus aureus is essential for iron-regulated synthesis of staphyloferrin A, but not staphyloferrin B: The benefit of a second citrate synthase. *Mol Microbiol* **92**, 824–839 (2014) DOI:10.1111/mmi.12593.

347. Cheung, J., Murphy, M. E. P. & Heinrichs, D. E. Discovery of an iron-regulated citrate synthase in staphylococcus aureus. *Chem Biol* **19**, 1568–1578 (2012) DOI:10.1016/j.chembiol.2012.10.003.

348. Tang, J., Ju, Y., Gu, Q., Xu, J. & Zhou, H. Structural Insights into Substrate Recognition and Activity Regulation of the Key Decarboxylase SbnH in Staphyloferrin B Biosynthesis. *J Mol Biol* **431**, 4868–4881 (2019) DOI:10.1016/j.jmb.2019.10.009.

349. Tang, J. *et al.* Structural and Biochemical Characterization of SbnC as a Representative Type B Siderophore Synthetase. *ACS Chem Biol* **15**, 2731–2740 (2020) DOI:10.1021/acschembio.0c00523.

350. Malachowa, N. *et al.* Global changes in staphylococcus aureus gene expression in human blood. *PLoS One* **6**, (2011) DOI:10.1371/journal.pone.0018617.

351. Majerczyk, C. D. *et al.* Direct targets of CodY in Staphylococcus aureus. *J Bacteriol* **192**, 2861–2877 (2010) DOI:10.1128/JB.00220-10.

352. Pohl, K. *et al.* CodY in Staphylococcus aureus: A regulatory link between metabolism and virulence gene expression. *J Bacteriol* **191**, 2953–2963 (2009) DOI:10.1128/JB.01492-08.

353. Halsey, C. R. *et al.* Amino acid catabolism in Staphylococcus aureus and the function of carbon catabolite repression. *mBio* **8**, (2017) DOI:10.1128/mBio.01434-16.

354. Kobylarz, M. J. *et al.* Synthesis of L-2,3-diaminopropionic acid, a siderophore and antibiotic precursor. *Chem Biol* **21**, 379–388 (2014) DOI:10.1016/j.chembiol.2013.12.011.

355. Thomas, M. G., Chan, Y. A. & Ozanick, S. G. Deciphering tuberactinomycin biosynthesis: Isolation, sequencing, and annotation of the viomycin biosynthetic gene cluster. *Antimicrob Agents Chemother* **47**, 2823–2830 (2003) DOI:10.1128/AAC.47.9.2823-2830.2003.

356. Kobylarz, M. J. *et al.* Deciphering the Substrate Specificity of SbnA, the Enzyme Catalyzing the First Step in Staphyloferrin B Biosynthesis. *Biochemistry* **55**, 927–939 (2016) DOI:10.1021/acs.biochem.5b01045.

357. Zhao, C., Song, C., Luo, Y., Yu, Z. & Sun, M. l-2,3-Diaminopropionate: One of the building blocks for the biosynthesis of Zwittermicin A in Bacillus thuringiensis subsp. kurstaki strain YBT-1520. *FEBS Lett* **582**, 3125–3131 (2008) DOI:10.1016/j.febslet.2008.07.054.

358. Felnagle, E. A., Rondon, M. R., Berti, A. D., Crosby, H. A. & Thomas, M. G. Identification of the biosynthetic gene cluster and an additional gene for resistance to the antituberculosis drug capreomycin. *Appl Environ Microbiol* **73**, 4162–4170 (2007) DOI:10.1128/AEM.00485-07.

359. Dawlaty, J., Zhang, X., Fischbach, M. A. & Clardy, J. Dapdiamides, tripeptide antibiotics formed by unconventional amide ligases. *J Nat Prod* **73**, 441–446 (2010) DOI:10.1021/np900685z.

360. Raboni, S., Pioselli, B., Bettati, S. & Mozzarelli, A. The molecular pathway for the allosteric regulation of tryptophan synthase. in *Biochimica et Biophysica Acta - Proteins and Proteomics* vol. 1647 157–160 (Elsevier, 2003). DOI:10.1016/S1570-9639(03)00084-0.

361. Bettati, S. *et al.* Role of pyridoxal 5'-phosphate in the structural stabilization of O-acetylserine sulfhydrylase. *Journal of Biological Chemistry* **275**, 40244–40251 (2000) DOI:10.1074/jbc.M007015200.

362. Campanini, B. *et al.* Surface-exposed tryptophan residues are essential for O-acetylserine sulfhydrylase structure, function, and stability. *Journal of Biological Chemistry* **278**, 37511–37519 (2003) DOI:10.1074/jbc.M305138200.

363. Shibamura-Fujiogi, M. *et al.* GltS regulates biofilm formation in methicillin-resistant Staphylococcus aureus. *Commun Biol* **5**, (2022) DOI:10.1038/s42003-022-04239-2.

364. O'Neill, J. Tackling Drug-Resistant Infections Globally: Final Report and Reccomendations. *Rev. Antimicrob. Resist.* 1–80 (2016).

365. Kumar, K. K. *et al.* Structural basis for hemoglobin capture by Staphylococcus aureus cell-surface protein, IsdH. *Journal of Biological Chemistry* **286**, 38439–38447 (2011).

366. Schneewind, O. & Missiakas, D. Sortases, Surface Proteins, and Their Roles in Staphylococcus aureus Disease and Vaccine Development . *Microbiol Spectr* **7**, (2019) DOI:10.1128/microbiolspec.psib-0004-2018.

367. Cheng, A. G. *et al.* Genetic requirements for Staphylococcus aureus abscess formation and persistence in host tissues. *FASEB Journal* **23**, 3393–3404 (2009) DOI:10.1096/fj.09-135467.

368. Diep, B. A. *et al.* Identifying potential therapeutic targets of methicillin-resistant staphylococcus aureus through in vivo proteomic analysis. *Journal of Infectious Diseases* **209**, 1533–1541 (2014) DOI:10.1093/infdis/jit662.

369. Thomsen, I. P. & Liu, G. Y. Targeting fundamental pathways to disrupt Staphylococcus aureus survival: clinical implications of recent discoveries. *JCI Insight* **3**, (2018) DOI:10.1172/jci.insight.98216.

370. Jonsson, I.-M. *et al.* On the Role of Staphylococcus aureus Sortase and Sortase-Catalyzed Surface Protein Anchoring in Murine Septic Arthritis. *J Infect Dis* **185**, 1417–1424 (2002) DOI:0022-1899/2002/18510-0006$02.00.

371. Jonsson, I. M., Mazmanian, S. K., Schneewind, O., Bremell, T. & Tarkowski, A. The role of Staphylococcus aureus sortase A and sortase B in murine arthritis. *Microbes Infect* **5**, 775–780 (2003) DOI:10.1016/S1286-4579(03)00143-6.

372. Mazmanian, S. K., Ton-That, H. & Schneewind, O. Sortase-catalysed anchoring of surface proteins to the cell wall of Staphylococcus aureus. *Mol Microbiol* **40**, 1049–1057 (2001) DOI:10.1046/j.1365-2958.2001.02411.x.

373. Weiss, W. J. *et al.* Effect of srtA and srtB gene expression on the virulence of Staphylococcus aureus in animal models of infection. *Journal of Antimicrobial Chemotherapy* **53**, 480–486 (2004) DOI:10.1093/jac/dkh078.

374. Wang, J. *et al.* Baicalin acts as an adjuvant to potentiate the activity of azithromycin against Staphylococcus saprophyticus biofilm: an in vitro, in vivo, and molecular study. *Vet Res* **53**, 83 (2022) DOI:10.1186/s13567-022-01088-z.

375. Wang, G. *et al.* Novel inhibitor discovery of staphylococcus aureus sortase b and the mechanism confirmation via molecular modeling. *Molecules* **23**, (2018) DOI:10.3390/molecules23040977.

376. Wang, G., Gao, Y., Wang, H., Niu, X. & Wang, J. Baicalin Weakens Staphylococcus aureus Pathogenicity by Targeting Sortase B. *Front Cell Infect Microbiol* **8**, (2018) DOI:10.3389/fcimb.2018.00418.

377. Kim, H. K. *et al.* IsdA and IsdB antibodies protect mice against Staphylococcus aureus abscess formation and lethal challenge. *Vaccine* **28**, 6382–6392 (2010) DOI:10.1016/j.vaccine.2010.02.097.

378. Brewitz, H. H., Hagelueken, G. & Imhof, D. Structural and functional diversity of transient heme binding to bacterial proteins. *Biochim Biophys Acta Gen Subj* **1861**, 683–697 (2017) DOI:10.1016/j.bbagen.2016.12.021.

379. Wakeman, C. A., Stauff, D. L., Zhang, Y. & Skaar, E. P. Differential activation of Staphylococcus aureus heme detoxification machinery by heme analogues. *J Bacteriol* **196**, 1335–1342 (2014) DOI:10.1128/JB.01067-13.

380. Redi, D., Raffaelli, C. S., Rossetti, B., De Luca, A. & Montagnani, F. Staphylococcus aureus vaccine preclinical and clinical development: current state of the art. *New Microbiologica* **41**, 1121–7138 (2018).

381. Pancari, G. *et al.* Characterization of the mechanism of protection mediated by CS-D7, a monoclonal antibody to Staphylococcus aureus iron regulated surface determinant B (IsdB). *Front Cell Infect Microbiol* **2**, 36 (2012) DOI:10.3389/fcimb.2012.00036.

382. Jansen, K. U., Girgenti, D. Q., Scully, I. L. & Anderson, A. S. Vaccine review: 'Staphyloccocus aureus vaccines: Problems and prospects'. *Vaccine* **31**, 2723–2730 (2013) DOI:10.1016/j.vaccine.2013.04.002.

383. Ster, C. *et al.* Evaluation of some Staphylococcus aureus iron-regulated proteins as vaccine targets. *Vet Immunol Immunopathol* **136**, 311–318 (2010) DOI:10.1016/j.vetimm.2010.03.010.

384. Kim, H. K., Missiakas, D. & Schneewind, O. Mouse models for infectious diseases caused by Staphylococcus aureus. *J Immunol Methods* **410**, 88–99 (2014) DOI:10.1016/j.jim.2014.04.007.

385. Nishitani, K. *et al.* A Diagnostic Serum Antibody Test for Patients With Staphylococcus aureus Osteomyelitis. *Clin Orthop Relat Res* **473**, 2735–2749 (2015) DOI:10.1007/s11999-015-4354-2.

386. Foster, C. E. *et al.* Adhesin genes and biofilm formation among pediatric Staphylococcus aureus isolates from implant-associated infections. *PLoS One* **15**, (2020) DOI:10.1371/journal.pone.0235115.

387. Fowler, V. G. *et al.* Effect of an Investigational Vaccine for Preventing Staphylococcus aureus Infections After Cardiothoracic Surgery A Randomized Trial. *JAMA* **309**, 1368 (2013).

388. McNeely, T. B. *et al.* Mortality among recipients of the Merck V710 Staphylococcus aureus vaccine after postoperative S. aureus infections: An analysis of possible contributing host factors. *Hum Vaccin Immunother* **10**, 3513–3516 (2014) DOI:10.4161/hv.34407.

389. Nishitani, K. *et al.* IsdB antibody-mediated sepsis following S. aureus surgical site infection. *JCI Insight* **5**, (2020) DOI:10.1172/jci.insight.141164.

390. Inoue, M. *et al.* Safety, tolerability, and immunogenicity of a novel 4-antigen Staphylococcus aureus vaccine (SA4Ag) in healthy Japanese adults. *Hum Vaccin Immunother* **14**, 2682–2691 (2018) DOI:10.1080/21645515.2018.1496764.

391. Creech, C. B. *et al.* Safety, tolerability, and immunogenicity of a single dose 4-antigen or 3-antigen Staphylococcus aureus vaccine in healthy older adults: Results of a randomised trial. *Vaccine* **35**, 385–394 (2017) DOI:10.1016/j.vaccine.2016.11.032.

392. Frenck, R. W. *et al.* Safety, tolerability, and immunogenicity of a 4-antigen Staphylococcus aureus vaccine (SA4Ag): Results from a first-in-human randomised, placebo-controlled phase 1/2 study. *Vaccine* **35**, 375–384 (2017) DOI:10.1016/j.vaccine.2016.11.010.

393. Begier, E. *et al.* SA4Ag, a 4-antigen Staphylococcus aureus vaccine, rapidly induces high levels of bacteria-killing antibodies. *Vaccine* **35**, 1132–1139 (2017) DOI:10.1016/j.vaccine.2017.01.024.

394. Jiang, X. Y. *et al.* The safety and immunogenicity of a recombinant five-antigen Staphylococcus aureus vaccine among patients undergoing elective surgery for closed fractures: A randomized, double-blind, placebo-controlled, multicenter phase 2 clinical trial. *Vaccine* **41**, 5562–5571 (2023) DOI:10.1016/j.vaccine.2023.07.047.

395. Clegg, J. *et al.* Staphylococcus aureus Vaccine Research and Development: The Past, Present and Future, Including Novel Therapeutic Strategies. *Front Immunol* **12**, (2021) DOI:10.3389/fimmu.2021.705360.

396. Proctor, R. A. Is there a future for a Staphylococcus aureus vaccine? *Vaccine* **30**, 2921–2927 (2012) DOI:10.1016/j.vaccine.2011.11.006.

397. Fowler, V. G. & Proctor, R. A. Where does a Staphylococcus aureus vaccine stand? *Clinical Microbiology and Infection* **20**, 66–75 (2014) DOI:10.1111/1469-0691.12570.

398. Kuklin, N. A. *et al.* A novel Staphylococcus aureus vaccine: Iron surface determinant B induces rapid antibody responses in rhesus macaques and specific increased survival in a murine S. aureus sepsis model. *Infect Immun* **74**, 2215–2223 (2006) DOI:10.1128/IAI.74.4.2215-2223.2006.

399. Harro, C. *et al.* Safety and immunogenicity of a novel Staphylococcus aureus vaccine: Results from the first study of the vaccine dose range in humans. *Clinical and Vaccine Immunology* **17**, 1868–1874 (2010) DOI:10.1128/CVI.00356-10.

400. Stranger-Jones, Y. K., Bae, T. & Schneewind, O. Vaccine assembly from surface proteins of Staphylococcus aureus. *PNAS* **103**, 16942–16947 (2006) DOI:10.1073/pnas.0606863103.

401. Delfani, S. *et al.* In silico analysis for identifying potential vaccine candidates against Staphylococcus aureus . *Clin Exp Vaccine Res* **4**, 99 (2015) DOI:10.7774/cevr.2015.4.1.99.

402. Delfani, S., Mohabati Mobarez, A., Imani Fooladi, A. A., Amani, J. & Emaneini, M. Protection of mice against Staphylococcus aureus infection by a recombinant protein ClfA–IsdB–Hlg as a vaccine candidate. *Med Microbiol Immunol* **205**, 47–55 (2016) DOI:10.1007/s00430-015-0425-y.

403. Sibbald, M. J. J. B. *et al.* Mapping the Pathways to StaphylococcalPathogenesis by Comparative Secretomics. *Microbiology and Molecular Biology Reviews* **70**, 755–788 (2006) DOI:10.1128/mmbr.00008-06.

404. Zhu, F. C. *et al.* Evaluation of a recombinant five-antigen Staphylococcus aureus vaccine: The randomized, single-centre phase 1a/1b clinical trials. *Vaccine* **40**, 3216–3227 (2022) DOI:10.1016/j.vaccine.2022.04.034.

405. Zeng, H. *et al.* Rapid and broad immune efficacy of a recombinant five-antigen vaccine against Staphylococcus aureus infection in animal models. *Vaccines (Basel)* **8**, (2020) DOI:10.3390/vaccines8010134.

406. Speziale, P., Rindi, S. & Pietrocola, G. Antibody-based agents in the management of antibiotic-resistant staphylococcus aureus diseases. *Microorganisms* **6**, (2018) DOI:10.3390/microorganisms6010025.

407. Vuong, C., Yeh, A. J., Cheung, G. Y. C. & Otto, M. Investigational drugs to treat methicillin-resistant Staphylococcus aureus. *Expert Opin Investig Drugs* **25**, 73–93 (2016) DOI:10.1517/13543784.2016.1109077.

408. Valenciano-Bellido, S. *et al.* Targeting hemoglobin receptors IsdH and IsdB of Staphylococcus aureus with a single VHH antibody inhibits bacterial growth. *Journal of Biological Chemistry* **299**, (2023) DOI:10.1016/j.jbc.2023.104927.

409. Brown, M. *et al.* Selection and characterization of murine monoclonal antibodies to Staphylococcus aureus iron-regulated surface determinant B with functional activity in vitro and in vivo. *Clinical and Vaccine Immunology* **16**, 1095–1104 (2009) DOI:10.1128/CVI.00085-09.

410. Ebert, T. *et al.* A fully human monoclonal antibody to Staphylococcus aureus iron regulated surface determinant B (IsdB) with functional activity in vitro and in vivo. *Hum Antibodies* **19**, 113–128 (2010) DOI:10.3233/HAB-2010-0235.

411. Yeung, Y. A. *et al.* Germline-encoded neutralization of a Staphylococcus aureus virulence factor by the human antibody repertoire. *Nat Commun* **7**, (2016) DOI:10.1038/ncomms13376.

412. Bennett, M. R. *et al.* Human VH1-69 gene-encoded human monoclonal antibodies against staphylococcus aureus IsdB use at least three distinct modes of binding to inhibit bacterial growth and pathogenesis. *mBio* **10**, (2019) DOI:10.1128/mBio.02473-19.

413. Ezzeddine, Z. & Ghssein, G. Towards new antibiotics classes targeting bacterial metallophores. *Microb Pathog* **182**, (2023) DOI:10.1016/j.micpath.2023.106221.

414. Braun, V., Pramanik, A., Gwinner, T., Köberle, M. & Bohn, E. Sideromycins: Tools and antibiotics. *BioMetals* **22**, 3–13 (2009) DOI:10.1007/s10534-008-9199-7.

415. Górska, A., Sloderbach, A. & Marszałł, M. P. Siderophore-drug complexes: Potential medicinal applications of the 'Trojan horse' strategy. *Trends Pharmacol Sci* **35**, 442–449 (2014) DOI:10.1016/j.tips.2014.06.007.

416. Möllmann, U., Heinisch, L., Bauernfeind, A., Köhler, T. & Ankel-Fuchs, D. Siderophores as drug delivery agents: Application of the 'trojan Horse' strategy. *BioMetals* vol. 22 615–624 Preprint at https://doi.org/10.1007/s10534-009-9219-2 (2009) DOI:10.1007/s10534-009-9219-2.

417. Neumann, W., Sassone-Corsi, M., Raffatellu, M. & Nolan, E. M. Esterase-Catalyzed Siderophore Hydrolysis Activates an Enterobactin-Ciprofloxacin Conjugate and Confers Targeted Antibacterial Activity. *J Am Chem Soc* **140**, 5193–5201 (2018) DOI:10.1021/jacs.8b01042.

418. Lin, Y. M., Ghosh, M., Miller, P. A., Möllmann, U. & Miller, M. J. Synthetic sideromycins (skepticism and optimism): selective generation of either broad or narrow spectrum Gram-negative antibiotics. *BioMetals* (2019) doi:10.1007/s10534-019-00192-6 DOI:10.1007/s10534-019-00192-6.

419. Milner, S. J. *et al.* Staphyloferrin A as siderophore-component in fluoroquinolone-based Trojan horse antibiotics. *Org Biomol Chem* **11**, 3461–3468 (2013) DOI:10.1039/c3ob40162f.

420. Ballouche, M., Cornelis, P. & Baysse, C. Iron Metabolism: A Promising Target for Antibacterial Strategies. *Recent Pat Antiinfect Drug Discov* **4**, 190–205 (2009) DOI:10.2174/157489109789318514.

421. Cela, E. M., Urquiza, D., Gómez, M. I. & Gonzalez, C. D. New Weapons to Fight against Staphylococcus aureus Skin Infections. *Antibiotics* **12**, (2023) DOI:10.3390/antibiotics12101477.

422. Tripathi, A. *et al.* Baulamycins A and B, broad-spectrum antibiotics identified as inhibitors of siderophore biosynthesis in staphylococcus aureus and bacillus anthracis. *J Am Chem Soc* **136**, 1579–1586 (2014) DOI:10.1021/ja4115924.

423. Challis, G. L. A widely distributed bacterial pathway for siderophore biosynthesis independent of nonribosomal peptide synthetases. *ChemBioChem* **6**, 601–611 (2005) DOI:10.1002/cbic.200400283.

424. Gupte, A. *et al.* Inhibition of siderophore biosynthesis by 2-triazole substituted analogues of 5'-O-[N-(salicyl)sulfamoyl]adenosine: Antibacterial nucleosides effective against Mycobacterium tuberculosis. *J Med Chem* **51**, 7495–7507 (2008) DOI:10.1021/jm8008037.

425. Neres, J. *et al.* Inhibition of siderophore biosynthesis in Mycobacterium tuberculosis with nucleoside bisubstrate analogues: Structure-activity relationships of the nucleobase domain of 5'-O-[N-(salicyl)sulfamoyl]adenosine. *J Med Chem* **51**, 5349–5370 (2008) DOI:10.1021/jm800567v.

426. Ferreras, J. A., Ryu, J. S., Di Lello, F., Tan, D. S. & Quadri, L. E. N. Small-Molecule Inhibition of Siderophore Biosynthesis in Mycobacterium Tuberculosis and Yersinia Pestis. *Nat Chem Biol* **1**, 29–32 (2005) DOI:10.1038/nchembio706.

427. McLellan, T. Electrophoresis Buffers for Polyacrylamide Gels at Various pH. *Anal Biochem* **126**, 94–99 (1982).

428. De Bei, O. Complex between S. aureus hemophore and human hemoglobin as a target for novel antimicrobial agents: from complex characterization to compounds identification. (Università degli Studi di Parma, Parma, 2019).

429. Cozzi, M. *et al.* Chasing new targets to fight antimicrobial resistance: identification of small molecules affecting the interaction of human hemoglobin with the IsdB hemophore of Staphylococcus aureus. *ChemRxiv. This content is a preprint and has not been peer-reviewed.* Preprint at https://doi.org/10.26434/chemrxiv-2024-h23vm (2024) DOI:10.26434/chemrxiv-2024-h23vm.

430. Segel, I. H. *Enzyme Kinetics: Behavior and Analysis of Rapid Equilibrium and Steady-State Enzyme Systems*. (1993).

431. Marchesani, F. *et al.* A novel assay for phosphoserine phosphatase exploiting serine acetyltransferase as the coupling enzyme. *Life* **11**, (2021) DOI:10.3390/life11060485.

432. Ferreira, C. M. H., Pinto, I. S. S., Soares, E. V. & Soares, H. M. V. M. (Un)suitability of the use of pH buffers in biological, biochemical and environmental studies and their interaction with metal ions-a review. *RSC Adv* **5**, 30989–31003 (2015) DOI:10.1039/c4ra15453c.

433. Ding, Y. *et al.* Metabolic sensor governing bacterial virulence in Staphylococcus aureus. *Proc Natl Acad Sci U S A* **111**, E4981–E4990 (2014) DOI:10.1073/pnas.1411077111.

434. Itaya, K. & Ui, M. A New Method For The Colorimetric Determination Of Inorganic Phosphate. *Clin. Chim. Acta* **14**, 361–366 (1966).

435. Pegan, S. D., Tian, Y., Sershon, V. & Mesecar, A. D. A Universal, Fully Automated High Throughput Screening Assay for Pyrophosphate and Phosphate Release from Enzymatic Reactions. *Comb Chem High Throughput Screen* **13**, 27–38 (2010).

436. Phosphate Assay Kit Catalog Number MAK308. *Merck*.